The Henryk Niewodniczański
INSTITUTE OF NUCLEAR PHYSICS
Polish Academy of Sciences
Kraków
October 2017

REAL TIME RADIATION DOSE ASSESSMENT AT CIVIL FLIGHT ALTITUDES DUE TO GALACTIC COSMIC RAYS AND SPONTANEOUS SOLAR PARTICLE EVENTS

PhD Thesis
by Marcin Latocha, MSc

Advisory supervisor

Dr Peter Beck, MSc, MBA
Seibersdorf Laboratories
A-2444 Seibersdorf
Austria

Supervisor

Dr hab. Maciej Budzanowski (prof. IFJ PAN)
Institute of Nuclear Physics
Polish Academy of Sciences
Kraków, Poland

For the memory of my brother, Wojciech
(✶1977 – ✞2008)

Contents

List of Figures

List of Tables

List of acronyms and abbreviations

ACR	Anomalous Cosmic Radiation
AIT	Austrian Institute of Technology (formerly ARCS)
ALARA	As Low As Reasonably Achievable
ARCS	Austrian Research Centers (since 2007 AIT and Seibersdorf Laboratories)
AU	Astronomical Unit
AVIDOS	Aviation Dosimetry
CAATER	Co-ordinated Access to Aircraft for Transnational Environmental Research
CERF	CERN-EU High Energy Reference Field
CME	Coronal Mass Ejection
DOSMAX	Dosimetry of aircrew exposure to radiation during solar maximum
EASA	European Aviation Safety Agency
EC	European Commission
ESA	European Space Agency
EURADOS	European Radiation Dosimetry Group
FAQ	Frequently Asked Questions
FWHM	Full Width at Half Maximum
GCR	Galactic Cosmic Radiation
GLE	Ground Level Enhancement
GOES	Geostationary Operational Environment Satellites
HTML	Hypertext Markup Language
HZE	High-Z High-Energy (particles)
ICRP	International Commission on Radiological Protection
ICRU	International Commission on Radiation Units and Measurements
IGRF	International Geomagnetic Reference Field
ISO	International Standard Organization
iTL	iThemba Labs
JAA	Joint Aviation Authorities
LET	Linear Energy Transfer
NASA	National Aeronautics and Space Administration
NOAA	National Oceanic and Atmospheric Administration
NSO	Non-Space System Operation
PC	Personal Computer
PIAF	PTB's Ion Accelerator Facility
PIC	Precision Ionization Chamber
PMMA	Poly(methyl methacrylate) - Plexiglas
PTB	Physikalisch-Technische Bundesanstalt
SCR	Solar Cosmic Radiation
SDP	Solar Deceleration Potential
SEP	Solar Energetic Particle
SILSO	Sunspot Index and Long-term Solar Observations
SOAP	Simple Object Access Protocol
SPS	Super Proton Synchrotron
SSA	Space Situational Awareness
SSCC	Space Weather Coordination Centre
SWE	Space Weather (portal)
TEPC	Tissue Equivalent Proportional Counter
TSP	Termination Shock Particles
UCL	Université Catholique de Louvain
WSDL	Web Service Description Language

Introduction and motivation

Cosmic radiation from the Sun and outer space is part of our natural environment. Until recent decades, cosmic radiation was considered of minor relevance however, recent technological developments in aviation and space sectors awaken a concern about possible effects of cosmic radiation on humans and technical infrastructure.

Already from 1990s, the European Commission supported several projects focused on characterization of radiation exposure due to cosmic radiation. International institutes worked on aircrew exposure assessment by characterizing instruments' responses, performing in-flight measurements, developing and verifying codes estimating radiation dose. In 1996, the European Community Council Directive 96/29/EURATOM laid down in its Article 42, a basic safety standard for the protection of aircrew against cosmic radiation considered as a natural radiation source. Due to an initiative by the European Radiation Dosimetry Group (EURADOS), a working group on Aircraft Crew Dosimetry was established with the aim to perform measurements of cosmic radiation exposure, and develop models and codes estimating galactic cosmic ray exposure. Furthermore, on an international level, ISO standards were developed to set conceptual basis for cosmic radiation measurements (ISO 20785-1:2006) and provide standards on characterization of instruments (ISO 20785-2:2011). In 2010, the International Commission on Radiological Protection (ICRP) and International Commission on Radiation Units and Measurements (ICRU) published a joint report with a set of reference data derived from measurements for the purpose of validation and benchmarking of codes assessing galactic cosmic radiation exposure in routine radiation protection practice. By now, the European Commission's directive is implemented in laws of most European countries. Recently published ICRP Publication 132 strengths aspects of radiological protection from cosmic radiation for pilots and additionally is dragging experts' attention towards radiation exposure of frequent flyers and pubic. ICRP notes that codes estimating radiation exposure due to GCR in radiation protection service are generally accepted and widely used in practice.

Solar phenomena, like solar flares or coronal mass ejections (CME) are sudden ejections of solar mass into interplanetary space. Occurrence of solar energetic particle (SEP) events is currently not predictable, and not all of them hit and reach the Earth's surface causing an increased and measured dose rate on the ground - so-called ground level enhancements (GLE). While there are many measurements of radiation exposure due to galactic cosmic radiation, measurements due to solar energetic particle events are scarce. Some codes estimating radiation exposures due to SEP were developed in the past, but comparison with measurements showed, that they still need to be improved. Dose assessment due to SEP is a scientifically challenging, laborious and a time-consuming task performed only by experts. First results usually are published few weeks or months after the event. A system providing nowcasting of GCR and SEP induced radiation environment in Earth's atmosphere is of great

importance for radiation protection institutions, aviation, governmental organizations, research, and public.

My motivation for the work presented here were scientific investigations, developments and justifications of a model that could be used in radiation protection service in Austria fulfilling the basic safety standards of EC Directive 96/29/EURATOM and Austrian governmental regulations on radiation protection of aircraft crew. I was also motivated to increase public awareness on cosmic radiation at civil flight altitudes and to develop an easy to use tool for self-assessment of radiation doses on-board aircrafts, what stays in line with the recent ICRP recommendations on radiological protection from cosmic radiation for pilots, frequent flyers and public.

Abstract

The main goal of my work is to present scientific investigations, developments and justifications of a semi-empirical model for real-time radiation dose assessment at civil flight altitudes due to galactic cosmic radiation (GCR) and solar energetic particles (SEP) events, that I have carried out as scientific employee at the Seibersdorf Labor GmbH (former Austrian Research Center Seibersdorf) in Austria. All presented results have been published in journals, conferences and scientific workshops.

In the chapter 1 of this work, I describe a brief introduction to the basics of microdosimetry as one of methods that is used, and which I used, in measurements of cosmic radiation.

In chapter 2, I present short description of cosmic radiation with the aim to emphasize those aspects of this topic, which are important for the work that I present here.

In the next chapter 3, I describe a summary of the usage of a tissue equivalent proportional counter (TEPC) for measurements in various radiation fields. I performed calibration of that instrument and practically used it to exercise measurements in laboratory radiation fields (e.g. CERF at CERN).

In chapter 4, I am describing several cosmic radiation measurements carried out on-board aircraft. I used the TEPC dosimeter system in the international campaign CAATER (Co-ordinated Access to Aircraft for Transnational Environmental Research). I participated in the preparation and the design of the campaign, and I analyzed the measurements I have performed. I have summarized the results in a joint publication with me as the first author. Taking advantage of my experience in information technology, I designed and took care of a database for on-board measurements of cosmic radiation performed by various institutes for EURADOS working group on Aircraft Crew Dosimetry. The gathered data was published as a EURADOS report as well as a report on Aircraft Crew Dosimetry by the European Commission. Regarding on-board measurements during extraordinary solar conditions, as part of a team at Seibersdorf Laboratories, I analyzed TEPC data measured during the so-called Halloween Storms, a solar storm during October and November 2003. The measurements and data analysis have been published with me as a co-author.

In chapter 5, I present investigations on radiation doses in atmosphere due to cosmic radiation using numerical simulations. First, I simulated radiation exposure in the atmosphere due to GCR. Further, I performed and analyzed numerical simulations of three different solar energetic particle events that led to temporary elevated radiation levels not only in the atmosphere but also on the Earth – so-called ground level enhancements (GLE). Results of these investigations are published in a report by the Seibersdorf Laboratories for the Austrian governmental office for radiological protection.

Based on the experience that I got in practical measurements and numerical simulations, I describe in chapter 6 the design of a semi-empirical model for the assessment of radiation dose due to cosmic radiation at civil flight altitudes. Model that

I propose consists of two parts. The first part models radiation doses only due to galactic cosmic radiation (GCR). Second, also for additional doses due to SEP.

The first part is called AVIDOS-FDS (AVIDOS Flight Dosimetry Service), and is integrated with the accredited flight-dosimetry-service of Seibersdorf Laboratories. The flight-dosimetry-service is fully compliant with EN ISO/IEC 17025 standard and is offered to Seibersdorf Laboratories' customers. The second part is called AVIDOS 2.0 and is used by Seibersdorf Laboratories as its service federated with Space Weather Service Network – an internet portal of the European Space Agency, ESA (http://swe.ssa.esa.int/swe). Users registered at ESA Space Weather portal, can access four different user-modes of AVIDOS 2.0. AVIDOS 2.0 at ESA's portal is the first Europe-wide publicly available software for real-time radiation dose assessment at civil flight altitudes due to galactic cosmic radiation (GCR) and solar energetic particle (SEP) events.

In chapter 7, I summarize the presented work. In chapter 8, I give an outlook on planned further activities in the field of aircrew dosimetry.

Streszczenie

Głównym celem mojej pracy jest przedstawienie badań naukowych, opracowanie oraz wdrożenie semi-empirycznego modelu do oszacowania w czasie rzeczywistym dawek promieniowania kosmicznego na wysokościach cywilnego ruchu lotniczego na skutek galaktycznego promieniowania kosmicznego (galactic cosmic radiation - GCR) oraz spontanicznych wybuchów słonecznych (solar energetic particles - SEP), które dokonałem jako pracownik naukowy w Seibersdorf Labor GmbH (dawniej Austrian Research Center Seibersdorf) w Austrii. Wszystkie zaprezentowane wyniki zostały opublikowane w czasopismach, na konferencjach i warsztatach naukowych.

W rozdziale pierwszym mojej pracy zamieszczam krótki wstęp do podstaw mikrodozymetrii jako jednej z metod stosowanych, również przeze mnie, w pomiarach promieniowania kosmicznego.

W rodziale drugim zamieszczam zarys tematyki promieniowania kosmicznego starając się zaznaczyć podstawowe aspekty zagadnienia promieniowania kosmicznego ważne z punktu widzenia ninejszej pracy.

W rozdziale następnym, trzecim, opisuję podsumowanie zastosowania tkankopodobnego licznika proporcjonalnego (TEPC) do pomiarów różnych pól promieniowania. Dokonałem kalibracji tego instrumentu oraz użyłem go w pomiarach laboratoryjnych pól promieniowania (np. CERF w CERN).

W rozdziale czwartym opisuję kilka pomiarów promieniowania kosmicznego jakie dokonałem na pokładzie samolotu. W międzynarodowej kampanii pomiarowej CAATER (Co-ordinated Access to Aircraft for Transnational Environmental Research) do pomiarów użyłem licznika TEPC. Uczestniczyłem w przygotowaniach i projektowaniu kampanii, wykonałem i zanalizowałem własne pomiary. Wyniki podsumowałem, jako pierwszy autor, we wspólnej publikacji. Korzystając ze swojego doświadczenia informatycznego zaprojektowałem i opiekowałem się bazą danych dla wyników pomiarów promieniowania kosmicznego dokonanych na pokładach samolotów przez różne instytuty dla grupy roboczej EURADOS zajmującej się zagadnieniem ekspozycji personelu lotniczego na promieniowanie kosmiczne. Zebrane dane zostały opublikowane jako raport EURADOS oraz jako raport Komisji Europejskiej nt. ekspozycji personelu lotniczego na promieniowanie kosmiczne. Jako członek grupy zajmującej się ekspozycją personelu lotniczego na promieniowanie kosmiczne w Seibersdorf Laboratories, analizowałem niezwykle ciekawe pomiary dokonane przy użyciu TEPC podczas spontanicznych wybuchów na Słońcu w październiku i listopadzie 2003 roku – tak zwanych Halloween Storms. Pomiary te i analiza danych zostały opisane w publikacji, której byłem współautorem.

W rozdziale piątym prezentuję badania nad dawkami promieniowania w atmosferze na skutek promieniowania kosmicznego, przy użyciu numerycznych symulacji komputerowych. Najpierw wykonałem symulacje galaktycznego promieniowania kosmicznego (GCR) w atmosferze. Następnie wykonałem i analizowałem symulacje komputerowe trzech różnych spontanicznych wybuchów słonecznych, które spowodowały tymczasowy wzrost poziomów promieniowania nie tylko w atmosferze,

lecz także na Ziemi – tak zwane ground level enhancements (GLE). Wyniki tych badań zostały opublikowane w raporcie Seibersdorf Laboratories dla austriackiego rządowego Urzędu Ochrony Radiologicznej.

Na podstawie doświadczenia zdobytego podczas wykonywania praktycznych pomiarów jak i symulacjach komputerowych, w rodziale szóstym, opisuję projekt semi-empirycznego modelu do oszacowania dawek promieniowania kosmicznego na pokładach samolotów. Model, który proponuję składa się z dwóch cześci. Pierwsza oszacowuje dawki tylko dla galaktycznej części promieniowania kosmicznego (GCR). Druga, oszacowuje dawki również dla spontanicznych wybuchów słonecznych (SEP).

Pierwsza część modelu ma nazwę AVIDOS-FDS (AVIDOS Flight Dosimetry Service) i jest zintegrowana z akredytowanym serwisem dozymetrycznym prowadzonym przez Seibersdorf Laboratories dla personelu lotniczego. Serwis ten jest w pełni zgodny ze standardem EN ISO/IEC 17025 i jest oferowany przez Seibersdorf Laboratories dla swoich klientów. Druga część modelu ma nazwę AVIDOS 2.0 i jest internetowym serwisem Seibersdorf Laboratories zintegrowanym z portalem internetowym Europejskiej Agencji Kosmicznej (ESA) – Space Weather Service Network (http://swe.ssa.esa.int/swe). Użytkownicy zarejestrowani na portalu pogody kosmicznej ESA mają dostęp do czterech różnych modułów AVIDOS 2.0. Program AVIDOS 2.0 na portalu ESA jest pierwszym w Europie darmowym i ogólnodostępnym programem komputerowym działającym w czasie rzeczywistym służącym do oszacowania dawek promieniowania pochodzących od galaktycznego promieniowania kosmicznego (GCR) i spontanicznych wybuchów słonecznych (SEP).

W rozdziale siódmym podsumowuję zaprezentowaną pracę. W rozdziale ósmym przedstawiam perspektywy planowanych dalszych działań dotyczących zagadnienia ekspozycji personelu lotniczego na promieniowanie kosmiczne.

1. Introduction to microdosimetry

There is no sharp definition of microdosimetry. According to the International Commission on Radiation Units and Measurements (ICRU), the main objective of microdosimetry is to improve understanding of radiation effects and to develop concepts to relate principal features of the absorption of ionizing radiation in matter to the size (and nature) of affected structures [1].

Particles traversing a matter interact with its atoms and molecules losing their energy. If in such interaction, one or more matter's electrons are liberated, an ionization process occurred. Ionizing radiation are charged particles (e.g. protons, electrons) or uncharged ones (e.g. photons, neutrons) that can produce ionizations (or nuclear reactions leading to ionizations) in a medium. Microdosimetry studies the number, magnitude, spatial and temporal distribution of energy deposits. It is a systematic study with system of concepts, physical quantities and their measurements. Below author reproduces a set of definitions of quantities defined ICRU that are used in this work.

1.1. Radiometric quantities

Radiometric quantities characterize the radiation field (e.g. photons, electrons, protons, neutrons) at the point of interest. This characterization refers either to number of particles or to their energy. Here, based on ICRU Report No. 85 [2], author presents only those basic radiometric quantities that refer to the number of particles.

The **particle number, *N***, is the number of the (emitted, transferred or received) particles.

Flux, $\dot{N}$, is the increment of particle number dN in the time interval dt, (unit: s^{-1})

$$\dot{N} = \frac{\mathrm{d}N}{\mathrm{d}t}$$

The **fluence, Φ,** is the number of particles dN incident on a sphere of cross-sectional area da, (unit: m^{-2})

$$\Phi = \frac{\mathrm{d}N}{\mathrm{d}a}$$

For practical applications, especially for numerical simulations, it is useful to note that:

1. Since particle number N does not distinguishes a selected direction, then flux describes particles emitted in (or transferred or received from) all directions.

2. The use of sphere of cross-sectional area d*a* in the definition of fluence means that fluence considers that the area d*a* is perpendicular to the direction of each particle. Therefore, fluence does not distinguishes the direction. In a scenario with selected direction, this selection must be taken into account. For example, when a parallel beam is incident at an angle θ (with respect to normal direction) on a given surface then the fluence is $\Phi\, cos(\theta)$.
3. In numerical simulations, fluence Φ is often expressed as the sum of the lengths of particles trajectories d*l* in the volume d*V*:

$$\Phi = \frac{\mathrm{d}l}{\mathrm{d}V}$$

1.2. Quantities related to interactions

In previous chapter, author presented basic quantities to characterize radiation field. Particles of a radiation filed interact with matter. Here, based on ICRU Report No. 85 [2], author presents selected quantities that are related to interactions.

Mass stopping power of a material, for charged particles of a given type and energy, is the mean energy lost, d*E,* by those particles when traversing a distance d*l* in the material of density, ρ.

$$\frac{S}{\rho} = \frac{1}{\rho}\frac{\mathrm{d}E}{\mathrm{d}l}$$

Unit of mas stopping power is: eV m^2 kg^{-1} (or conveniently multiplied e.g. MeV cm^2 g^{-1})

Mass stopping power focuses on energy loss of the particle. It has three components:

1. mass electronic stopping power (due to interactions with atomic electrons leading ionizations or excitations),
2. mass radiation stopping power (due to emission of bremsstrahlung in the electric field of atomic electrons or nuclei),
3. mass nuclear stopping power (due to elastic Coulomb interactions in which recoil energy is imparted to atoms).

Linear Energy Transfer, ***LET***, or **restricted linear electronic stopping power**, $\mathbf{L_\Delta}$, of a material for charged particles of a given type and energy, is the mean energy lost, d*E,* of those particles due to electronic interactions when traversing a distance

d*l*, but without the mean sum of kinetic energies, greater than Δ, of all electrons released when traversing a distance d*l*.

$$L_\Delta = \frac{\mathrm{d}E_\Delta}{\mathrm{d}l}$$

In other words, LET considers “locally transferred” energy, that is, energy lost by primary charged particles in interactions with electrons along the distance dl, but without energies taken away by secondary electrons having initial kinetic energy greater than Δ. The unit of LET is joule per meter (J m^{-1}) but also commonly used is keV μm^{-1}.

L_∞ (often denoted as *L* or LET) is the (unrestricted) linear energy transfer where all δ-rays are taken into account. L_∞ is equal to the linear electronic stopping power. L_0 refers to the energy lost that does not reappear as kinetic energy of secondary electrons.

LET is a measure of an average ionization density along the path of radiation.

1.3. Dosimetric quantities

Effects of radiation on matter depend on radiation field and on interactions between radiation and matter (precisely, on interaction coefficients – cross-sections). Radiation interacts with matter in a series of processes in which particle energy is converted and finally deposited in the matter. Dosimetric quantities describe these processes and provide physical measure to correlate with effects. Based on ICRU Report No. 85 [2], author presents selected dosimetric quantities.

The **energy deposit**, ε_i, is the elementary dosimetric quantity describing process of deposition of energy. It is the energy deposited in a single interaction *i*:

$$\varepsilon_i = \varepsilon_{in} - \varepsilon_{out} + Q$$

where:

ε_{in} – energy of the incident ionizing particle (without rest energy) interacting in the point *i*

ε_{out} – sum of energies of all ionizing particles leaving the interaction (without rest energy)

$Q_{\Delta m}$ – the change in rest energies of the nucleus and of the all particles involved in the interaction.

The **energy imparted**, **ε**, to matter in a volume is the sum of all energy deposits, ε_i, which took place in that volume.

$$\varepsilon = \sum_i \varepsilon_i$$

Energy imparted is due to one or more energy deposition events e.g. coming from several independent particle trajectories but resulting in energy deposition events in the considered volume.

Both, energy deposit and energy imparted are stochastic quantities. The unit of energy deposit and energy imparted is joule (J) but in practice expressed also in eV.

The **absorbed dose**, ***D***, is defined as the mean value of the energy imparted into matter, $\bar{\varepsilon}$, per unit mass, *m*, at the point of interest.

$$D = \frac{\mathrm{d}\bar{\varepsilon}}{\mathrm{d}m}$$

Absorbed dose is a non-stochastic quantity. The unit for absorbed dose is joule per kilogram (J kg^{-1}). The special name for unit of absorbed dose is gray (Gy).

1.4. Microdosimetric quantities

While dosimetry investigates the mean imparted energy in a point of irradiated volume, microdosimetry emphasizes stochastic nature of energy deposition events. Microdosimetry studies the whole energy deposition process and results are expressed as probability distributions of energy depositions in a volume that is crossed by a single ionizing particle. In microdosimetry, new stochastic quantities have been introduced to conceptually replace the old non-stochastic ones [1].

A random analogue of absorbed dose *D* is the quantity **specific energy**, ***z*** defined as

$$z = \frac{\varepsilon}{m}$$

where ***ε*** is the energy imparted by ionizing radiation to matter of mass *m*. Specific energy and absorbed dose are defined as quotient of energy by mass and have similar units – joule per kilogram (J kg^{-1}). The special name for unit of specific energy is gray (Gy). Specific energy is a stochastic quantity and one can consider its probability distribution function or its probability density function (see Appendix A). The analogy between absorbed dose, *D*, and specific energy, *z*, is:

$$D = \lim_{m \to 0} \bar{z}$$

Microdosimetric quantity analogous to linear energy transfer LET, is the **lineal energy**, ***y***, defined as

$$y = \frac{\varepsilon}{\bar{l}}$$

where ε is the energy imparted to the matter in a volume of interest by a single energy deposition event and $\bar{l}$ is mean chord length of the volume.

Mean chord length of a volume is its geometrical property, and is the mean length of randomly oriented chords in that volume. For a convex body of the volume *V*, and the surface area *S*, the mean chord length is $\bar{l} = 4V/S$.

The difference between LET and *y* is that LET considers mean energy lost, d*E*, in electronic collisions by a charged particle traversing a distance d*x* and includes energy transferred to δ-rays while lineal energy is subject to geometric cutoff: ε is only the energy deposited in the volume *V*.

Both, linear energy transfer and lineal energy are defined as quotient of energy by length and therefore have similar units – J/m, or e.g. keV/µm. Lineal energy is a stochastic quantity and one can consider its probability distribution function or its probability density function (see Appendix A).

1.5. Quantities used in radiological protection

Dosimetric quantities have been developed to assess the dose from radiation exposure. The purpose of protection quantities is to specify exposure limits to ensure that the occurrence of stochastic health effects is kept below acceptable levels [3]. Quantities used in radiological protection base on measurements of energy deposited in human tissues and organs, and aim at a relation between radiation dose to radiation risk. For this, two facts must be taken into account. First: variations in the biological effectiveness of radiations of different quality, and second: variations in the sensitivity of organs and tissues to ionizing radiation.

In 1977, in its Publication 26, the International Commission on Radiological Protection (ICRP) introduced two radiological protection quantities: dose equivalent and effective dose equivalent [4]. In 1990, in its Publication 60 [5], the ICRP introduced conceptually new protection quantities based on radiation weighting factors and tissue weighting factors – the equivalent dose and effective dose. In 2007, in its Publication 103 [3], the ICRP revised and updated the radiation weighting factors and tissue weighting factors. In 2011, the OECD (Organisation for Economic Co-operation and Development) Nuclear Energy Agency (NEA) released a publication [6] that presents the evolution of the ICRP Recommendations identifying the major changes in the underlying science and its understanding, as well as development and evolution of protection policy.

Radiation weighting factors, w_R, were introduced (ICRP-60 [5]) to weight the absorbed dose with the type and energy of the radiation in order to assess radiation effects. Comparing recommendations from ICRP-60 [5] and ICRP-103 [3] two important changes have to be noted. For protons radiation weighting factor was decreased from five to two. For neutrons, the step function was replaced by continuous one with a decrease of w_R in low energy range.

Table 1 Radiation weighting factors.

Radiation type and energy	Radiation weighting factor (ICRP-60) w_R	Radiation weighting factor (ICRP-103) w_R
Photons	1	1
Electrons, muons	1	1
Neutrons < 10 keV 10 keV – 100 keV 100 keV – 2 MeV 2 MeV – 20 MeV > 20 MeV	 5 10 20 10 5	 $2.5+18.2e^{-[\ln(E_n)]^2/6}, E_n < 1MeV$ $5.0+17.0e^{-[\ln(2E_n)]^2/6}, 1MeV \le E_n \le 50MeV$ $2.5+3.25e^{-[\ln(0.04E_n)]^2/6}, E_n > 50MeV$
Protons	5	2
Alpha particles, fission fragments, heavy nuclei	20	20

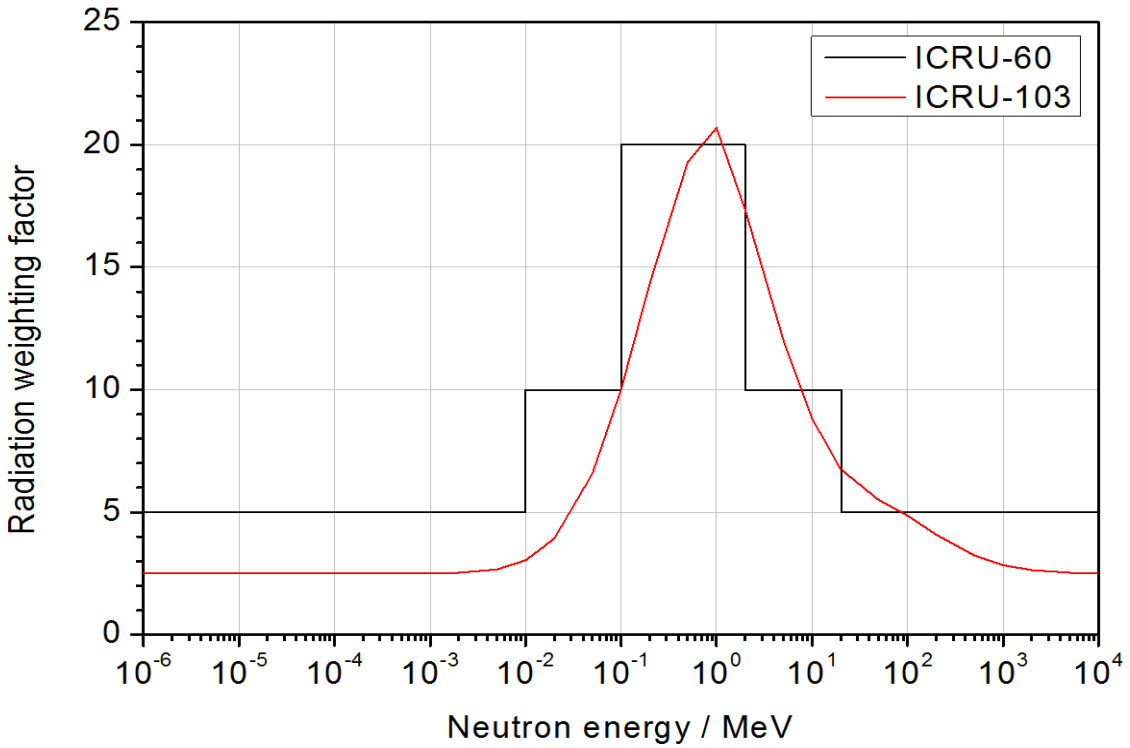

Figure 1 Radiation weighting factors, w_R, for neutrons as recommended in ICRU-60 (black step function) and ICRP-103 (continuous red curve).

Different organs or tissues show different sensitivity due to stochastic radiation damages caused by the same type of radiation [5]. This fact was reflected by establishing **tissue weighting factors**, w_T. Those factors were revised based on epidemiological studies and risk assessment. A modified set was published in 2007 [3]. Table 2 presents tissue weighting factors as recommended in ICRU-60 [5] and ICRU-103 [3].

Table 2 Tissue weighting factors as recommended in ICRP-60 (left) and ICRP-103 (right)

Organ	w_T (ICRU-60)		Organ	w_T (ICRU-103)
Gonads	0,20		Bone marrow (red), Colon, Lung, Stomach, Breast, Adrenals, remainder tissues	0.12
Bone marrow (red), Colon, Lung, Stomach	0,12		Gonads	0.08
Bladder, Breast, Liver, Esophagus, Thyroid gland	0,05		Bladder, Liver, Esophagus, Thyroid	0.04
Skin, Bone surface	0,01		Bone surface, Brain, Salivary glands, Skin	0.01
Bone surface	0,01			
Adrenals, brain, small intestine, kidney, muscle, pancreas, spleen, thymus, uterus (the weighting factor 0.05 is applied to the average dose of these organs)	0,05			

The protection quantity equivalent dose, H_T (ICRP-60 [5]), is conceptually different from the dose equivalent, H (ICRP-26 [4]). The dose equivalent, H, is based on the absorbed dose at a "point" in tissue and weighted by quality factor Q (see chapter 1.6) which is related to the LET. New quantity, the equivalent dose H_T, is based on average absorbed dose in a tissue or an organ, $D_{T,R}$, and weighted by the radiation weighting factors w_R for the radiation(s) impinging on the body.

The **equivalent dose H_T**, in a tissue or organ is defined as

$$H_T = \sum_R w_R D_{T,R}$$

where $D_{T,R}$ is the mean absorbed dose in considered tissue or organ T, produced by radiation of type R, and w_R is corresponding radiation weighting factor for radiation of the type R. The sum goes over all types of radiation involved. Since w_R are

dimensionless, the SI unit of equivalent dose is J kg^{-1}, but to distinguish it from the unit of absorbed dose (unit of special name: gray) its special name is sievert (Sv).

The effective dose, *E*, is intended to provide means for handling non-uniform irradiation situations, when various tissues or organs are irradiated. Since different tissues or organs show different sensitivity to the same type of radiation, equivalent doses, H_T, must be weighted by tissue weighting factors.

The **effective dose**, ***E***, is given as:

$$E = \sum_T w_T H_T = \sum_T w_T \sum_R w_R D_{T,R}$$

where H_T is the equivalent dose in the tissue or organ T, and w_T is the corresponding tissue weighting factor. The unit of effective dose is J kg^{-1} with special name: sievert (Sv).

The quantity $D_{T,R}$ cannot be experimentally measured; therefore both quantities equivalent dose and effective dose are not measurable in practice. For measurement purposes, operational quantities are used (see 1.6).

After the publication of the ICRP103 recommendations, questions have arisen on practical applications of effective dose and confusion between equivalent dose and effective dose. To address these issues, a Task Group 79 in the IRCP has been created. The Task Group recommends [7] that equivalent dose is no longer used as protection quantity but only as an intermediate steps in calculations of effective dose. The Task Group 79 also recommends that effective dose (introduced for risk management purposes for risk limitation and optimization) should not be used as a measure of risk (particularly for low doses) but only as a rough indicator of possible risk. Both recommendations are under ICRP considerations. Definitions of radiological protection quantities have a dynamic history driven mostly by new findings and experimental data. Author expects a publication of new ICRP's recommendations coming soon.

1.5.1. Dose limits

On the basis on the effective dose and the equivalent dose the ICRP in its Publication 60 [5] established recommendations on dose limits. Dose limits are defined separately for public and occupationally exposed workers, and additionally for stochastic and deterministic effects – Table 3. The ICRP-103 recommendations [3] did not change the limits.

Table 3 Dose limits as recommended by ICRP.

	Quantity	Occupational dose limits	Public dose limits
Based on stochastic effects:	Effective dose, *E*	50 mSv/y But not more than 20 mSv/y averaged over 5 years	1 mSv/y And, if needed, higher value, but the average over 5 years should not exceed 1 mSv/y
Based on deterministic effects	Equivalent dose, *H* to:		
	Lens of eye	150 mSv/y	15 mSv/y
	Skin	500 mSv/y	50 mSv/y
	Hands and feet	500 mSv/y	-

1.5.2. Reference levels

Since chapters 4, 5 and 6 of this work discuss measurements and models for dose assessment at aviation altitudes, author presents here few considerations on reference levels for aircrew. A reference level is the dose above which it is judged that it is inappropriate to allow such exposures to occur. It is a dose level at which protective actions should be planned and optimized but taking into account ALARA principles.

In 1996, the European Community Council Directive 96/29/EURATOM [8] laid down, in its Article 42, a basic safety standard for the protection of aircraft crew against cosmic radiation considered as a natural radiation source. In 1997, European Commission published a more technical interpretation of the Article 42 requirements [9]. For the first time a conventional set of control limits appeared:

- no further control for aircrew with dose less than 1 mSv/year,
- for doses 1 mSv/year – 6 mSv/year: individual dose estimate is required,
- for doses greater than 6 mSv/year: record keeping, medical surveillance (“highly exposed aircrew”)

The interpretation also says:

- although frequent flyers are not mentioned in the EC directive, they should have dose determination similar to that of aircraft crew,
- computer programs may be used to determine doses below 6 mSv/year,
- for flights at altitudes higher than 15 km, an active dosemeters to detect variation in dose levels (e.g. due to solar flares) should be on board.

In 2007, civil aviation organizations like Joint Aviation Authorities – JAA (JAA has been disbanded in 2009, its functions overtook the European Aviation Safety Agency – EASA) – released an operational standard [10] adopting the published interpretations.

By 2009, the EC directive has been implemented into law in many European countries [11]. In 2012, the European ALARA Network conducted a survey on how the radiation protection requirements for aircraft crew have been implemented in selected European countries [12]. Conclusion from these two surveys shows that in most countries, individual doses are estimated using computational codes, and the conventional limit of 6 mSv/year is set, however, in some countries there are lower limits. Specific requirements (additional protection actions) are implemented if exposure is higher than 6 mSv/year.

Recently, a new ICRP report has been published [13]. It focuses on radiological protection from cosmic radiation in aviation. In its report, the ICRP recommends a graded approach for the implementation of optimization principle of radiological protection. Radiation exposure of occasional flyers due to cosmic radiation is considered as negligible, but passengers should have access to general information about cosmic radiation. The ICRP very clearly notes a group of public that travels by air for private or duty reasons - frequent flyers. Commission recommends that this group should not only have access to general information about cosmic radiation but encourages self-assessment of their doses, and if necessary, to limit flight frequency. For a fraction of frequent flyers which exposure is comparable to those of aircraft crew, the commission recommends solutions on a case-by-case basis aiming at interactions between employees and the employer. In commission's recommendation, exposure of both groups, occasional and frequent flyers, is public exposure. Finally, for the aircraft crew, the commission sustains its recommendation from ICRP-60 [5] to consider them as occupationally exposed group. For aircraft crew, the commission recommends individual educational program about cosmic radiation, assessment of dose by calculation programs, archive of the assessed dose for sufficient time, and, when cumulative dose approaches selected levels, to respect those levels by adjusting flight schedules. The commission recommends that for protection against cosmic radiation in aviation, a reference level in the range of 5 – 10 mSv/year should be selected.

1.6. Operational quantities

Based on unrestricted linear energy transfer, L_∞, in water, the **quality factor**, ***Q(L)***, has been defined in ICRP-26 [4]. It has been introduced in order to weight the absorbed dose for the biological effectiveness of the charged particles since the effects caused by radiation depend not only on absorbed dose but also on radiation type (i.e. ionization density). The quality factor at a point in tissue is given by:

$$\bar{Q} = \frac{1}{D}\int_0^\infty Q\,(L)D(L)dL$$

where *D* is the absorbed dose at that point, *D(L)* is the distribution of absorbed dose, *D*, in linear energy transfer, *L*, and *Q*(*L*) is the corresponding quality factor at the point of interest. The relation between the quality factor and unrestricted linear energy transfer was specified in ICRP-60 [5]:

Table 4 Q-L relationships according to ICRP-60 [5].

Unrestricted linear energy transfer, L_∞, in water keV μm^{-1}	**Quality factor, Q(L)**
$L_\infty \leq 10$	1
$10 < L_\infty < 100$	0.32 L - 2.2
$L_\infty \geq 100$	$300/\sqrt{L}$

For protection quantities, the quality factor Q was replaced by radiation weighting factors, w_R, in ICRP-60 [5] but it is still used in calculating the operational dose equivalent quantities used in area and individual monitoring.

To identify and quantify the effects of ionizing radiation on health (so including biological effects) in routine radiation protection applications the quantity **dose equivalent**, ***H***, was introduced. The dose equivalent at a point is defined as

$$H = \bar{Q}D = \int_0^\infty Q\,(L)D(L)dL$$

where *Q(L)* is the quality factor for particles with linear energy transfer *L*, *D(L)* is the distribution of absorbed dose, *D*, in linear energy transfer, *L*, at the point of interest. The unit for dose equivalent is joule per kilogram (J kg^{-1}) but there is also a special name – sievert (Sv).

For practical measurements, ICRU has introduced an operational quantity based upon dose equivalent – the **ambient dose equivalent**, ***H*(d)***. According to ICRU's definition, the ambient dose equivalent, *H**(*d*), at a point of interest in the actual radiation field is the dose equivalent which would be produced by the corresponding expanded and aligned field, in the ICRU sphere at a depth, *d*, on the radius opposing the direction of the aligned field. The ambient dose equivalent should be a conservative estimate the effective dose.

Terms: *expanded and aligned field* and *ICRU sphere* used in ambient dose equivalent definition need further explanation. An *expanded field* is the field that is at the point of reference but is expanded throughout the whole volume of interest in this way, that fluence and its directional and energy distributions at every point

of considered volume have the same values as in the reference point. An *expanded and aligned field* is the expanded field but the fluence is unidirectional. It is an idealized radiation field as showed in Figure 2.

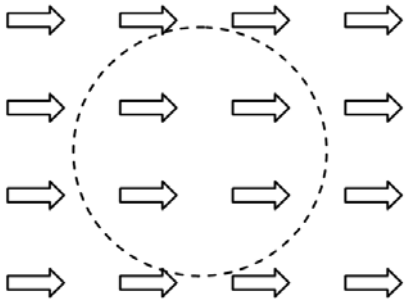

Figure 2 Schematic representation of expanded and aligned field.

The *ICRU sphere* [14] is a phantom approximating human body, and it is 30-cm diameter tissue-equivalent sphere with a density of 1 g cm^{-1} and a proper elemental composition for tissue equivalence (mass composition: 76.2% oxygen, 11.1% carbon, 10.1% hydrogen, 2.6% nitrogen).

The unit of ambient dose equivalent is the same as for dose equivalent. It is recommended that for strongly penetrating radiation a depth of 10 mm should be used – *H**(*10*).

2. Introduction to cosmic radiation

At the beginning of the XX century, radiation observed in atmosphere was believed to originate from radioactive elements of Earth's crust [15]. Between 1911 and 1913, an Austrian-American physicist, Victor Franz Hess, conducted a series of balloon flights (up to 5300 meters of altitude) and showed that the radiation increased with altitude [16]. He suggested also its extraterrestrial origin [17]. The studies of Hess were rewarded in 1936 with the Nobel Prize.

In 1925, Robert Andrew Millikan confirmed Hess's theory and gave 'cosmic rays' name to the newly discovered radiation [18, 19]. The term 'cosmic rays' is widely used in literature but may be misleading since it's known today that this radiation are not rays but high energy particles impinging the Earth (predominantly protons and helium nuclei). Terms 'cosmic radiation' or 'cosmic rays particles' are often used to avoid this misnomer.

Cosmic radiation is often distinguished between primary and secondary. As primary cosmic radiation, one considers cosmic radiation of extraterrestrial origin coming mainly from outside of the Solar system. When cosmic rays collide with nuclei of Earth's atmosphere (mainly nitrogen and oxygen), a cascade of lighter particles is produced – these particles are referred to as secondary cosmic radiation. The produced cascade has a form of a cone with a 1-2 degree of width around primary particle's path and the cascade is often described in literature as air shower.

Primary cosmic radiation is composed in about 98-99% of nuclei and about 1-2% of electrons. Protons are strongly dominating fraction (about 89-90%) of the nuclei part, alpha particles are about 9-10%, and the remaining 1% are nuclei of heavier elements – so called HZE particles [20, 21]. Composition of secondary cosmic radiation is more complex due to variety of nuclear reactions occurring in the Earth's atmosphere. Typical particles are neutrons, protons, electrons, but also mesons like positive or negative kaons and pions – which then decay into muons. Gammas and X-rays are also present in secondary cosmic radiation.

Another common way of how cosmic radiation can by divided depends on its origin:

- Solar Cosmic Radiation (SCR) also known as Solar Energetic Particles (SEP)
- Galactic Cosmic Radiation (GCR)
- Anomalous Cosmic Radiation (ACR)

2.1. Solar Cosmic Radiation

Solar cosmic radiation (SCR) is often called solar energetic particles (SEP) since this type of cosmic radiation are in fact particles released from the Sun through solar phenomena like solar wind, solar flares and coronal mass ejections (CME).

Solar wind is a continuous stream of solar mass released from Sun's corona into interplanetary space. It is fully ionized, magnetized, hot plasma and consists mainly of protons and electrons with a few heavier ions.

The main sources of solar wind are coronal holes, which are regions where the magnetic field lines of the Sun are open, and Sun's equatorial region – so called "streamer belt". Solar wind drags Sun's magnetic field outwards the Sun and forms in this way the heliospheric magnetic field (historically called interplanetary magnetic field). Due to the rotation of the Sun, this field has spiral form (garden hose effect). The simplest situation is when the Sun has a stable magnetic configuration (solar minimum). At this time, the slow solar wind originates from streamer belt (region of about 20 degree width around magnetic equator), and fast solar wind from polar coronal holes. During solar maximum, the situation is much more complex and not fully understood due to a more complex magnetic field configuration [22]. Physical properties of solar wind like density, temperature and speed vary over time and the place of origin – solar latitude and longitude. Generally, one distinguishes slow and fast solar wind. Slow solar wind has a speed of about 300 - 400 km/s, fast solar wind has a typical velocity of 750 km/s. Fluence rate varies between 1 – 100 particles/cm^2/s, density varies between 0.4 – 100 part/cm^3, and dragged-in magnetic field varies in ranges 0.2 – 800 nT [23].

Several different periodicities are found in the temporal variation of solar wind – from the shortest time scale as waves and turbulences, through ~25.4-day variation related with solar rotating period, even up to century scale – evident from geomagnetic records [22]. For this work however, the most important is the approximately 11-years solar cycle. This cycle reflects variations in Sun's activity that is variation of the Sun's internal magnetic field and the surface disturbance level. Solar activity is continuously monitored by many scientific organizations [e.g. 24, 25, and 26]. A good indicator of solar activity is the number of sunspots which can be observed [27] on the surface of the Sun. Sunspot maxima correspond to periods of high solar activity. Equally, sunspot minima indicate quiet periods of the Sun.

A correlation between observed number of sunspots and the frequency of solar events is observed. On average, during maximum solar activity there are up to about 10 events occurring, while during solar minimum only one [20]. For this work, the most important types of such phenomena are solar flares and coronal mass ejections (CME). In both cases, magnificent visual effects are usually associated what can be observed on the surface of the Sun.

Solar flares develop in few minutes and are outbursts of γ, X, radio waves and energetic particles. Flares are related to magnetically disturbed conditions of Sun's surface observed as sunspots. During a flare, large currents and moving magnetic field are generated which can accelerate released charged matter [e.g. 22, 23, and 28]. Flares are classified depending on their peak flux in soft X-rays [28] as measured by GOES satellites [29]. Solar flares may affect high frequency radio communications (1 – 30 MHz) even leading to a radio blackout especially on the dayside of the Earth and when the Sun is directly overhead. National Oceanic and Atmospheric Administration (NOAA) developed a scale of radio blackouts that is directly linked with solar flare classes [30]. Massive solar flares are sometimes accompanied by coronal mass ejections (CMEs).

CMEs are ejections of massive bubbles of solar plasma into space. CMEs are very often collocated with solar flares – as flares, CMEs originate from active regions as group of sunspots, but are separate events, not triggered by flares. Ejected mass is accelerated in CME driven shocks in the corona and interplanetary medium [e.g. 22, 23, and 31]. CMEs last from several hours up to days. The CMEs can travel with the different speeds: from 100 – 3000 km/s. When CME speed is faster than the speed of solar wind, a shock wave is generated – this manifests itself as sudden increase of satellite measured plasma density. Fastest CMEs can reach the Earth in 14 - 17 hours, slowest need few days [31]. CMEs can disturb Earth's magnetic field and create geomagnetic storms especially, when the direction of the magnetic field inside CME is opposite to the Earth's one. Solar energetic particles can create aurorae, similarly like flares, CME can disturb radio communication, and finally, can lead to an increased radiation levels not only in atmosphere but also on the ground.

Typical occurrence of these events varies with Sun's activity between several per day in active Sun's phase to about one per week in solar minimum [23, 31]. Only a fraction of them is reaching the Earth.

Solar particles that are incoming to the Earth are mostly protons, about 10% of alpha particles and less than 1% of heavier nuclei which composition varies from solar event to event. Energies of these particles are usually lower than 100 MeV but sometimes reach even 10 GeV [32]. Due to irregularities of magnetic field and shocks in the interplanetary medium the usual spectrum of solar energetic particles varies from event to event (see Figure 3) [20]. Additionally, spectra of solar energetic particles change in time (see Figure 4) [33]. As depicted in Figure 4, the fluence rate of protons for low energies is several orders of magnitude greater than that of galactic origin. Rarely, during some events, even at several hundred MeV, fluence rate of solar protons can be much higher than those of galactic origin.

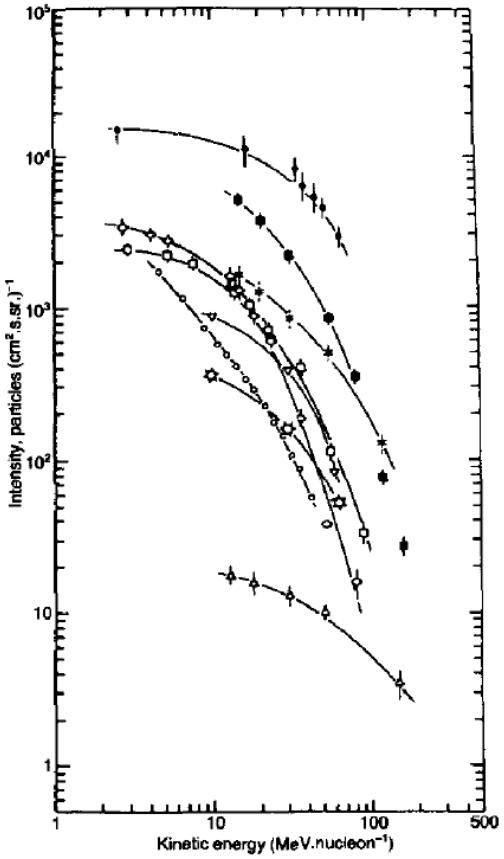

Figure 3 Usual spectra of solar particles for different solar flare events. Figure taken from Reitz et al [20].

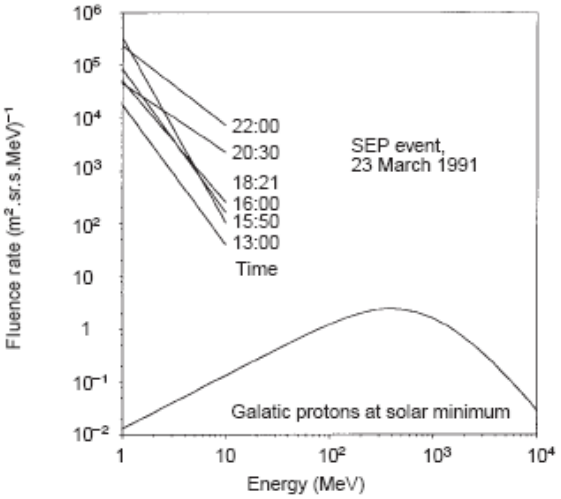

Figure 4 A comparison of proton fluence rate for galactic cosmic radiation and SEP. SEP shows time dependent structure. Figure taken from Heinrich et al [33].

2.1.1. Ground Level Enhancements

The intensity of cosmic radiation is in real time measured both in space and on the surface of the Earth. In space, satellites (e.g. GOES Space Environment Monitor [34]) record proton, electron, X-ray fluence rates, and magnetic field as well. On the ground level, many neutron monitors [35] placed at many locations all over the world measure secondary neutrons produced by cosmic radiation in nuclear reactions with atmosphere. Data from many neutron monitor stations are collected in a common database – the Neutron Monitor Database [36]. Variations of cosmic radiation due to the 11-years cycle are clearly visible in the neutron monitors data (Figure 5). Figure 5 shows correlation between observed sunspot number (lower diagram) and records of two neutron monitors: Climax (has been closed in 2006), and Newark station (located on similar magnetic latitude as Climax neutron monitor) – upper diagram.

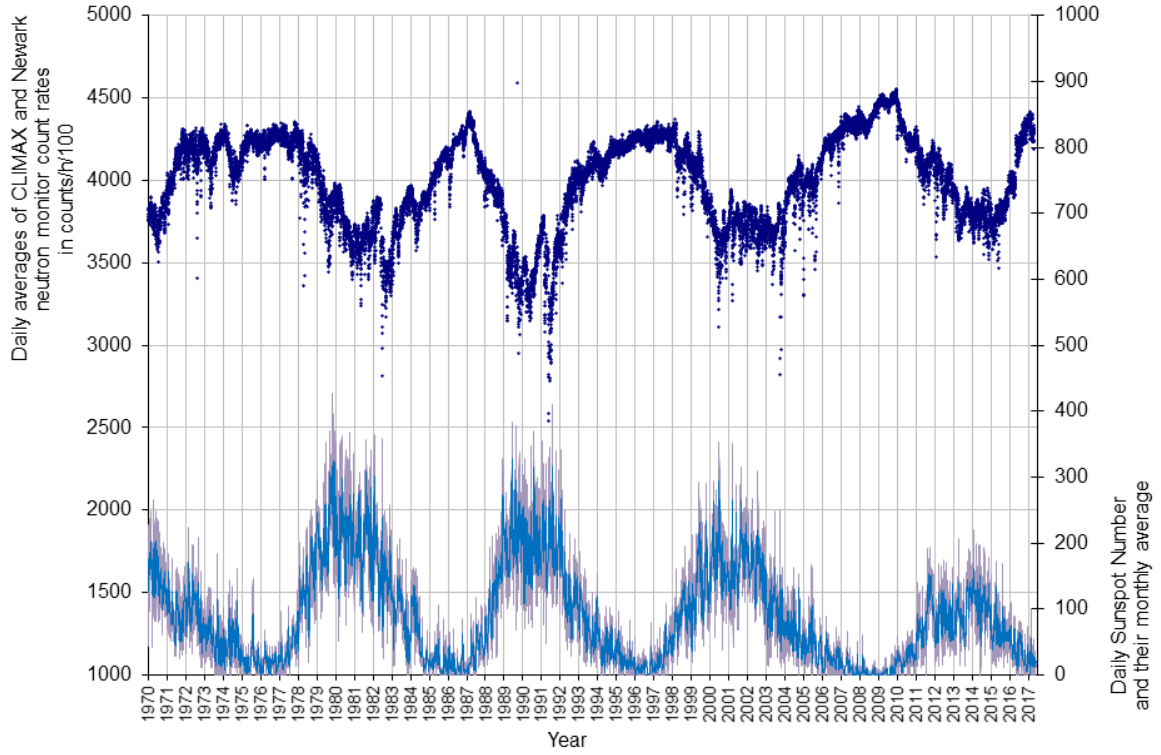

Figure 5 A correlation between sunspot number (lower diagram) and neutron monitor data (upper diagram). Chart produced based on sunspot numbers from SILSO [27] and data from Climax and Newark neutron monitor stations obtained from NMDB [36].

From many occurring solar flares and CMEs originating on the Sun, only some of them affect the Earth. If an ejection of solar mass happens at solar longitudes, where its magnetic field lines are well connected to the Earth, then satellite systems can measure enhanced radiation fluxes at Earth orbit (e.g. GOES system [34]). Some of these events are strong enough that can lead to effects observed on the ground - so called Ground Level Enhancements (GLE). There is no strong definition of a GLE, but it is commonly understood that a Ground Level Enhancement is a sudden increase of cosmic radiation observed on the ground by a few (at least two) neutron monitor stations recording at the same time increased count rate (by at least 1% in 5-min averaged data) [37]. Since 1942, there have been about 71 GLEs observed [38].

After an increase of solar radiation due to solar event, a decrease of galactic cosmic radiation can be observed that can last even for several days. This phenomenon is known as Forbush decrease and is used to be defined as at least 10% decrease of galactic cosmic radiation intensity. The observed decrease occurs owing to incoming magnetic field (e.g. dragged by CME) that sweeps out less energetic part of galactic cosmic radiation [39].

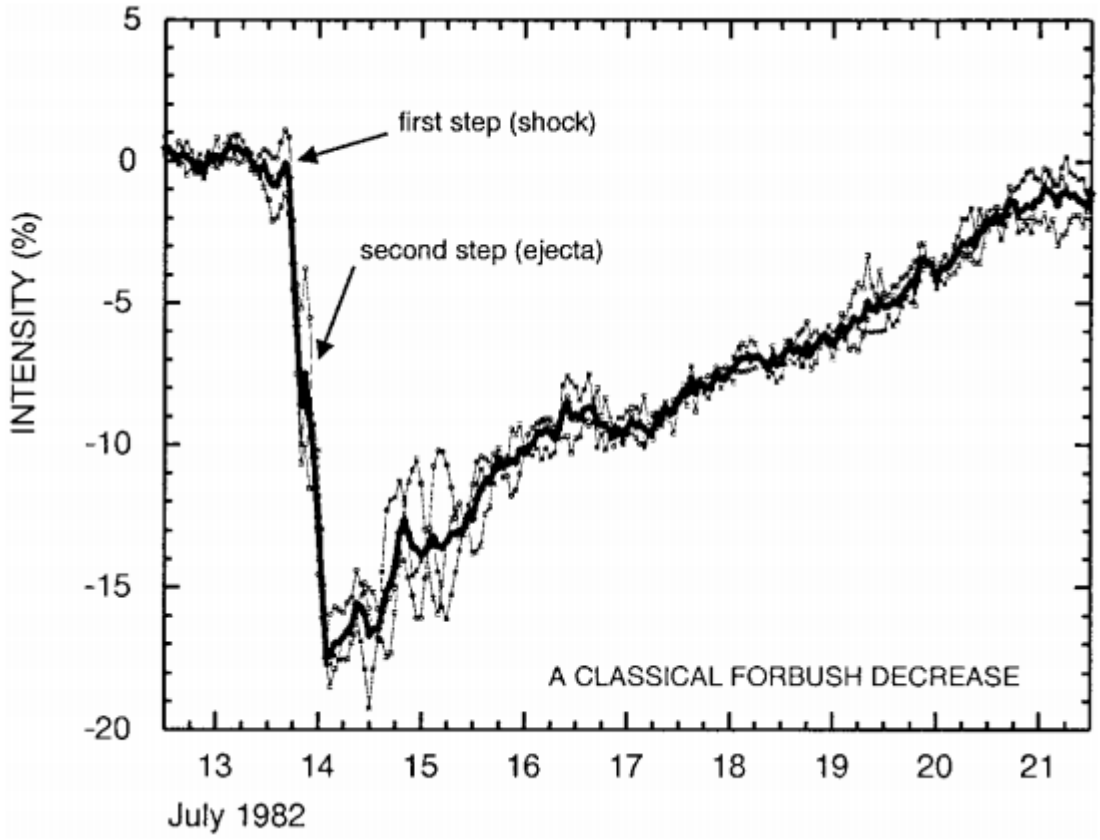

Figure 6 An example of a classical Forbush Decrease. Figure shows percentage decrease for three neutron monitor stations spaced about equally in longitude (Deep River, Mt.Wellington, and Kerguelen). The heavy line indicates the average of the count rates [Picture taken from 39].

2.2. Galactic cosmic radiation

Galactic cosmic radiation are charged particles that are coming from far outside of the solar system. The origin and acceleration mechanisms of GCRs are not fully understood; however, it has been considered that GCR particles come from supernova explosions and are accelerated by shock waves that are associated with those explosions [40]. Recent experiments like Pierre Auger Project [41] or Cherenkov Telescope Array [42] as well as recent studies on earlier data [43] support that.

GCR consists of 98% atomic nuclei and 2% of electrons. Nuclei fraction is composed of about 85% protons, about 14% helium ions, and 1% heavier ions often referred to as HZE (High-Z High-Energy) particles [20, 33, and 44]. HZE particles cover the full range of elements. Some of them (Li, Be, B) are more abundant than others. This abundance difference come from nuclear spallation and reactions of cosmic particles with interstellar and interplanetary matter and magnetic fields [20].

The energies of GCRs extend from about 100 MeV to over 10^{20} eV. Astrophysical theories and recent studies show that protons of ultra-high energies (greater than 10^{19} eV) have extragalactic origin [32, 42], however it happens only few times a year that

a particle of 10^{16} eV will reach the ground, and once a century when it comes to 10^{20} eV particles [41].

Energy spectrum of GCRs is usually given as kinetic energy per nucleon (Figure 7). Above a few thousands MeV/nucleon energy spectrum follows a power function

$$N(E) = E^{-\gamma}$$

The spectrum has a maximum fluence rate at around few hundreds MeV/nucleon and towards low energies the fluence rate decreases.

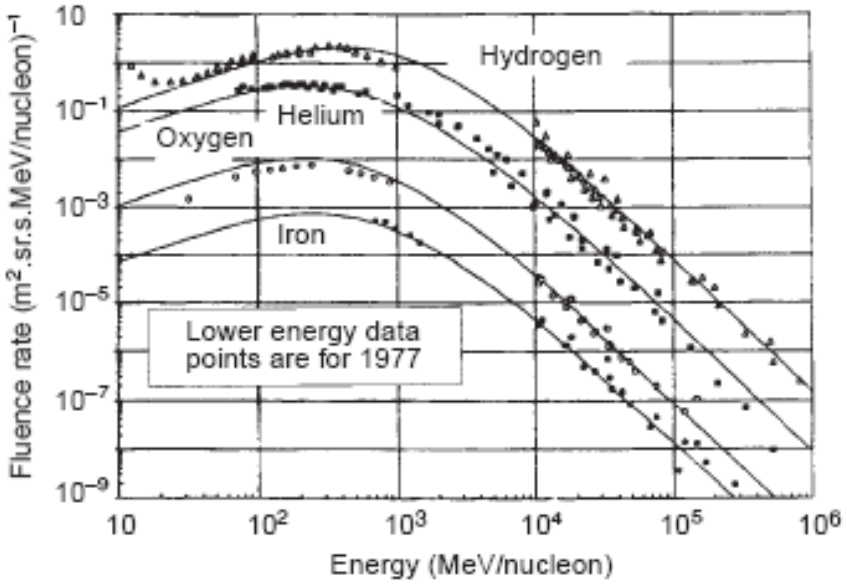

Figure 7 Energy spectra of some cosmic ray particles. Figure taken from [33].

2.2.1. Solar modulation

The 11-years solar cycle has a significant influence on GCR. At the beginning of a cycle (solar activity minimum), the solar magnetic field resembles a dipole which is aligned with Sun's rotation axis. In this phase, the intensity of solar wind is low. The GCR incoming to the solar system experience weak deceleration and GCR fluence rate is at maximum. The dipolar configuration of the solar magnetic field changes in the next five, six years towards cycle's maximum. During this phase, the solar wind gains in intensity and transported frozen-in magnetic field is stronger. At the cycle's maximum, solar magnetic field is in disorganized state. The GCR entering heliosphere interacts with intense solar wind what leads to a significant decrease of GCR intensity [45, 46]. During the latter years of a cycle, the dipole shape is renewed (but with opposite polarity) and then the whole cycle repeats. The modulation affects GCR particles below some GeV/nucleon what is shown in Figure 8 for helium ions. The

figure shows fluence rate for helium nuclei for solar minimum (1997) and two solar maxima (1989 and 1986).

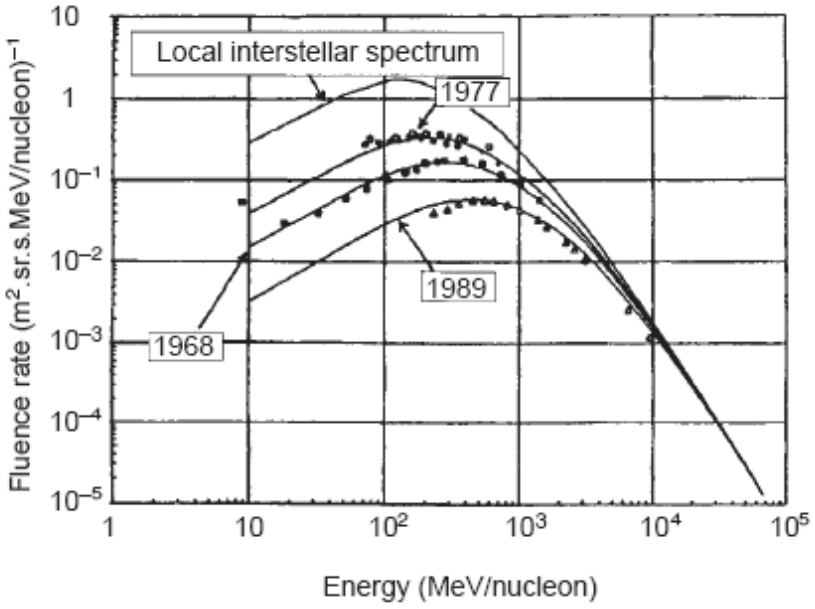

Figure 8 Spectral fluence rate of helium nuclei without solar modulation – interstellar spectrum (upper curve), for solar minimum (1997), strong (1989) and weak (1968) solar maximum. Figure taken from [33].

2.3. Anomalous cosmic radiation

Anomalous Cosmic Radiation (ACR) is a low-energy component of cosmic rays with kinetic energies ~ 10 – 100 MeV/nuc. Their spectra show different behavior than normal CR. While flux of CR decreases with decreasing energy, flux of ACR increases. ACR contain large amount of ions with high ionization potential, more helium than protons and are less than fully ionized – primarily singly ionized. The mechanism of ACR production and acceleration is uncertain and highly debated among cosmic rays physicists especially after Voyager 1 crossed the termination shock in 2004 (a boundary of our Solar System, where solar wind slows down and is pressed together by interstellar medium). ACR most probably are produced from neutral interstellar atoms flowing into inner heliosphere where they are ionized and accelerated in solar wind. Cosmic rays of even lower energies ~ 1 – 10 MeV/nuc are accelerated in termination shock and are called Termination Shock Particles (TSP) [45]. ACRs and TSPs are interesting for studying particle acceleration processes or particle transport in heliosphere but are less important for the work presented here. More information on ACR can be found elsewhere [e.g. 45, 47].

2.4. Cosmic radiation at flight altitudes

Cosmic radiation exposure in Earth's atmosphere depends mainly on altitude, geographical position latitude and longitude, and the Sun's activity. All these parameters will be shortly described in the following chapters.

2.4.1. Solar activity

As described in earlier chapters, the Sun loses continuously mass from its corona through an ejection of coronal gas into the space what is referred to as solar wind. The solar wind drags the solar magnetic field outwards the Sun forming interplanetary magnetic field. This magnetic field redirects charged particles, thus reducing galactic component of the cosmic radiation reaching the Earth's magnetosphere [33]. The Sun shows an approximately 11 years cycle of its magnetic activity what is manifested through a variation of observed sunspot number [27]. Changes in the solar magnetic field carried by solar wind cause changes in the intensity of cosmic radiation what is reflected in recorded values of neutron flux measured by ground level neutron monitors [Figure 5, 36].
To determine the influence of the solar modulation on the intensity of the cosmic radiation a diffusion–convection model has been developed by the National Aeronautics and Space Administration (NASA) – Johnson Space Centre (JSC) [48]. In this model, the strength of the solar modulation is described by a parameter called solar deceleration potential (Φ, often denoted as SDP) which calculations are based on ground level Climax neutron monitor records. This is then used to modify the intensity and energy distribution of GCR at a distance of 60 to 100 AU (an AU is astronomical unit, is the average Sun to Earth distance) with a time-lag of 95 days, which is approximately the time needed for lower energy component of the GCR to pass that distance [36].

The value of Φ at a time T depends on Climax neutron monitor count rate averaged over $\pm$ 14 days around time T' = T – 95 days, and a polarity of sun's magnetic field:

$$\text{positive filed: } \Phi(T) = 3957.89 - 0.8124\,\langle C(T)\rangle_{\pm 14\text{ days}}$$
$$\text{negative filed: } \Phi(T) = 4202.76 - 0.8563\,\langle C(T)\rangle_{\pm 14\text{ days}}$$
$$\text{reversal filed: } \Phi(T) = 4772.86 - 0.9528\,\langle C(T)\rangle_{\pm 14\text{ days}}$$

Values of Φ are inversely proportional to the intensity of cosmic radiation measured in the atmosphere. When the Sun is in a calm phase of its cycle, the low energy part of GCR is less influenced by relatively weak solar wind and values of Φ are low. However, this means that GCR intensity measured in the atmosphere is at maximum. Oppositely for high values of Φ, during solar maximum. Strong solar wind efficiently dumps low energy part of GCR reducing its intensity in atmosphere and that measured

by ground level neutron monitor stations. This dependence is more visible for high altitudes and low vertical cut – off rigidity (Polar Regions). Under such conditions, ambient dose equivalent due to GCR could vary even up to 50% throughout the full range of solar cycle [Figure 70].

2.4.2. Earth's magnetic field

Primary cosmic radiation approach the Earth's magnetic field on their way towards the Earth. Each charged particle that has not been deflected by solar wind in the heliosphere interacts with the Earth's magnetic field before it enters the atmosphere. The penetrating ability of a charged particle is dependent on its angle of incidence, momentum, geomagnetic latitude and altitude of the entry point [49, 33]. A particle can enter the atmosphere if its magnetic rigidity, r_p, is greater than so called vertical cut–off rigidity, r_c, of the Earth's magnetic field at the point of entry. A particle with a rigidity value below the vertical cut–off rigidity is deflected by the Lorenz force and cannot penetrate deeper atmosphere. The particle's rigidity, r_p, depends on its momentum and charge and is given by equation:

$$r_p = \frac{pc}{q}$$

where *p* is particle's momentum, *q* is particle's charge and *c* is the speed of light [50].

The cut–off rigidities can be analytically calculated when the Earth's magnetic field is approximated by a simple dipole. Description that is more accurate is based on measured magnetic field values and contains higher order poles like quadrupole. Such fields are called International Geomagnetic Reference Field (IGRF) and for them, the cut–off rigidity values have to be calculated by numerical procedures. The Earth's magnetic field changes with time and the reference field for different periods must be newly calculated [49]. This is periodically done and the calculations are valid for a time period called epoch (for example Epoch 1995.0, or Epoch 2000.0).

In this work a matrix of vertical cut–off rigidity values determined by Shea *et al* [51] is used. These values have been determined for vertical direction of incidence at the altitude of 20 km, for the magnetic field in the year 1990.

The parameter vertical cut–off rigidity is often used instead of geographical latitude and longitude to describe geographical location e.g. for the location of cosmic radiation measurements. Another approach is to use simplified dipole model for the Earth magnetic field and calculate geomagnetic latitudes. Geomagnetic latitudes B_m for given geographic latitude and longitude can be calculated using the formula [52]:

$$\sin B_m = \sin\lambda \sin\lambda_p \cos\lambda \cos\lambda_p \cos\left(\varphi - \varphi_p\right)$$

where λ is geographic latitude, φ is geographic longitude λ_p is geographical latitude of geomagnetic North Pole (1990: 79.13°N) and φ_p is geographical longitude of geomagnetic North Pole (1990: 288.88°E).

There is a general dependence between the shape of Earth's magnetic field and the values of cut–off rigidity. Over the equatorial region, where the lines of magnetic field are parallel to the Earth's surface the values of cut–off rigidities are the highest reaching 17 GV. Oppositely, over the Polar Regions, the magnetic field lines are approximately perpendicular to the Earth's surface and therefore the cut–off values are close to zero. As a result primary cosmic radiation are under little deflection only over Polar Regions while over equatorial region particle with low rigidity values are efficiently deflected [49]. Figure 9 shows vertical cut-off rigidities as calculated by Shea *et al* [51].

Earth's magnetic field is very efficient in reduction of cosmic radiation exposure. Ratio of measured ambient dose equivalent due to GCR at Polar Regions to that measured over equatorial region can be from a factor of 2 (low altitudes, solar maximum) to a factor of about 6 (solar minimum, high altitudes) [Figure 71].

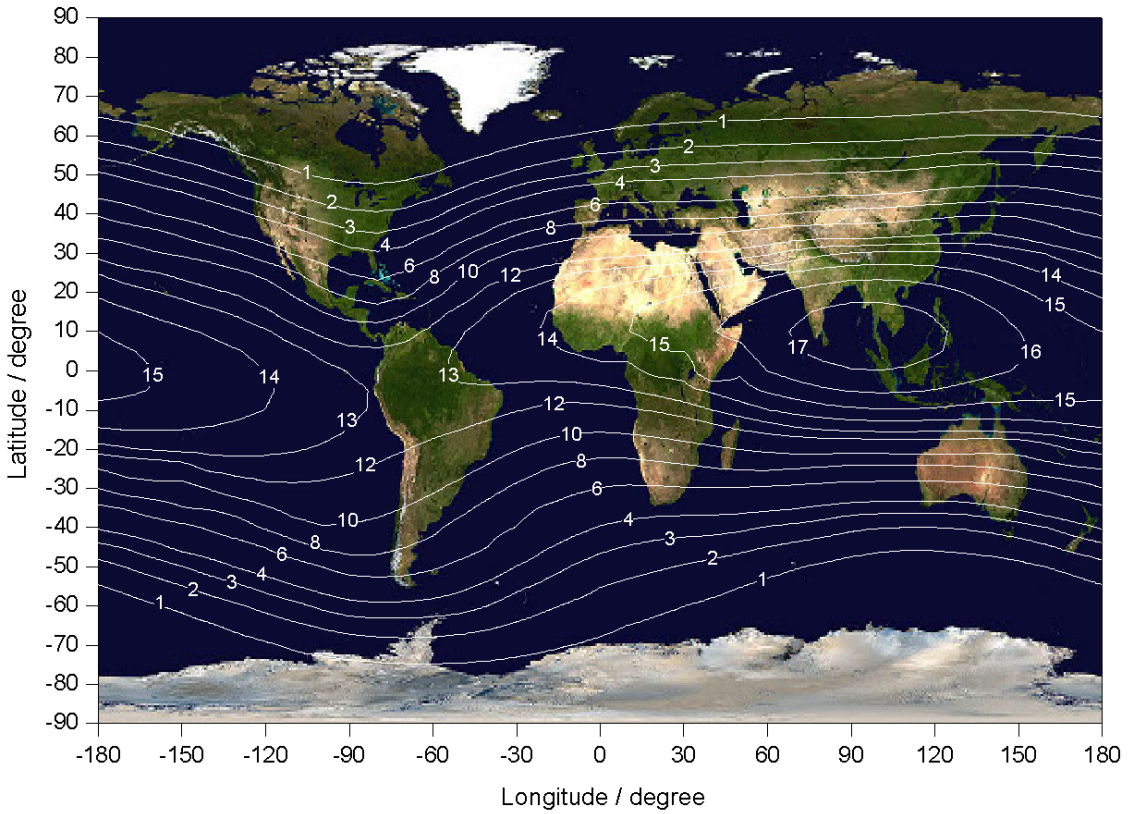

Figure 9 Vertical cut-off rigidities in GV based on data in 1990 at a 20 km altitude [51]. The background world map was taken from NASA's "Visible Earth" catalog http://visibleearth.nasa.gov/view.php?id=57752

2.4.3. Altitude

The altitude influence on the intensity of cosmic radiation is related to the transport of the cosmic particles through the atmosphere. Primary cosmic radiation particles interact through nuclear reactions with elements of the top layer of atmosphere producing as a result secondary particles of different types. These, having enough high energy take part in further interactions. In this way, primary and secondary cosmic radiation create whole cascades of particles that penetrate the atmosphere. The build-up process of secondary particles competes with simultaneous processes that lead to a reduction of particles fluence rate. As a result, fluence rate is changing with the depth of atmosphere. Starting with the top of atmosphere and going downwards the fluence rate first increases up to around 20 km of altitude, then reaches maximum, what is known as Regener–Pfotzer maximum (or, due to historical reasons misleadingly called the Pfotzer maximum [53]), and afterwards decreases going down deep into the atmosphere. The relative contribution of different type of particle types to the total dose vary with altitude [e.g. Figure 44 - Figure 47], but particles fluence spectra at altitudes relevant for civil flights (8 – 15 km) stay similar [37].

On–board aircraft measurements confirm that dose increases with altitude [54, 55]. Balloon measurements show that measured particle flux reaches maximum values at altitudes of around 20 km and going higher decreases [56].

Ratio of measured ambient dose equivalent due to GCR high civil altitudes (~ 15 km) to that measured at low altitudes (~ 8 km) can be from a factor of 2 (equatorial region, solar maximum) to a factor of about 6 (solar minimum, Polar Regions) [Figure 69].

3. Tissue Equivalent Proportional Counter (TEPC)

This chapter describes a tissue equivalent proportional counter (TEPC), its calibrations, and investigations at CERF facility at CERN as performed by the author.

One of microdosimetric techniques used in practice bases on a study and interpretation of single-event energy deposition spectra measured by proportional counters. Proportional counters have three properties that make them useful in microdosimetry:

- each individual charged particle interaction with counter gas triggers a signal,
- triggered signal is proportional to initial ionization generated by triggering event,
- each individual triggering event experiences the same gas multiplication.

Because of these three properties, proportional counters are able to determine microdosimetric energy deposition spectra [57].

In this technique, in order to simulate microscopic sites of a tissue, proportional counters have tissue-equivalent characteristics owing to used materials, design, and operation under low gas pressure [Figure 10].

The tissue equivalence principle bases on a fact that the major parameter in radiation energy transfer is the atomic composition of traversing material, while chemical combination of material elements is not important. Therefore, human tissue can be replaced with substance providing the same as tissue energy absorbing properties. Such materials are usually a mixture of hydrogen, carbon, nitrogen and oxygen. One of these mixtures is A-150 plastic commonly used for the wall of a tissue equivalent proportional counter. Counter's chamber is filled with methane or propane based tissue equivalent gas.

In order to study the distribution of radiation energy deposition in micrometer-size volume of tissue, proportional counter should be operated under low gas pressure. The pressure must be adjusted in such a way that a charged particle crossing the counter volume with a size of a few centimeters deposits the same amount of energy, as that particle would cross a tissue volume of micrometer dimensions. This can be written as:

$$\left(\frac{1}{\rho}\frac{\mathrm{d}E}{\mathrm{d}x}\right)_g \rho_g \Delta X_g = \left(\frac{1}{\rho}\frac{\mathrm{d}E}{\mathrm{d}x}\right)_t \rho_t \Delta X_t$$

where the left part of above equation is energy deposited in gas ("g" index), right part is energy deposited in tissue ("t" index), $\left(\frac{1}{\rho}\frac{\mathrm{d}E}{\mathrm{d}x}\right)$ is mass stopping power, ρ is density, and ΔX is chord length of a target (Figure 11).

Applying now the tissue equivalence principle, mass stopping power is the same for tissue and tissue-equivalent gas; therefore, gas pressure must fulfill equation [57]:

$$\rho_g \Delta X_g = \rho_t \Delta X_t$$

Tissue equivalent proportional counter measures lineal energy *y*, which is defined as single energy deposition event in a defined volume per mean chord length in that volume. Recorded frequency distribution of event sizes can be converted into dose distribution spectra as a function of lineal energy. The lineal energy is an approximate measure of the linear energy transfer (LET) L_∞. Folding dose distribution with the quality factor Q(L), with $L \approx y$, one obtain dose equivalent distribution as a function of lineal energy. The quality factor is defined according to ICRU Report 51 [58].

$$\overline{Q}_D = \frac{1}{D}\int_L Q(L)D(L)dL \approx \frac{1}{D}\int_y Q(y)D(y)dy = \int_y Q(y)d(y)dy$$

This microdosimetric technique became widely used to measure microdosimetric spectra in complex mixed radiation fields. One of weaknesses of this technique are wall-effects that may occur due to density differences at wall-gas border. There are four types of wall effects: delta-ray effect, re-entry effect, V-effect and scattering effect. All of them lead to a superposition of energy deposition events due to particles that can be scattered at the wall-gas border and produce secondary and tertiary particles. Such superposition would not occur in a homogeneous medium [59]. A large size of proportional counters increases vulnerability to pile-up effects and give restrictions on spatial resolution what can be another disadvantage in some applications [59].

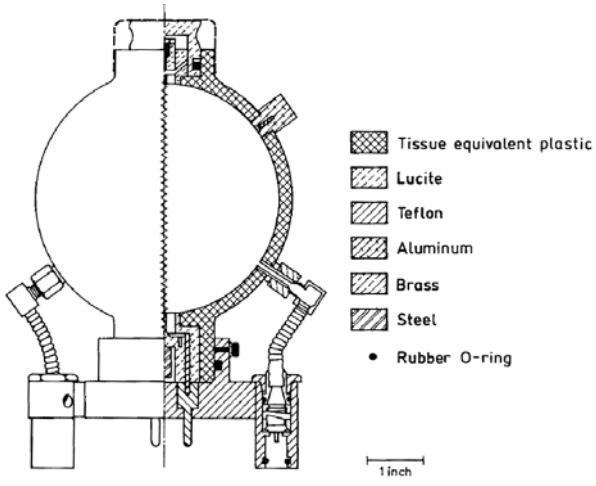

Figure 10 Typical walled proportional counter [59]

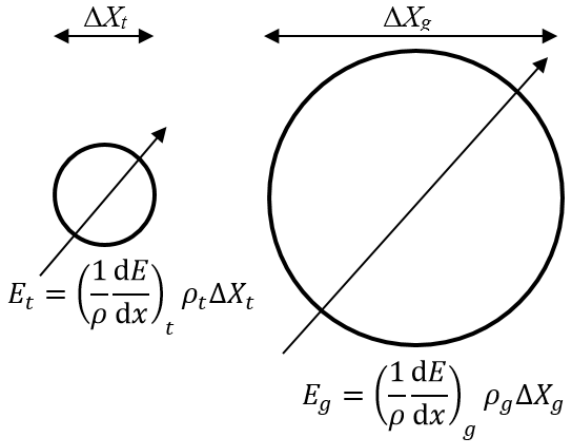

Figure 11 Visualization of how to simulate a small site (left) with a larger site of tissue-equivalent gas.

3.1. Hawk Environmental Radiation Monitor

The TEPCs used for the work presented here have been developed by Far West Technology. Technical parameters presented below were taken from the operation and repair manual [60]. The detector is a tissue equivalent proportional counter of Rossi type. It has a spherical chamber with inner diameter of 4.9 inch. The wall is made from A-150 tissue equivalent plastic, is 0.084 inch thick, and is covered with stainless steel container of 0.025-inch thickness. These geometrical dimensions give 1.4 µm of mean chord length. High voltage is applied to tissue equivalent plastic while anode is electrically isolated and held at virtual ground by the charge sensitive preamplifier. The sphere is filled with pure propane gas under 7 Torr (933.2 Pa) pressure and operated between -600 V to -900 V what provides simulation of 2 µm site size and a gas gain of 200 to 400 times.

As preamplifier, a charge sensitive resistive feedback preamplifier is used with 1 pF capacitor and 100 MΩ resistor. Shaping of the signal is provided by a unipolar CR-RC shaping circuit with 3 µm time constant. This circuit has six stages of signal shaping and enables to shape signal to approximately 15 µs of rising time and 20 µs of falling time. Noise is less than 0.2 keV/µm FWHM.

The TEPC provides also micro-phonic reduction circuit since high gain TEPC detectors respond to small vibrations and shocks. These fake pulses have different rise and fall times than correctly shaped radiation pulses and therefore can be partially removed.

Since the dynamic range of event sizes and therefore pulse height can cover several orders of magnitude, the multichannel analyzer of the TEPC is divided into two parts with different gains. The low-gain part is 10-bit (1024 channels) analogue/digital converter with range 0 – 1024 keV/µm and measures lineal energy spectra of radiation fields with a resolution of 1 keV/µm. The high-gain part is 8 bit (256 channels) analogue/digital converter with range 0 – 25.6 keV/µm and has a resolution of 0.1keV/µm. Due to electronic noise the TEPC has an instrumental threshold at approximately 0.5 keV/µm of lineal energy scale. A special treatment owing to the threshold is usually applied in the data analyses process.

The dead time per event is 64 µs, which is negligible for typical measurements. When the measured count rate exceeds 30000 counts per minute, additional adjustments to recorded values have to necessarily be applied.

The gathered data is written to Compact-Flash card every minute. Serial RS232 link can be used for interactive mode to display data as it is taken, upload and download data, reconfigure unit or communicate with internal operating system. The instrument can be operated with internal batteries or external power supply. For coordinates data an optional GPS antenna can be plugged.

The TEPC sphere is contained in an aluminum cylindrical structure together with the required electronics. The complete assembly, cased inside a portable trolley with dimensions of an aircraft hand-baggage is referred to as Hawk Environmental Radiation Monitor (Figure 12).

The TEPC has been investigated at AIT against emission of radio frequencies and successfully passed the requirements of RTCA/DO-160D Section 21 document what allow installing it on-board aircrafts [61].

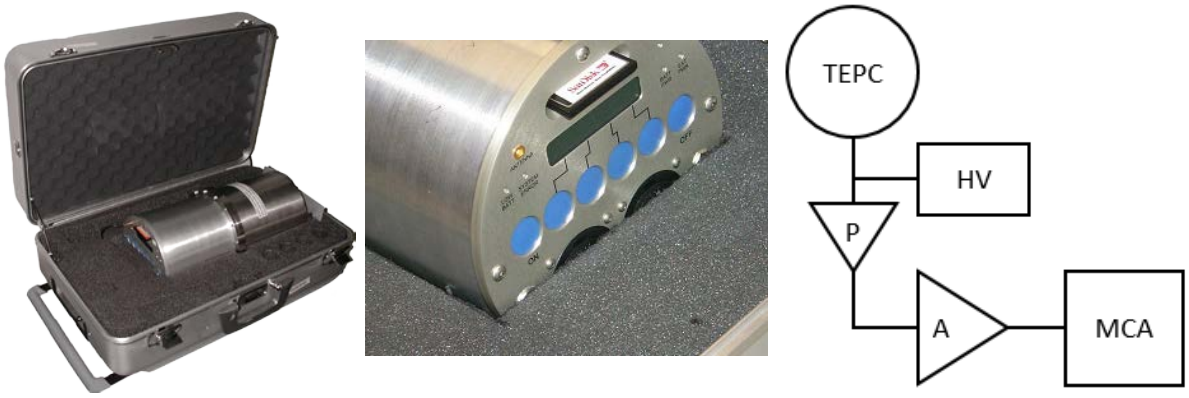

Figure 12 Hawk Environmental Radiation Monitor (left, middle). Right: typical arrangement for the measurement of the pulse height spectrum with a TEPC (HV-high voltage, p – preamplifier with CR-RC shaping circuit, A - main amplifier, MCA - multi-channel analyzer

3.1.1. Calibrations

The TEPC is calibrated usually in two steps. Initial calibration is for correct linearity of the lineal energy scale. Since TEPC measures energy deposited in its gas, an additional calibration is needed to express instrument response in terms of ICRU operational quantity, the ambient dose equivalent, *H**(10). The total ambient dose equivalent is given by the sum of a low-LET and a high-LET component. These components are defined as the contributions below and above 10 keV/µm of the lineal energy scale and are calibrated separately for K_{low} and K_{high} calibration factors.

$$H^*(10) = H^*(10)_{low} + H^*(10)_{high} = K_{low}\int_0^{10} Q(y)D(y)dy + K_{high}\int_{10}^{\infty} Q(y)D(y)dy$$

3.1.2. Calibration for linearity of lineal energy scale

Initial calibration is for correct linearity of the lineal energy scale. An internal ^{244}Cm source emits 5.8 MeV alpha particles that cross the cavity diameter. For proper gas gain, the alpha peak should be located approximately between channels 145 and 150 (145 keV/µm – 155 keV/µm) [60]. Figure 13 shows microdosimetric spectrum of such internal ^{244}Cm source as measured by the author. An analysis done by the author, shows that the alpha peak is located in a logarithmic interval (146.78 keV/µm – 158.49 keV/µm) which geometrical mean corresponds to 152.52 keV/µm. This assures

correct linearity of lineal energy scale. The smaller peak in the low-LET region visible around 1 keV/µm arises from the background.

If the alpha peak is shifted, a correction has to be done in the high voltage applied to detector's cathode, changing the gas gain. In the case of HAWK instrument, one can do it by editing proper parameter in the HAWK configuration file.

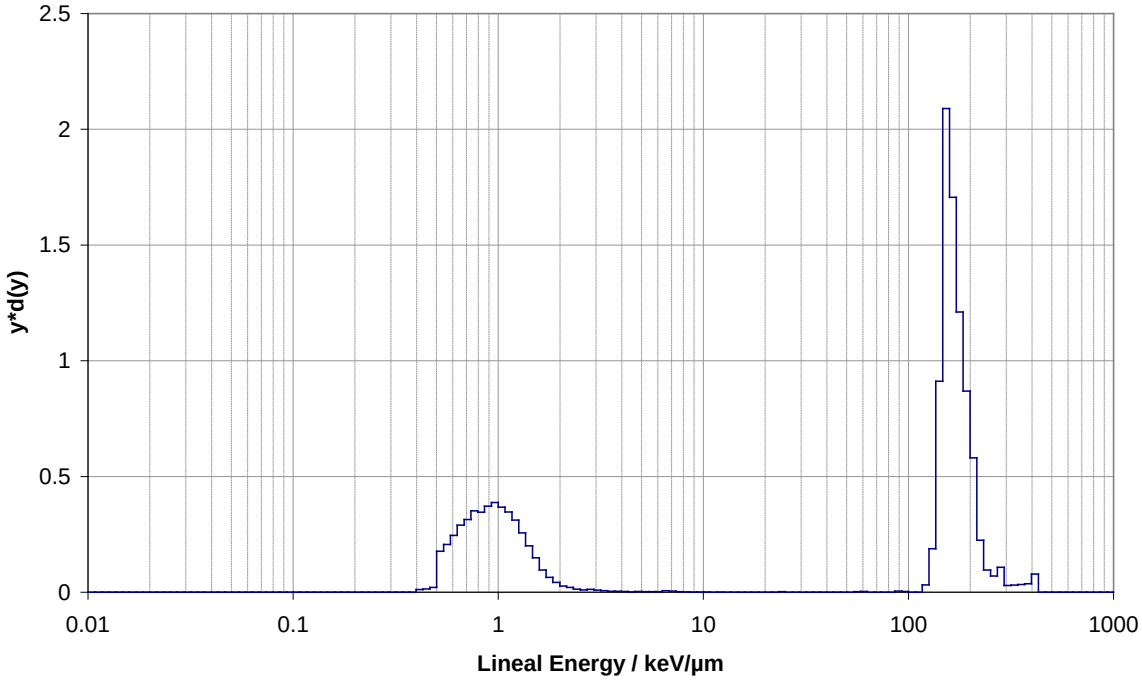

Figure 13 Microdosimetric spectrum of a pre-calibration with Cm-244 internal source. Alpha peak is located between 146.78 keV/µm – 158.49 keV/µm. The smaller peak in the low-LET region visible around 1 keV/µm arises from the background.

3.1.3. Calibration at the photon radiation fields

An almost monoenergetic 4.4 MeV and 6-7 MeV photon fields were accessible at the accelerator facility of the PTB, Germany. These fields can be used as reference radiation fields for calibration purposes. According to the ISO 4037-3 standard on calibration of area and personal dosemeters in photon fields [62], in the reference photon radiation fields with energies exceeding 2 MeV, the true value of *H*(10)* is determined by measuring air kerma at the point of interest. Results in terms of *H*(10)* are obtained by engaging appropriate conversion coefficients. Instrument was also investigated in standard ^{60}Co (662 keV) and ^{137}Cs (1.17 MeV and 1.33 MeV) radiation fields – results are reported elsewhere [63 and 64].

3.1.3.1. Brief description of the 4.44 MeV photon radiation field

At PTB, a nearly monoenergetic 4.44 MeV gamma radiation is produced by bombarding a carbon target of 2 mm thickness with 5.7 MeV protons which are produced at the cyclotron. On the carbon target, a nuclear reaction $^{12}C(p, p'\gamma)^{12}C$ takes place. Produced radiation consists in 97.4% of 4.44 MeV photons. Due to $^{13}C(p, n)^{13}N$ reaction occurring on the target, produced radiation is contaminated by low energy neutrons ($E_n \leq 2.56$ MeV). Further, ^{13}N nuclides are not stable and subsequent $\beta+$ decay occurs – $^{13}N(\beta+)^{12}C$. As a result, a small amount of 511 MeV annihilations photons additionally contribute to the radiation field [65].

Table 5 Photon energies, the relative fluence, and relative air collision kerma contributions for 4.44 MeV photon radiation field [65].

Nuclear reaction	Eγ MeV	Relative Fluence %	Relative Kerma %
$^{13}C(p, n)$	0.511	1.7	0.3
$^{13}C(p, p'\gamma)$	3.111	0.9	0.7
$^{12}C(p, p'\gamma)$	4.443	97.4	99.0

For this radiation field, the fluence-weighted and air kerma-weighted mean photon energies are:

$$\overline{E}_{\Phi} = 4{,}36 MeV$$
$$\overline{E}_{K_a} = 4{,}42 MeV$$

3.1.3.2. Brief description of the 6-7 MeV photon radiation field

At PTB, the 6-7 MeV photon radiation is produced using a 3.5 MV Van-de-Graaf accelerator. A 6-7 mg/cm^2 layer of CaF_2 is evaporated onto a 2 mm thick carbon substrate. This layer is bombarded by 2.7 MeV protons. At such proton energy, the photon spectrum has three high-energy components: 6.13 MeV, 6.92 MeV, and 7.12 MeV. Additionally, the $^{19}F(p, p'\gamma)^{19}F$ reaction occurs and the photon field is contaminated with low energy photons. There is also a high-energy electron contamination coming from the decay of the first excited state of ^{16}O from the air. This decay leads to a production of electrons and positrons of 2.5 MeV. Both of these must be eliminated with low-Z material filter placed in front of the target, but due to annihilation processes, the 511 MeV photons play a role in the resulting photon radiation field [65].

Table 6 Photon energies, the relative fluence, and relative air collision kerma contributions for 6-7 MeV photon radiation field [65].

Nuclear reaction	Eγ MeV	Relative Fluence %	Relative Kerma %
$^{19}F(p, p'\gamma)$	0.110	12.0	0.4
	0.197	21.3	1.6
	1.235	1.0	0.4
	1.353	1.2	0.6
	1.451	0.5	0.3
$^{19}F(p, \alpha\gamma)$	6.130	15.2	21.5
	6.920	14.4	22.1
	7.120	34.4	53.1

For this radiation field, the fluence-weighted and air kerma-weighted mean photon energies are:

$$\overline{E}_{\Phi} = 4{,}49 MeV$$
$$\overline{E}_{K_a} = 6{,}66 MeV$$

The significant difference between the fluence-weighted and air kerma-weighted mean energies comes from great contribution of low-energy photons into fluence-weighted mean energy (33%) which however is a small contribution into total air collision kerma – only 3.3% [65].

3.1.3.3. Calibration procedure for the operational quantity ambient dose equivalent, H*(10)

The PTB determined the true value of *H*(10)* by measuring air kerma at the point of interest and by engaging appropriate conversion coefficients. The coefficients are calculated in the kerma approximation [62]. Because of kerma approximation, the coefficients are valid only under the conditions of secondary electron equilibrium. This influences calibration procedure. Instruments investigated in such radiation field must be irradiated in the secondary electron equilibrium state. Author, during his investigations, has established the secondary electron equilibrium by adding a PMMA plate in front of the detector.

3.1.3.4. Calculations of calibration factor

Author calibrated two TEPC systems (TEPC#4 and TEPC#10) in both reference fields. Irradiations were done for different angles to reveal angle dependency of calibration factor. The reference point is the center of detector, 0° defines irradiation of a side of the instrument at the height of the center of detector, and 90° defines irradiation of the front plate of the instrument as depicted in Figure 14.

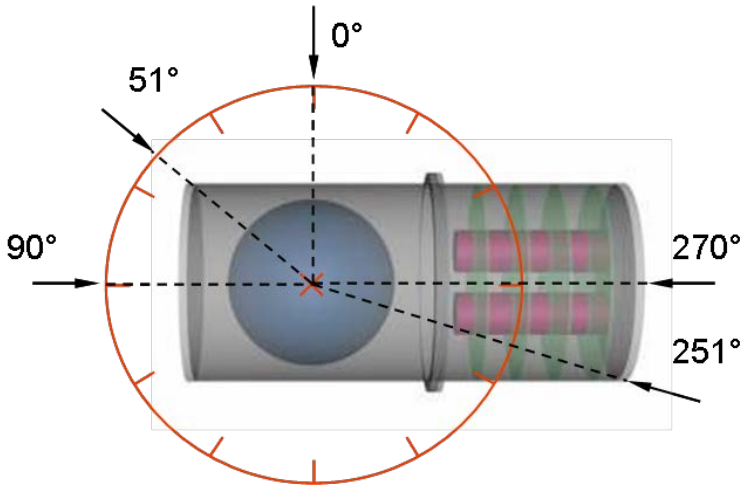

Figure 14 A sketch of TEPC with marked angles at which the TEPC was irradiated.

Figure 15 presents the microdosimetric spectrum as obtained with TEPC#4 oriented at 0 degree and exposed to 6.6 MeV photons.

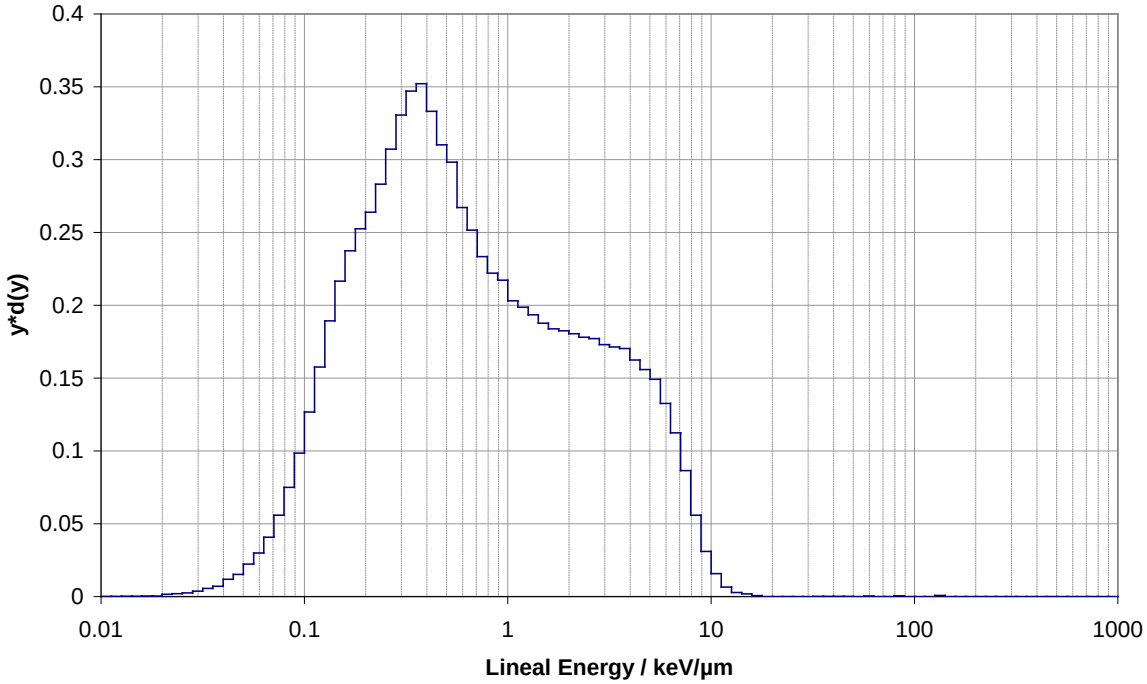

Figure 15 Microdosimetric spectrum obtained with TEPC#4 oriented at 0 degree and irradiated with 6.6 MeV photons.

A spectrum corresponding to that showed in Figure 15 but obtained for 4.44 MeV photons is presented below in Figure 16. Comparing Figure 15 with Figure 16, one can see that in Figure 16 there is an additional high-LET component. This component comes from low energetic neutrons as described above (see 3.1.3.1) and is not taken into account in the process of low-LET calibration factor calculation. Spectra for other angular arrangements are similar to the ones showed in Figure 15 and Figure 16.

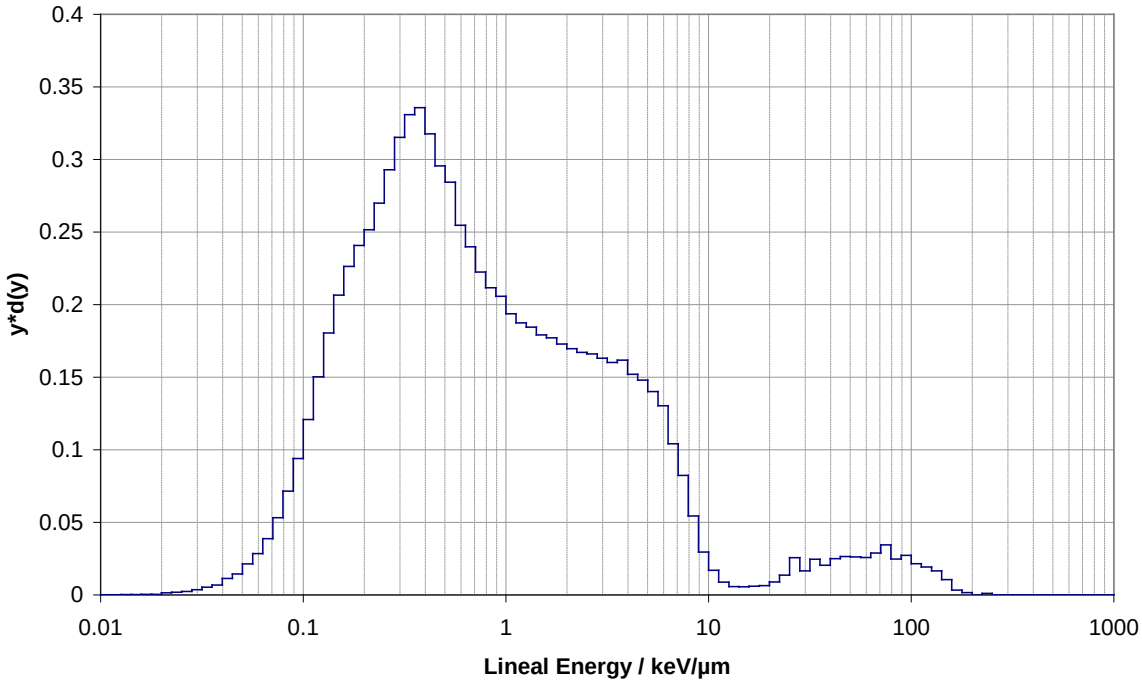

Figure 16 Microdosimetric spectrum obtained with TEPC#4 oriented at 0 degree and irradiated with 4.4 MeV photons.

Calibration factor is defined with the equation:

$$K_{\mathrm{ph}} = \frac{H^{*}(10)_{\mathrm{low,ref}}}{\int_{0}^{10} Q(y)D(y)\mathrm{d}y} = \frac{H^{*}(10)_{\mathrm{low,ref}}}{\int_{0}^{10} H_{tepc}(y)\mathrm{d}y}$$

where $H^{*}(10)_{low,ref}$ are reference values provided by the PTB and the denominator is low-LET part of measured dose equivalent. The low-LET part is defined as less than 10 keV/µm.

Calculated calibration factors for both TEPCs and for different angular orientation are given in Table 7 and Table 8. Uncertainties are determined according to “GUM” [66] and include uncertainty of measurements and uncertainty of reference values.

Table 7 Calibration factors calculated for all instruments oriented at specific angle irradiated with 6.6 MeV photons.

Instrument	α=0°	α=51°	α=90°	α=251°	α=270°
TEPC#04	1.16 ± 4.09%	-	-	-	-
TEPC#10	1.21 ± 4.31%	1.31 ± 4.65%	1.36 ± 4.79%	1.65 ± 5.9%	1.76 ± 6.19%

Table 8 Calibration factors calculated for all instruments oriented at specific angle irradiated with 4.4 MeV photons.

Instrument	α=0°	α=51°	α=90°	α=251°	α=270°
TEPC#04	1.17 ± 3.60%	1.23 ± 5.11%	1.33 ± 4.99%	-	1.69 ± 4.25%
TEPC#10	1.19± 4.21%	-	-	-	-

In Figure 17 and Figure 18, data from Table 7 and Table 8 are presented but as relative responses with respect to reference values. In these figures, 100% denotes situation when calibration factor would be one what means that TEPC would measure reference value.

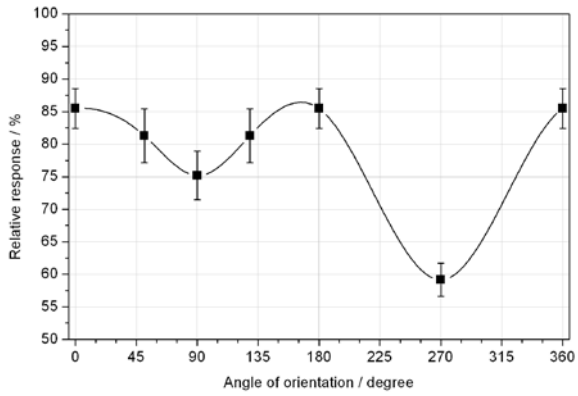

Figure 17 Relative response of TEPC#10 exposed to 6.7 MeV photons.

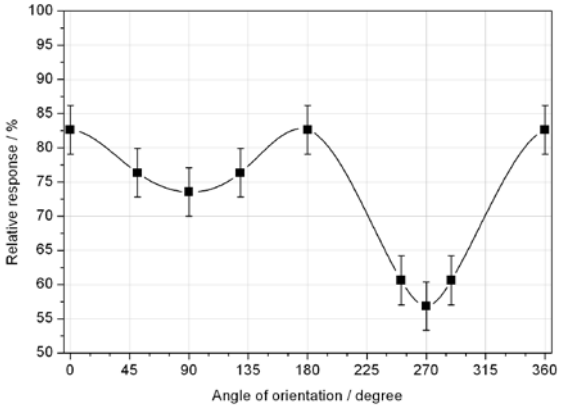

Figure 18 Relative response of TEPC#4 exposed to 4.4 MeV photons.

Calculated mean calibration factors independent on energy, independent on angular orientation is in Table 9.

Table 9 Calculated low-LET calibration factors with one standard uncertainty (coverage factor k = 1) for 4.4 MeV and 6.7 MeV photons.

Instrument	K_{ph} (k=1)
TEPC#04	1.26 ± 7.9%
TEPC#10	1.36 ± 7.5%

3.1.4. Calibrations with neutrons

TEPC have been investigated also in neutron fields with different neutron energies. Author contributed to the data analysis for the following calibrations:

- 0.5 MeV – 14.8 MeV at Physikalisch-Technische Bundesanstalt (PTB), Braunschweig, Germany
- 61 MeV at Université Catholique de Louvain (UCL), Louvain, Belgium
- 100 MeV – 200 MeV at iThemba Labs (iTL) South Africa.

3.1.4.1. Brief description of low-energy neutron fields

The PTB ion accelerator facility (PIAF) provides quasi-monoenergetic low-energy neutron reference fields with peak energies ranging from 24 keV up to 19 MeV. The beam is produced by bombarding low-Z materials (D, T, ^{7}Li) with light ions (p, d) accelerated by cyclotrons or van der Graaf accelerators. The resulting neutrons' spectral fluence shows usually a "monoenergetic" peak produced by non-collided neutrons and a low-energy continuum produced by neutrons scattered in the target [63]. Some characteristics of the PTB quasi-monoenergetic ISO reference fields are given in Table 10 – mean neutron energy: $<E_n>$, width (FWHM) of the peak: ΔE, type of target, neutron fluence rate $d\Phi/dt$ and ambient dose equivalent rate ($dH^*(10)/dt$) both at 1 meter distance and maximum proton or deuteron current, relative contribution of neutrons scattered in the target Φ_{sc}/Φ.

Table 10. Characteristics of the PTB quasi-monoenergetic ISO reference neutron fields [63].

Reaction	$<E_n>$ MeV	ΔE MeV	Target	$d\Phi/dt$ /cm^2 /s	Φ_{sc}/Φ %	$dH^*(10)/dt$ mSv/h
^{7}Li(p,n)^{7}Be	0.024	0.002	LiOH	1.7*10^2	3.6	0.012
^{7}Li(p,n)^{7}Be	0.144	0.024	LiOH	5.0*10^2	2.0	0.23
^{7}Li(p,n)^{7}Be	0.25	0.019	LiOH	2.5*10^2	6.2	0.19
^{7}Li(p,n)^{7}Be	0565	0.015	LiOH	1.2*10^3	1.8	1.5
^{3}H(p,n)^{3}He	1.2	0.091	Ti(T)	2.0*10^3	3.1	3.1
^{3}H(p,n)^{3}He	2.5	0.127	Ti(T)	4.9*10^3	1.4	7.3
^{2}H(d,n)^{3}He	5.0	0.200	D2-gas	5.2*10^3	<1.0	7.5
^{2}H(d,n)^{3}He	8.0	0.200	D2-gas	1.9*10^4	<1.0	27.5
^{3}H(d,n)^{4}He	14.8	0.431	Ti(T)	1.3*10^4	3.0	24.3
^{3}H(d,n)^{4}He	19.0	0.300	Ti(T)	8.5*10^2	1.2	1.8

3.1.4.2. Brief description of intermediate- and high-energy neutron fields

Neutron beam facility of the Université Catholique de Louvain (UCL), Louvain-la-Neuve, Belgium, provides neutrons of intermediate energies. The beams are produced using ^{7}Li(p,n)^{7}Be reaction. Three peak energies are possible: 33 MeV, 45 MeV and 60 MeV. The same reaction is used at iThemba Lab (iTL) in Cape Town, South Africa, but peak energies are higher – 99 MeV, 148 MeV, and 198 MeV. The ratio of the fluence in the peak-energy to the total fluence, Φ_{peak}/Φ, ranges from 0.65 at 198 MeV (iTL) to 0.40 at 33 MeV (UCL). The ambient dose equivalent, $dH^*(10)/dt$, are given at about 9 meter distance – at this distance the beam at UCL has 8 cm diameter, and the beam at iTL has area of 11 cm by 11 cm. The values of ambient dose equivalent rates range from 2 mSv/h for 200 MeV beam to 120 mSv/h for 33 MeV beam. The ^{7}Li(p,n)^{7}Be reaction shows angular dependency. The low-energy part is relatively isotropic, while the high-energy peak is forward-directed. This can be used: iTL facility allows for measurement at 0 and 16 degrees. At 0°, both low-energy continuum and high-energy peak contribute to the field, while at 16° the peak is strongly suppressed [63].

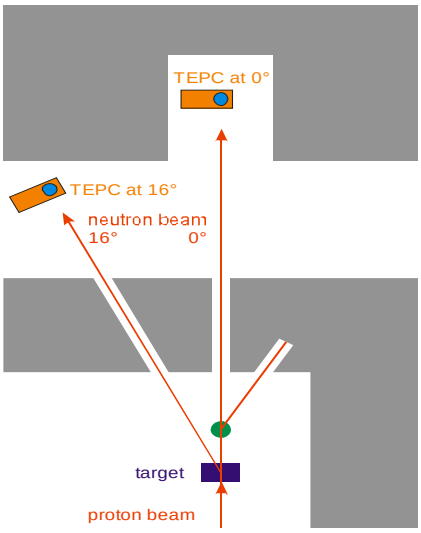

Figure 19 Schema of the iThemba Labs facility.

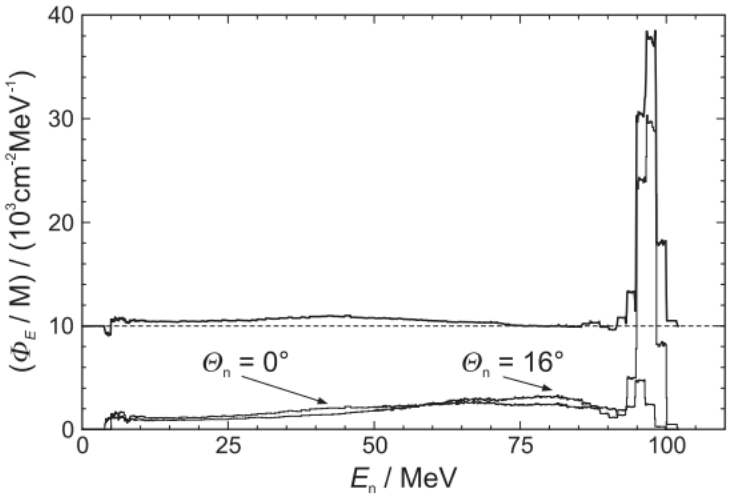

Figure 20. Spectral fluence per unit proton for 100MeV protons at the iThemba Labs for 0 and 16 degrees [63].

3.1.4.3. Calibration factor for neutrons

The microdosimetric spectra measured in neutron fields of different energies are summarized in Figure 21. The spectra have been folded with ICRP-60 Q factor and dose equivalent as measured by the TEPC - H_{tepc} - was calculated by spectra integration.

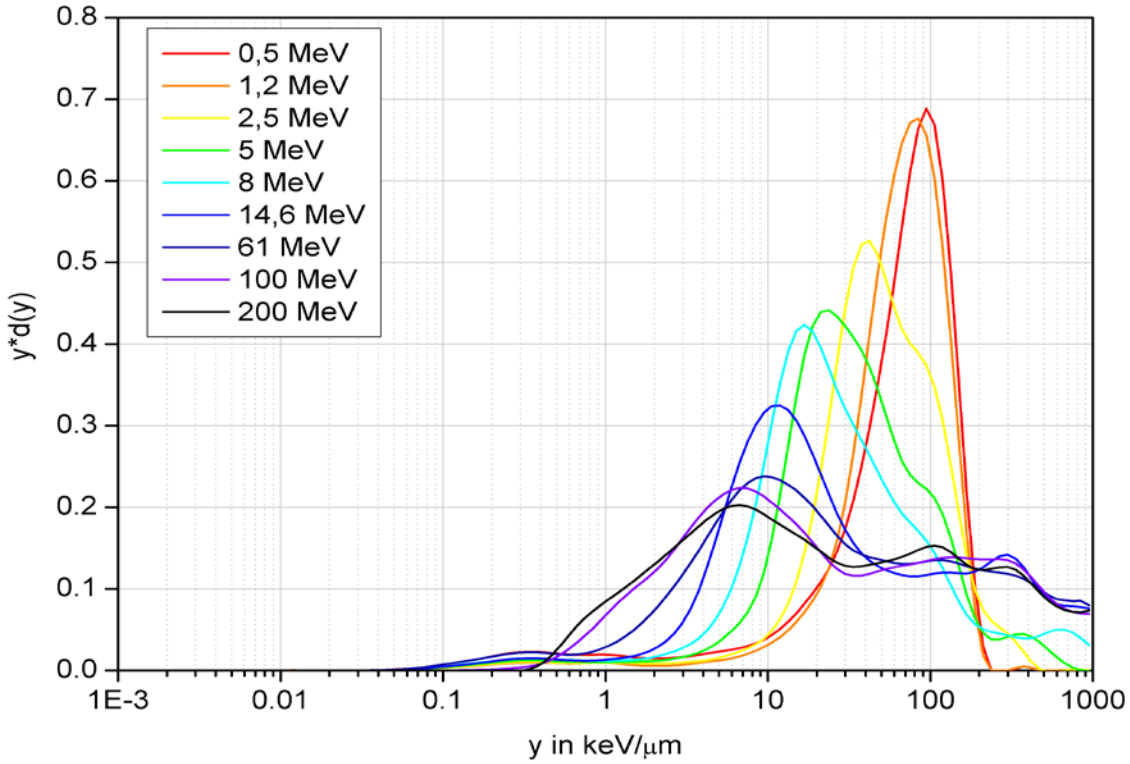

Figure 21. Microdosimetric spectra obtained with TEPC irradiated with neutrons of energies 0.5 MeV – 14.8 MeV (at PTB), 61 MeV (at UCL) and 100 MeV – 200 MeV (at iThemba Labs). [based on 68]

Reference values (Table 11) for measurements as provided by the facilities (neutron dosimetry for measurements at iThemba Labs was conducted by PTB and up to 100 MeV).

Table 11 Comparison of reference and measured ambient dose equivalent for neutrons of different energies [67].

E_n MeV	$dH^*(10)_{ref}/dt$ µSv/h	dH_{tepc}/dt µSv/h
0.5	439	627
1.2	529	746
2.5	59	93
5.0	73	123
8.0	86	119
14.6	77	100
100	309	712

Calibration factor is defined as a ratio of reference ambient dose equivalent to the measured dose equivalent:

$$K_{\mathrm{n}} = \frac{H^{*}(10)_{\mathrm{ref}}}{\int_{0}^{\infty} Q(y)D(y)\mathrm{d}y} = \frac{H^{*}(10)_{\mathrm{ref}}}{\int_{0}^{\infty} H_{tepc}(y)\mathrm{d}y}$$

Uncertainties were taken into account according to “GUM” [66]. Calculated mean calibration factors independent of energy, and angular orientation is given in Table 12.

Table 12. Calculated high-LET-calibration factor with one standard uncertainty (coverage factor k = 1) [67].

Instrument	K_n (k=1)
TEPC#004	0.70 ± 10%

3.1.5. Investigations at CERF facility

3.1.5.1. Overview on the CERF facility

The CERN-EU High Energy Reference Field (CERF) facility is installed on the secondary beam lines coming from the Super Proton Synchrotron (SPS) at CERN. The beam consists of positive hadrons with momentum of 120 GeV/c and is stopped in a copper cylinder with 7 cm diameter and 50 cm length. The particles produced in the target traverse a roof–shielding what is either 80 cm concrete or 40 cm iron which results in almost uniform radiation fields over areas of 2 × 2 m^2. This area is divided into 16 squares of 50 × 50 cm^2 which are called reference exposure locations [69]. It is also possible to use lateral shielding with eight additional exposure locations with shielding of 80 cm or 160 cm of concrete. A sketch of the CERF facility is presented in Figure 22 with marked reference exposure locations for the roof shielding.

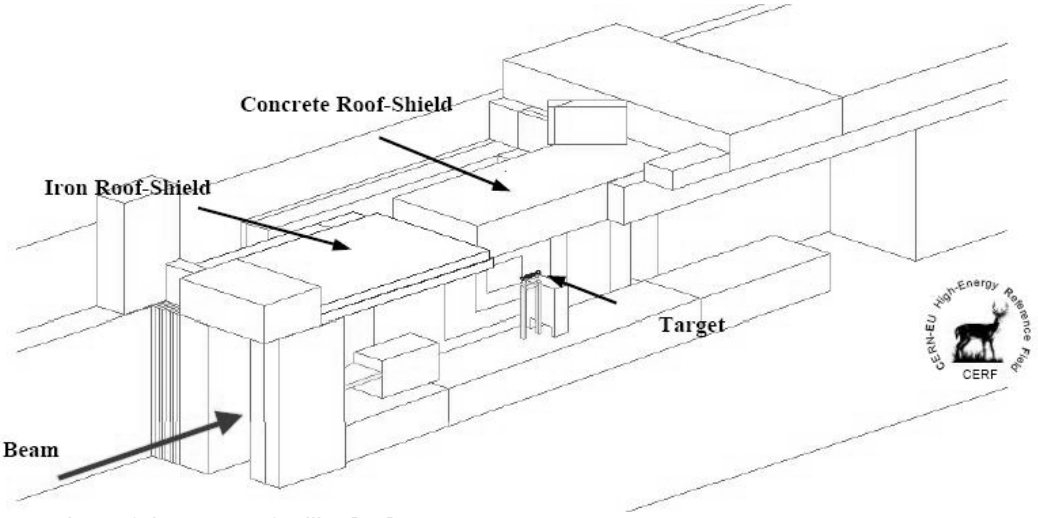

Figure 22 View of the CERF facility [69].

The intensity of primary beam is monitored by an air–filled Precision Ionization Chamber (PIC) operated at atmospheric pressure. One PIC-count corresponds to $2.2 \cdot 10^4$ (within ±10%) particles imparting on the target. During measurements, one burst took 5.1 seconds and interval between two adjacent bursts is 16.8 seconds [69].

Typically, values of dose equivalent rates are 1 – 2 nSv/PIC–counts on top of the iron roof – shielding and 0.3 nSv/PIC–counts outside the 80 cm concrete shields. It is possible to adjust the beam intensity and thus dose equivalent rates at the reference locations in ranges 25 µSv/h – 1 mSv/h for the iron shielding and 5 – 600 µSv/h for concrete shielding [69]. Reference total dose equivalent values (with usage of ICRP – 60 Q factor) on selected reference locations are presented in Table 13.

Table 13 Reference values of dose equivalent rate at specific reference locations as provided during experiments.

Position	**$\times 10^{-10}$ Sv/PIC-count.**		
	Total	Low LET < 6 keV/µm	High LET > 6 keV/µm
Concrete Top CT10	3.51 ± 0.30	0.51 ± 0.03	3.00 ± 0.28
Concrete Side CS3	4.47 ± 0.41	0.52 ± 0.03	3.95 ± 0.39

The energy distributions of various particles at various reference locations have been numerically calculated at CERN. An example of energy distributions for neutrons is showed below in Figure 23. The Figure 24 shows neutron spectrum on the concrete roof-shield (CT6) with the neutron spectrum at an altitude of 10.6 km (FL350).

Neutron energy distribution outside the concrete shield shows large relative contribution of 10 – 100 MeV and thus it is somewhat similar to the neutron field produced by cosmic radiation at flight altitudes. Relative high photon fluence on concrete shielding is the consequence of high contribution of (n,γ) reactions on the target. The electron fluence is one order of magnitude less than that for neutrons.

The CERF reference field is suitable for comparisons of instruments, which are intended to measure cosmic radiation exposure at flight altitudes.

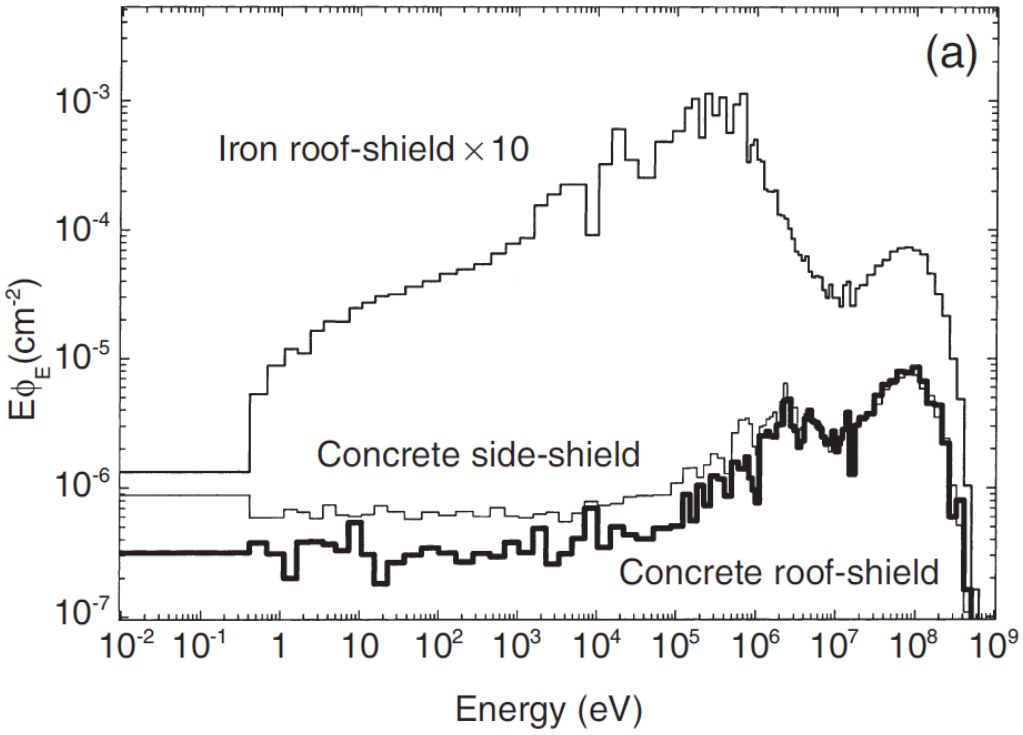

Figure 23 Neutron spectral fluencies on the iron and 80 cm concrete roof-shielding [69].

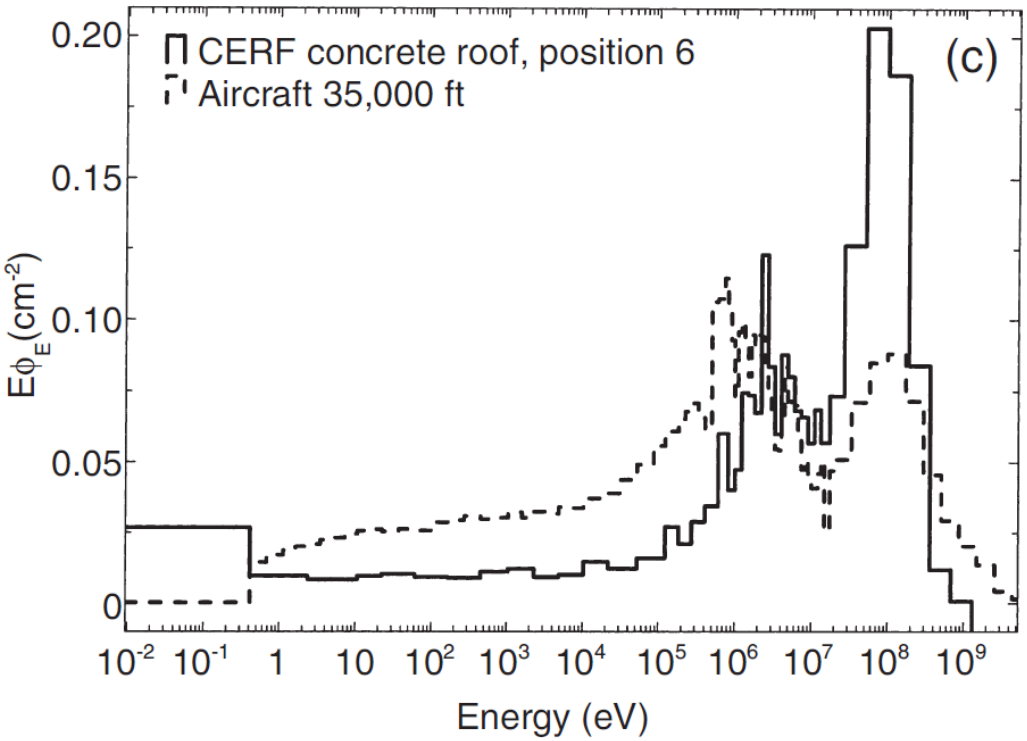

Figure 24 Comparison of the CERF neutron spectrum on the concrete roof-shield (CT6 with the neutron spectrum at an altitude of 10.6 km (FL350) as calculated by Heinrich et al [33]. Figure taken from [69].

3.1.5.2. TEPC investigations

Two TEPC units (TEPC#4 and TEPC#10) have been studied at two different reference positions behind concrete shielding. One was located at roof (CT10), second at the side (SC3). Investigations included measurements of absorbed dose distribution, dose equivalent distribution and background estimation. Additionally, the possibility to change beam intensity gave opportunity to check the linearity of the TEPC responses for absorbed dose, dose equivalent, ambient dose equivalent and their rates.

A correction for the dead time is not necessary for cosmic radiation measurements at flight altitude, but during investigations with high intensity beams sometimes has to be applied due to a high-count rate. The data has been corrected for dead time when necessary; the correction was always less than 4% [70].

Normalized absorbed dose distributions for different beam intensities (41, 168 and 353 µSv/h) and for the background are shown in Figure 25. As seen in the figure, the beam intensity influences the low-LET part of the spectrum while it does not the high-LET part. The changes are caused by background (i.e. muons) which does not depend on beam intensity but changes with other factors as neighboring beams thus is not reproducible. Figure 25 presents also absorbed dose distribution as measured for CS3 position. Figure 26 shows that for CS3 position background does not influence the measurements.

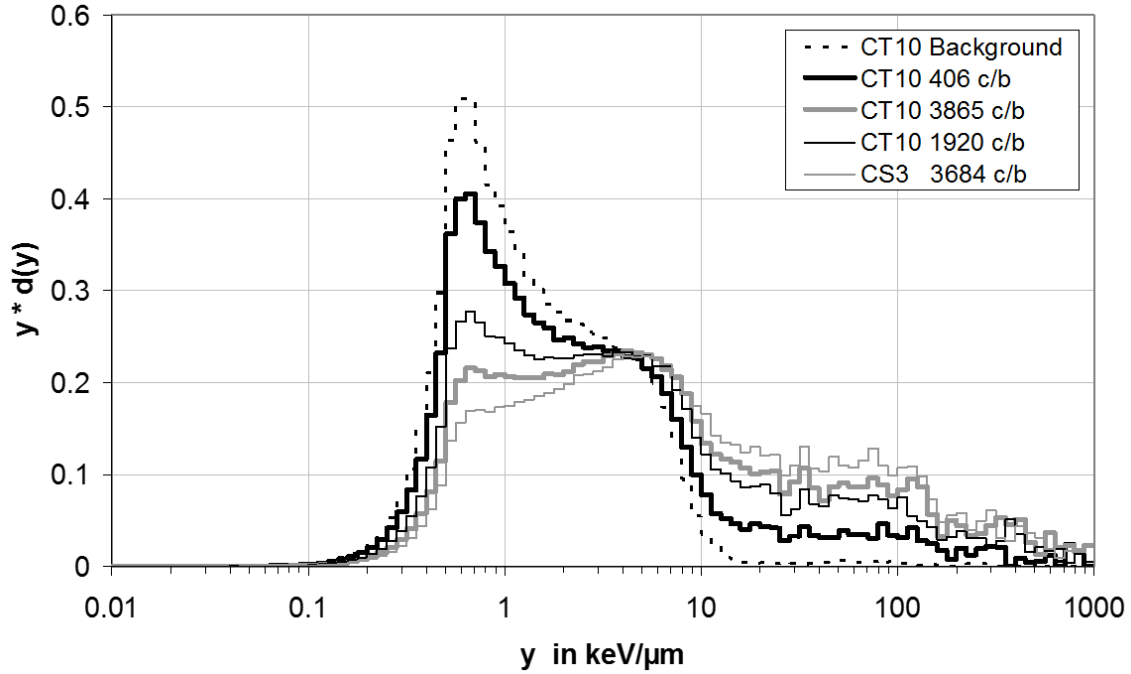

Figure 25 Normalized absorbed dose distributions for background and different beam intensities as a function of lineal energy measured with a TEPC at CT10 and CS3 positions [70].

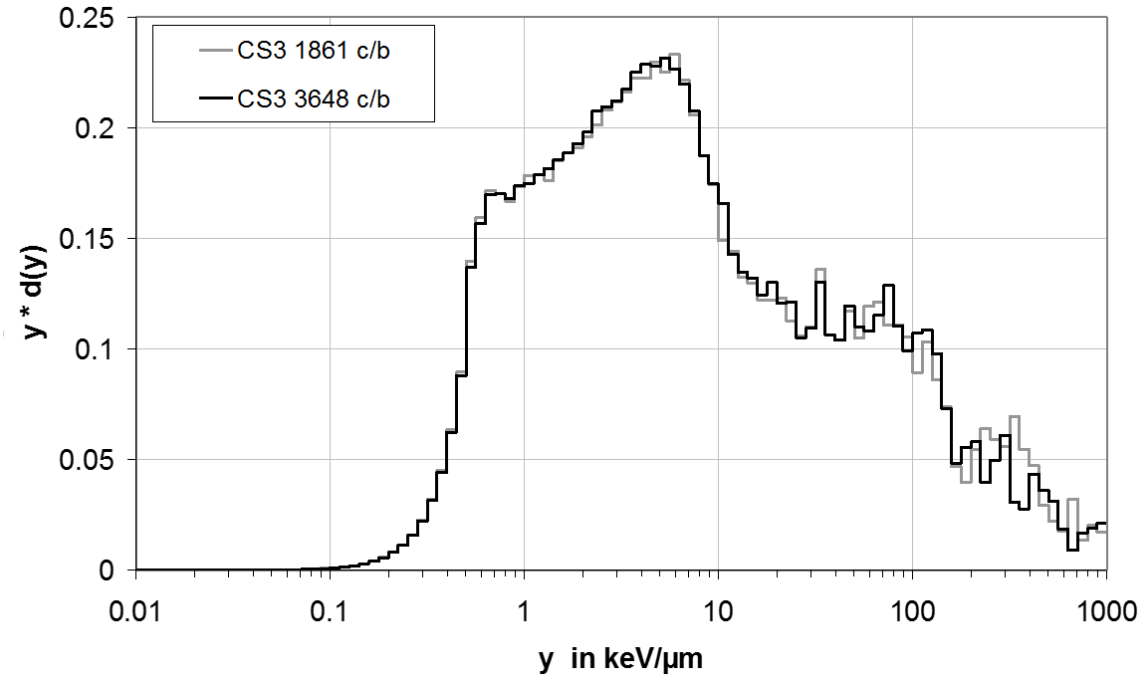

Figure 26 Normalized absorbed dose distributions for different beam intensities as a function of lineal energy measured with a TEPC at CS3 position [70].

For further analyses, the data were corrected for the background since it would be a source of detector response nonlinearity. To demonstrate it, ratios of low-LET and high-LET before and after background subtraction were calculated for both reference positions CT10 and CS3. Figure 27 presents the results as a function of measured absorbed dose rate. For CT10 position, without background subtraction, the ratio R of low-to-high LET decreases with beam intensity from about 11 down to three. After subtraction, the ratio is constant and similarly like for CS3 position is about two.

After background subtraction, the linearity of absorbed dose rate, ambient dose equivalent rate and their low-LET and high-LET components were checked as shown in Figure 28 and Figure 29 Calculated correlation coefficient is greater than 0.99 in every case what confirms very good linearity.

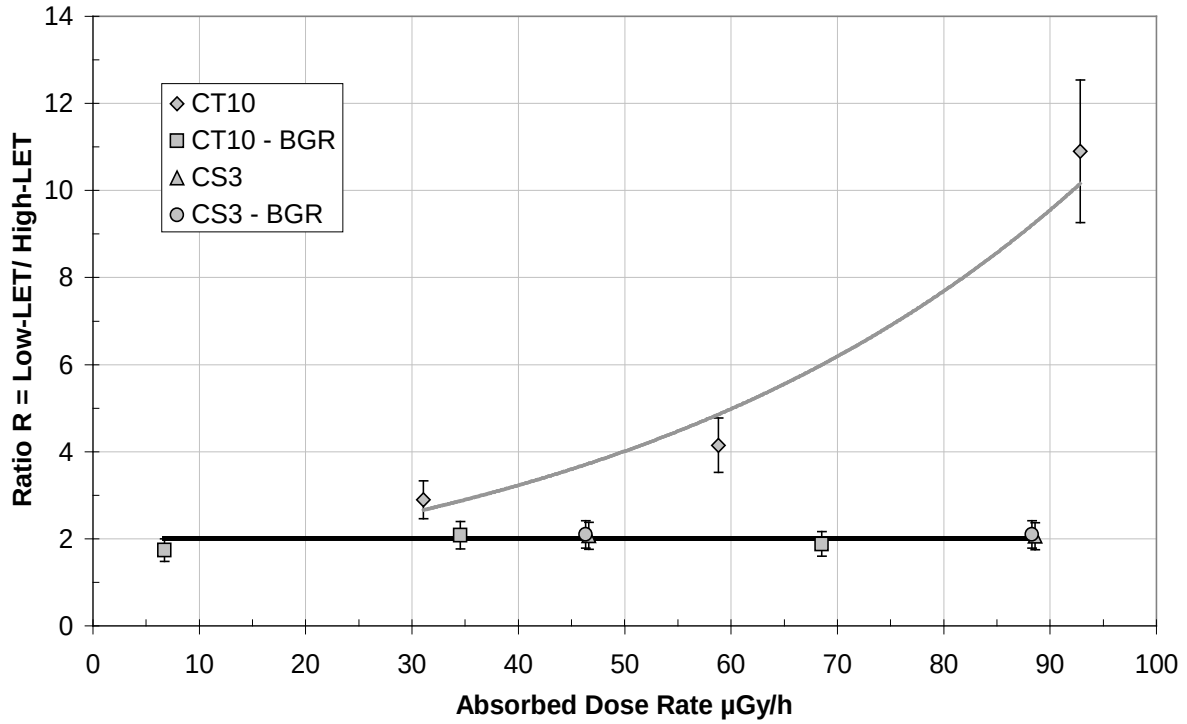

Figure 27 Ratios of low-LET and high-LET before and after the correction as a function of measured absorbed dose rate for CT10 and CS3 reference locations [70].

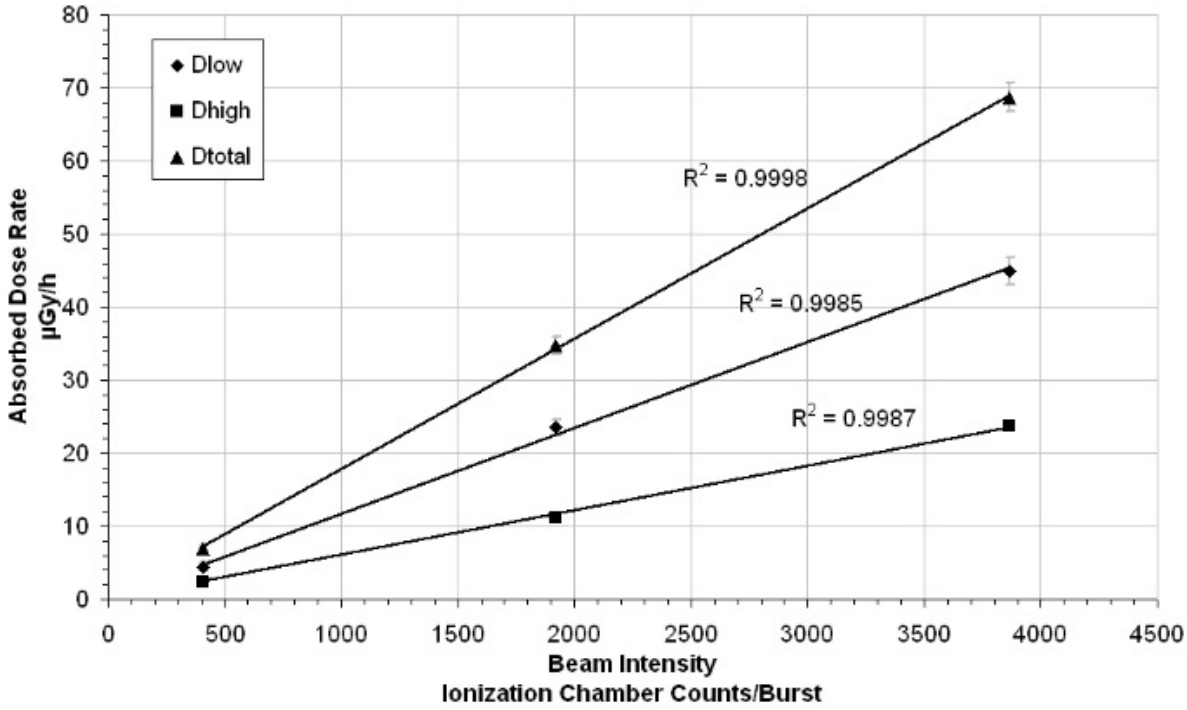

Figure 28 Linearity of absorbed dose rate, with subtracted background at the CT10 reference location [70].

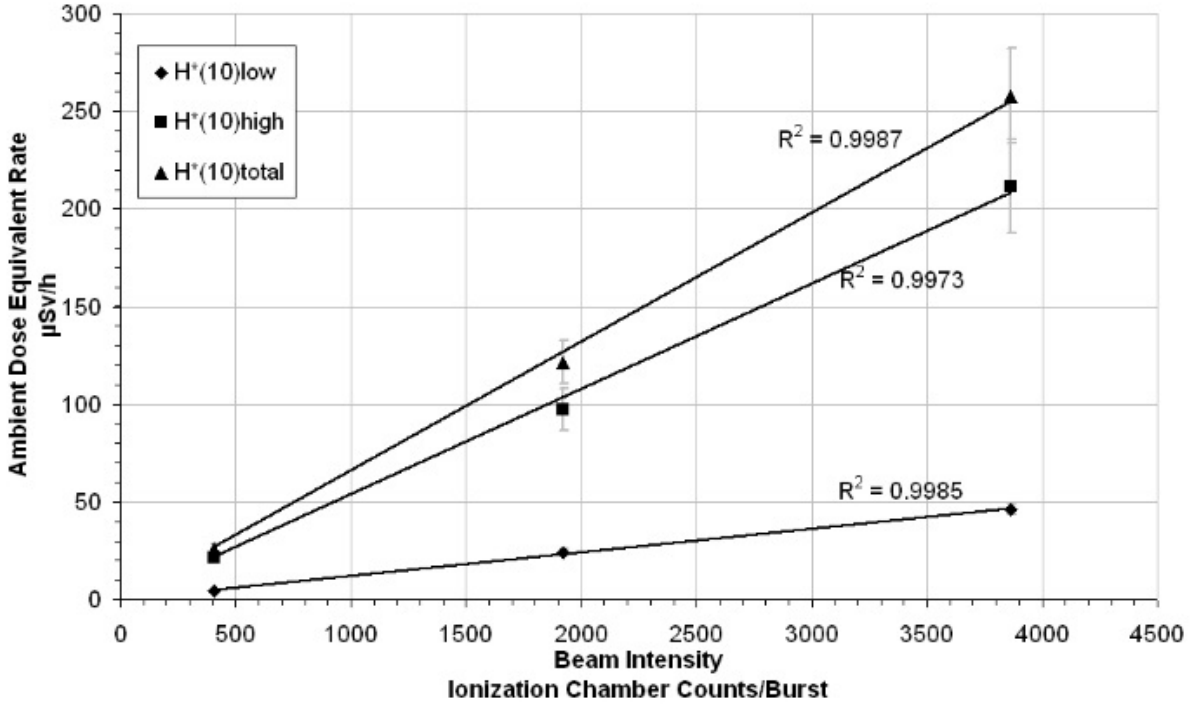

Figure 29 Linearity of ambient dose equivalent rate, with subtracted background at the CT10 reference location [70].

Ambient dose equivalent values have been calculated by folding absorbed dose distribution with ICRP-60 quality factor Q and then applying two calibration factors, separately for low-LET and high-LET as obtained from calibrations: 1.03 ± 4.6% and 0.70 ± 10.4% respectively.

Complementary numerical simulations to these investigations were performed. Resulting simulated absorbed dose distributions for neutrons and photons as well as dose equivalent distribution were published [70]. A comparison of simulated and measured dose equivalent distribution shows good agreement.

As a member of EURADOS Working Group 11 on “High Energy Radiation Field”, author has co-organized a measurement campaign that took place in August 2017. Several TEPC instruments have measured CERF field under very similar conditions (beam intensity, shielding type, and reference position). A publication is planned that shall aim at a comparison of results obtained by different TEPCs, as well as comparison with measurements presented above.

4. Cosmic radiation on-board aircraft measurements

A properly calibrated instrument allows for cosmic radiation measurements. This chapter gives examples on the use of TEPC for measuring cosmic radiation. In this chapter author describes his measurements during well-defined and stable flight and solar conditions [71], and data analysis done for measurements conducted during distorted Earth magnetic field when Ground Level Enhancements occurred due to solar flares [72].

4.1. CAATER flight campaign

CAATER stands for “Co-ordinated Access to Aircraft for Transnational Environmental Research”. The CAATER campaign consisted of several different projects. One of them was a flight campaign arranged by the DOSMAX project group [73] with the main objective to compare different cosmic radiation measurement instruments under the same flight conditions. Six different European institutes participated in common flights providing and operating instrumentations for different measurement techniques. For the work presented here, AIT (formerly ARC Seibersdorf research ARCS) contributed with TEPC measurements.

During a typical, commercial flight, the altitude of a flight can vary significantly. Additionally, the flight route can cross a wide range of geomagnetic latitudes especially for North – South routes. Both of these parameters have major impact on measurements. The flights in CAATER campaign were non-commercial what provided a unique opportunity to customize their altitude and route. For results reliability the measurements were done at fixed geographical positions. In practice, the aircraft circled above one location in a tight measuring pattern slightly stretched in an East – West direction (Figure 31, Figure 32 and wavy pattern of vertical cut-off rigidity in Figure 33). The variations of geographical latitude and longitude in every case were less than 1 degree so the geographical position was taken as being constant.

As mentioned in chapter 2, cosmic radiation exposure depends on altitude, geographical position and solar activity. To appreciate in fluence of atmospheric shielding, two altitudes were chosen: one higher at FL 400 (12.2 km) and the second lower at FL 320 (9.8 km) (Figure 33). To see the effect of Earth’s magnetic field, two locations were chosen. One near and above Aalborg (57N, 10E), Denmark, for less magnetic shielding (low value of vertical cut-off rigidity, r_c = 1.8 GV) and one near and above Rome (42N, 12E), Italy, for greater magnetic shielding (higher value of vertical cut-off rigidity, r_c = 6.4 GV) (see Figure 30). Finally, to improve statistical uncertainties, measurements during each flight lasted at least two hours [71].

In summary, during the CAATER flight campaign four flights were performed, each with measuring pattern lasting more than 2 hours. Two flights were over Aalborg, one at FL 400, the second at FL 320 and two others over Rome at the same altitudes.

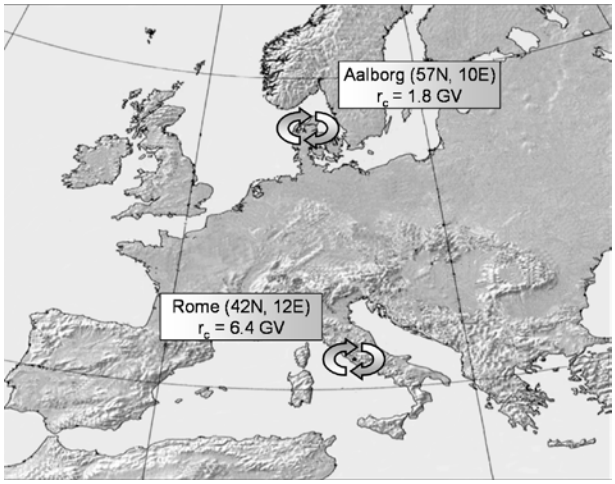

Figure 30 Geographical locations of the CAATER flights [71].

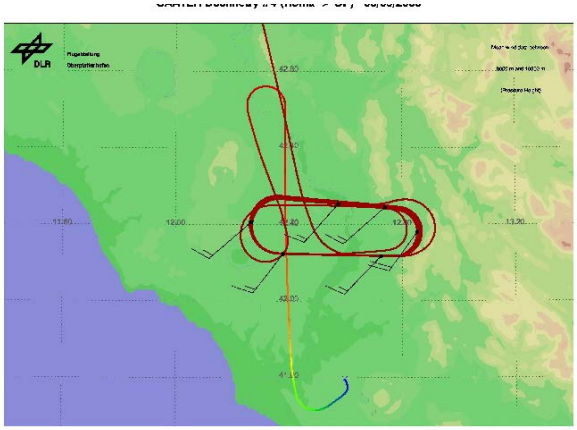

Figure 31 Real measuring pattern trace over Rome, Italy

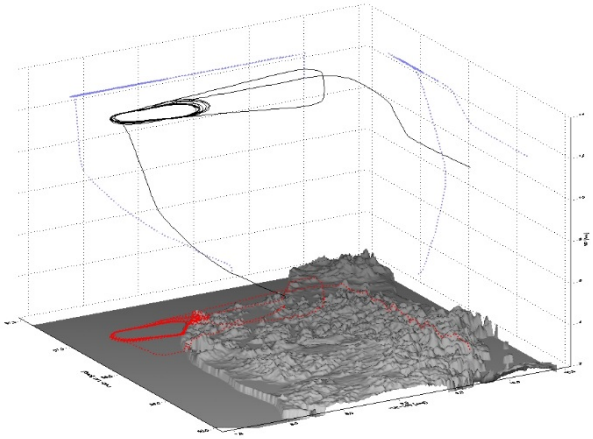

Figure 32 Real measuring pattern trace over Aalborg, Denmark

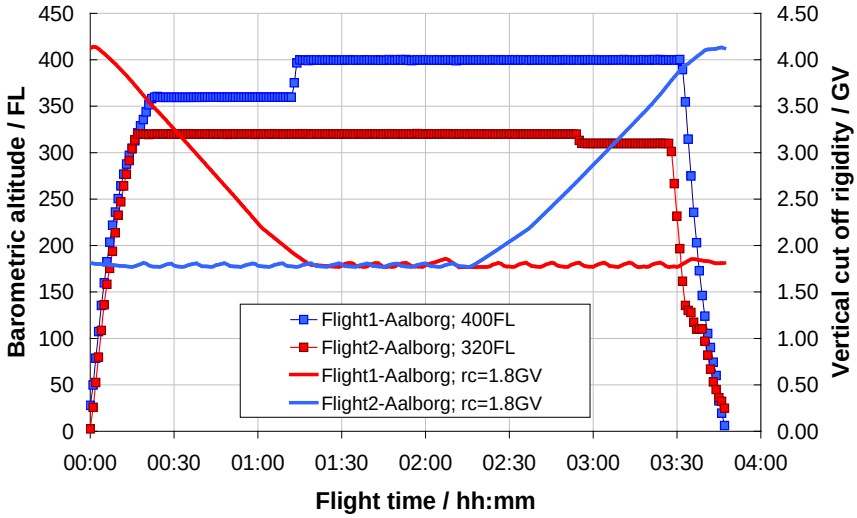

Figure 33 Flight profiles for flights performed over Aalborg. Altitudes are marked with squares, vertical cut-off rigidities with solid lines. Flight-1 (400FL) is marked with blue, flight-2 (320FL) with red.

Six different institutes participated with different measuring techniques. Most of the instrumentations were based on single-event technique (see Chapter 3) One of the

instruments used variance or the variance-covariance method [74]. For the full list of instrumentations with detailed description and techniques they employ, see reference [75].

The measurements gave results in terms of average quality factor, $\overline{Q}_D$, total and low-LET ambient dose equivalent rates, $\dot{H}^*(10)$, $\dot{H}^*(10)_{low}$ respectively, as well as microdosimetric quantities obtained from microdosimetric spectra: total dose-mean lineal energy, $\bar{y}_D$, and dose-mean lineal energy calculated for low-LET and high-LET parts of the spectra $\bar{y}_{D,low}$, $\bar{y}_{D,high}$.

Microdosimetric spectrum of absorbed dose shown in Figure 34 is normalized to absorbed dose rate as calculated from appropriate measurements. Spectra show that main contribution to absorbed dose rate comes from low-LET (below 10 keV/µm) part. In order to obtain dose equivalent distributions (Figure 35), absorbed dose spectra were folded with the quality factor Q as defined in ICRP Publication 60 [5]. The quality factor, Q, is equal to one in the low-LET part, but greater than one for high-LET therefore these parts of dose equivalent distributions are enhanced and contribute to the total dose equivalent rates approximately equally as low-LET part. Figure 35 shows also that statistics of the low-LET part are much better than in high-LET.

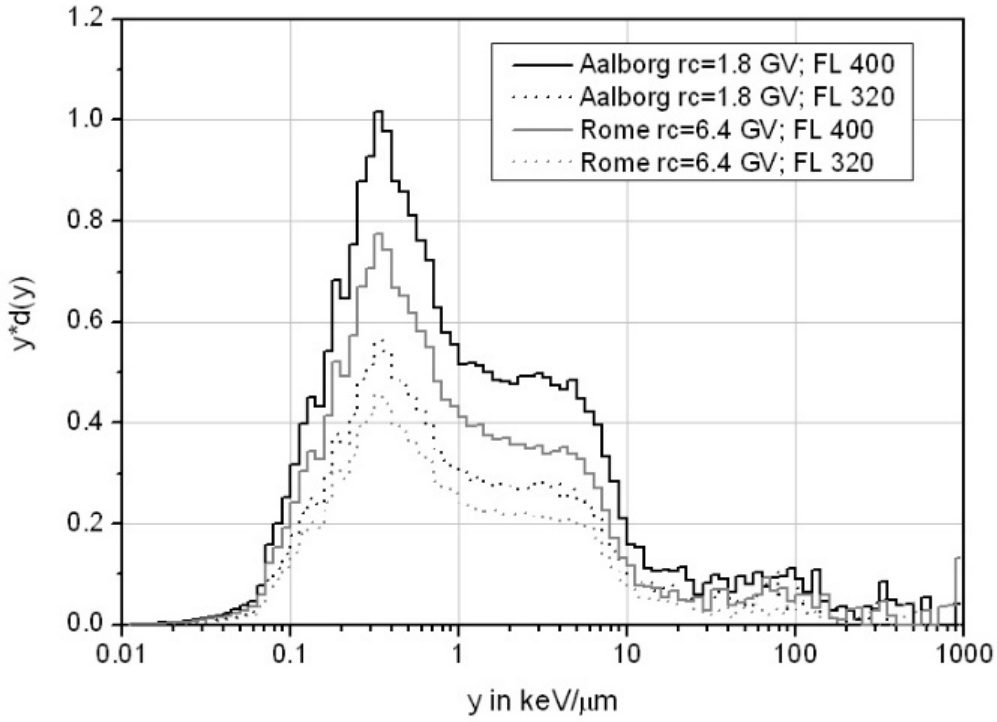

Figure 34 Measured absorbed dose distributions as function of lineal energy. The areas under the curves give the respective values of the absorbed dose in one hour [71].

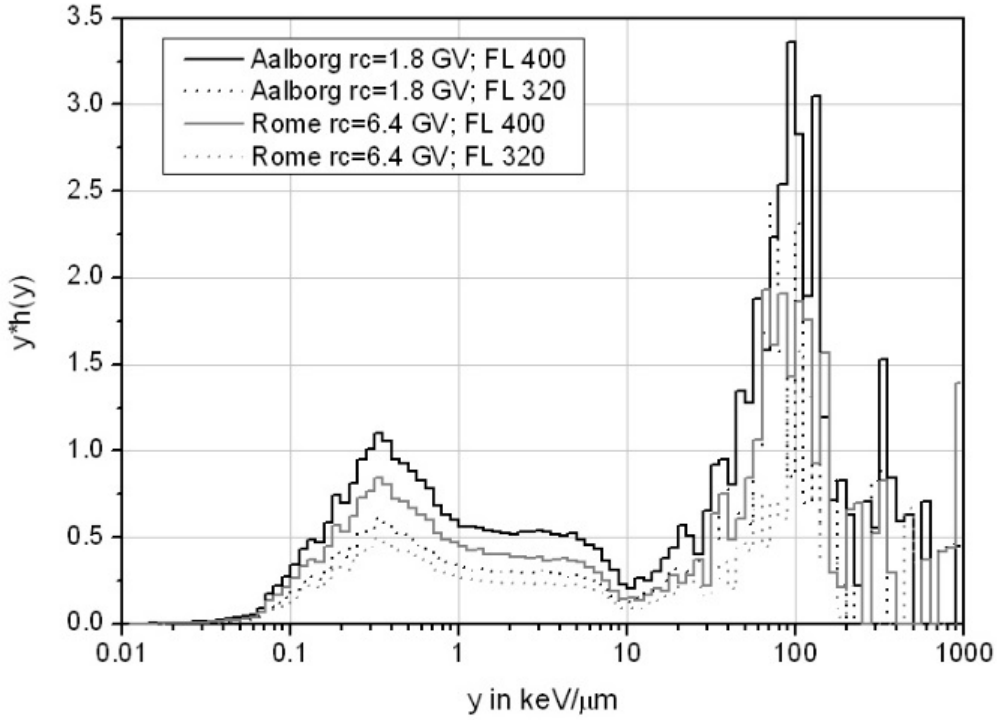

Figure 35 Measured dose equivalent distributions as a function of lineal energy. The areas under the curves give the respective values of the dose equivalent in one hour [71].

Table 14 Measurement results in terms of absorbed dose rate, ambient dose equivalent rate, mean quality factor and dose-mean lineal energy [75].

Flight; Altitude; Cut-off;	**Absorbed dose rate, *dD/dt*** µGy/h	**Ambient dose equivalent rate, *dH*(10)/dt*** µSv/h	**Mean quality factor,** $\overline{Q}_D$	**Total dose-mean lineal energy** $\bar{y}_D$ keV/µm	**Low-LET dose-mean lineal energy** $\bar{y}_{D,low}$ keV/µm	**High-LET dose-mean lineal energy** $\bar{y}_{D,high}$ keV/µm
Flight #1 400 FL 1.8 GV	3.1 ± 0.3	6.0 ± 0.9	2.4 ± 0.1	13	1.6	110
Flight #2 320 FL 1.8 GV	1.7 ± 0.2	3.4 ± 0.5	2.4 ± 0.1	13	1.6	103
Flight #3 400 FL 6.4 GV	2.3 ± 0.2	4.3 ± 0.7	2.3 ± 0.1	18	1.6	172
Flight #4 320 FL 6.4 GV	1.3 ± 0.1	2.4 ± 0.4	2.2 ± 0.1	9	1.5	89

Table 14 above presents measurement results together with combined standard uncertainties. Comparing two flights at the same altitude, greater doses are recorded for northern flight performed at lower magnetic shielding. Similarly, comparing two flights performed at the same position but different altitudes, greater doses are

obtained for flights at higher altitude. The combined standard uncertainties for absorbed dose are about 10%, and about 15% for ambient dose equivalent. Low-LET dose-mean lineal energy is about 1.6 keV/µm for all flights. Interestingly, flight #3 (400 FL, 6.4 GV) shows noticeably higher dose-mean lineal energy than any other flight. The reason for this are events recorded in the last channel of the TEPC (y ≥ 1024 keV/ µm in Figure 35). FLUKA Monte Carlo simulations of TEPC response to cosmic radiation does not show similar effect [71]. Such effects could appear when a fragmentation of heavy ion occurs on a steel plate of the instrument, but a technical origin cannot be excluded.

Studies performed by different groups on the measured data showed good agreement of ambient dose equivalent obtained with different measuring systems [71, 74, and 75], good agreement with simulations [71, and 76] and calculation codes [76]. Average standard deviation as obtained in measurements has been reported as remarkably good and ranges from 6% to 21% [75].

As a member of EURADOS Working Group 11 on “High Energy Radiation Field”, author has committed to take part in future on-board measurements of cosmic radiation that in planned for Autumn/Winter 2017. It will be an activity that is complementary to already performed investigations at CERF radiation field. The campaign aims at a comparison of results obtained by various instruments. A publication is planned that shall aim at a comparison of results obtained by different TEPCs, as well as comparison with measurements presented above.

4.2. The EURADOS Aircraft Crew In-Flight Database

In 2000, the Working Group 5 on “Cosmic Radiation Exposure of Aircraft Crew” of European Radiation Dosimetry Group, EURADOS, coordinated effort of about 24 international research institutes involved in aircraft crew dosimetry. The intention was to provide public information of the assessment of individual doses in aircraft crew workplaces, to assess the legitimacy of different approaches, and to provide an input to technical recommendations. The EURADOS WG5 final report [77] covers these issues, gives a detailed summary on gathered experimental dataset, results of calculations, and descriptions of applied measurements methods and simulations techniques. A part of this report is the EURADOS Aircraft Crew In-Flight Database, which was implemented by ARCS - ARC Seibersdorf research (today Seibersdorf Laboratories). Author has established, organized, maintained the database and conducted his first data analysis towards modelling of cosmic radiation at flight altitudes.

The database collects in-flight data measured by various types of active and passive instruments such as ionization chambers, Bonner spheres, REM counters, Tissue Equivalent Proportional Counters (TEPC), Si-spectra dosemeters (Liulin-type),

track detectors and thermo-luminescent detectors, or dedicated systems consisting of combination of instruments and algorithms like for example ACREM system [78, 79]. A detailed description of these instruments, their calibration procedures and measurement method employed are given in the EURADOS WG5 final report [77].

The measurements collected in the database are arranged in a systematic way according to the three main parameters: barometric altitude, geographical position and solar activity. The database contains also additional information on measurements such as integration time or uncertainty. The Table 15 below presents a short summary of the final status of the database.

Table 15 Status of the EURADOS Aircraft Crew In-Flight Database

Description	Data
Time period	May 1992 – Nov 2007
Range of solar deceleration potential	471 MV – 1320 MV
Range of geographical longitude	180° West – 180° East
Range of geographical latitude	97° North – 62° South
Range of vertical cut-off rigidity	0 – 17.4 GV
Range of barometric altitude	up to 16500 m
Number of datasets	16921

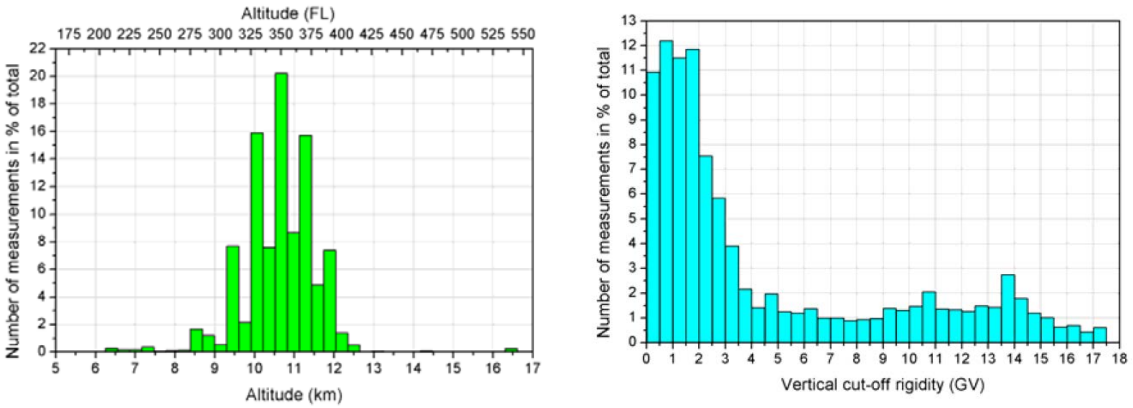

Figure 36 Frequency distributions of in-flight measurements as a function of altitude (left) and vertical cut-off rigidity (right) [79].

Author analyzed the collected data. The Figure 36 shows frequency distributions of in-flight measurements as a function of altitude and as a function vertical cut-off rigidity as present in the database at its stage in 2005 [79]. Other data visualizations for selected conditions are published in the EURADOS WG5 final report [77]. Author has also performed his first attempts of modelling of radiation exposure at flight altitudes [79].

4.3. Measurements during solar flares

During October and November 2003 an unusual extended solar storms, commonly referred to as the Halloween Storms, have been observed. Geostationary Operational Environment Satellites (GOES) operated by National Oceanic and Atmospheric Administration (NOAA) recorded several orders of magnitude increase of fluence rates of charged particles, electromagnetic waves (X-rays, radiofrequencies) and severe distortions in Earth's magnetic field.

Solar flares are commonly classified according to their X-rays peak fluence rate. The largest increase of X-rays occurred during Halloween Storm, on 4th of November, and it was the most powerful solar flare ever recorded up to day. Associated Coronal Mass Ejections (CME) led to significant increase of measured solar charged particles. The largest increase of measured proton fluence rate, about four orders of magnitude, occurred on 28th of October (Figure 37 b). When the Solar Energetic Particles (SEP) reached the Earth, the shock wave disturbed Earth's magnetic field causing geomagnetic storms (Figure 37 d). On ground, neutron monitors installed at different locations recorded sudden at least 5%-increase of continuously measured cosmic radiation, noting therefore three Ground Level Enhancements (GLE65, GLE66 and GLE67), and, recorded associated large 25%-decrease of measured intensities – so called Forbush decrease (Figure 37 c and Figure 38).

Between September and December 2003, the TEPC operated by Seibersdorf Laboratories (formerly ARCS) was fix-installed on board an A340 Lufthansa Airbus. Continuous, long-term cosmic radiation measurements of 220 flights were conducted (Figure 37 a). A rich set of data was collected before, during and after the storm at flight altitudes. For the analysis of the radiation exposure at flight altitudes, eight flights performed on similar routes between Chicago and Munich were selected and analyzed in details (Figure 38). The mean ambient dose equivalent rate during cruising phase of those flights in September 2003 was 4.3±0.3 µSv/h. During flight 3 (Figure 39), a 35% increase of ambient dose equivalent rate due to GLE65 was noted. During flight 5 (Figure 39), on the other hand, a 31% decrease was noted what is attributed to the 25% Forbush decrease (Figure 38). The overall variation of ambient dose equivalent between these two flights that were conducted just one day one after each other was 70%. The exposure during flight 3 was 64 µSv of ambient dose equivalent, during flight 5 38 µSv; typically, in September 2003, during quiet solar conditions it was 48 µSv. More detailed information on those measurements including seven stages analysis and possible scenarios for flights at different altitude is published elsewhere [72].

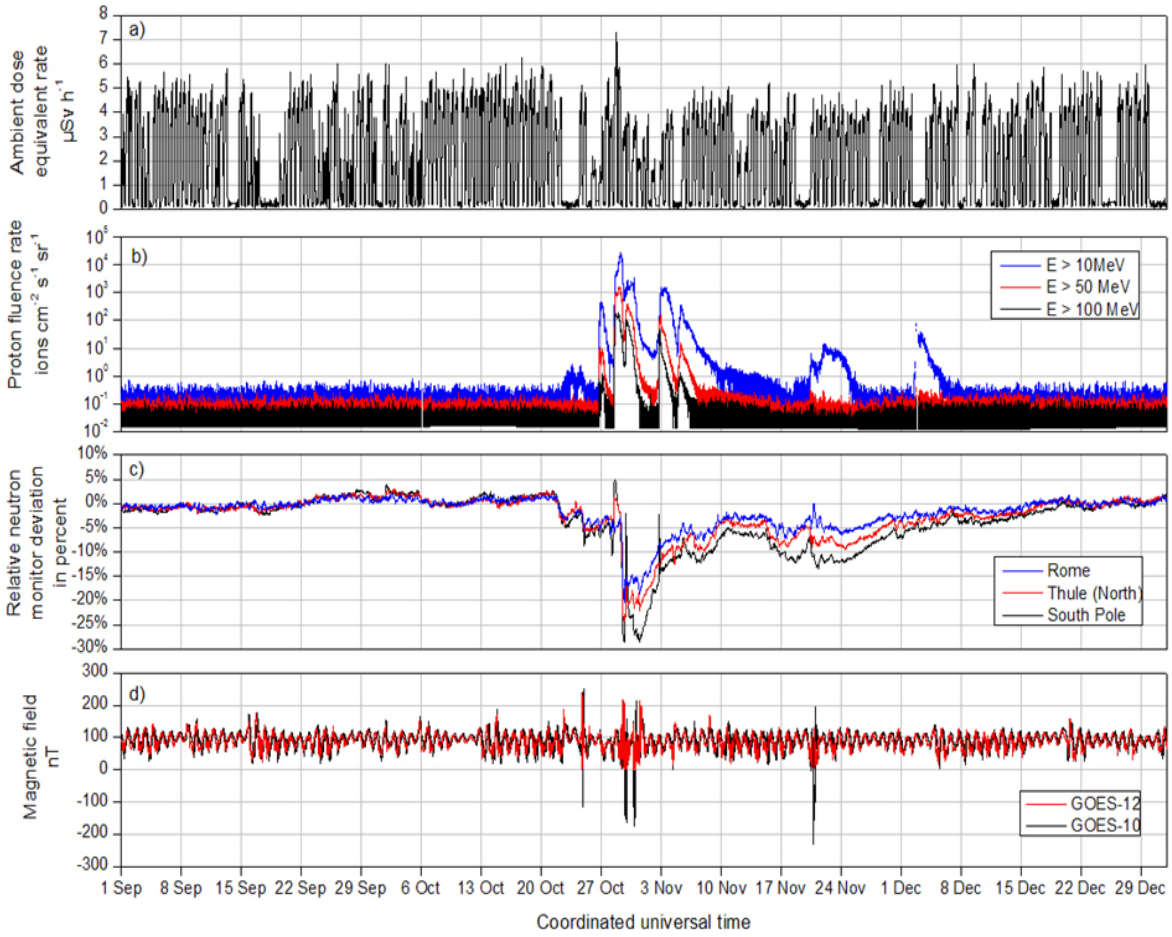

Figure 37 Measurements performed during September and December 2003 of the: a) radiation exposure in terms of ambient dose equivalent rates measured by TEPC, b) cosmic proton fluence rate measured by GOES satellites, c) deviations of neutron monitor records located on ground in Rome, Thule and at South Pole, d) Earth's magnetic field as measured by GOES satellites. Figure taken from [72].

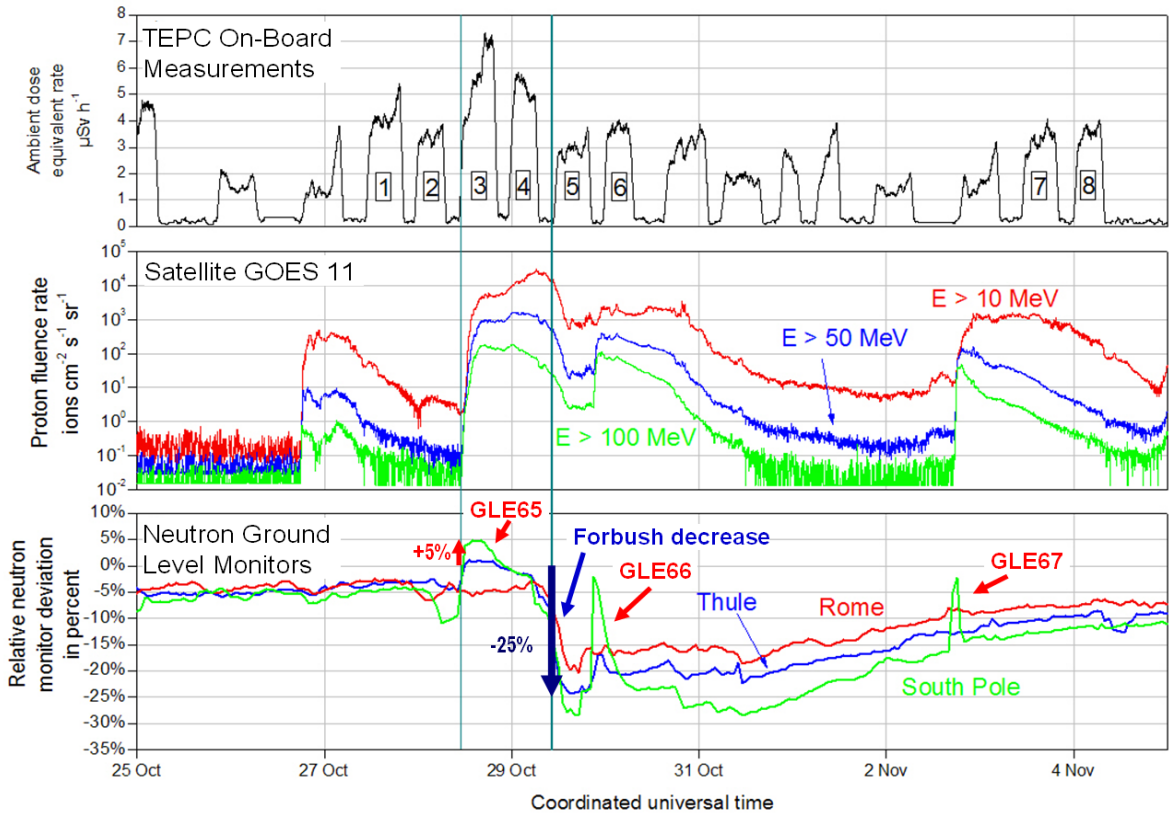

Figure 38 TEPC measurements during Halloween Storms with flights between Munich and Chicago selected for analyses (top); proton fluence rate as measured by GOES satellite (middle); relative deviations of neutron monitor records located at Thule, Rome and South Pole with marked increases noting GLE65, GLE66 and GLE67, and Forbush decrease (bottom). Figure taken from [72].

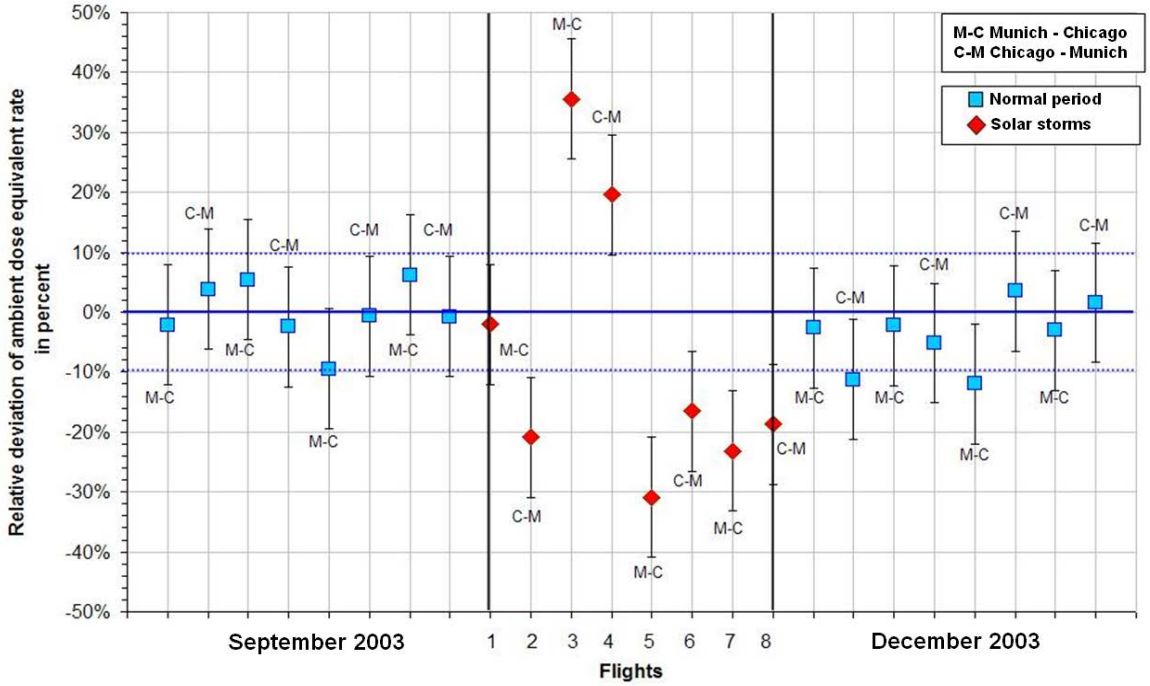

Figure 39 Relative deviation of ambient dose equivalent rate from the reference value during cruising phase of selected flights before, during and after Halloween Storms. Figure taken from [72].

5. Monte Carlo simulations of radiation exposure due to GCR and SEP events

There is a rich set of GCR measurements published [e.g. 77, 78, and 79], but most of them are done during normal civil flights under typical flight conditions. Only some measurements are conducted under special conditions. For example, measurements at very high altitudes were done during Concorde flights [77]; measurements carried out at constant geomagnetic conditions needed a special flight campaign in which author took part [71, 75, and 76]. Beck et. al [81] provide a compilation of measurements done during extraordinary solar conditions, but one has to conclude that such measurements are scarce. From this point of view, numerical simulations of radiation transport is a great and indispensable tool for modelling of radiation exposure at civil flight altitudes. The great advantage is that one can perform simulations at any desired conditions, for example during strong GLEs. This chapter presents Monte Carlo numerical simulations as performed by the author. Emphasis is laid on simulation of Solar Energetic Particle events. Simulations of GCR were carried out as a comparison between GCR and SEP results.

5.1. Overview on Geant4 toolkit

Geant4 [82, 83] is a software toolkit for simulating the passage of particles through matter. It is developed and maintained by the Geant4 Collaboration, which is a worldwide teamwork of physicists and software engineers.
The toolkit offers a large set of physical processes (e.g. electromagnetic, hadronic and optical), different type of particles (leptons, bosons, mesons, baryons, etc.) and databases with properties of matter and elements. Particle propagation in magnetic and electric fields can be taken into account. Physics processes cover a wide range of energy spanning from 250 eV (and even some eV in Geant4-DNA project http://geant4-dna.org) up to TeV depending on the case. Geant4 is successfully used for detector design, medical applications, space applications, high-energy physics (accelerators), and radiation protection.

The toolkit is implemented in C++ programming language using object oriented programming technique. This approach allows users effectively to manage complexity and limit dependencies by defining a uniform interfaces and common organizational principles in order to create their own applications for solving a specific problem.

5.2. Overview on Geant4 application: PLANETOCOSMICS

PLANETOCOSMICS [84] is Geant4 application that allows computing the hadronic and electromagnetic interactions of cosmic radiation with Earth, Mars, and Mercury

environment. In the case of Earth, it is possible to take into account the presence of Earth's magnetic field, atmosphere and soil. The main purposes for the code are:

- Computation of fluxes of particles resulting from the interaction of cosmic radiation the planet's atmosphere.
- Computation of the propagation of charged particles in the Earth magnetosphere.
- Computation of cut off rigidity at given position on the Earth and for different direction of incidence.
- Visualization of magnetic field lines, and the trajectories of primary and secondary particles in the Earth environment.

PLANETOCOSMICS is controlled by a set of input files that define necessary parameters for simulations: geometry, atmosphere models, magnetic field models, spectrum of primary particles impinging on the geometry, set of physical processes that shall be simulated, and type of requested output. The application has open code, so advanced users can influence even the set of interaction cross sections for a selected model, or define ranges of energies in which the user-selected interaction model shall be used instead of the default one. The author used the latest available version of PLANETOCOSMICS [85] in this advanced mode for all simulations presented in this work.

5.3. Monte Carlo simulations and results

Monte Carlo simulations of radiation transport in Earth atmosphere requires to choose simulation geometry, atmospheric model, influence of Earth magnetic field, selection of simulated physical interaction models, primary input spectra, and finally scored quantities.

Figure 40 shows schematically selected geometry for simulations. A block of atmosphere of defined dimensions (500 km x 500 km x 150 km) and centered at a defined position (geographical latitude and longitude) is considered as a place where interactions of cosmic radiation occur. The block is high enough (150 km of height) that it contains full vertical atmospheric profile and additionally some layer of space above. The parallelepiped is divided into several parallel layers, which define detection levels i.e. altitudes at which results of simulations are recorded. Soil has 1 km of thickness to count for backscattered radiation in lower detection layers. The input spectra is considered as a one-point source of primaries located at the top of the atmosphere (100 km), and the angular distribution is defined according to the cosine law in order to reproduce isotropic fluence of cosmic radiation.

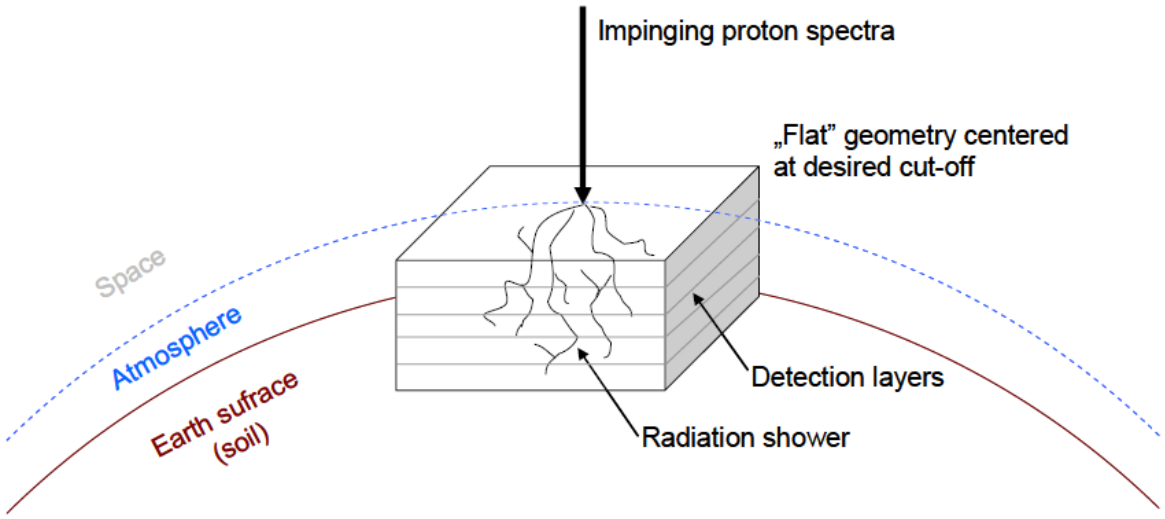

Figure 40 Schema of the geometry used for describing the ionizing particle transport (radiation shower) through the atmosphere.

To model atmosphere, author used the NRLMSISE2000 [86, 87] model. Density profile of the atmosphere is dependent on several parameters like geographic latitude, longitude, universal time (UT), the $F_{10.7}$ index (10.7 cm solar radio flux used as solar UV proxy) and the geomagnetic index Ap. The influence of the last two indices is negligible below 80 km.

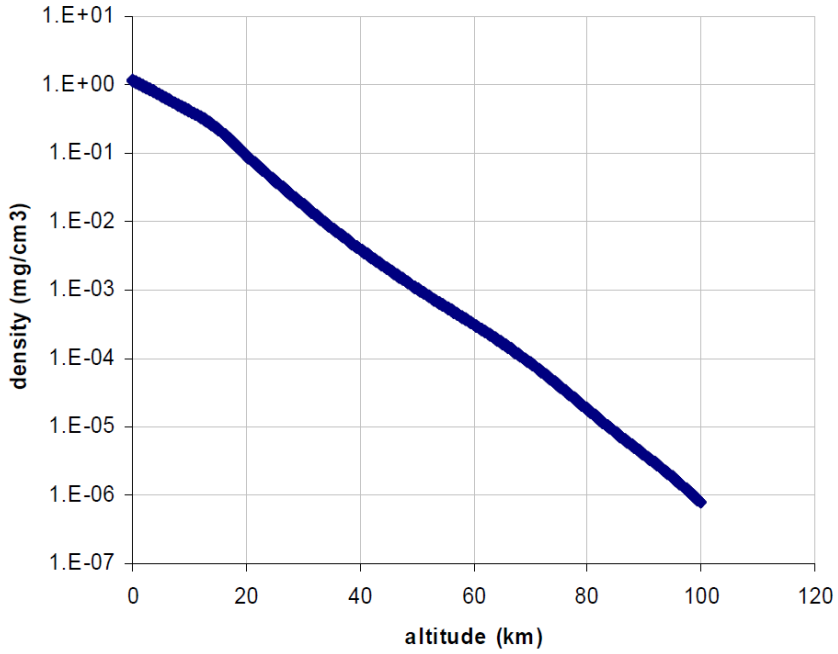

Figure 41 Density of the atmosphere over altitude according the model NRLMSISE2000 [85].

To count for the influence of Earth magnetic field, author used the vertical cut-off rigidity model as described in chapter 2.4.2. In practice, each primary particle which rigidity (or equivalent kinetic energy) is lower than vertical cut-off rigidity is deflected by Earth's magnetic field and therefore rejected for simulations - primary particle spectra is cut as schematically depicted in Figure 42.

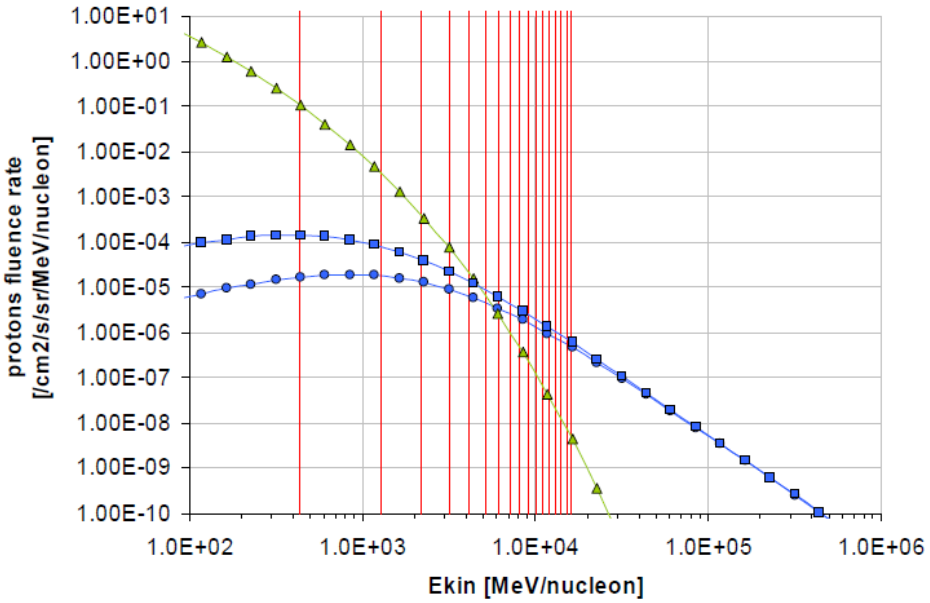

Figure 42 An example of GCR protons spectra for solar maximum (blue circles) and solar minimum (blue squares), an example of SEP event that lead to GLE42 on 29.09.1989 (green triangles) as simulated by the author. Vertical red lines show kinetic energies of a proton impinging in vertical direction that is equivalent to vertical cut-off rigidity as described in chapter 2.4.2.

Monte Carlo simulations of radiation transport in Earth atmosphere requires a selection of physical models to simulate hadronic and electromagnetic interactions. For simulations presented here, author selected one predefined list of physical processes among those available in Geant4: the QGSP_BERT_HP list. The QGSP list bases on Quark Gluon String model for high-energy interactions of protons, neutrons, pions and kaons, and nuclei. Such interactions usually result in an excited nucleus. The precompound model handles the de-excitation of such nucleus. For hadronic interactions below some 10 GeV, the Bertini cascade model is used. To transport neutrons below 20 MeV, a high precision neutron package is used. The QGSP_BERT_HP list contains a standard physics list for electromagnetic processes: multiple scattering of electrons and muons, bremsstrahlung and the photoelectric effect. To take care about other electromagnetic processes like Compton scattering, Rayleigh scattering, gamma conversion, fluorescence and Auger electron emission, author added the Livermore electromagnetic package.

Monte Carlo modelling of radiation exposure due to GCR and due SEP events differ primarily in the primary radiation spectra. To model GCR conditions, author used the default models [88, 89] implemented in PLANETOCOSMICS. In this model, the flux of protons that arrives at 1 AU, j_{1AU}, is an effect of a modulation (modulation potential, Φ) of an undisturbed GCR proton flux in the local interstellar medium, j_{LIS}, according to solar activity.

$$\frac{j_{1AU}(E_{kin})}{E^2 - m_0^2} = \frac{j_{LIS}(E_{kin} + |z|e\Phi)}{(E + |z|e\Phi)^2 - m_0^2}$$

The solar modulation parameter Φ is a function of solar activity expressed in MV. The *E* is the total energy, m_0 – rest mass, and E_{kin} the kinetic energy of the considered particle. The expression |z| e Φ is the energy loss of a charged particle during its travel through heliosphere until reaching 1 AU distance.
In PLANETOCOSMICS, the flux of protons in the local interstellar medium, j_{LIS}, is based on the Garcia-Munoz [89] model:

$$j_{LIS}(E_{kin}) = 1.244 \cdot 10^6 \left(E_{kin} + 780 \cdot \exp(-2.5 \cdot 10^{-4} E_{kin})\right)^{-2.65}$$

The cosmic ray station in Oulu, Finland, provides reconstructed monthly modulation potentials, back from 1936 (http://cosmicrays.oulu.fi/phi/phi.html), however, this modulation potential, Φ_{Oulu}, is obtained for a different j_{LIS} model as described above. Therefore, owing this difference, the author applied a correction as described by Usoskin et al. [90]:

$$\Phi = m\Phi_{Oulu} + b$$

where m = 1.04 and b = -76.

To simulate the selected SEP events for this work, author used spectra published in literature [91, 92] - Figure 43.

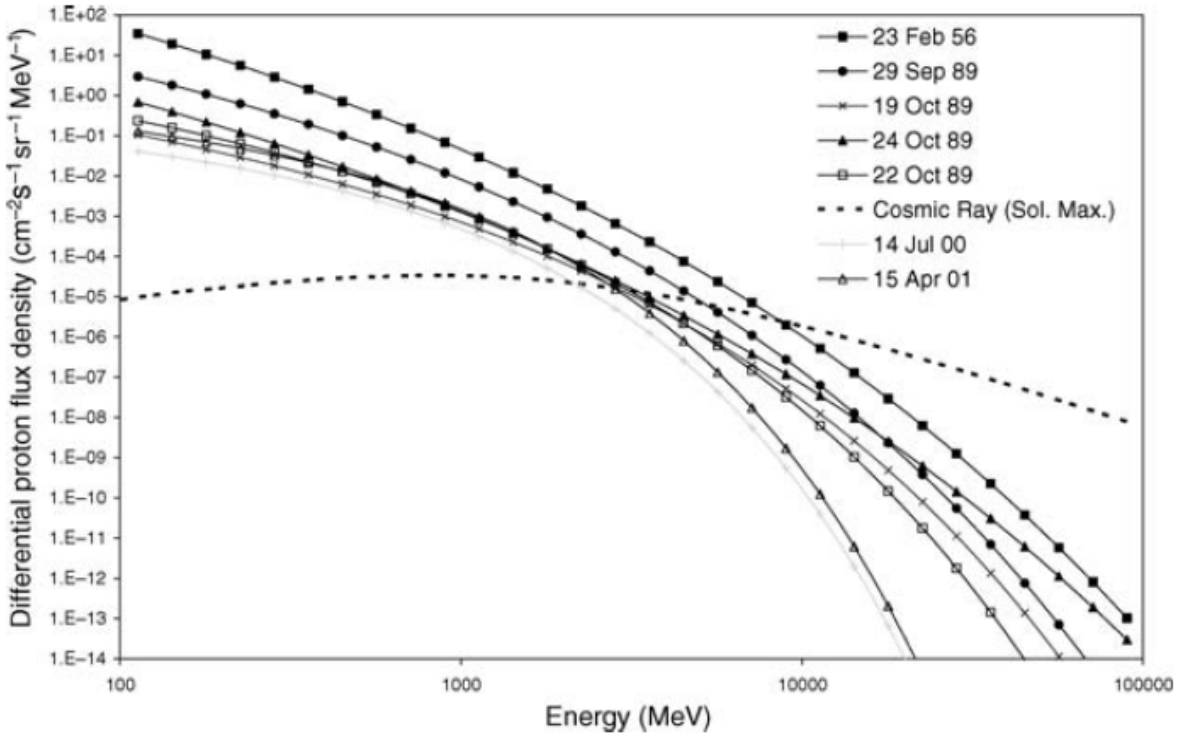

Figure 43 Comparison of GCR proton spectra with proton spectra of some historical SEP events [91].

The next step in preparing a Mote Carlo simulation is to define the quantity to be recorded. Author selected particle fluence as a function of energy scored at fixed, defined altitudes separately for a defined set of particle types. Range of energy has been appropriately chosen with a special attention to neutrons in order to have a good resolution of the spectrum also in the thermal energy region.

For simulations, author chosen GCR (solar minimum) – as reference, GLE5 (23 Feb 1956) – often considered as the worst-case event, GLE42 (29 Sep 1989) – considered as the second largest event, and GLE43 (19 Oct 1989) – as relatively weak event. Simulations were performed on a 12-cores SGI ALTIX 450 mid-range server that was maintained and configured by the author for FLUKA, and Geant4 Monte Carlo simulations.

Figure 44 - Figure 47 present scored, energy-integrated fluence spectra as a function of altitude for various particle types (protons, electrons, positrons, muons, pions, photons and neutrons) as obtained from simulations performed for Polar Regions (R_c < 0.1 GV) with GCR (solar minimum) GLE5, GLE42 and GLE43 proton spectra, respectively. The altitude in the atmosphere at which the rate of production of ionization becomes a maximum is called Regener–Pfotzer maximum. Such maximum occurs due to two competing processes: decreasing of ionization rate caused by primary radiation and increase of ionization rate caused by secondary radiation. Figure 44 shows such maximum at ~15km of altitude for GCR over Polar Regions. For GLEs (Figure 45 - Figure 47) the Regener–Pfotzer maximum over Polar Regions is higher (at ca. 30 - 40 km) but is not that well distinguished.

Every single point in Figure 44 - Figure 47 is an integral of appropriate particle fluence rate in energy. In Figure 48, an example of a non-normalized energy distribution of neutron fluence rate is shown. For comparison, Figure 49 presents the same energy distribution for neutron fluence rate simulated for different solar conditions and published in the ISO standard [37]. Spectra are very similar – this assures that the setup for all simulations has been selected correctly.

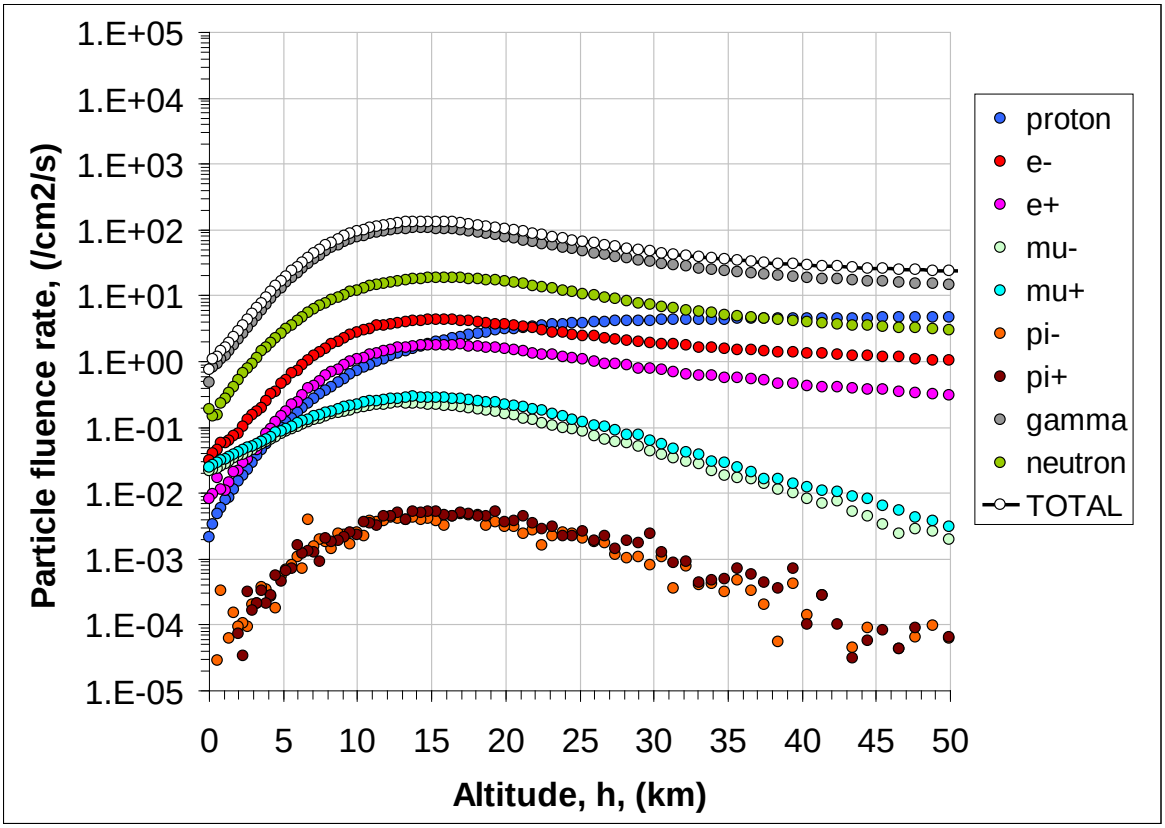

Figure 44 Particle fluence rate as a function the altitude as simulated for GCR during solar minimum at Polar Region [94].

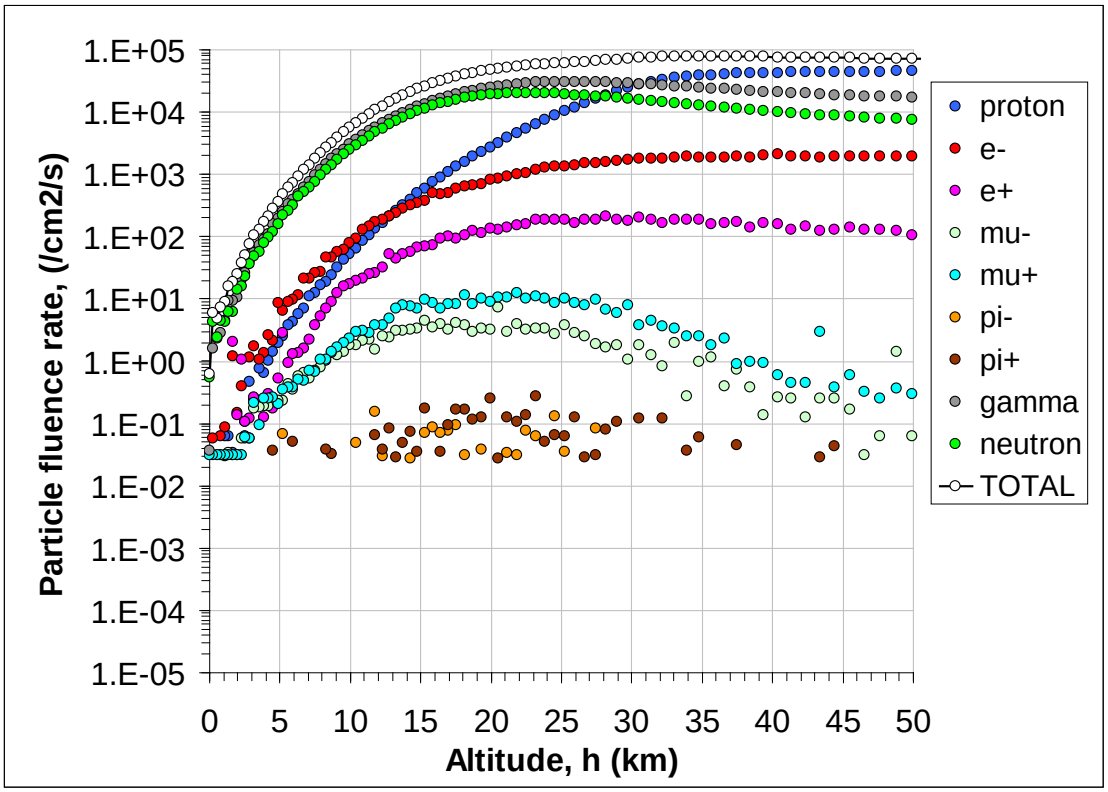

Figure 45 Particle fluence rate as a function the altitude as simulated for GLE5 (23 Feb 1956) at Polar Region [94].

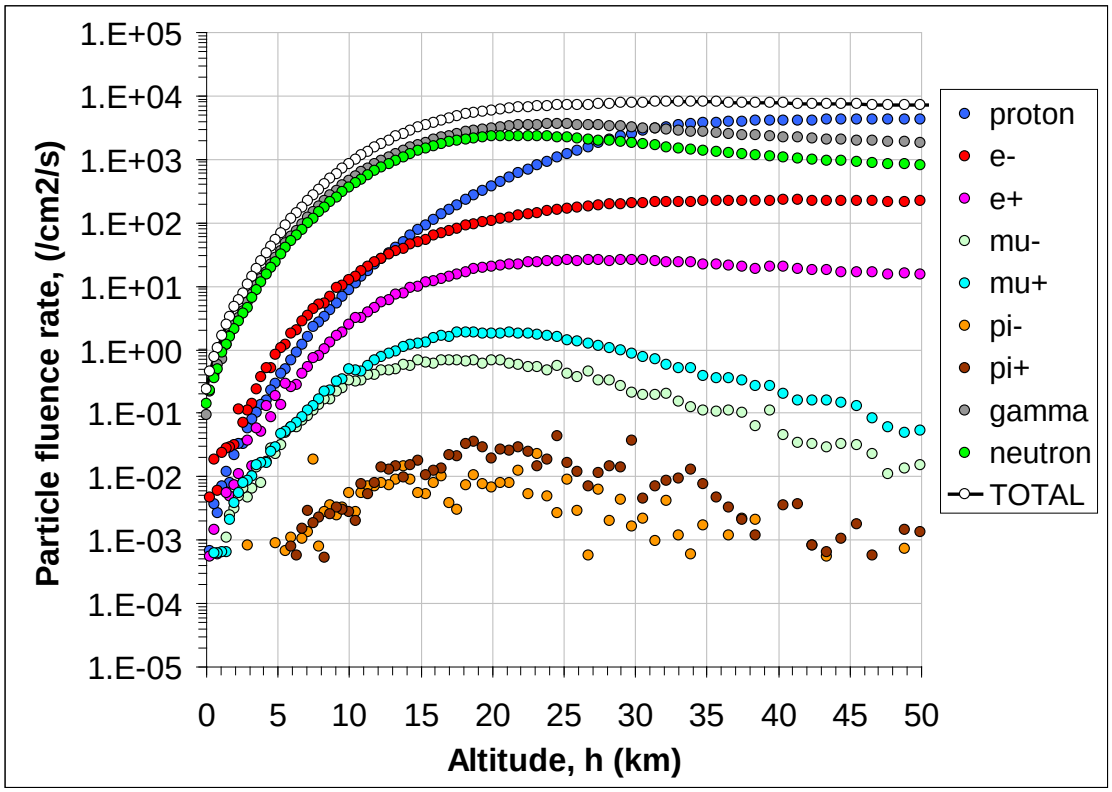

Figure 46 Particle fluence rate as a function the altitude as simulated for GLE42 (29 Sep 1989) at Polar Region [94].

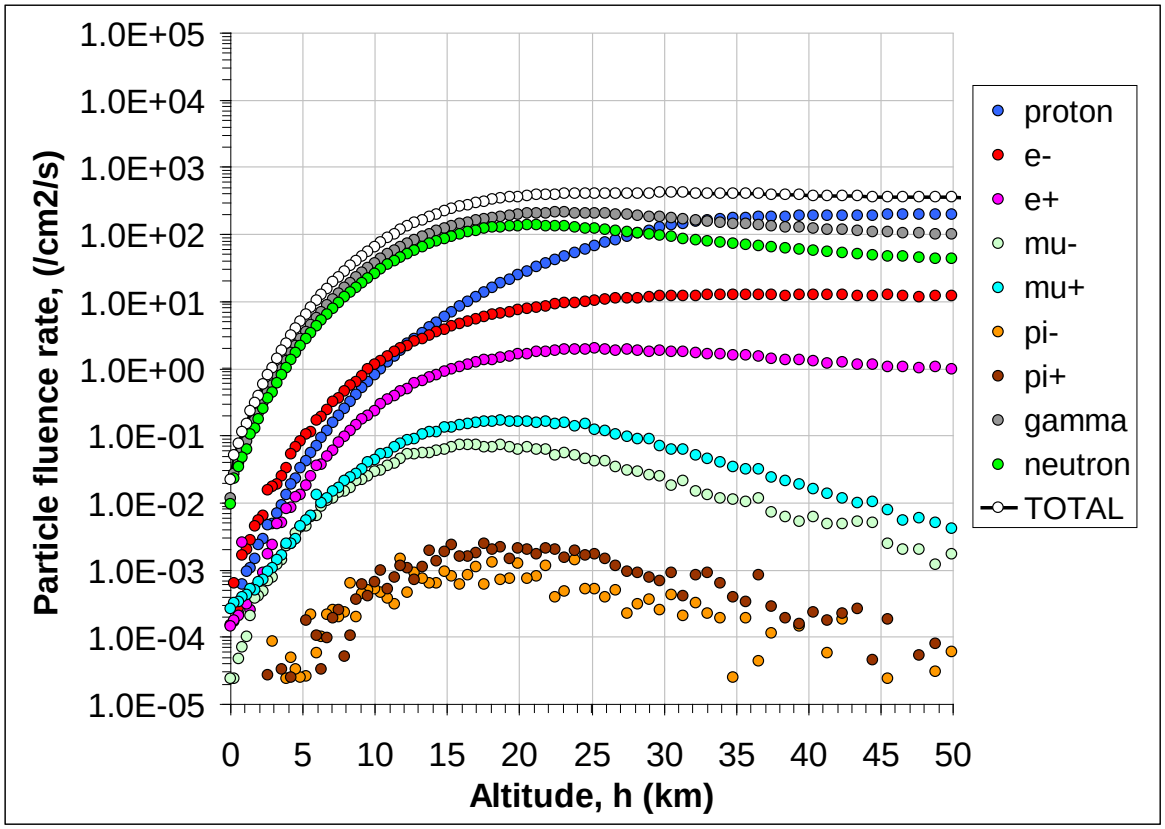

Figure 47 Particle fluence rate as a function the altitude as simulated for GLE43 (19 Oct 1989) at Polar Region [94].

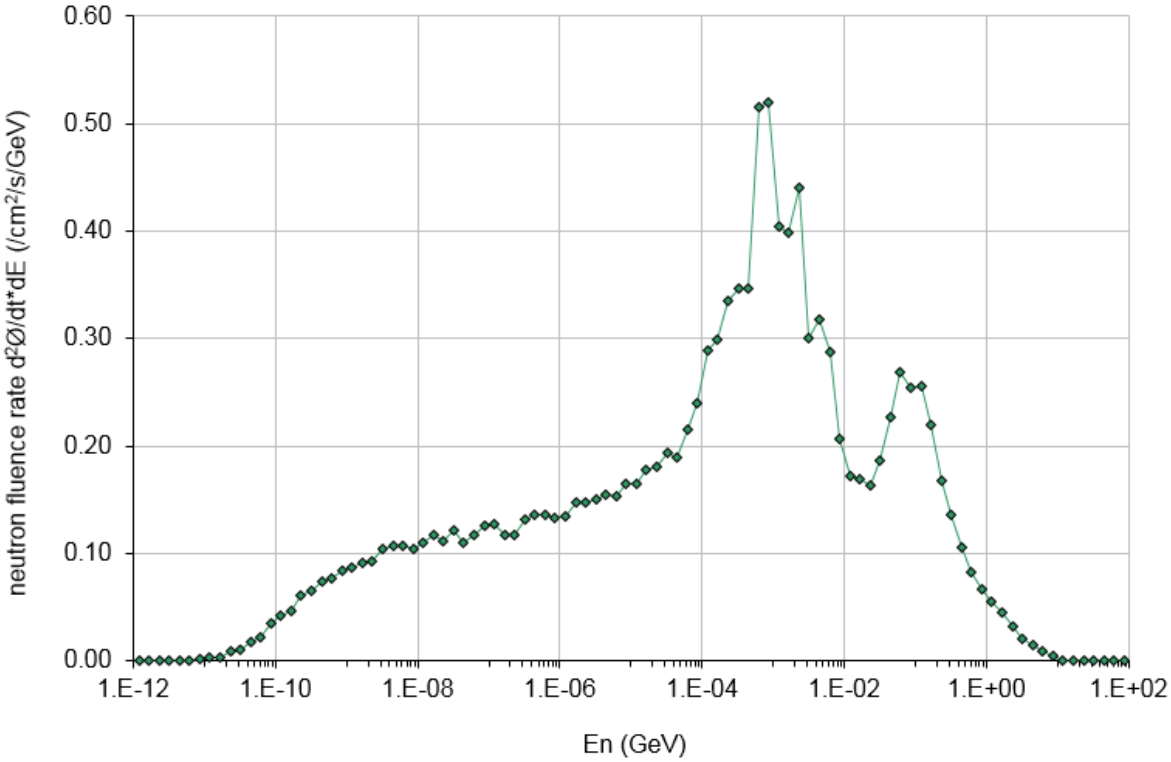

Figure 48 Non-normalized neutron fluence rate energy distribution as simulated for GCR (solar minimum) at 10.41 km of altitude and Polar Regions (0 GV cut-off rigidity) [94].

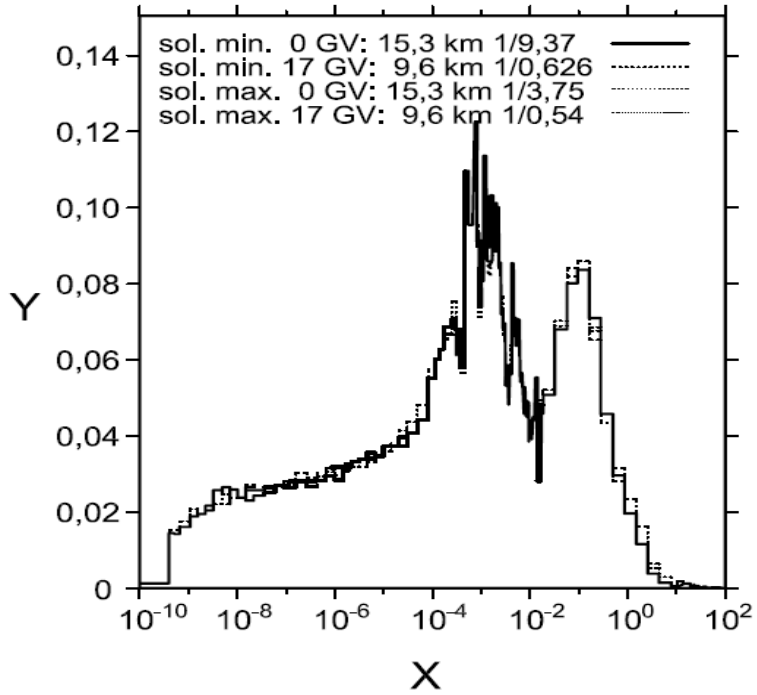

Figure 49 Normalized neutron fluence rate energy distribution (Y axis) $d^2\Phi/dt \cdot dE$ (in /cm²/s/GeV) against neutron energy in GeV (X axis) calculated as expected for civilian aircraft at extreme conditions of solar activity, geomagnetic cut-off and altitude [37].

In order to obtain results in terms of effective dose, *E*, and ambient dose equivalent, *H*(10)*, author folded the obtained particle fluence spectra with fluence-to-dose conversion coefficients for isotropic irradiation geometry as published by Pelliccioni [93] (calculated for ICRP-60 radiation weighting factors) – see Figure 50.

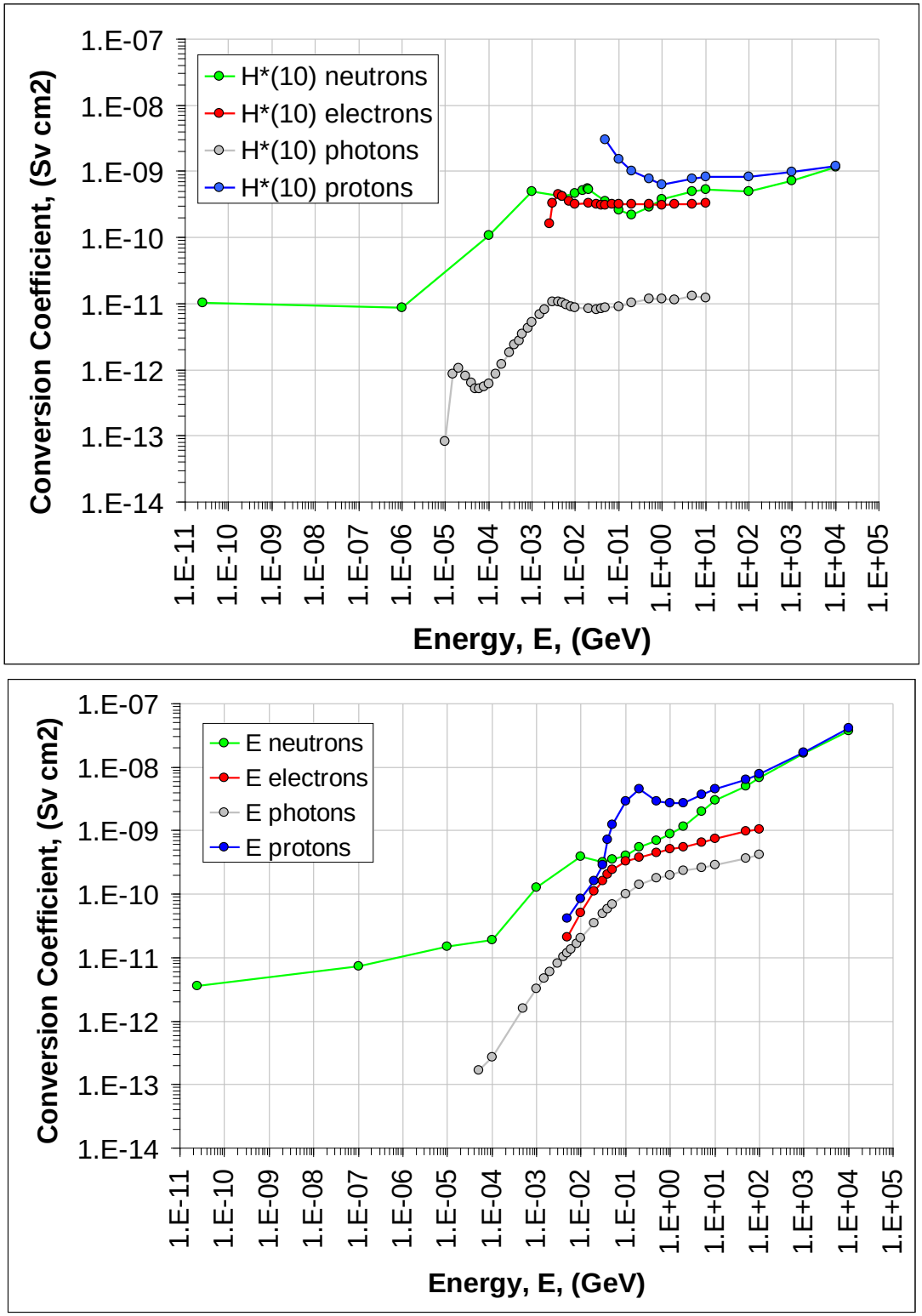

Figure 50 Fluence-to-dose conversion coefficients for ambient dose equivalent (upper diagram) and effective dose (lower diagram) for neutrons, electrons, photons, and protons (isotropic geometry) [data from 93]

Figure 51 - Figure 54 show the result of such folding for ambient dose equivalent rate d*H**(10)/d*t*, separately for each considered particle type and the sum as simulated over Polar Regions for GCR (solar minimum), GLE5, GLE42, and GLE43 proton spectra, respectively. At civil aviation altitudes (10 km – 12 km) over Polar Regions and for GCR, the greatest contribution to the total ambient dose equivalent comes in the first line from neutrons, then roughly equally from protons and electrons. It holds for simulated SEP events, but the importance of neutrons rises, and protons dominate over electrons.

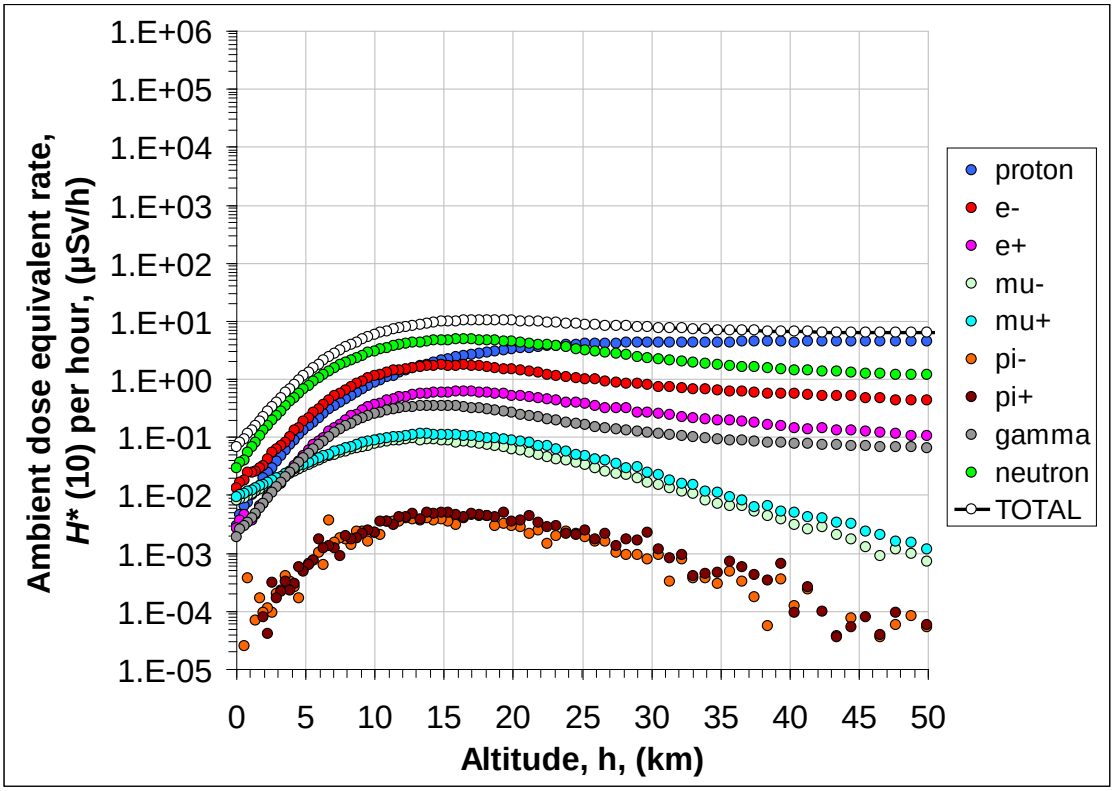

Figure 51: Ambient dose equivalent rates, d*H**(10)/d*t*, as a function of altitude as simulated for GCR during solar minimum at Polar Region [94].

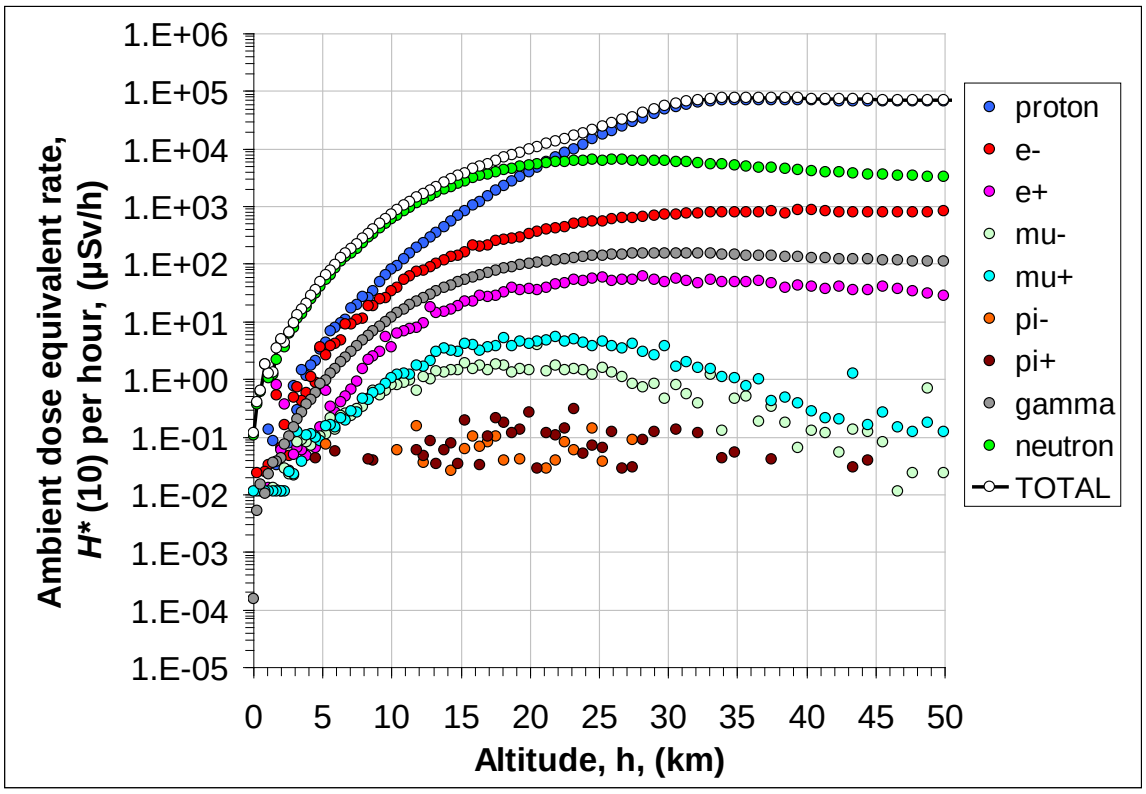

Figure 52: Ambient dose equivalent rates, d*H**(10)/d*t*, as a function of altitude as simulated for GLE5 (23 Feb 1956) at Polar Region [94].

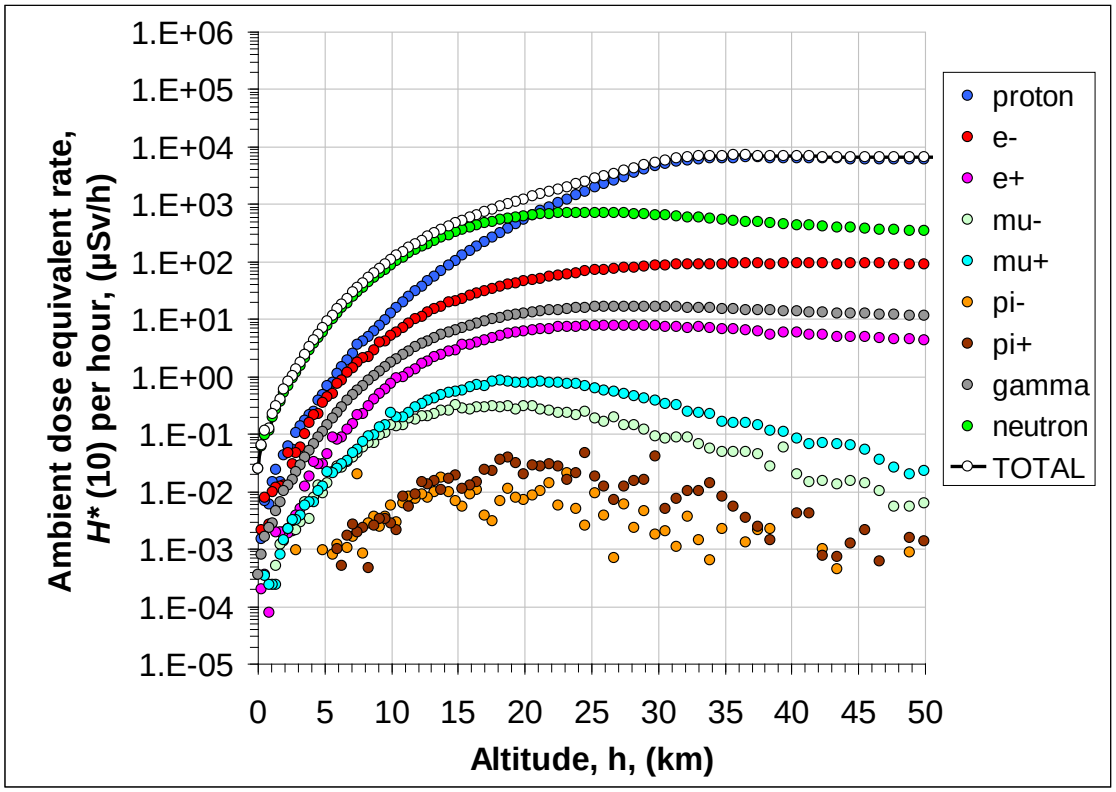

Figure 53: Ambient dose equivalent rates, d*H**(10)/d*t*, as a function of altitude as simulated for GLE42 (29 Sep 1989) at Polar Region [94].

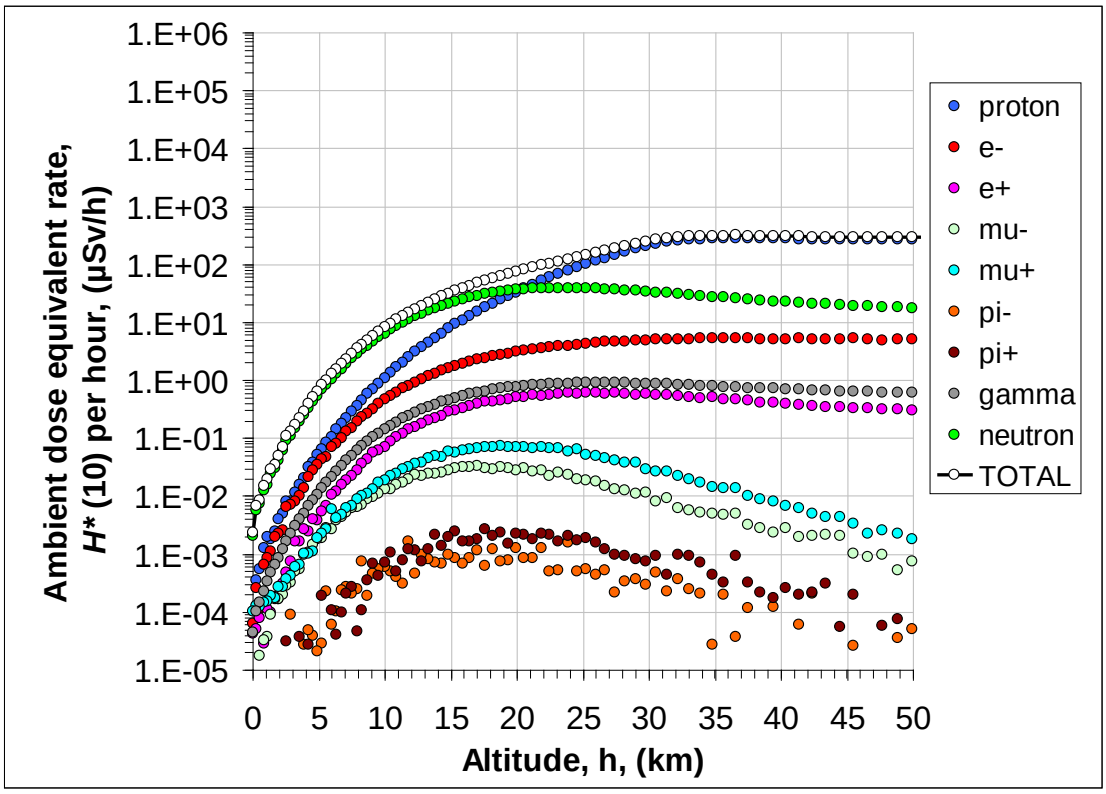

Figure 54: Ambient dose equivalent rates, d*H**(10)/d*t*, as a function of altitude as simulated for GLE43 (19 Oct 1989) at Polar Region [94].

Figure 55 - Figure 58 show the result of the folding for effective dose rate d*E*/d*t*, separately for each considered particle type and the sum as simulated over Polar Regions for GCR (solar minimum), GLE5, GLE42, and GLE43 proton spectra, respectively. At civil aviation altitudes (10 km – 12 km) and for GCR, the greatest contribution to the total effective dose comes in the first line from neutrons and protons (neutrons contribute more for lower altitudes), then from photons and electrons. For simulated SEP events, neutrons slightly dominate over protons and the altitude at which neutrons and protons contribute equally is higher (~ 12 km) compared to that for GCR (~ 7km). In addition, contribution from photons is greater than that from electrons. This is different than it was for ambient dose equivalent and it is due to electrons-over-photons ratio, which is larger for effective dose than for ambient dose equivalent (see Figure 50).

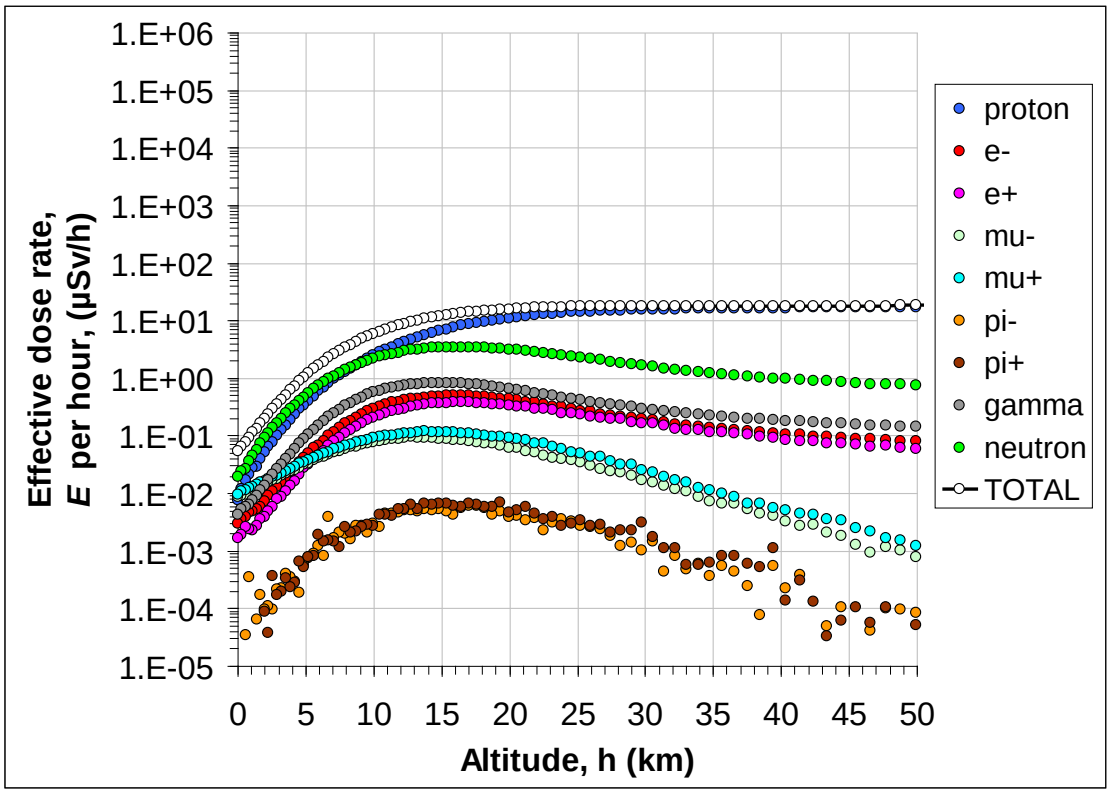

Figure 55: Effective dose rates, d*E*/d*t*, as a function of altitude as simulated for GCR during solar minimum at Polar Region [94].

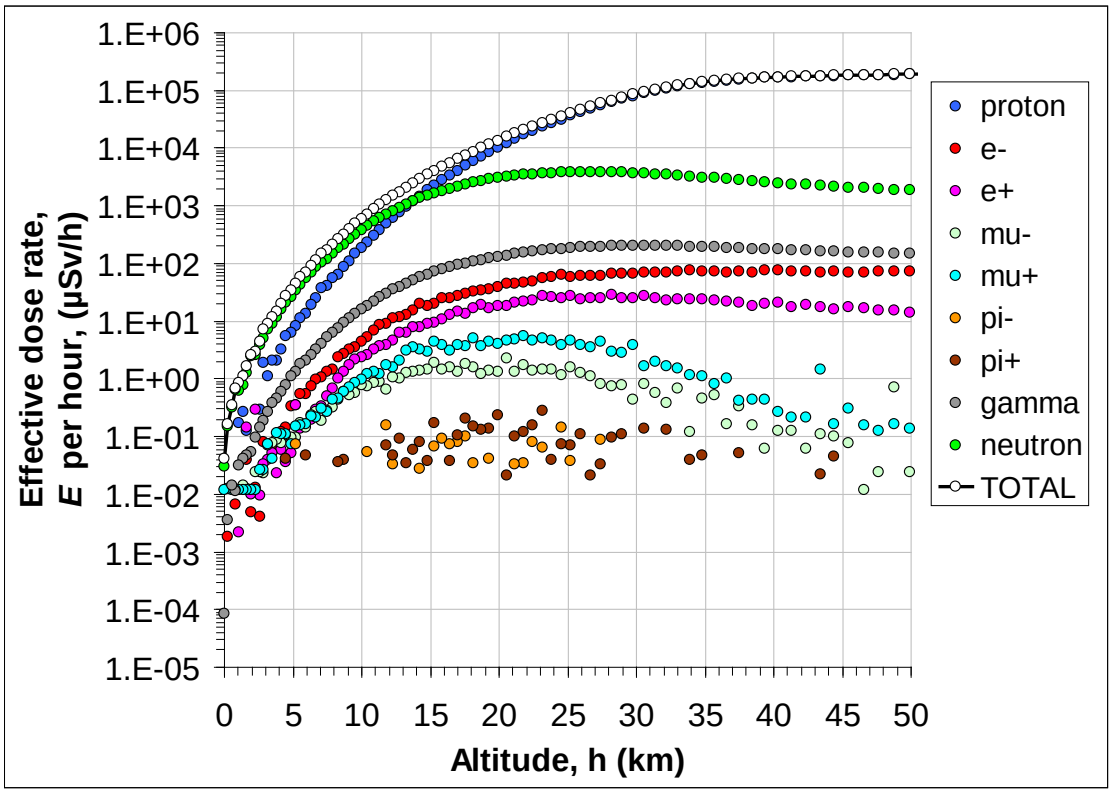

Figure 56: Effective dose rates, d*E*/d*t*, as a function of altitude as simulated for GLE5 (23 Feb 1956) at Polar Region [94].

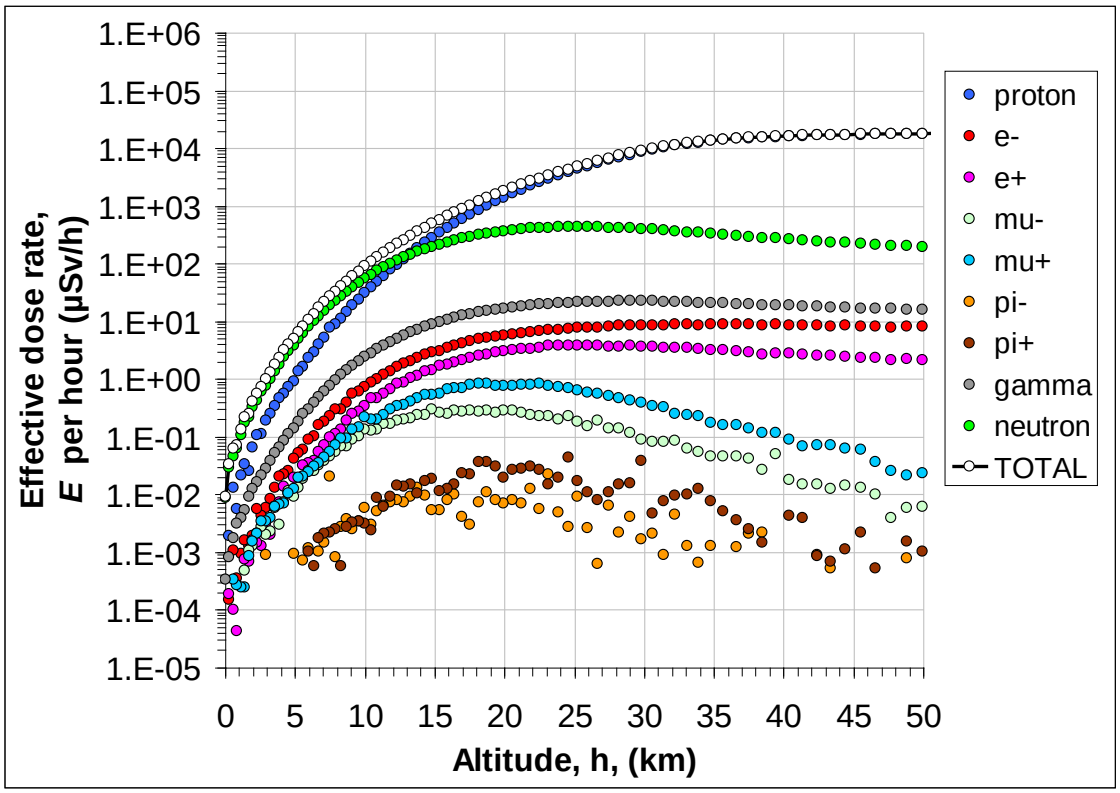

Figure 57: Effective dose rates, d*E*/d*t*, as a function of altitude as simulated for GLE42 (29 Sep 1989) at Polar Region [94].

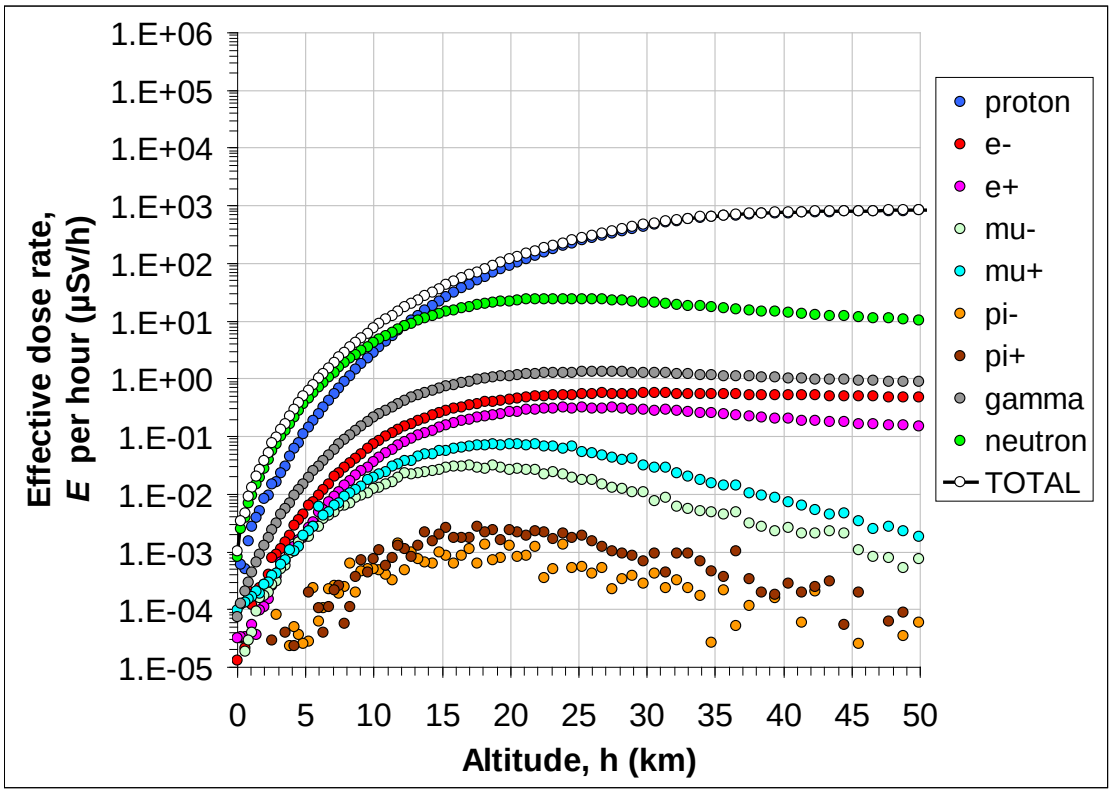

Figure 58: Effective dose rates, d*E*/d*t*, as a function of altitude as simulated for GLE43 (19 Oct 1989) at Polar Region [94].

Figure 59 - Figure 62 show the results as world maps of effective dose rates at typical civil flight altitude 10.86 km (≈ FL350) for simulated input proton spectra: GCR (solar minimum), GLE5, GLE42 and GLE43. Figure 63 - Figure 66 show similar results but for higher altitude: 15.31 km (≈ FL500). Comparing the figures one can notice that the elevated radiation levels in atmosphere due to SEP events concern mainly Polar Regions. This holds even for the strongest considered GLE5 and subsonic flight altitudes (such high altitudes are not used in civil flights) - see Figure 64. Figure 68 clearly presents this feature. This is due to efficient shielding of Earth magnetic field (see Figure 42) and the fact, that fluence of SEP protons at few tens of GeV have low intensities. In fact, at these energies, SEP fluxes are lower than GCR flux (see Figure 43). Therefore, radiation exposure at flight altitudes above Equatorial Regions is always shaped by GCR only. This feature is shown in Figure 68 for GLE42. Below 1.5 GV majority of effective dose comes from SEP event; above 1.5 GV majority of effective dose is due to GCR; above ~ 5 GV contribution of SEP to the total effective dose is negligible.

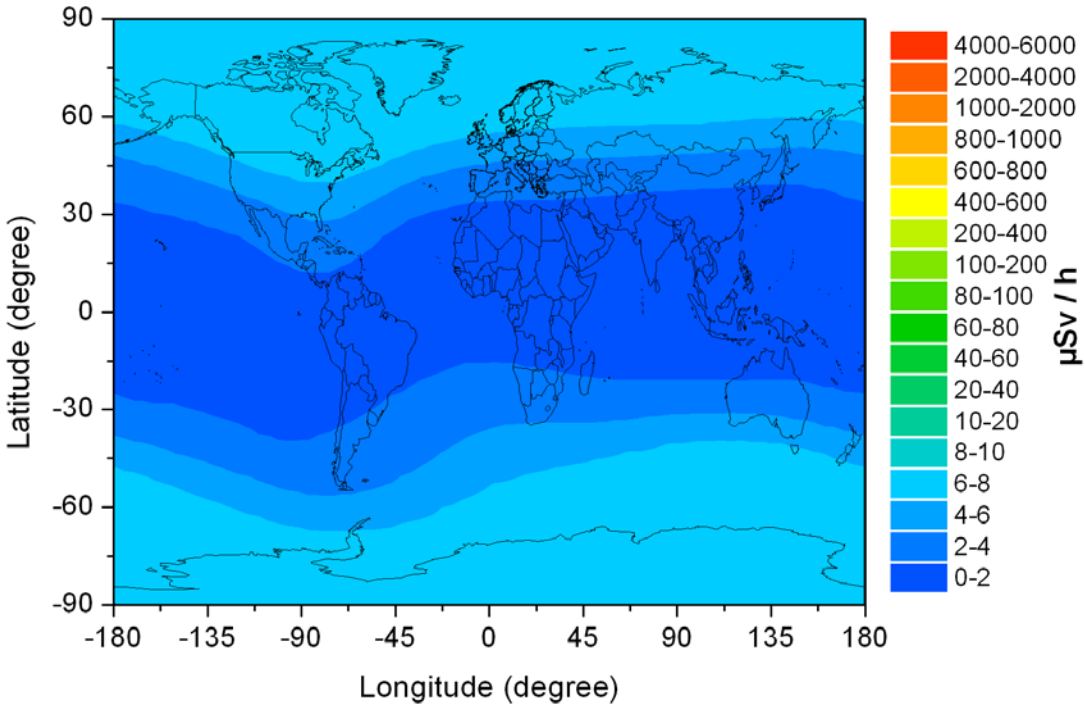

Figure 59: World map of effective dose rate, d*E*/d*t*, at the altitude of 10,86 km (≈ FL350) as simulated for GCR (solar minimum) [94].

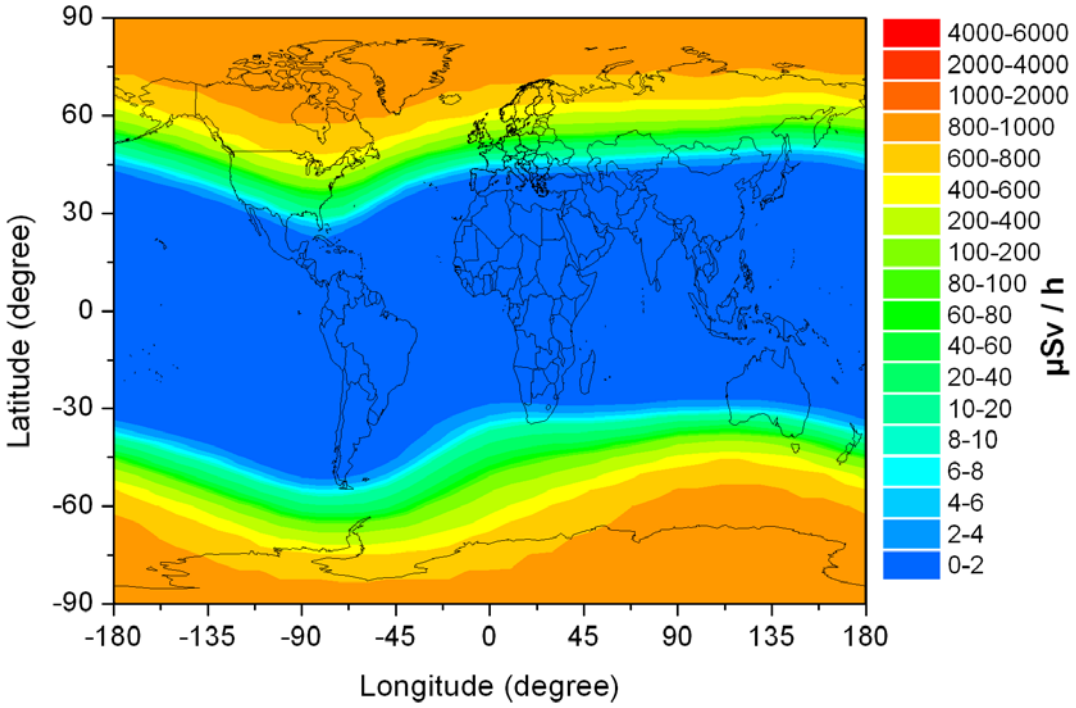

Figure 60: World map of effective dose rate, d*E*/d*t*, at the altitude of 10,86 km (≈ FL350) as simulated for GLE5 (23 Feb1956) [94].

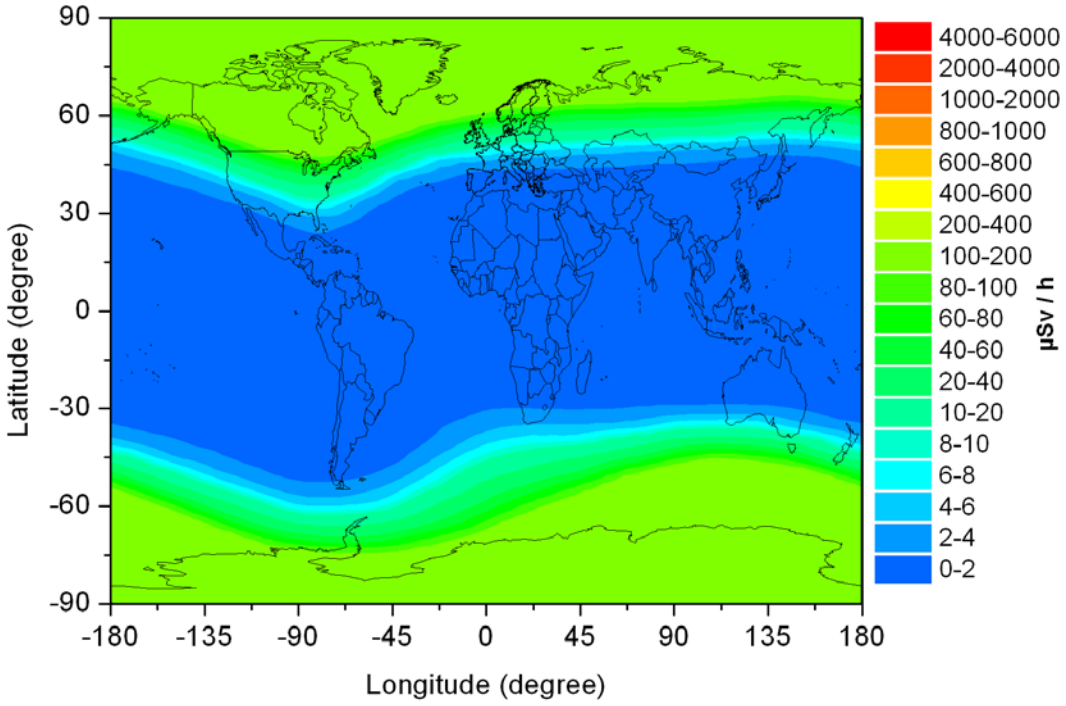

Figure 61: World map of effective dose rate, d*E*/d*t*, at the altitude of 10,86 km (≈ FL350) as simulated for GLE42 (29 Sep 1989) [94].

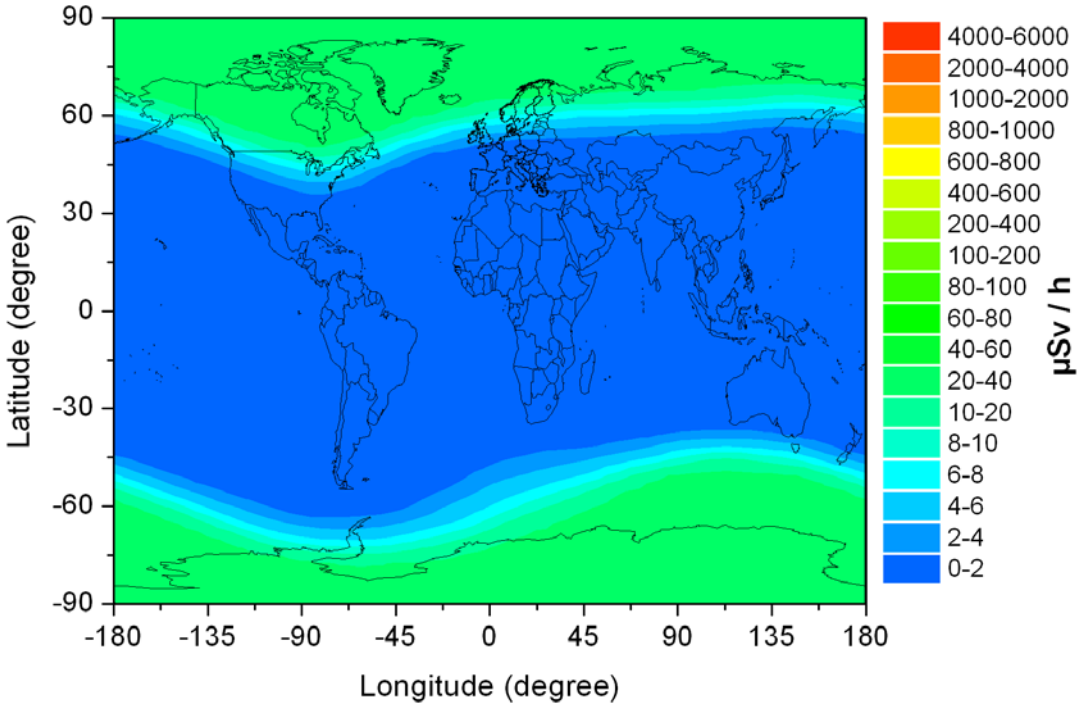

Figure 62: World map of effective dose rate, d*E*/d*t*, at the altitude of 10,86 km (≈ FL350) as simulated for GLE43 (19 Oct 1989) [94].

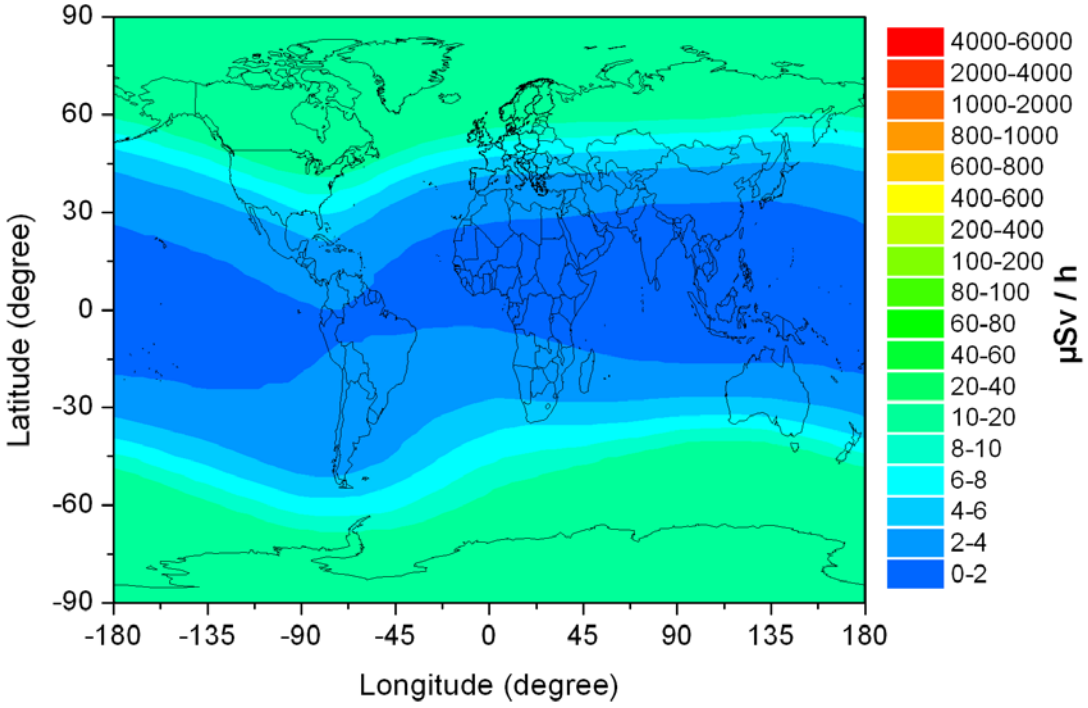

Figure 63: World map of effective dose rate, d*E*/d*t*, at the altitude of 15,31 km (≈ FL500) as simulated for GCR (solar minimum) [94].

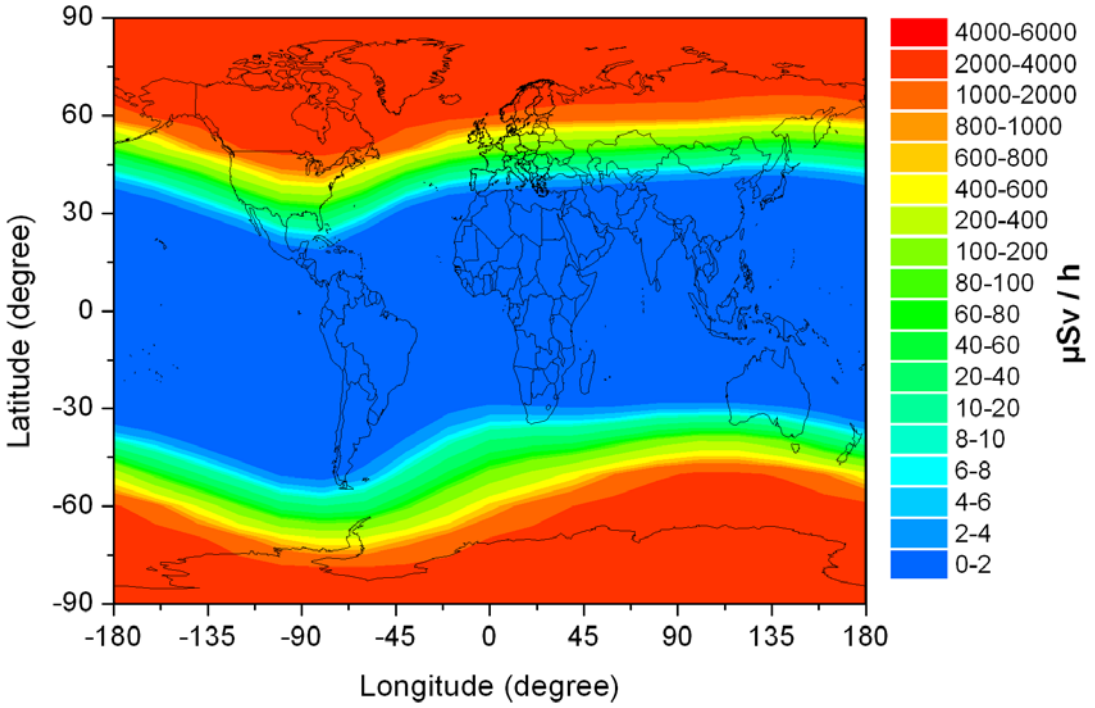

Figure 64: World map of effective dose rate, d*E*/d*t*, at the altitude of 15,31 km (≈ FL500) as simulated for GLE5 (23 Feb1956) [94].

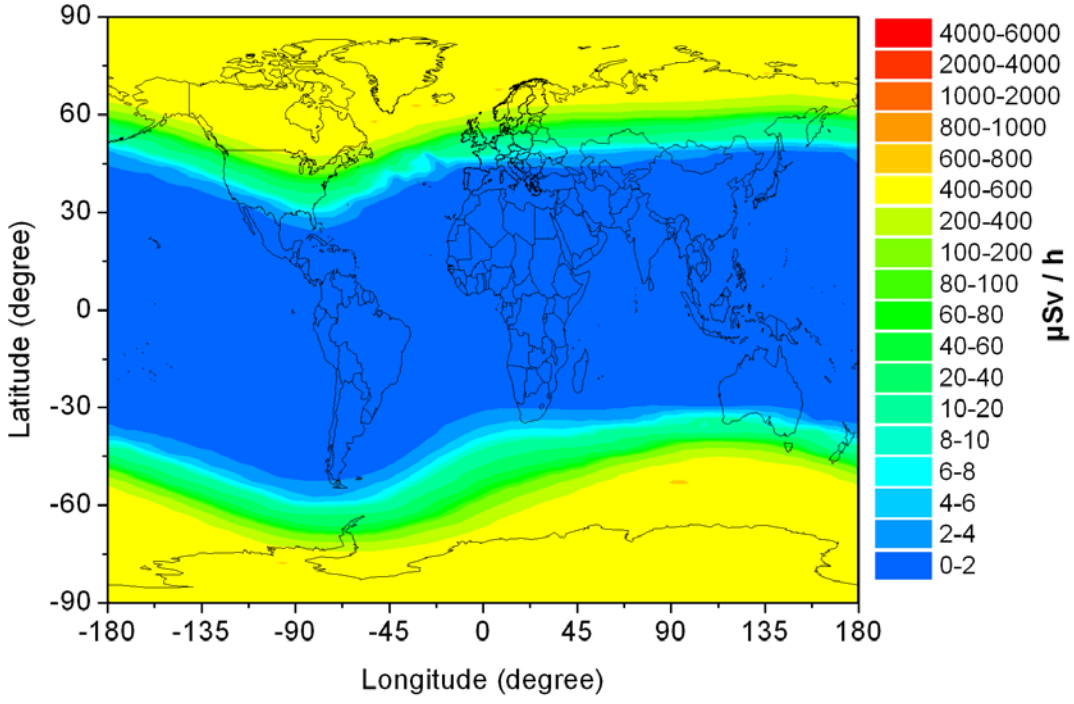

Figure 65: World map of effective dose rate, d*E*/d*t*, at the altitude of 15,31 km (≈ FL500) as simulated for GLE42 (29 Sep 1989) [94].

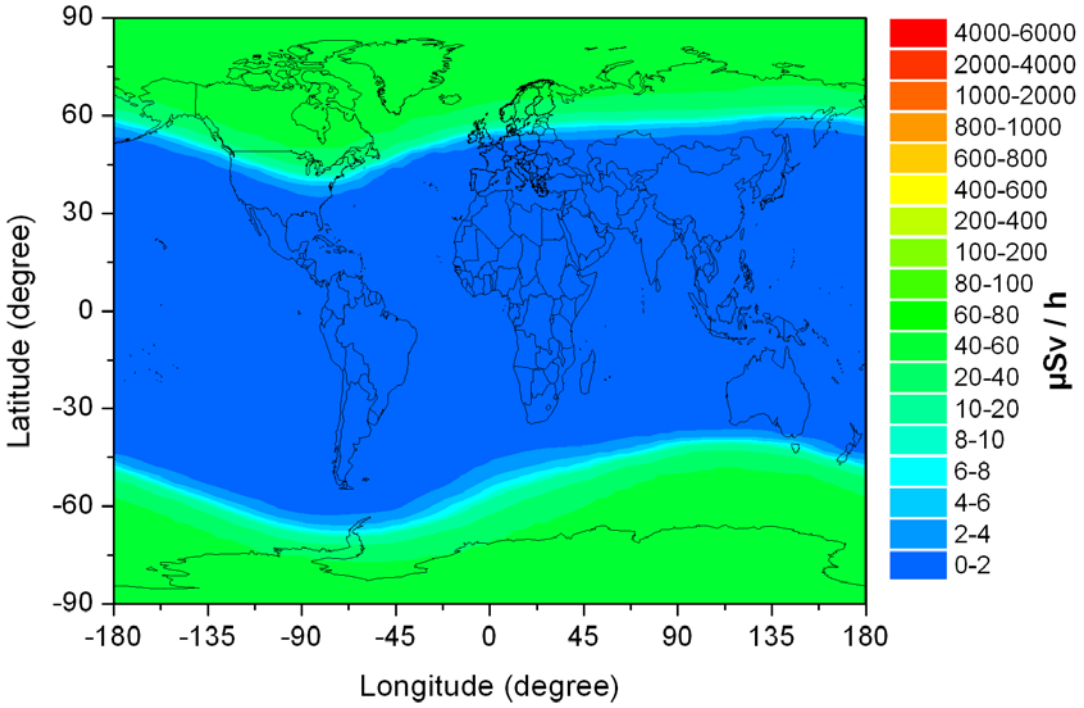

Figure 66: World map of effective dose rate, d*E*/d*t*, at the altitude of 15,31 km (≈ FL500) as simulated for GLE43 (19 Oct 1989) [94].

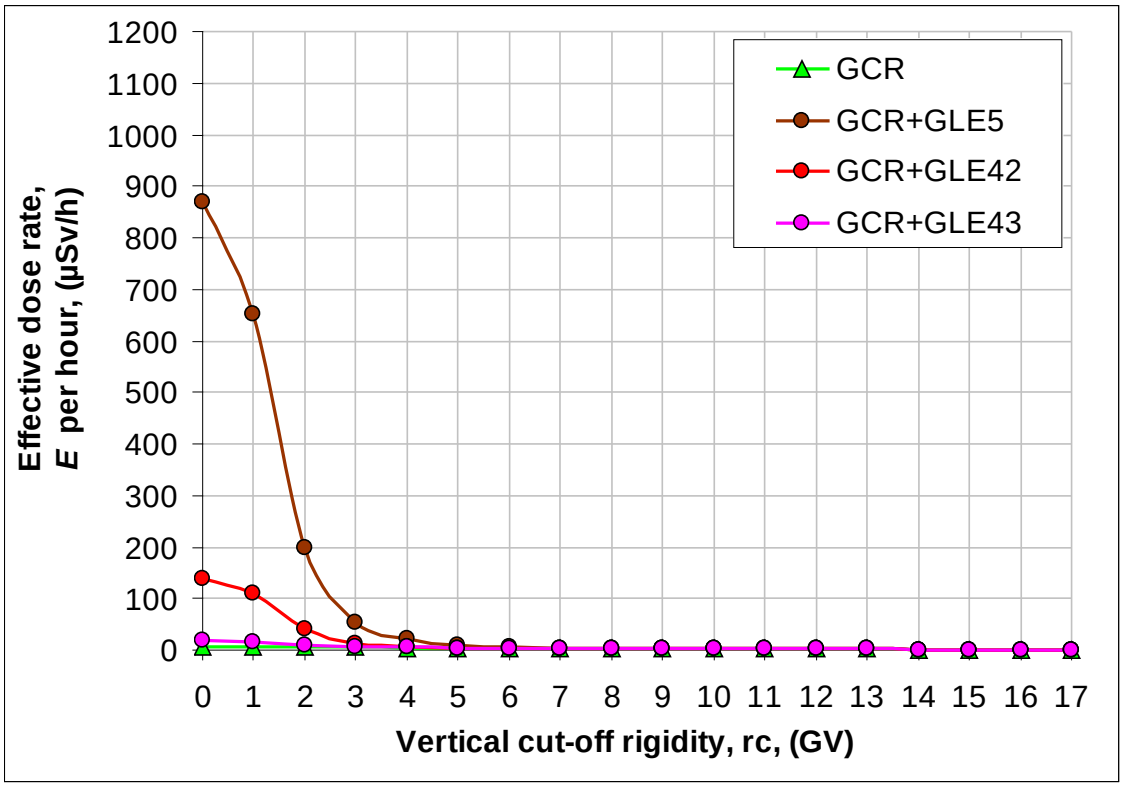

Figure 67 Effective dose rate, d*E*/d*t*, as a function of vertical cut-off rigidity, r_c, as simulated for GCR, GLE5 (23 Feb 1956), GLE42 (29 Sep 1989), and GLE43 (19 Oct 1989) at the altitude of 10,86 km (≈ FL350) [94].

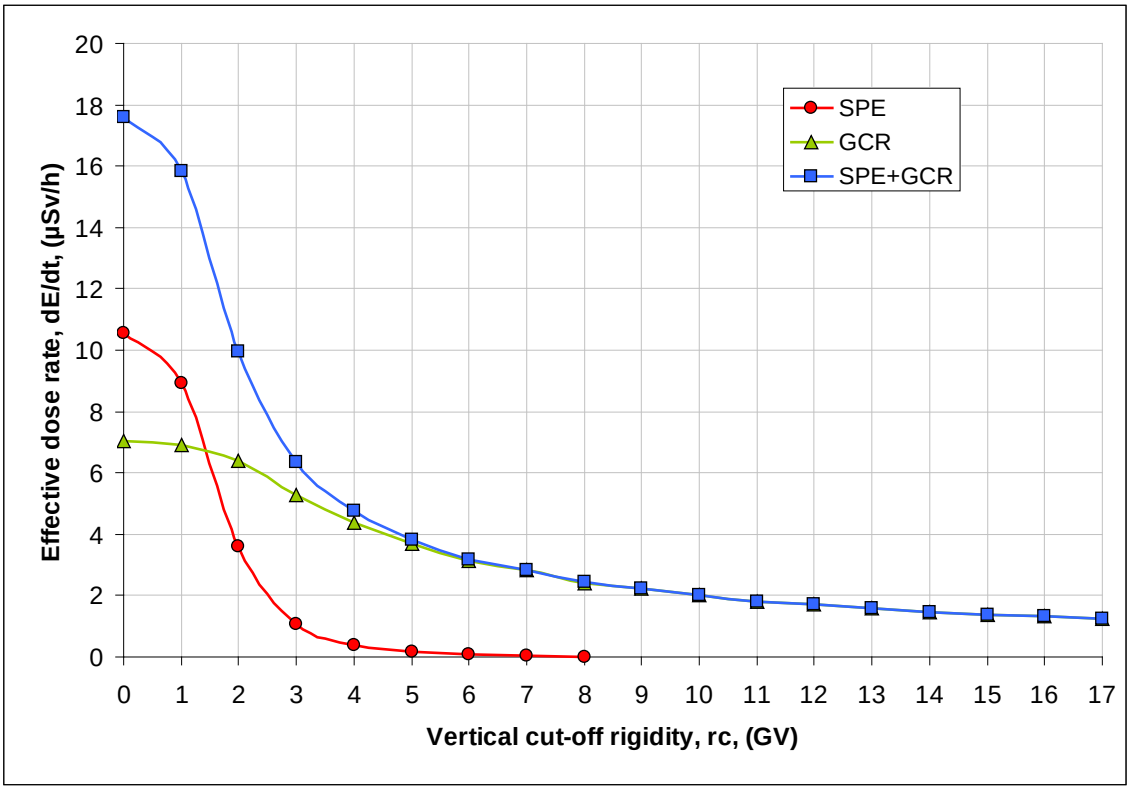

Figure 68 Effective dose rate d*E*/d*t*, as a function of vertical cut-off rigidity, r_c, at 10.86 km (≈ FL350) of altitude caused by SPE on 19th October 1989 (red line), GCR during solar minimum (green triangles) and the sum of GCR and SPE (blue line) [94].

Effective dose values obtained by the author from presented simulations agree with previous investigations. Author estimated maximum effective dose rate for worst-case (GLE5 at subsonic flight altitudes) in the range of 4-6 mSv/h in the peak of the event, and for typical flight altitude close to 1 mSv/h. For GLE42, author estimated maximum effective dose rate for 140 µSv/h at typical flight altitudes. Author's estimations are supported by similar figures reported in literature. Foelsche reports that passing through the impact zone of GLE5 would result in 4.5 mSv [95]. Beck et. al note that in literature it is reported that radiation exposure due to SEP during strong events may reach 1 mSv/h at typical flight altitudes [81]. Finally, Dyer et. al estimates the peak dose for GLE42 to be around 100 µSv/h, what supports author's findings; Dyer et. al additionally state that in the absence of measured data, calculations can be easily out even by a factor of three [91].

Comparison that is more exact is very difficult due to complexity of the task, variety of used methods (not always based on Monte Carlo simulations), discrepancies in the description of SEP proton spectra, and finally scarce of measured data. The EURADOS' Working Group 11 on "high-energy radiation filed" is currently taking an extended effort to compare codes estimating radiation exposure at flight altitudes due to SEP. Author of this work is member of this group and actively contributes to that effort.

Results presented in this chapter are published in a report [94] by the Seibersdorf Laboratories for the Austrian governmental Office for Radiological Protection.

6. AVIDOS model

After author gathered practical experience with measurements of cosmic radiation, data analysis, and numerical simulations, a natural next step is a development of a practical tool for quick assessments of radiation exposure in atmosphere.

This chapter presents the AVIDOS model developed by the author for routine dose assessment in aircrafts during typical flights at commercially used altitudes.

6.1. Model development for Galactic Cosmic Rays

Model proposed by the author is based on existing results from Monte Carlo simulations performed with the FLUKA code (version 2005) [96, 97] and a set of fitting functions developed by the author. In the numerical calculations, several components were considered: Earth's atmosphere, Earth's magnetic field, and primary cosmic radiation with solar modulation. For the geometry used in simulations a three-dimensional spherical representation of the Earth's atmosphere including height-density profile with a proper mixture of nitrogen, oxygen, and argon was organized in 100 concentric shells spanning over an altitude range from ground up to 70 km. The description of galactic cosmic radiation was based on primary proton spectrum published by Gaisser *et al.* [96] and modified by experimental data that included satellite and balloon measurements [99]. Based on this spectrum, fluence rates for galactic cosmic radiation of all elemental groups from Z=1 to Z=28 were obtained and modulated using a solar deceleration potential model [48] which bases on neutron monitors count rates. The influence of Earth's magnetic field on penetration abilities of charged particles in the atmosphere was considered by a vertical cut-off rigidity model [51]. Primary spectra were propagated down the atmosphere at different geographical locations and solar activities taking into account cross sections for different nuclear reactions and finally resulting in particles fluence rates. Resulting fluence rates were converted into ambient dose equivalent $H^*(10)$ and effective dose E by employing appropriate conversion coefficients [93] calculated according to ICRP 60 recommendations [5]. Numerical simulations were performed for many different combinations of solar deceleration potential and vertical cut-off rigidity along broad altitude profile.

Based on the simulations, author developed a set of fitting functions to describe the radiation dose depending on three parameters: solar deceleration potential, Φ, that reflects influence of solar activity, vertical cut-off rigidity, r_c, which is related to Earth's magnetic field and therefore geographical location, and barometric altitude, h, that counts for atmospheric shielding. The three parameters were considered separately in such a way that when analyzing one of them the two others were kept constant. For each parameter a function fitting the simulations was found: $f_1(h)$, $f_2(\Phi)$, and $f_3(r_c)$. Analytical expressions of the functions with graphical examples calculated for selected

conditions are shown in Figure 69 to Figure 71. In these figures, black lines show typical conditions, while gray lines are calculated for arbitrary chosen extreme conditions: maximal shielding (gray dashed lines) and minimal shielding (gray solid lines).

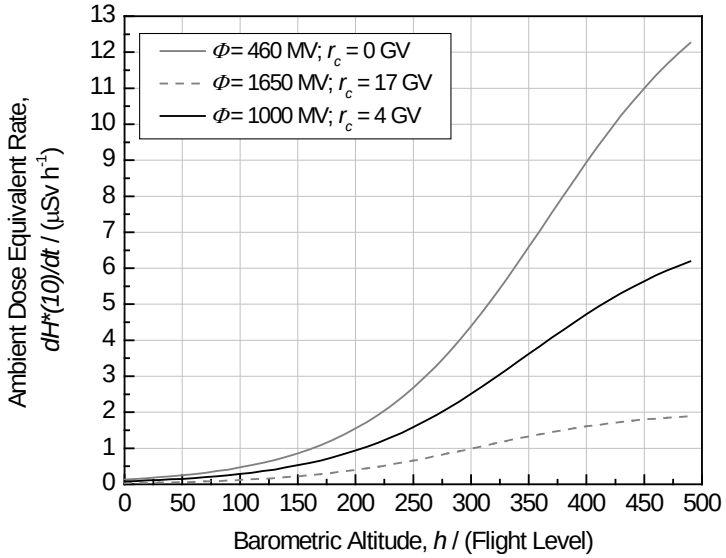

$$f_1(h) = \frac{f_{1\max}}{1 + \frac{f_{1\max} - f_{1\min}}{f_{1\min}} e^{-4ah/\,f_{1\max}}}$$

Figure 69 Graphical representation of the function $f_1(h)$ describing the dependency of ambient dose equivalent rate, dH^*(10)/dt, with barometric altitude, h, at selected constant solar deceleration potential, Φ, and vertical cut-off rigidity, r_c. Right: $f_1(h)$ analytical expression [101].

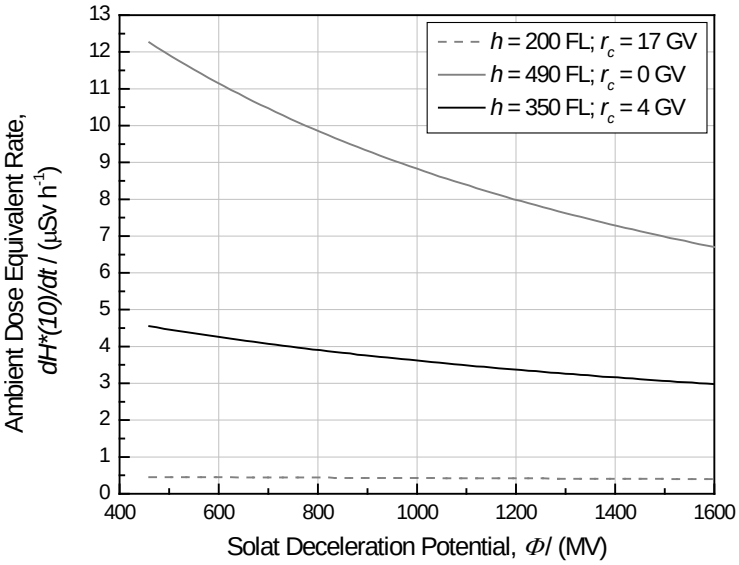

$$f_2(\Phi) = \frac{f_{2\max}}{1 + b\Phi}$$

Figure 70 Graphical representation of the function $f_2(\Phi)$ describing the dependency of ambient dose equivalent rate, dH^*(10)/dt, with solar deceleration potential, Φ, at selected constant barometric altitude, h, and vertical cut-off rigidity, r_c. Right: $f_2(\Phi)$ analytical expression [101].

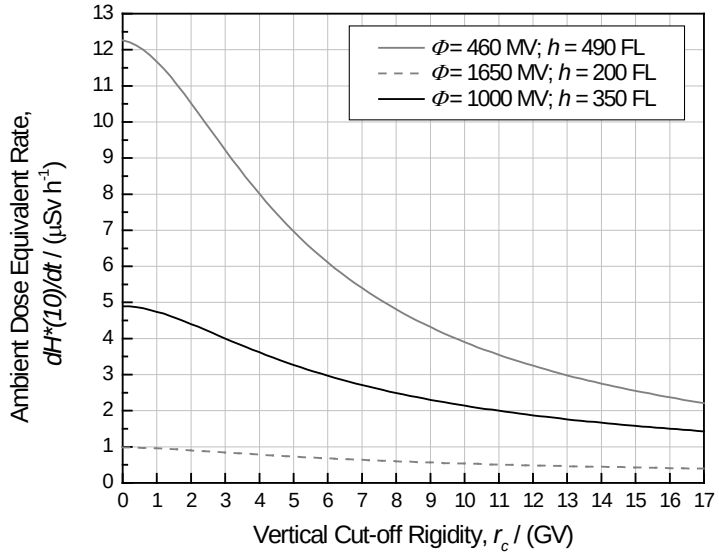

$$f_3(r_c) = \frac{f_{3\max}}{\sqrt{1+\left(\frac{r_c}{c}\right)^2}}$$

Figure 71 Graphical representation of the function $f_3(r_c)$ describing the dependency of ambient dose equivalent rate, dH^*(10)/dt, with vertical cut-off rigidity, r_c, at selected constant barometric altitude, h, and solar deceleration potential, Φ. Right: $f_3(r_c)$ analytical expression [101].

Complete ranges of h, Φ and r_c were divided in several groups. For each group the same approach was applied and fitting functions were found. A combination of the three functions allows for assessing ambient dose equivalent rate at any geographical location, over the whole range of solar activity and altitude up to 15km (≈ FL490).

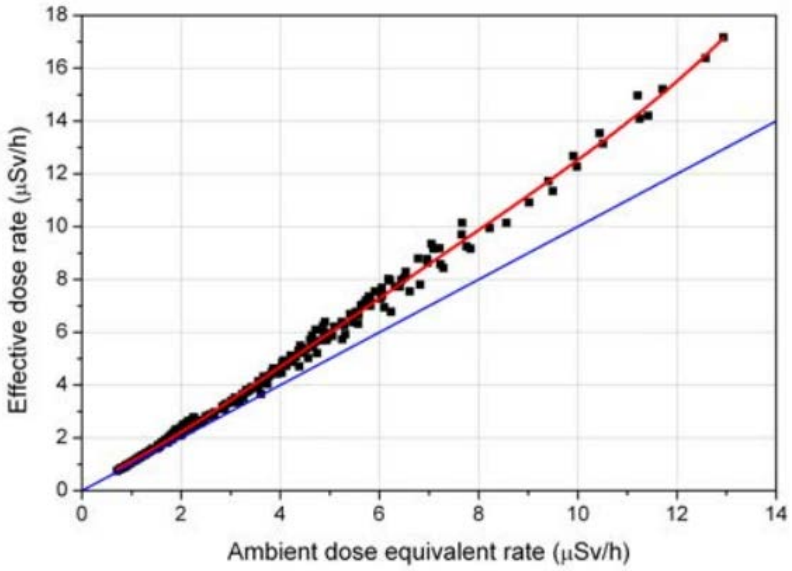

Figure 72 Effective dose rate as a function of ambient dose equivalent rate calculated with FLUKA2005 for 14 different solar deceleration potentials, vertical cut-off rigidities and for altitude between 7.9 km (FL258) and 15.9 km (FL520) (black squares) together with fitted polynomial (red line). The blue line represents the situation when effective dose would be equal to H^*(10). [102, 79]

In the proposed model, the calculation of effective dose is based on the ratio of H^*(10)/E since both, ambient dose equivalent and effective dose were derived from simulations. This approach is driven by practice – effective dose is not measurable, while H^*(10) is the appropriate quantity in which measurements shall be expressed.

The same approach was used in the joint report of ICRU and ICRP for publishing reference dose values for code validations [100]. The full set of fitting functions including the radio $H^*(10)/E$ constitute the radiation dose assessment model AVIDOS for GCR [101].

With the model described above it is possible to calculate the ambient dose equivalent and effective dose at any geographical position during whole cycle of solar activity and at commercially used flight altitudes. As an example, a matrix of the $dH^*(10)/dt$ have been calculated. Calculations have been performed for full range of vertical cut–off rigidity, one selected altitude of 11.9 km (≈ FL390) and solar deceleration potential SDP = 500 MV. In total almost 5500 calculated points were smoothed in order to plot them as surfaces below in Figure 73. In the figure, as expected, the $dH^*(10)/dt$ is significantly lower over equatorial region with regards to Polar Regions due to shielding provided by Earth's magnetic field.

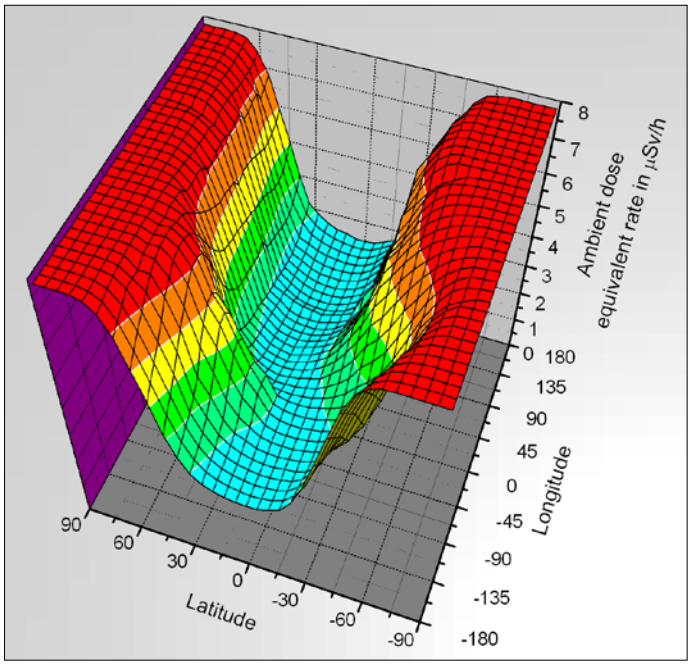

Figure 73 Ambient dose equivalent rate calculated with the model AVIDOS for full range of vertical cut–off rigidity at solar deceleration potential of 500 MV and at altitude of 11.9 km (≈FL390). Figure taken from scientific poster related to reference [79].

AVIDOS is also able to predict radiation dose assessment due to GCR up to one year in advance. Such prediction is possible, since changes of solar activity are nearly periodic and show approximately 11-years cycle. Variation in solar activity can be best described by the number of sunspots due to the advantage of long-term records of direct observations. Recently, the conventionally used Sunspot Number data were revised [105] and after July 1, 2015, a new, entirely updated data series is available [27]. Models forecasting monthly sunspot numbers already exist and stake out on the fitting to the existing data by applying least-square method with a set of defined curves and smoothing filters. Currently used techniques allow for 12-month ahead predictions

of the monthly smoothed sunspot number. Recent developments improved the prediction technique by 5 - 57% [107].

For its radiation dose predictions due to GCR, AVIDOS uses a revised monthly-averaged sunspot numbers. The predicted monthly-smoothed sunspot number is obtained from the World Data Center for the sunspot index [27], and then the number is converted into the value of solar deceleration potential using a simple linear regression. With this, AVIDOS can forecast radiation exposure at aviation altitudes due to GCR for up to 12 months ahead. The quality of such prediction depends mainly on the quality of the forecasted sunspot number. Uncertainties on the predicted sunspot number as observed by the author since 2015 has always been better than 25%. Sensitivity analysis show, that 25% uncertainty on the predicted monthly-smoothed sunspot number results in about 15% variation of the assessed radiation exposure, which is a reasonable figure [108].

In the current approach, where ICRP 60 recommendations are used for fluence-to-dose conversion coefficients, $H^*(10)$ underestimates the effective dose up to 30% [102, 103] at commercial flight altitudes. With publication of ICRP 103 recommendations [3] where radiation weighting factors for protons and neutrons were lowered author expects, that $H^*(10)$ will be similar to effective dose. A similar expectation was expressed in ICRP's report on radiological protection from cosmic radiation in aviation [13]. The Commission expects that application of new radiation weighting factors will result in changing of doses even by 30%. Sato et. al. published new fluence-to-dose conversion coefficients that are calculated with ICRP 103 recommendations [104]. G. Dietze reports [105] that changes of conversion coefficients for neutrons lead to only few percent lower effective dose compared to that calculated with ICRP 60 neutron weighting factors. For protons, the change is more important. Lowering the radiation weighting factor from five to two, will reduce proton contribution to the total effective dose in the range of 10%, and the effective dose for radiation fields at aviation altitudes will be reduced by 13-16% depending on flight route.

6.2. Model Validation for Galactic Cosmic Rays

The aim of this chapter is to present a validation of AVIDOS. Usually, calculation codes are validated against measurements. However, when the measurements are lacking or quantity to be compared is not measurable, often calculations performed with one method are compared with others conducted in another way. Yet another way of validation could be a direct comparison with reference values laid down by regulatory bodies or given by law. In this chapter, AVIDOS calculations are compared with measurements, with other codes, and with reference values.

6.2.1. Comparison with measurements

Usually calculation codes are validated through comparison with measurements. Here an example of comparison of AVIDOS calculations with measurements conducted during the CAATER flight campaign [71] is presented. As described in earlier chapter, CAATER measurements were undertaken at two fixed geographical locations, over each at two constant altitudes: FL400 (≈ 12.19 km) and FL320 (≈ 9.75 km). One location was over Aalborg, Denmark (57N, 10E) for low magnetic shielding (r_c = 1.8 GV), the other over Rome, Italy, (42N, 12E) for greater magnetic shielding (r_c = 6.4 GV). To decrease statistical uncertainties, each measurement lasted at least 2 hours. In the Figure 74 below, model's predictions are compared with two TEPC systems. The figure shows that calculations agree with measurements within the standard uncertainty. When the average over all instruments that participated in the campaign is considered, calculated ambient dose equivalent rates deviate from measured ones by less than 15% [101].

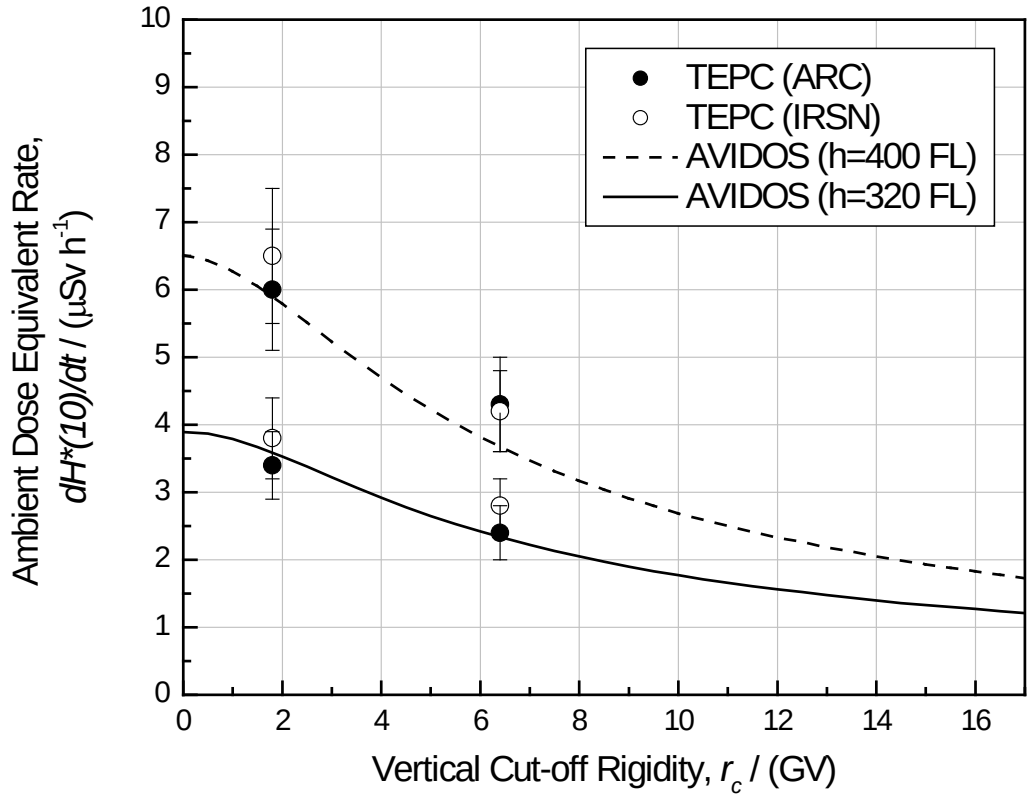

Figure 74 A comparison between TEPC measured (13) ambient dose equivalent rates (circles) over two locations (r_c = 1.8 GV, r_c = 6.4 GV) at two altitudes and values calculated with AVIDOS for *h* = FL320 (≈ 9.75 km) – solid line, *h* = FL400 (≈ 12.19 km) – dashed line [101].

In the next figure, a comparison of AVIDOS calculations with measurements taken from the EURADOS Aircraft Crew Database is presented. In Figure 75 the d*H**(10)/d*t* is presented as a function of altitude. Measurements (color points – legend describes type of instrument and institute that took the measurement; for details see reference [77]) were conducted for vertical cut-off rigidity, r_c, between 0 GV and 2 GV and solar deceleration potential in the range of 470–490 MV. Calculations with AVIDOS (at the time of publishing of the reference [79] called ARCS model - red line) and EPCARD in version 3.2 (black line) were done for r_c = 1 GV and solar deceleration potential Φ = 475 MV. As the figure shows, AVIDOS predictions are satisfactory.

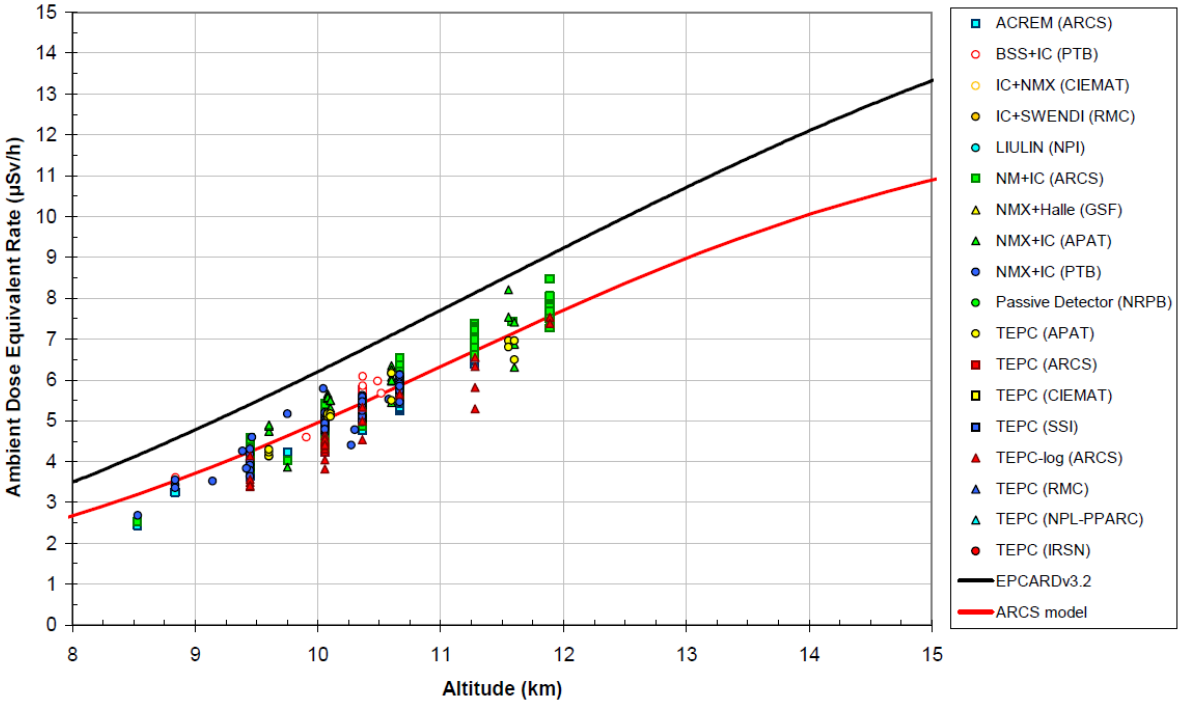

Figure 75 Ambient dose equivalent rate as a function of altitude for measurements (color points), EPCARDv3.2 calculation (black line) and the AVIDOS model (red line – at the time of publishing of reference [79] ARCS model, later renamed to AVIDOS). Measurements are selected from the EURADOS database for Φ = [470 – 490] MV and r_c = [0 – 2] GV. EPCARD and AVIDOS calculations assumed Φ = 475 MV and r_c = 1 GV [79].

Another comparison is showed in Figure 76 where d*H**(10)/d*t* is plotted against vertical cut – off rigidity. Rich set of experimental data (color points – legend describes type of instrument and institute that took the measurement; for details see reference [77]) for altitude between FL325 (≈ 9.9 km) and FL335 (≈ 10.2 km) and solar deceleration potential range of 470 MV to 610 MV was selected from the EURADOS Aircraft Crew Database. Calculations with AVIDOS (at the time of publishing of the reference [79] called ARCS model - red line) and EPCARD in version 3.2 (black line) were done for middle values of parameters: FL330 (≈ 10.06 km) and solar deceleration potential Φ = 475 MV. Calculations with AVIDOS fit well to measurements.

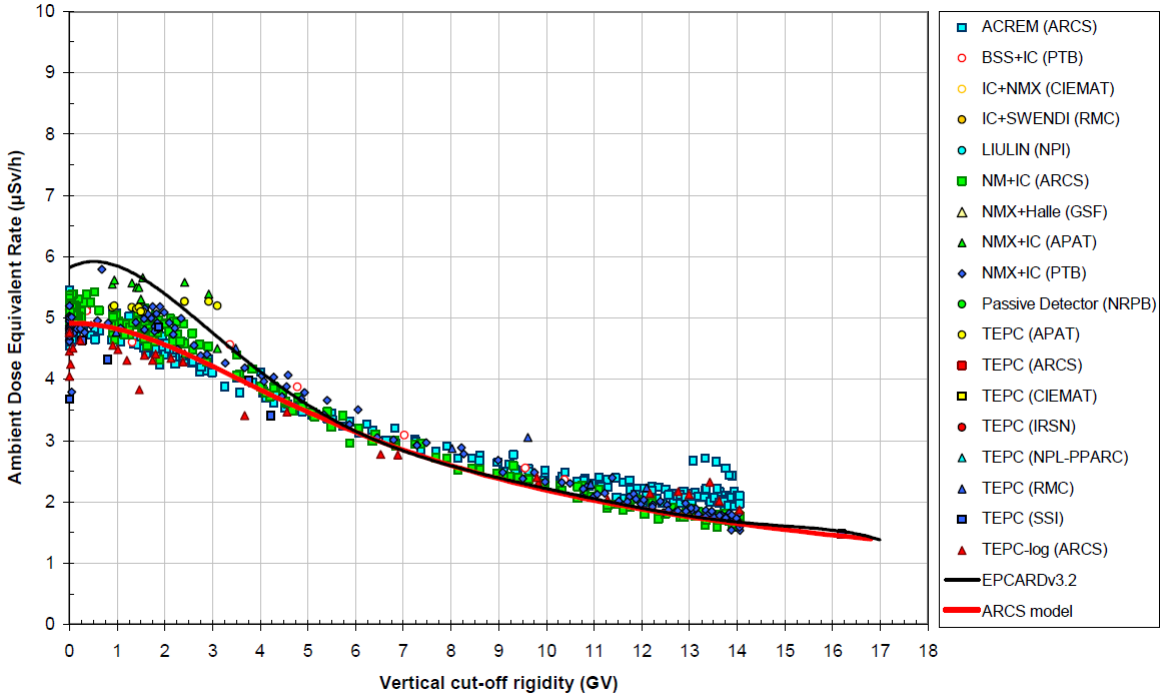

Figure 76 Ambient dose equivalent rate as a function of vertical cut off rigidity for measurements (color points), EPCARDv3.2 calculations (black line) and AVIDOS model (red line – at the time of publishing of reference [79] ARCS model, later renamed to AVIDOS). Measurements are selected from the EURADOS database for Φ = [470 – 610] MV and *h* = [9.9 – 10.2] km (FL325 – FL335). Calculations assumed Φ = 550 MV and *h* = 10.06 km (FL330) [79].

6.2.2. Comparison with other codes

The ambient dose equivalent, *H**(10), is an operational quantity commonly used in measurement practice, but finally one is interested in radiation protection quantity, the effective dose, *E*, or its rate [58]. Since effective dose is not directly measurable quantity, it is not possible to compare codes' predictions with measurements. However, one can compare different codes with each other. Such effort was taken within EURADOS Working Group 5 [109] on Aircrew Dosimetry. AVIDOS was part of this comparison. For the comparison, a set of 23 realistic flight profiles was selected. That included transatlantic flights, flights over Polar Regions, flights over Equatorial Region, and flights on southern hemisphere. In the comparison, 11 different codes using different methods to evaluate effective doses took part. The members of EURADOS Working Group 5 decided to publish obtained data in an anonymous way because some codes were actively used in commercial radiation protection service. Figure 77 shows the comparison of the effective dose rate, d*E*/d*t*, due to GCR at those waypoints of different flights that are at typical flight altitudes (FL370, ≈11.28 km), for solar minimum and maximum. Figure 78 shows the comparison of the effective dose rate, d*E*/d*t*, due to GCR during solar minimum and maximum as a function of altitude for those waypoints that are over Polar Regions (r_c < 0.25 GV) and Equatorial Region (r_c > 16.75 GV). Both figures show, that calculated effective doses by AVIDOS do not differ much from other codes. Because the number of codes in the comparison was small (less than 8 in every case), the members of EURADOS Working Group 5 decided to present the data with median instead of average as reference level. Figure 79 summarizes discrepancies of AVIDOS results from the median. AVIDOS results vary not more than 10% from the median. Authors of reference [109] report that, for all flights and codes, calculated effective dose, *E*, differ by less than 30% from the median (at 95% confidence level).

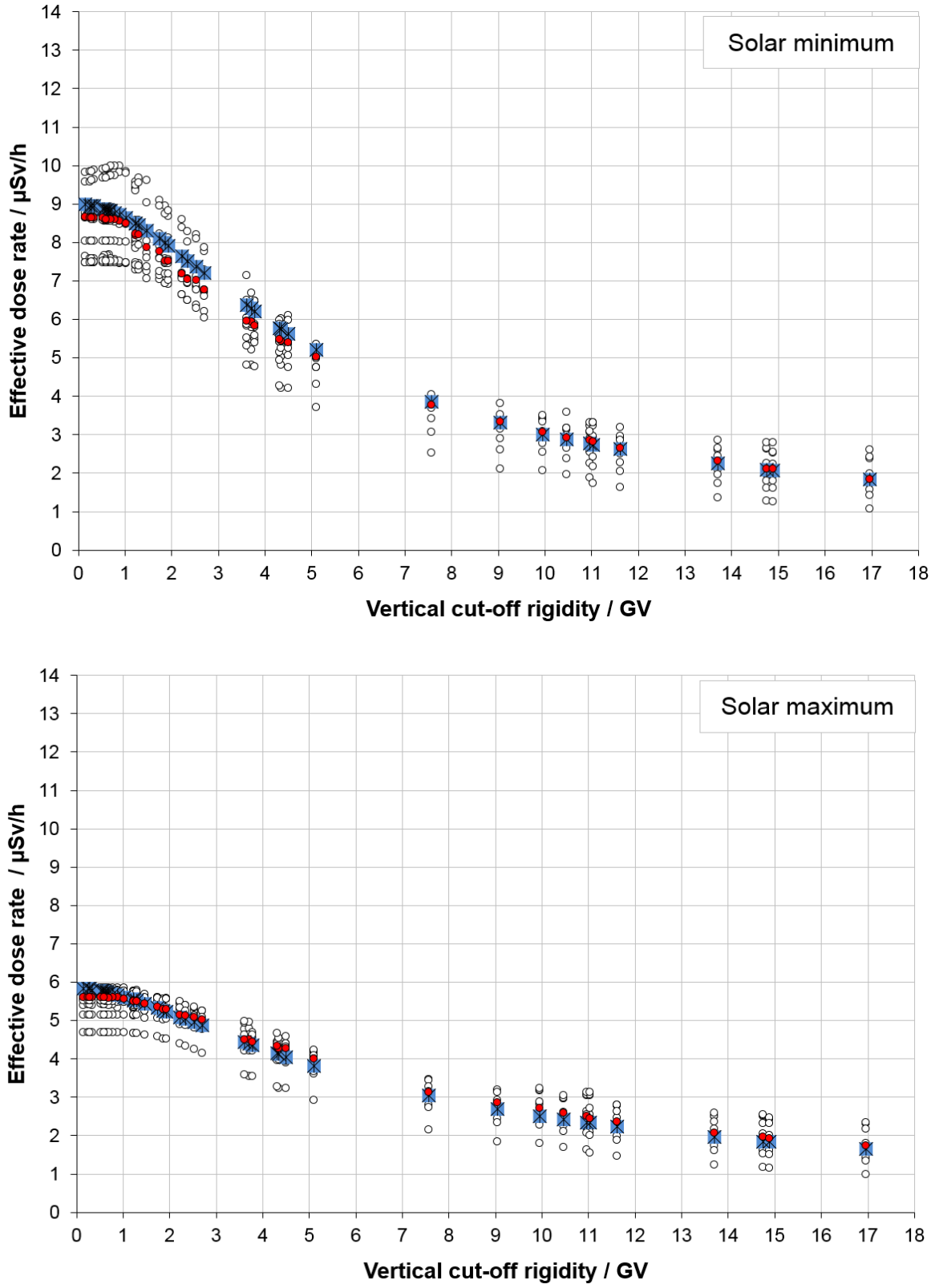

Figure 77 Anonymous comparison of the effective dose rate, d*E*/d*t*, due to galactic cosmic radiation during solar minimum (upper diagram) and solar maximum (lower diagram) for waypoints at FL370 (≈ 11.28 km). The median is marked with red symbols. AVIDOS data are marked with blue squares are overlaid on other data reproduced from [109].

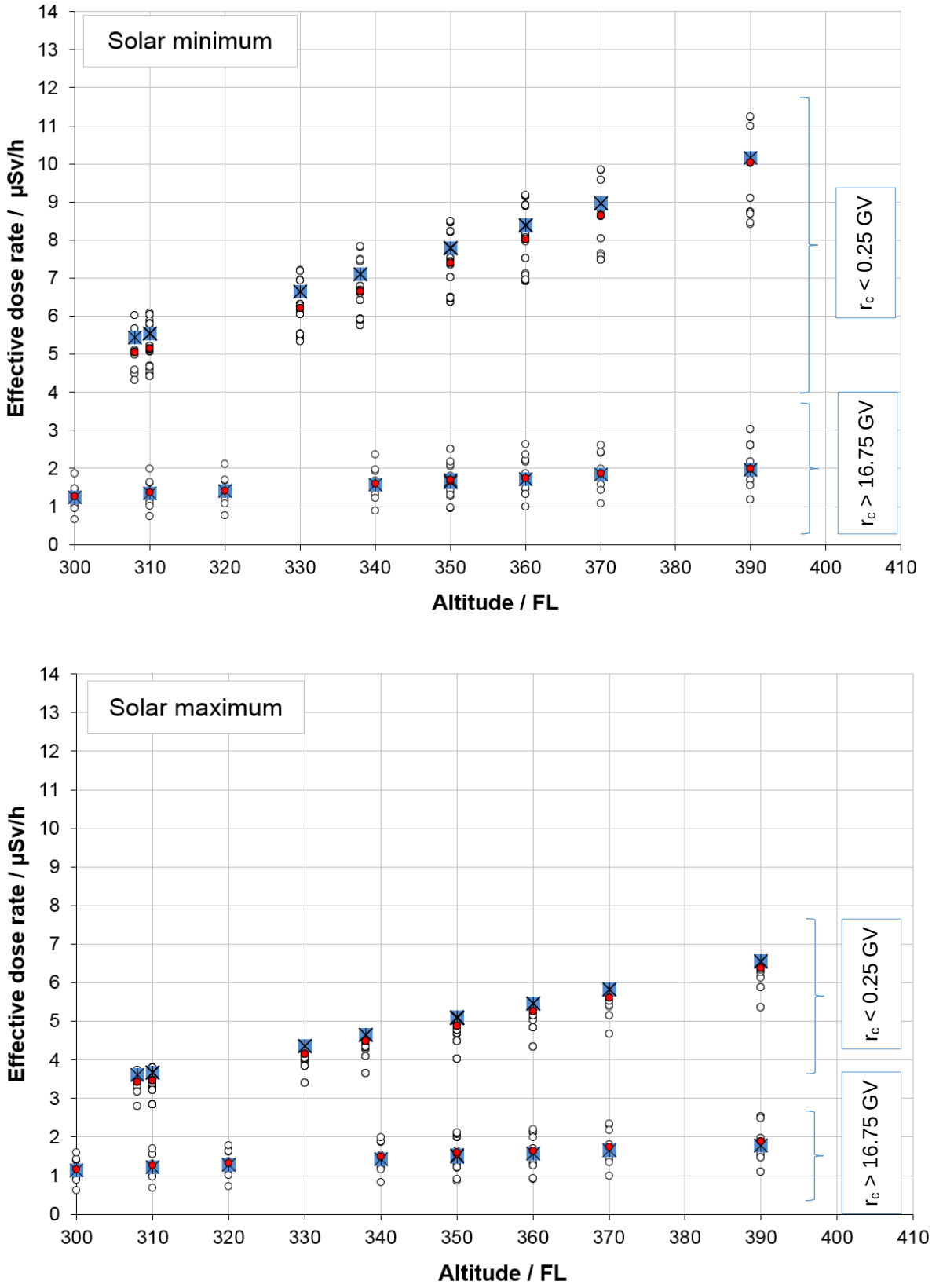

Figure 78 Anonymous comparison of the effective dose rate, d*E*/d*t*, due to galactic cosmic radiation during solar minimum (upper diagram) and solar maximum (lower diagram) as a function of altitude for waypoints at rigidity values r_c < 0.25 GV (upper data group) and r_c > 16.75 GV (lower data group). The median is marked red symbols. AVIDOS data are marked with blue squares are overlaid on other data reproduced from [109].

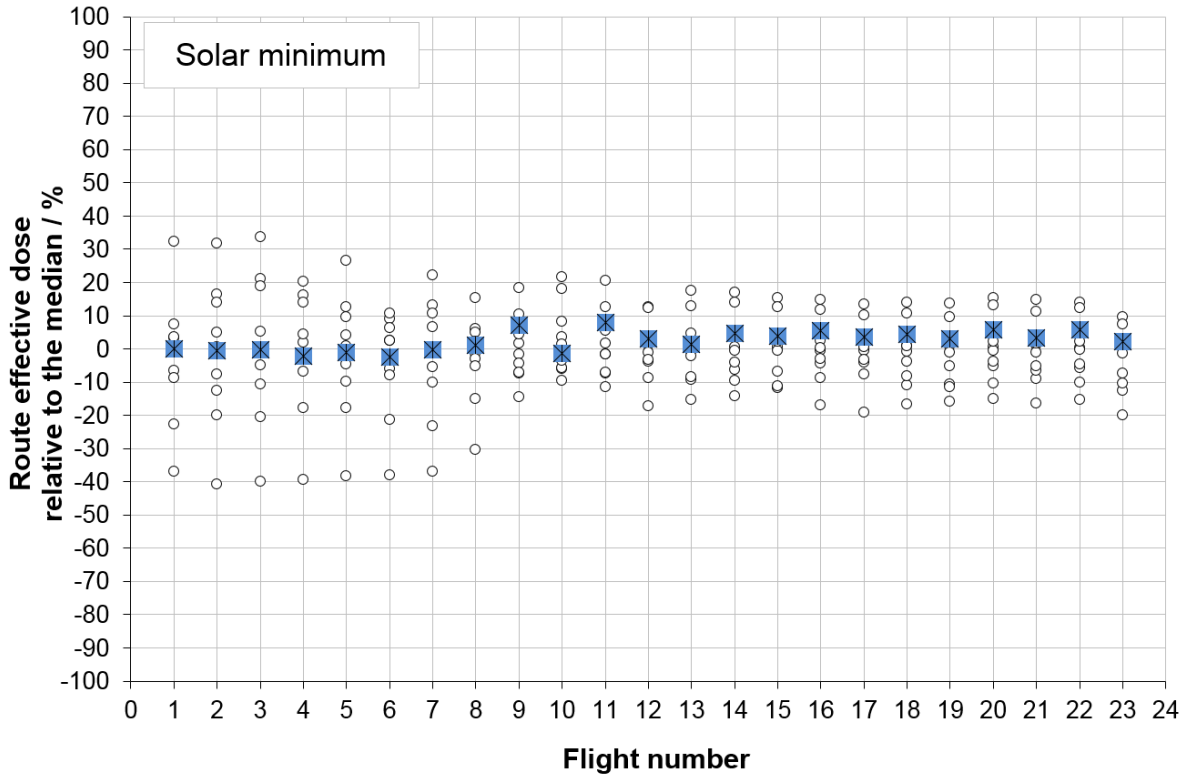

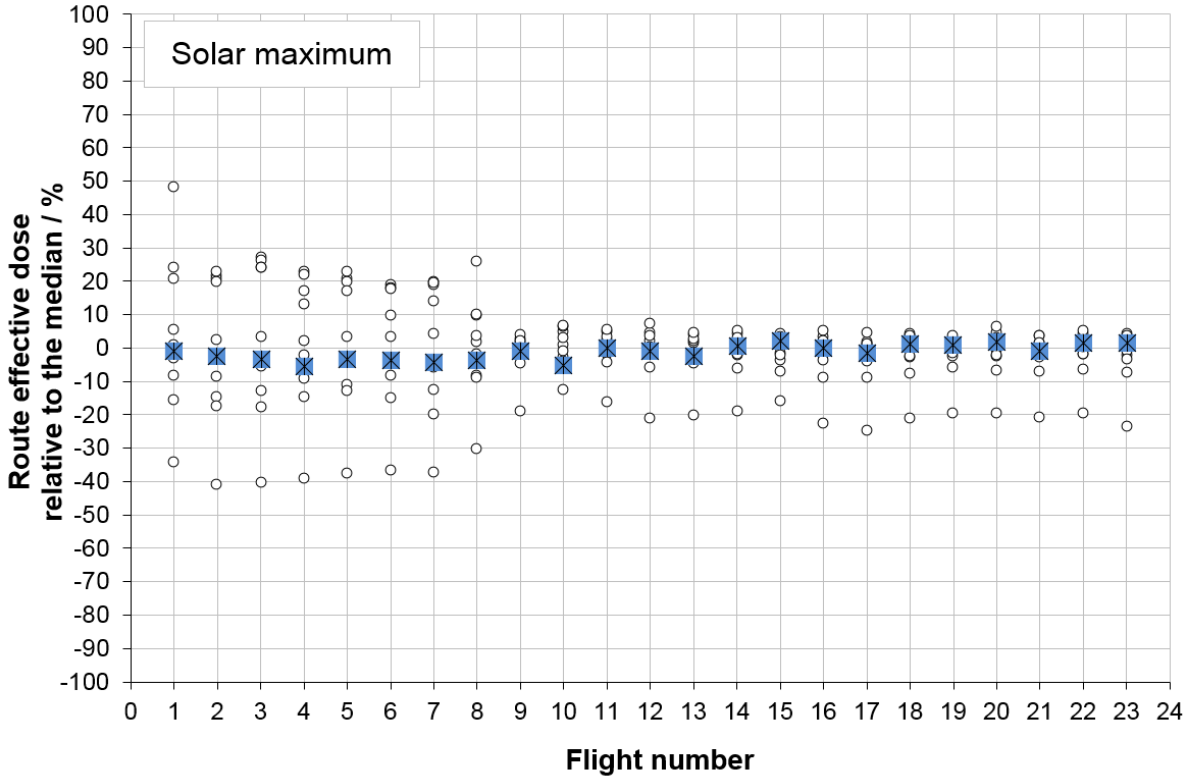

Figure 79 Anonymous comparison of the deviation of the effective dose, *E*, relative to the median at solar minimum (left) and solar maximum (right). AVIDOS data are marked with blue squares are overlaid on other data reproduced from [109].

6.2.3. Comparison with reference values

In 2010, the ICRU and ICRP jointly published the Report 84 [100] on Reference Data for the Validation of Doses from Cosmic-Radiation Exposure of Aircraft Crew. The core point of this report is to define a set of reference values of aircraft crew exposure due to cosmic radiation. The reference values are given in terms of ambient dose equivalent rates because they are based on measurements. The values are given for three different periods of solar cycle 23 (January 1998, January 2000, and January 2002) and three different altitudes – FL310 (≈ 9.45 km), FL350 (≈ 10.67 km), FL390 (≈ 11.89 km) for the full range of vertical cut-off rigidity (from 0 GV to 17 GV with 1GV step). Additionally, the report gives a set of coefficients allowing for conversion from ambient dose equivalent into effective dose. The report states also that any code predicting aircrew exposure should stay within ±30% maximum accepted interval from reference values. A short independent review on the report can be read in reference [110].

In Figure 80, Figure 81 and in Figure 82 a comparison between AVIDOS calculations and the ICRU/ICRP reference values is presented for January 1998, January 2000 and January 2002, respectively. In all cases, AVIDOS data is within the recommended ±30% maximum accepted interval from reference values. On average, AVIDOS calculations of ambient dose equivalent rates agree with reference values within 10%. Maximum deviation from reference values is 20% and is observed in few cases only.

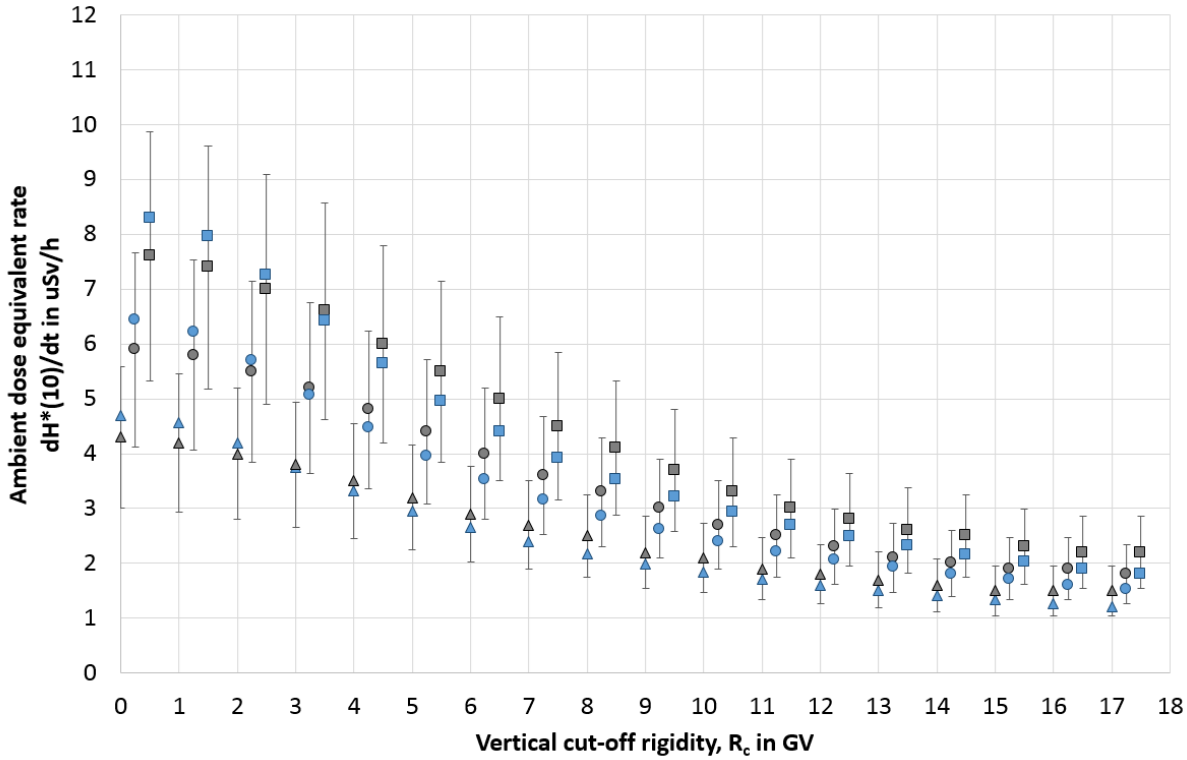

Figure 80 Comparison of ICRU/ICRP reference values of ambient dose equivalent rates, d*H**(10)/d*t*, for January 1998 for FL310 (≈ 9.45 km, gray triangles), FL350 (≈ 10.67 km, gray circles), and FL390 (≈ 11.89 km, gray squares) as a function of vertical cut-off rigidity, R_c, (as published in [100]), and corresponding AVIDOS calculations for FL310 (≈ 9.45 km, blue triangles), FL350 (≈ 10.67 km, blue circles), and FL390 (≈ 11.98 km, blue squares). In all cases, AVIDOS data is within the recommended ±30% maximum deviation (marked as error bars) from reference values. For visibility reasons, data for FL350 (≈ 9.45 km, circles) and FL390 (≈ 10.67 km, squares) is shifted to the right.

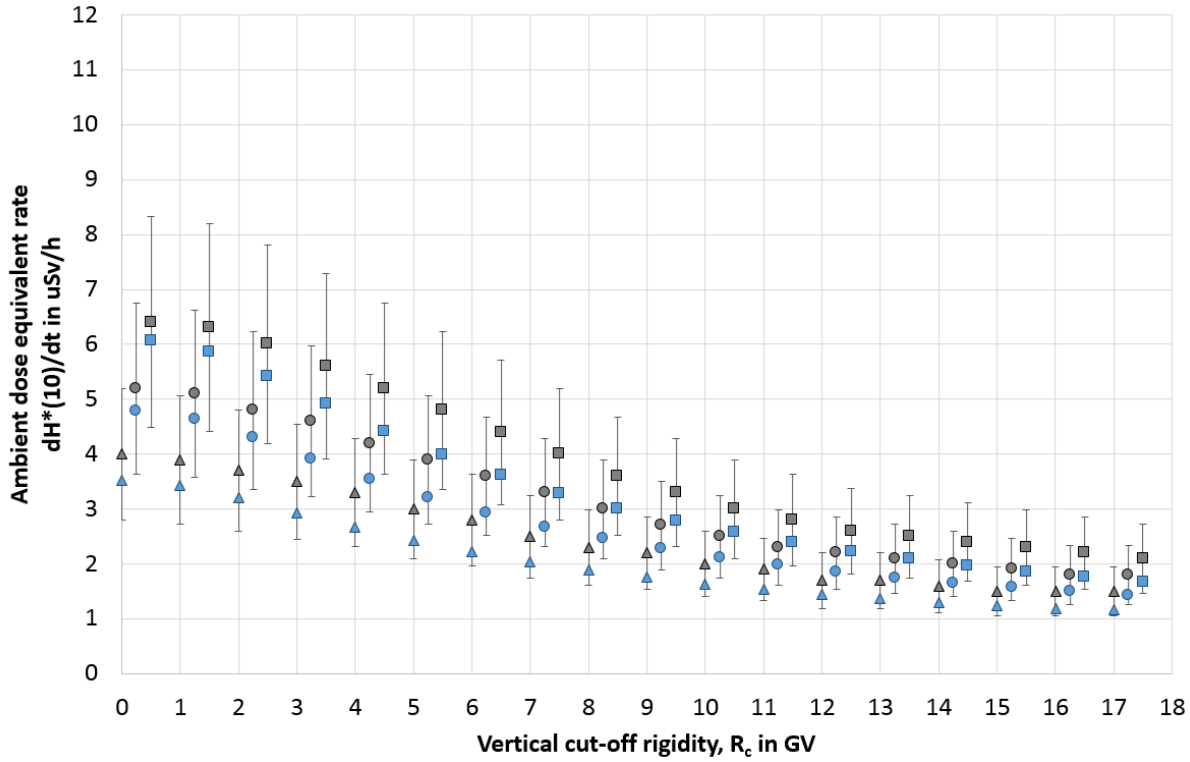

Figure 81 Comparison of ICRU/ICRP reference values of ambient dose equivalent rates, d*H**(10)/d*t*, for January 2000 for FL310 (≈ 9.45 km, gray triangles), FL350 (≈ 10.67 km, gray circles), and FL390 (≈ 11.89 km, gray squares) as a function of vertical cut-off rigidity, R_c (as published in [100]), and corresponding AVIDOS calculations for FL310 (≈ 9.45 km, blue triangles), FL350 (≈ 10.67 km, blue circles), and FL390 (≈ 11.89 km, blue squares). In all cases, AVIDOS data is within the recommended ±30% maximum deviation (marked as error bars) from reference values. For visibility reasons, data for FL350 (≈ 9.45 km, circles) and FL390 (≈ 10.67 km, squares) is shifted to the right.

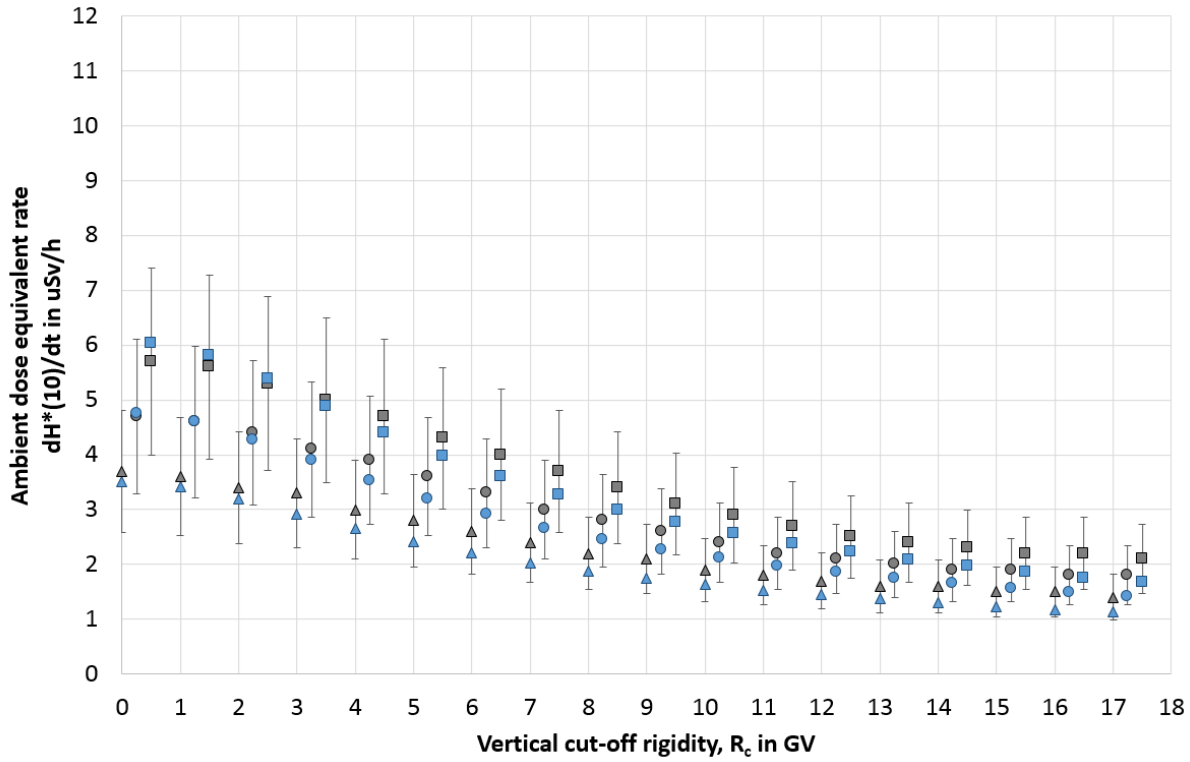

Figure 82 Comparison of ICRU/ICRP reference values of ambient dose equivalent rates d*H**(10)/d*t* for January 2002 for FL310 (≈ 9.45 km, gray triangles), FL350 (≈ 10.67 km, gray circles), and FL390 (≈ 11.89 km, gray squares) as a function of vertical cut-off rigidity, R_c (as published in [100]), and corresponding AVIDOS calculations for FL310 (≈ 9.45 km, blue triangles), FL350 (≈ 10.67 km, blue circles), and FL390 (≈ 11.89 km, blue squares). In all cases, AVIDOS data is within the recommended ±30% maximum deviation (marked as error bars) from reference values. For visibility reasons, data for FL350 (≈ 9.45 km, circles) and FL390 (≈ 10.67 km, squares) is shifted to the right.

6.3. Model development for solar energetic particle events

One of the most interesting, but also the most challenging, part of the work presented here, is model development for the assessment of radiation exposure in atmosphere during solar energetic particle (SEP) events. First models estimating the exposures due to SPE were developed and first comparison with measurements have been carried out within the European research project CONRAD [111]. However, those models were still in development, the reported discrepancy between models' predictions was in the order of ten, and the models were not publicly available [112].

AVIDOS extension for SEP events consists of two main components: Monte Carlo pre-calculated data of radiation transport through atmospheric density-height profile, and a procedure for assessing primary protons spectrum during a GLE based on neutron monitor data [108].

6.3.1. Monte Carlo pre-calculated dose matrices

The Geant4 Monte Carlo calculations were performed with the same geometry, atmosphere model, physics lists, and scorers as described in chapter 5 for simulating GLE events. In this case, however, as input spectrum, a unitary flux of protons was taken. The energy scale covered energy range from tenths' of MeV and spanned over several orders of magnitude up to some 10^7 MeV. As previously, simulations resulted in fluence rates for secondary particles at all defined detection levels (altitudes) and for scored secondary particles: $\{p, n, e^-, e^+, \mu^-, \mu^+, \pi^-, \pi^+, \gamma\}$. Similarly as before, folding in energy the particles' fluencies with fluence-to-dose conversion coefficients [93] resulted in matrices of effective dose rates dE/dt and ambient dose equivalent rates $dH^*(10)/dt$ at all defined altitudes. The actual dose rates' values for a given input proton spectrum are calculated by weighting the dose-matrices that were pre-calculated for the unitary flux of input protons with the given, actual proton input spectrum. In this way, one can quickly assess radiation exposure at any desired geographical location, at any desired altitude (resolution and range is determined by scorers in simulations) for any given solar proton spectrum. A short summary of this step is published in reference [108]. This solution can be also easily implemented in a programming language resulting in a computer code.

6.3.2. Procedure for assessing primary protons spectrum

Second part of the proposed model is the construction of primary protons spectrum. Construction of primary protons spectra for a given GLE is a laborious and retrospective process performed typically, but not only, by teams operating Neutron Monitor stations. Results for the same GLE provided by different authors usually differ in a significant way. Figure 83 presents a relatively known and well described in the literature GLE60 from 15th of April 2001. As seen in Figure 83 the proton flux can easily differ by an order of magnitude in the main GLE's phase (left diagram in the figure). If additionally a temporal evolution of a GLE is considered, additional uncertainties occur (right diagram in the figure).

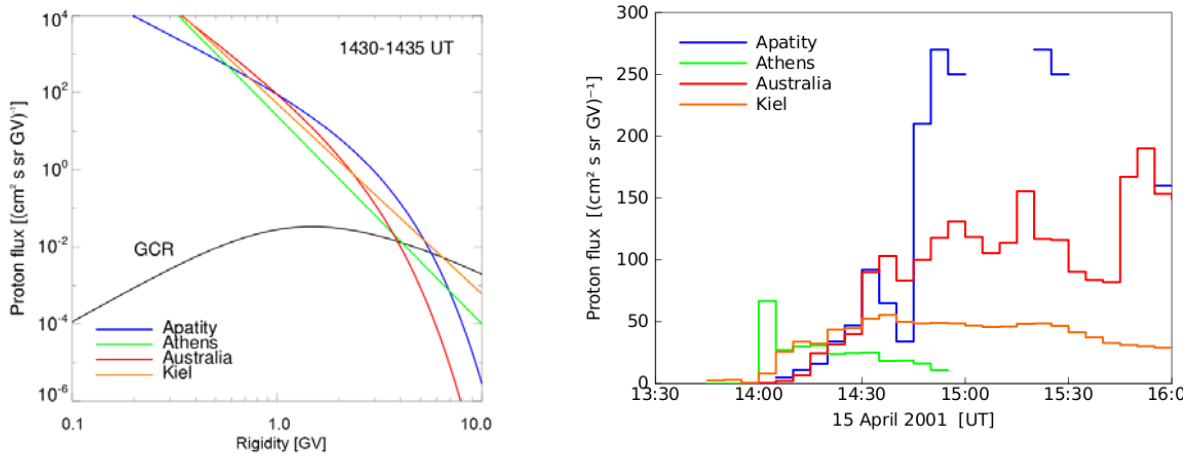

Figure 83 Primary proton spectra in the main phase of GLE60 (15/04/2001) (left) and primary proton flux at 1 GV, as calculated by different authors [119].

Model that is proposed here aims at a solution for providing radiation exposure in a reasonable time. To achieve this aim, an isotropic scenario is considered for every GLE. Analyzing different neutron monitor records and spectra reconstructions for different GLEs, one can conclude that the initial phase of GLE events are often (but not always) anisotropic. However, with time, after initial increase and maximum phases, that is typically after about 30 minutes, the situation evolves towards isotropy [e.g. 113, 114, 115, 116, 118]. The anisotropy effect induced on doses has been studied in reference [116]. Authors report that deviation in dose due to SEP only and caused by anisotropy can reach some 60% in extreme cases, but typically is up to 40% (depending on the choice of GLE and flight route). Taking into account that to the total radiation dose also isotropic GCR contribute (particularly in high energies) the figures on anisotropy effect become up to 50% in extreme cases and up to 20% typically. The main effect on accuracy of the assessment of radiation dose due to SEP is caused by the quality of SEP proton spectrum used. Literature investigations conclude that causes of discrepancies between different primary proton spectra obtained by different groups are manifold, cannot be conclusively identified at present, and that resulting deviation in the assessment of radiation dose can be easily a factor of two just for the fact of using different primary proton spectrum [119]. A similar conclusion emerges from EURADOS (http://eurados.org/) investigations on SEP code comparison (Working Group 11, Task Group 3 report - in editorial phase): the biggest factor in the discrepancy of calculated radiation dose during GLE is the input data. In the case of Monte Carlo based codes this is the quality of primary proton spectrum.

Here, to conclude on primary solar proton spectra, author uses one selected neutron monitor station – the Oulu station (http://cosmicrays.oulu.fi/). The location of the station has several advantages:

- it is in Europe, which is an advantage for assessing radiation levels for flights from and towards Europe
- is located at high geomagnetic latitude i.e. low cut-off rigidity which in turn makes it relatively sensitive to the changes of proton flux on top of the

atmosphere (SEP events have usually a softer energy spectrum than the galactic cosmic rays, i.e. the effect of SEP events is dominant at high geomagnetic latitudes).

- data of good quality,
- data in reasonable time resolution (1-minute at best),
- the operation of the station is reliable,
- data are accessible through a programming interface (online query).
- characteristics of this neutron monitor were published (e.g. [120])

The spectrum of primary protons is often expressed in the domain of particle rigidity (or equivalently particles' energy) as a pure power law or modified power law. Two important characteristics of pure power law function are: amplitude $A(t)$ and steepness $\gamma(t)$. The equation is:

$$J_{SCR}(R,t) = A(t) \cdot R^{-\gamma(t)}$$

where:
$J_{SCR}(R,t)$- Solar cosmic ray proton flux at time t $[\#/(cm^2 s\ sr\ GV)]$ as a function of particle rigidity R
$A(t)$ - Amplitude at time t $[\#/(cm^2 s\ sr\ GV)]$
R – particle rigidity $[GV]$
$\gamma(t)$ - steepness of SEP spectrum at time t

In modified power law $\gamma(t)$ is additionally modified by parameter $\delta\gamma$ which is applied after certain rigidity$R$, usually for $R > 1\ GV$ or $R > 2\ GV$ so the exponent is e.g. $-(\gamma + \delta\gamma\ (R-2))$ for $R > 2\ GV$. The effect on spectrum is that after $R > 1\ GV$ or $R > 2\ GV$ the spectrum is additionally bended. Different groups assessing the primary proton spectrum use different equations [e.g. 119]. Here, pure power law is used.

The steepness and anisotropy can be studied from past GLE events, for which spectra have been a posteriori calculated with larger set of neutron monitor detectors [e.g. 116, 121, 122, 123, 124, and 125]. Both amplitude and steepness are time dependent, constantly modifying the spectrum during a GLE. To cover the effect of steepness variation when working with only one neutron monitor, the model considers two fixed values for steepness: minimum $\gamma = 4$ for hard spectrum and maximum $\gamma = 7$ for soft spectrum. The choice is based on literature review [e.g. 115, 116, 117, 118, 122, 125, and 126].

The amplitude $A(t)$ is derived from the increase of the count rate of Oulu neutron monitor station and monitor's yield function. The yield function for a standard 6-NM64 neutron monitor can be expressed by the following formula [e.g. 127]:

$$logS_p(R,z) = \sum_{m,n=0}^{3} C_{mn} \cdot z^m \cdot (\log R)^n$$

z - atmospheric depth of the NM $[g/cm^2]$
c_{mn}- coefficients for a standard 6-NM64 neutron monitor [127]
S - yield function in $[m^2 sr]$

Count rates of the neutron monitor in Oulu are normalized to a pressure of 1000 mbar corresponding to atmospheric depth of z = 1019 g/cm. Furthermore, a normalization factor is introduced that considers that the monitor in Oulu is a 9-NM64 device with nine tubes. The count rate increase of the neutron monitor in Oulu station during a GLE is then given by:

$$\Delta N^{Oulu}(t) = N^{Oulu}(t) - N^{Oulu}(t_0) = \int_{R_C^{Oulu}=0.8\ GV}^{20\ GV} S^{Oulu}(R) \cdot J_{SCR}(R,t) \cdot dR$$

$N^{Oulu}(t)$ – count rate during GLE event at time t $[s^{-1}]$
$N^{Oulu}(t_0)$– baseline count rate, before the GLE $[s^{-1}]$
$S^{Oulu}(R)$– yield function for Oulu NM $[cm^2 sr]$
$J_{SCR}(R,t)$ – solar cosmic ray proton flux
$R_C{}^{Oulu}$ - Vertical cutoff rigidity of the Oulu NM station

Finally, the above equation can be solved for the amplitude $A(t)$. Having amplitude derived from actual relative increase of Oulu neutron monitor count rate and two fixed steepness values, one obtains temporal intensity of two primary spectra. With these, the dose matrix can by appropriately weighted resulting in minimum and maximum expected effective dose rates. This procedure can be done at any time t, for each recorded increase of Oulu neutron monitor count rate. Proceeding in this way results in a recipe that is suitable for real-time dose assessment of radiation exposure at aviation altitudes due to spontaneous solar particle events.

In practice, real time dose assessment at civil flight altitudes due to SEP events has three steps. In the first step, AVIDOS checks alert if a GLE is on-going. For this, AVIDOS constantly probes a real-time GLE-alerting service. There are several such services available, AVIDOS 2.0 uses ANeMoS service [127]. To issue a GLE alert, ANeMoS relies on the real-time Neutron Monitor Database (NMDB [36]) and watches every single minute whether a defined number of neutron monitor stations simultaneously show increased records. If yes, and if such state keeps up for a certain time, an alert is issued. When AVIDOS 2.0 receives GLE alert, the second step starts. In this step, AVIDOS obtains records from Oulu neutron monitor station in a regular time interval and two proton input spectra at the top of atmosphere are assessed as described above – a soft spectrum with lower maximum proton energies and hard one with higher maximum proton energies. Finally, in the third step, the spectra are used to weight Mote Carlo simulations resulting in effective dose rates and ambient dose

equivalent rates at any desired position of a flight. Based on those data AVIDOS 2.0 assess minimum and maximum expected increase of radiation doses due to SEP events.

6.3.3. GLE42 from 29 September 1989 in AVIDOS 2.0

Solution implemented in AVIDOS 2.0 was tested on few realistic flight profiles and GLE42 from 29th September 1989. Three flight profiles were selected from a rich set of flight profiles used for EURADOS comparison of codes calculating radiation dose exposure due to GCR [109]. Selected flights were: Sydney – Johannesburg on Southern hemisphere (Figure 84 top), transatlantic flight San Francisco – Paris (Figure 84 middle), and Chicago – Beijing flown over North Pole (Figure 84 bottom). All flights were modified for departure date and time with respect to the original profiles as used by EURADOS – here, all start on 29.09.1989 at 11:45, so that GLE could affect all of them.

Figure 85 presents considered scenario at maximum increase of count rates recorded by neutron monitor station in Oulu (upper diagram) – on 13:50 UTC. In the lower diagram, color area marks average calculated ambient dose equivalent rates as calculated from soft and hard spectra constructed for at maximum increase of count rates recorded by neutron monitor station in Oulu. As seen in the figure, at 13:50 UTC, the San Francisco – Paris and Sydney – Johannesburg flights have not yet reached the area with elevated radiation doses due to GLE. Oppositely, the flight Chicago – Beijing. This situation is reflected in Table 16 where accumulated (up to 13:50 UTC) doses due to GCR and assessed minimum and maximum doses due to SCR (caused by GLE42) are shown. Minimum assessed accumulated ambient dose equivalent for San Francisco – Paris is comparable to the accumulated $H^*(10)$ due to GCR. Maximum assessed value is about 2.5 times grated than that for GCR – the flight just enters the area affected by the GLE. Accumulated ambient dose equivalent values (both assessed minimum and maximum) for Sydney – Johannesburg are lower than that for GCR – the flight have not entered the area affected by GLE. The route of Chicago-Beijing flight is already in the area where elevated doses occur – maximum assessed $H^*(10)$ is 220 µSv, the minimum assessed is almost twice the $H^*(10)$ for GCR. The flights and the GLE takes about 10 hours. The considered scenario, when the flights and GLE are over is presented in Table 17. Minimum assessed route $H^*(10)$ in all cases is comparable to that of GCR. Maximum assessed route $H^*(10)$ is almost 1 mSv for Sydney – Johannesburg, almost 1.5 mSv for Chicago-Beijing and almost 2 mSv for San Francisco-Paris – this is due to the fact, that this flight is flown at highest altitudes (FL370 and FL390). The conclusion is that for typical flights during GLE42, the minimum, assessed by AVIDOS, ambient dose equivalent is roughly the same as for GCR, while the maximum can reach even few mSv particularly for high altitude and high latitude flights.

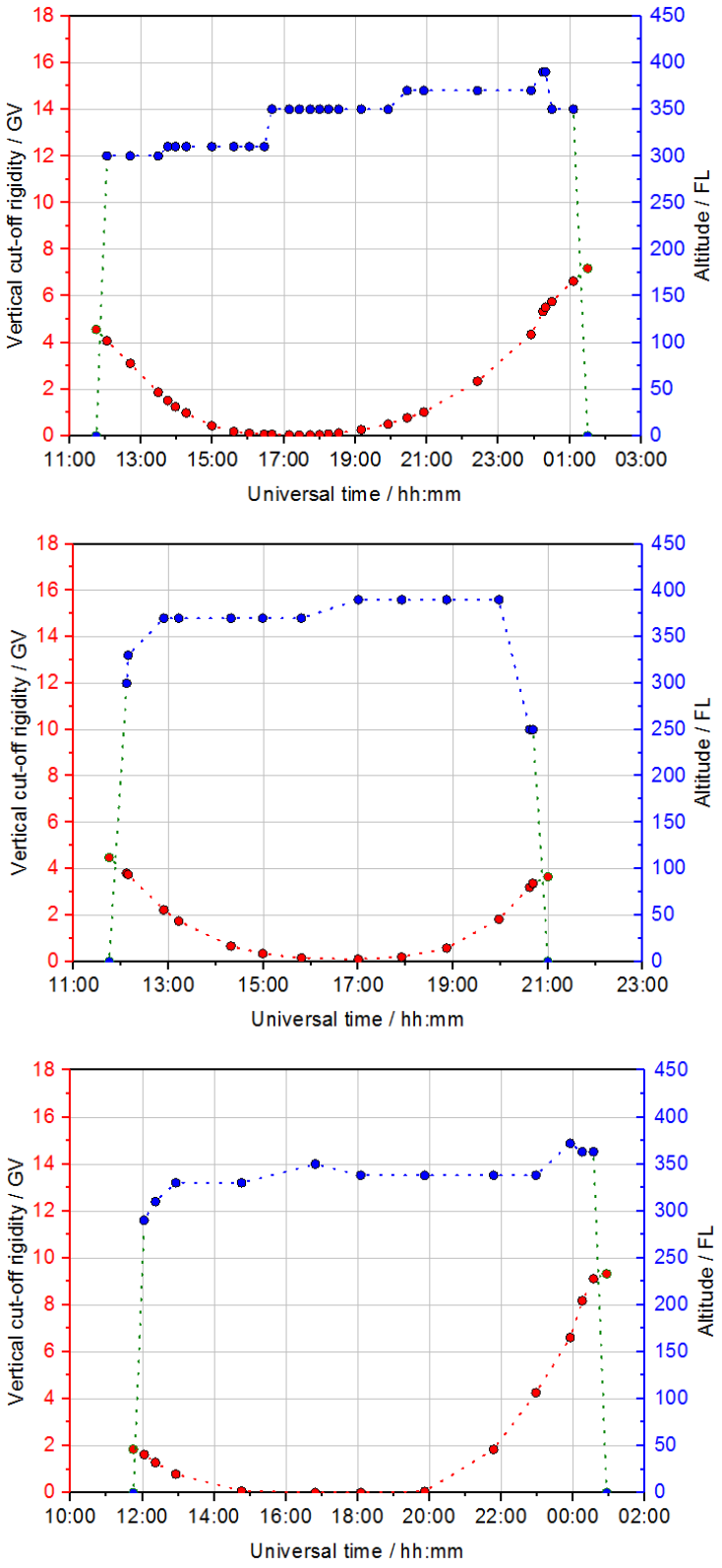

Figure 84 Three selected and modified flight profiles: Sydney – Johannesburg (top), San Francisco – Paris (middle), and Chicago – Beijing (bottom). Red dots mark values of vertical cut-off rigidity in GV at flight's waypoints – left axis; blue dots mark values of altitudes in FL at flight's waypoints. Flight profiles are based on EURADOS/EC report [109] but with modified departure date and time – all start on 29.09.2989 at 11:45 UTC.

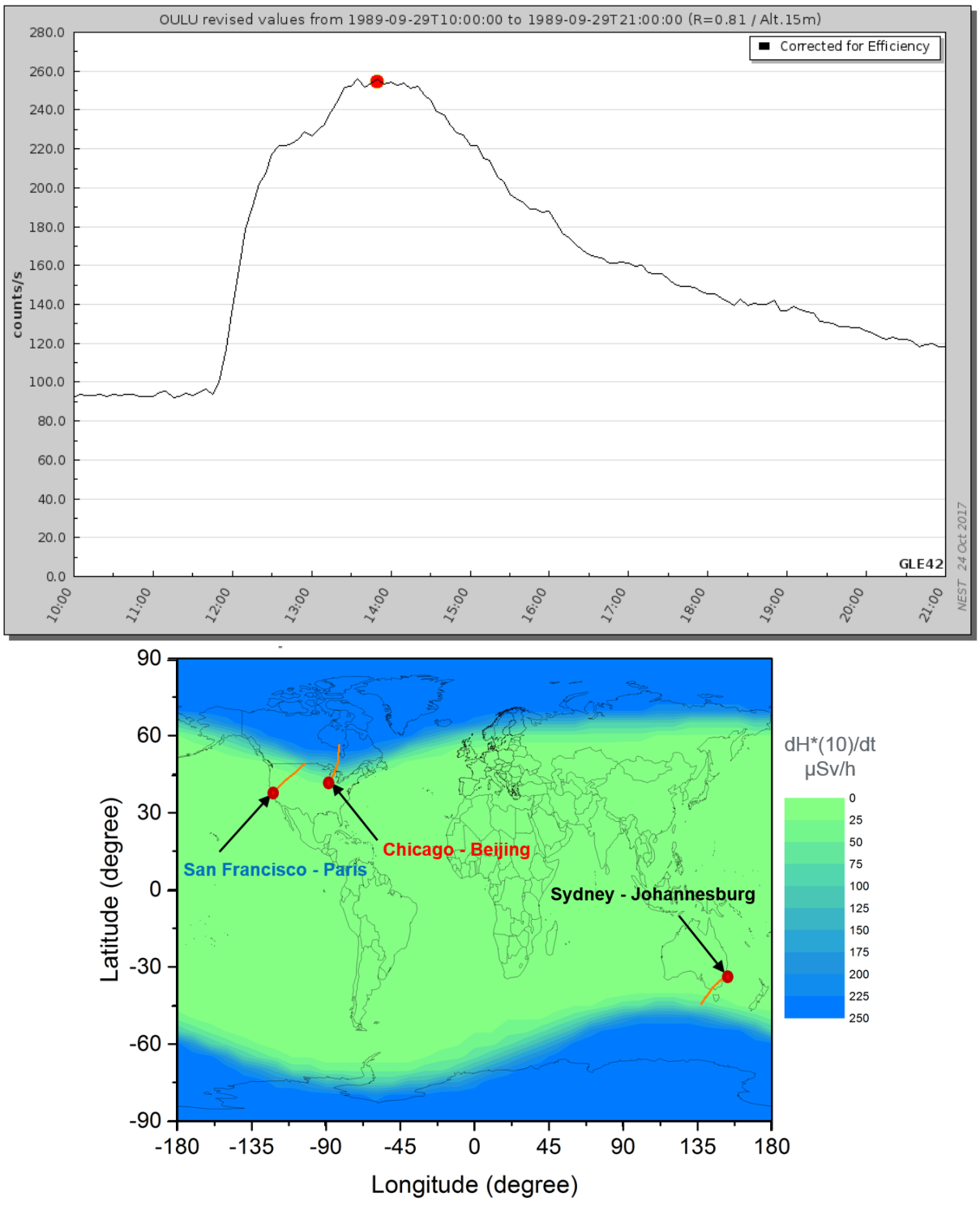

Figure 85 Upper diagram: temporal evolution of the neutron monitor station in Oulu during the whole GLE42. Red dot marks the maximum increase of count rates recorded by neutron monitor station in Oulu - data from NMDB [36]. Lower diagram: areas with elevated doses due to the GLE (color scale from green to blue) as calculated by AVIDOS and routes of selected flights (red paths) in the peak phase of GLE42 on 13:50 UTC [128].

Table 16 Accumulated (up to 13:50 UTC) doses due to GCR and assessed minimum and maximum doses due to SCR (caused by GLE42) for the three selected flights [128].

Flight	*H**(10) in µSv GCR	*H**(10) in µSv SCR min (hard spectrum)	*H**(10) in µSv SCR max (soft spectrum)
Sydney-Johannesburg	5	1	3
San Francisco-Paris	7	5	18
Chicago-Beijing	6	11	220

Table 17 Accumulated total doses (whole flights) due to GCR and assessed minimum and maximum doses due to SCR (caused by GLE42) for the three selected flights [128].

Flight	*H**(10) in µSv GCR	*H**(10) in µSv SCR min (hard spectrum)	*H**(10) in µSv SCR max (soft spectrum)
Sydney-Johannesburg	45	32	895
San Francisco-Paris	39	54	1882
Chicago-Beijing	40	47	1460

6.3.4. GLE72 from 10.09.2017 in AVIDOS 2.0

On September 10, 2017, the 72nd Ground Level Enhancement occurred. It was a long awaited GLE – the previous one, GLE71, happened in May 2012 [38]. Protons measured by GOES satellites showed increased fluence rates in all energy channels - Figure 86 – reaching S3 level (flux of >10 MeV protons greater than 10^3) in NOAA Space Weather Scale [127]. Several neutron monitor stations located at high northern or southern latitudes (low vertical rigidity cut-off values) showed increased count rates – Figure 87. On 17:03 UTC, the ANEMOS has issued a GLE alert since four neutron monitor stations (Inuvik, Kerguelen, South Pole and Thule) showed simultaneously increased measured count rates. The GLE was very short; it lasted only few minutes until 17:11 UTC. AVIDOS 2.0 has received the GLE alert and automatically downloaded records of the neutron monitor station in Oulu. When the event was over, AVIDOS generated its default-hard and default-soft spectra as described in chapter 6.3.2 and stored in its database. The generated spectra are available in AVIDOS' Science Mode. In this mode, there are three pre-defined flights available. Modifying the San Francisco – Paris flight in such a way, that it starts on 10th of September 2017

at 11:30 UTC, and increasing its altitude in the second phase of the flight from FL390 to FL490, the additional effective dose due to the GLE72 would be up to 10 µSv. This increase is relatively small, and is about 10% of effective dose that would come from GCR for such flight - Table 18. Results showed here were presented for the first time during SEPRAD Workshop on Forecasting of Solar Energetic Particle Radiation Effects on 18 - 19 September 2017 in Seibersdorf [129].

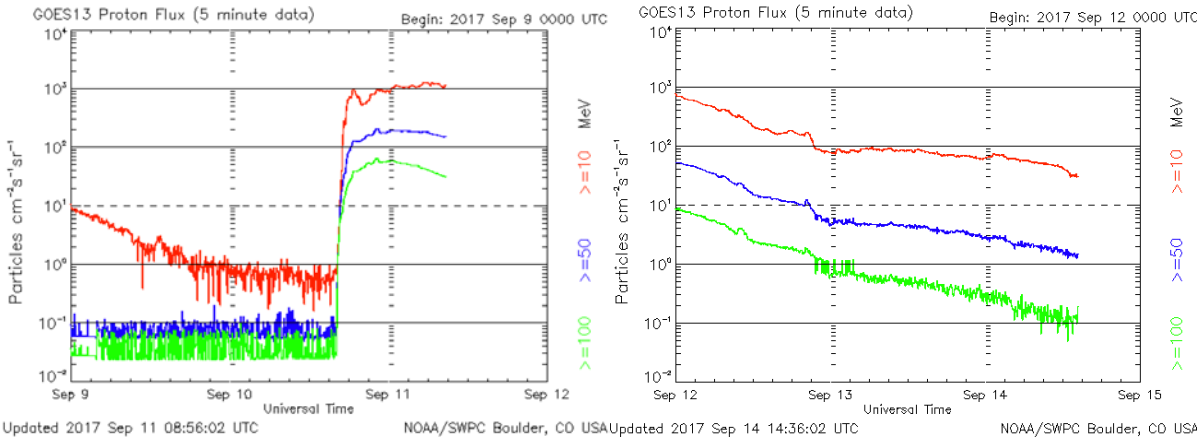

Figure 86 Integrated proton flux (>10 MeV – red; >50 MeV – blue; >100 MeV green) as measured by GOES 13 satellites (Source: http://www.swpc.noaa.gov/products/goes-proton-flux)

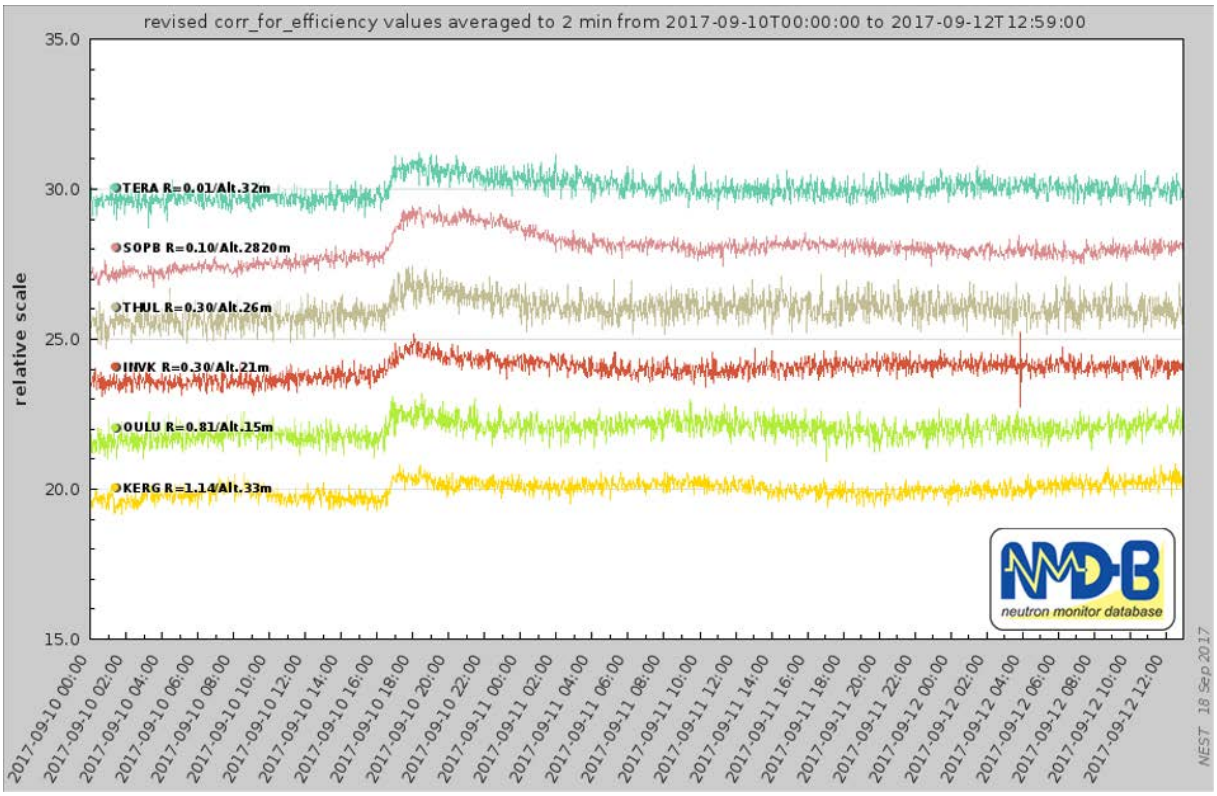

Figure 87 Relative increases of neutron monitor count rates as measured by six neutron monitor stations at Terre Adelie (Antarctica), South Pole (Antarctica), Thule (Greenland), Inuvik (Canada), Oulu (Finland), Kerguelen (Indian Ocean). Data from Neutron Monitor Database [36].

Table 18 Route effective doses due to GCR and GLE 72 from 10.09.2017 (soft and hard spectrum) as calculated by AVIDOS 2.0 for a modified San Francisco – Paris flight. Presented at SEPRAD Workshop, Seibersdorf, 2017 [129].

Departure time on 10/09/2017	Flight altitude FL	Effective dose (GCR) µSv	Effective dose (GLE soft spectrum) µSv	Effective dose (GLE hard spectrum) µSv
9:30	GLE at FL390	77	0.2	<0.1
11:30	GLE at FL390	77	2	<0.1
14:00	GLE at FL370	77	0.9	<0.1
11:30	GLE at FL490	100	10	<0.1

6.4. Radiation protection service with AVIDOS-FDS

AVIDOS 2.0 provided via ESA SSA SWE portal is an informational and educational tool to increase public awareness of space weather and its effects on radiation environment in atmosphere and aviation. Calculations performed with this version of AVIDOS 2.0 cannot be used for radiation protection service.

Based on the author's investigations, Seibersdorf Laboratories has qualified an offline copy of AVIDOS-FDS that fulfills all functional and non-functional requirements defined in the Austrian Ordinance of Radiation Protection for Flying Staff [133]. This enables AVIDOS-FDS usage for regular radiation protection purposes for routine dose assessment due to galactic cosmic radiation. Author took also an active part in the formulation of formal processes and instructions [135] for the assessment of radiation exposure in aircrafts. The developed documentation has been adopted into Seibersdorf Laboratories' quality management system compliant with ISO 9001:2008 standard. The defined procedures embrace measurements of radiation exposure in aircrafts, assessment of radiation exposure in aircrafts using model calculations, and validations of model calculations for the assessment of radiation exposure in aircrafts. A successful audit of the flight dosimetry processes based on AVIDOS resulted in an accreditation compliant with EN ISO/IEC 17025 standard. It confirms technical competences of Seibersdorf Laboratories' team in the assessment of radiation exposure in aircrafts by using AVIDOS as a dosimetry calculation method. Currently, the author is head of the aviation dosimetry service group.

7. Conclusions

In this dissertation, I presented my work as a scientific employee of Seibersdorf Laboratories towards development and implementation of a semi-empirical model for real-time radiation dose assessment at civil flight altitudes due to galactic cosmic rays and spontaneous solar particle events.

I achieved this aim coming through several steps. I described calibration and use of tissue equivalent proportional counter (TEPC) in measurements of laboratory radiation fields as well as on-board aircraft. I performed complementary to measurements numerical simulations of radiation exposure in atmosphere due to galactic cosmic radiation (GCR) and solar energetic particle (SPE) events. Based on the gathered knowledge and experience, I developed a model for real-time radiation dose assessment at civil flight altitudes due to galactic cosmic rays and spontaneous solar particle events. I implemented the proposed model into AVIDOS 2.0 code.

AVIDOS 2.0 is provided to public as a web service of the Seibersdorf Laboratories federated with ESA's Space Situational Awareness Space Weather portal (SSA SWE). It serves as informational and educational online software for the assessment of cosmic radiation exposure at flight altitudes. It is freely accessible. Regarding GCR, AVIDOS 2.0 can forecast radiation dose up to 12 months in advance. As for SEP, AVIDOS 2.0 provides real-time minimum and maximum expected dose. So far, AVIDOS 2.0 is the only publicly available software in Europe that provides this kind of real-time information.

AVIDOS 2.0 is also an active answer to the ICRP 132 [13] recommendations for frequent flyers and public serving as a tool for self-assessment of radiation dose, as well as providing general information of cosmic rays exposure at civil flight altitudes.

I developed also an offline version AVIDOS-FDS with formal procedures for routine aviation dosimetry for radiation protection service. This fits well into implementation of EC Directive [8]. Proposed solution is compliant with EN ISO/IEC 17025 standard for testing laboratories. Seibersdorf Laboratories is using AVIDOS-FDS for routine radiation protection purposes where I am the head of the aviation dosimetry service group.

8. Outlook

Concerning nowcasting and forecasting of radiation exposure due to GCR with AVIDOS 2.0, the next version of AVIDOS will have implemented the new ICRP 103 [3] recommendations regarding new radiation weighting factors for neutrons and protons. Currently, ICRP 60 recommendations [5] are used since this is the legally valid basis. Consequently, I expect that effective dose values calculated with new radiation weighting factors will change compared to the current effective dose values. Motivation for this work is the new EC Directive 2013/59/Euratom [136], which with 6th of January 2018, repeals the EC Directive 96/29/Euratom [8], and which directly calls for the implementation of the ICRP 103 [3] recommendations.

The most challenging part of AVIDOS 2.0 in the nowcasting of radiation exposure due to SEP is the assessment of solar proton spectrum and its temporal evolution. The current approach for the assessment of the spectrum uses data from a single neutron monitor station. This approach has limitations, which results in a range of radiation dose assessments. AVIDOS 2.0 gives expected minimum and maximum route dose for a selected flight. In addition, because of using a single neutron monitor station, an isotropic incidence of solar energetic particles is assumed in the current model, which in the first 20-30 minutes of a GLE event is often not the case. However, for the remaining part of GLE temporal evolution, the situation naturally falls into isotropic scenario and nowcast by AVIDOS 2.0 is reasonable. Working with at least two neutron monitor stations and using ratio of their measured count rates, one can improve the assessment of spectrum's steepness and therefore reduce uncertainty for the real-time assessment of radiation doses. One can also take a more ambitious approach and work not only with two neutron monitor stations but also with a network of e.g. 10 neutron monitor stations located all over the world. To obtain results for a near real-time solution, a parallel processing on a high performance computing cluster might be necessary.

9. Acknowledgements

First, I would like to thank to Karolina, my beloved fiancée and very soon wife. Thank you for your patience and for your support during the hours and days I spent writing my dissertation. Yes, this time could have been ours, but you kindly allowed me to take it for myself. Time is precious gift, and I will always be grateful to you for this; I hope I used the time well so you can be proud of the result.

I thank to my parents. There are countless reasons to thank you. On this particular occasion, I selected only a few. The most important one for me is for having freedom to study what I thought is the best for me – thank you also for financial support during that time. A strong handshake goes to my father who always told me “whatever you do, do it so well, that nobody needs to correct after you”. A warm hug goes to my mother for teaching me that things must not only work, but also look good.

Although I am currently living and working in Austria, I feel strong connection to Poland. When I was faintly thinking of a dissertation, I always thought it has to be accomplished in Poland. Many colleagues with whom I studied have obtained their PhD and are currently working at the IFJ - it seemed to me a natural place for applying for my dissertation. I would like to thank dr hab. Maciej Budzanowski, my main supervisor, who encouraged me to present my work in form of dissertation, and who helped me a lot in formal preparations for this important step in my scientific path.

I would like to thank and acknowledge Dr Peter Beck, my co-supervisor and head of our Radiation Hardness Assurance and Space Weather group in Seibersdorf Laboratories. Dr Beck introduced me to the topic of aircrew dosimetry. I have learnt a lot working with dr Beck on a daily basis. I acknowledge his engagement, patience, willingness to explain difficult aspects of aircrew dosimetry and his professional criticism. Thanks to dr Beck’s management skills, I had a stable platform for conducting my work.

I acknowledge other colleagues with whom I collaborated. It was always a pleasure to work together, to exchange information and discuss not only scientific matters but also cultural ones.

10. Disclaimer

AVIDOS 2.0 – a federated service of Seibersdorf Labor GmbH with ESA Space Weather portal is an informational and educational online software for the assessment of cosmic radiation exposure at flight altitudes and may not be used as a decision-making tool or as a radiation protection service.

11. List of references

1. International Commission on Radiation Units and Measurements, Microdosimetry, ICRU Report 36, Bethesda MD, USA, 1983.
2. International Commission on Radiation Units and Measurements, Fundamental quantities and units for ionizing radiation (revised), Oxford University Press, Journal of the ICRU Volume 11, No. 1, 2011.
3. International Commission on Radiological Protection, The 2007 Recommendations of the International Commission on Radiological Protection, ICRP Publication 103, Annals of the ICRP 37 (2-4), 2007.
4. International Commission on Radiological Protection, Recommendations of the International Commission on Radiological Protection, ICRP Publication 26, Annals of the ICRP 1 (3), 1977.
5. International Commission on Radiological Protection, 1990 Recommendations of the International Commission on Radiological Protection, ICRP Publication 60, Annals of the ICRP, Pergamon Press; 21 (1-3), 1991.
6. Nuclear Energy Agency of the Organisation for Economic Co-operation and Development, Changes in Underlying Science and Protection Policy and their Impact on European and UK Domestic Regulation, Radiological Protection, ISBN 978-92-64-99153-8, 2011
7. John Harrison at al., *Use of effective dose*, 3rd International Symposium on the System of Radiological Protection, Seoul, October 2015, Accessed in August 2017 under http://journals.sagepub.com/doi/pdf/10.1177/0146645316634566.
8. European Commission, Council Directive 96/29/EURATOM of 13 May 1996 laying down basic safety standards for the protection of the health of workers and the general public against the dangers arising from ionising radiation. Official Journal of the European Communities L159, Vol. 39 (29 June 1996).
9. European Commission's Directorate-General: Environment, Nuclear Safety and Civil Protection, *Radiation Protection 88, Recommendations for the implementation of Title VII of the European Safety Standards Directive (BSS) concerning significant increase in exposure due to natural radiation sources,* 1997, accessed on https://ec.europa.eu/energy/sites/ener/files/documents/088_en.pdf in July 2017.
10. Joint Aviation Authorities Committee, Joint Aviation Requirements, JAR-OPS 1, Commercial Air Transport, Global Engineering Documents, 2007.
11. S. Thierfeldt, C. Haider, P. Hans, M. Kaleve, F. Neuenfeldt (eds), Evaluation of the implementation of radiation protection measures for aircrew. European Commission, Radiation Protection Issue No 156, ISBN 978-92-79-08409-6, 2009.
12. F. Drouet, M. Michelet, *Results of the EAN request on radiation protection of aircraft crew*, 2012, Accessed on http://eu-alara.net/index.php/surveys-mainmenu-53/36-ean-surveys/275-radiation-protection-of-aircraft-crew.html in July 2017.
13. International Commission on Radiological Protection, Radiological Protection from Cosmic Radiation in Aviation, ICRP Publication 132, Annals of the ICRP 45 (1), 1-48, 2016
14. International Commission on Radiation Units and Measurements, Radiation Quantities and Units, ICRU Report 33, Bethesda MD, 1980.
15. B. Rossi, Cosmic Rays, McGraw-Hill Paperbacks in Physics, McGraw-Hill Inc., Library of Congress Catalog Card Number 64-17570, 1964
16. V. F. Hess, *Über Beobachtungen der durchdringenden Strahlung bei sieben Freiballonfahrten*, Physik. Zeitschr. 13. Jahrgang (21|22) pp. 1084-1091, 1912. Accessed in August 2017 on http://physik.uibk.ac.at/hephy/Hess/homepage/Hess_paper01.html
17. V. F. Hess, *Über den Ursprung der durchdringenden Strahlung*. Physik. Zeitschr. 14, pp. 610-617, 1913. Accessed in August 2017 on http://physik.uibk.ac.at/hephy/Hess/homepage/Hess_paper02.html

18. R. A. Millikan, High Frequency Rays of Cosmic Origin, Proceedings of the National Academy of Sciences of the United States of America, Vol. 12, No. 1 pp. 48-55, 1926.

19. G. Federmann, Viktor Hess und die Entdeckung der Kosmischen Strahlung, Thesis at Institut für Radiumforschung und Kernphysik, Wien, Austria, 2003.

20. G. Reitz, Radiation Environment in the Stratosphere, Radiat. Prot. Dosim. 48(1) 5-20, 1993.

21. R. A. Mewaldt, *Cosmic Rays*, California Institute of Technology, Article accepted for publication in the Macmillan Encyclopedia of Physics in 1996, Accessed in August 2017 on http://www.srl.caltech.edu/personnel/dick/cos_encyc.html

22. M. J. Owens, R. J. Forsyth, *The heliospheric magnetic field*, Living Rev. Solar Phys., 10, (2013), 5, Accesses online in August 2017 on https://link.springer.com/content/pdf/10.12942%2Flrsp-2013-5.pdf

23. R. Rasinkangas, K. Kaila, T. Asikainen, *Oulu Space Physics Textbook*, University of Oulu, last updated in May 2009, Accessed online in August 2017 on https://wiki.oulu.fi/display/SpaceWiki/Oulu+Space+Physics+Textbook

24. NOAA's Space Environment Center, http://www.swpc.noaa.gov

25. Lokhead Martin Solar and Astrophysics Laboratory, http://www.lmsal.com/solarsoft/latest_events/

26. ESA Space Situational Awareness portal, http://swe.ssa.esa.int/

27. SILSO - Sunspot Index and Long-term Solar Observations, World Data Center - Sunspot Number and Long-term Solar Observations, Royal Observatory of Belgium, on-line Sunspot Number catalogue: http://sidc.be/silso/home

28. Space Weather Prediction Center (SWPC) of the National Oceanic and Atmospheric Administration (NOAA). *Solar flares* article, Accessed online in August 2017 on http://www.swpc.noaa.gov/phenomena/solar-flares-radio-blackouts

29. Space Weather Prediction Center (SWPC) of the National Oceanic and Atmospheric Administration (NOAA). *GOES X-ray flux*, Accessed online in August 2017 on http://www.swpc.noaa.gov/products/goes-x-ray-flux

30. National Oceanic and Atmospheric Administration, *NOAA Space Weather Scales*, Accessed online in August 2017 on http://www.swpc.noaa.gov/noaa-scales-explanation

31. National Oceanic and Atmospheric Administration (NOAA). *Coronal Mass Ejections*, Accessed online in August 2017 on http://www.swpc.noaa.gov/phenomena/coronal-mass-ejections and https://solarscience.msfc.nasa.gov/CMEs.shtml

32. United Nations. Sources and Effects of Ionizing Radiation. United Nations Scientific Committee on the Effects of Atomic Radiation, UNSCEAR 2000 Report to the General Assembly, with scientific annexes. No. E.00.IX.3 (Volume I: Sources, No. E.00.IX.4, Volume II: Effects), 1-1220. 2000. New York, United Nations sales publications.

33. W. Heinrich, S. Roesler and H. Schraube, Physics of Cosmic Radiation Fields, Radiat. Prot. Dosim. 86(4), 253-258 (1999).

34. National Oceanic and Atmospheric Administration (NOAA), *GOES Space Environment Monitor*, Accessed in August 2017 on https://www.ngdc.noaa.gov/stp/satellite/goes/index.html.

35. N. Fuller, *Neutron Monitors* - Article on Neutron Monitor Database portal, 2009, Accessed in August 2017 on http://www.nmdb.eu/?q=node/142

36. Neutron Monitor Database portal, http://www.nmdb.eu/

37. International Standard Organization, Dosimetry for exposures to cosmic radiation in civilian aircraft, Part 1: Conceptual basis for measurements, ISO 20785-1:2012

38. Oulu Cosmic Ray Station of the University of Oulu, *GLE Database*, http://gle.oulu.fi/, last accessed in August 2017.

39. H. V. Cane, Coronal Mass Ejections and Forbush Decreases, Space Science Reviews, July 2000, Volume 93, Issue 1–2, pp 55–77, 2012.

40. T. K. Gaisser, Cosmic Rays and Particle Physics, Cambridge, Cambridge University Press (1990).

41. Pierre Auger Observatory, https://www.auger.org/
42. Cherenkov Telescope Array, https://www.cta-observatory.org/
43. S. Katsuda, *Supernova of 1006 (G327.6+14.6)*, Chuo University, Tokyo, Japan, Accessed in August 2017 on https://arxiv.org/pdf/1702.02054.pdf
44. W. Schimmerling, *The Space Radiation Environment: An Introduction*, NASA, Article last accessed in August 2017 on https://three.jsc.nasa.gov/concepts/SpaceRadiationEnviron.pdf
45. M. Potgieter, Solar Modulation of Cosmic Radiation, Living Rev. Solar Phys., 10, (2013), 3.
46. J. F. Ziegler, Terrestrial Cosmic Rays, IBM J. Res. Develep. Vol 42, No. 1, 1998
47. R. A. Mewaldt, A. C. Cummings, and E. C. Stone, Anomalous cosmic rays: Interstellar interlopers in the heliosphere and magnetosphere, EOS, 75, Number 16, 1994
48. G. D. Badhwar, The Radiation Environment in Low-Earth Orbit, Radiation Research, 148, 3-10, 1997.
49. W. Heinrich, Variation of Galactic Cosmic Radiation by Solar Modulation, Geomagnetic Shielding and Shielding by Material, Terrestrial Space Radiation and its Biological Effects. Plenum Publishing Corporation,1988.
50. S. Hayakawa, Cosmic Ray Physics: Nuclear and Astrophysical Aspects, New York: Wiley and Sons, 1969.
51. M. A. Shea, D. F. Smart, World grid of cosmic ray vertical cutoff rigidities for Epoch 1990, In Proceedings from 25th Int. Cosmic Ray Conference, Durban, South Africa, pp. 401-404, 1997.
52. Strahlenschutzkommission, Die Ermittlung der durch kosmische Strahlung verursachten Strahlenbelastung des fliegenden Personals, Report. Stellungnahme der Deutschen Strahlenschutzkommission, 1997. Gustav Fischer Verlag 1A, 12, 1998.
53. P. Carlson, and A. A. Watson, Erich Regener and the ionisation maximum of the atmosphere, Hist. Geo Space Sci., 5, 175–182, 2014, doi:10.5194/hgss-5-175-2014
54. P. Beck, P. Ambrosi, U. Schrewe, K. O'Brien, ACREM, Aircrew Radiation Exposure Monitoring, OEFZS Report, OEFZS-G-0008, 1999
55. P. Beck, D. Bartlett, K. O'Brien, U. Schrewe, In-flight Validation and Routine Measurements, Radiation Protection Dosimetry, Vol 83, p.303-308, 1999.
56. D. Pantel, Y. Gonzalez, M. Gredion, F. Wrobel, J.-R. Vaille , F. Saigne, Radiation Measurements in Stratosphere, Proceedings of 20th ESA Symposium on European Rocket and Balloon Programmes and Related Research, Heyre, France, 2011.
57. A. J. Walker, Principles of experimental microdosimetry, Radiat. Prot. Dosim. Vol. 61 Nr. 4, pp 297-308, 1995
58. International Commission on Radiation Units and Measurements, Quantities and Units in Radiation Protection Dosimetry, ICRU Report 51, Bethesda MD, 1993
59. H. H. Rossi, and M. Zaider, Microdosimetry and its Applications, Springer, Berlin (1994)
60. Far West Techn. Inc., Environmental radiation monitor with 5 inches tissue equivalent proportional counter, Operations and repair manual, Goleta, USA, December 2000.
61. ARC Seibersdorf research GmbH, Technischer Bericht Nr. EMV-E 30/02 über Emissionmessungen entsprechend RTCA-DO-160D, Section 21, ARC Seibersdorf research GmbH, 2002
62. International Organization for Standardization, ISO 4037-3:1999 X and gamma reference radiation for calibrating dosemeters and doserate meters and for determining their response as a function of photon energy—Part 3: Calibration of area and personal dosemeters and the measurement of their response as a function of energy and angle of incidence, 1999.
63. M. Autischer, P. Beck, S. Rollet, A. Ferrari, Comparing simulation and measuremets results of angular TEPC responce in standard radaition fields, Proceedings of The Monte Carlo

Method: Versatility Unbounded In A Dynamic Computing World, Chattanooga, Tennessee, April 17–21, 2005, on CD-ROM, American Nuclear Society, LaGrange Park, IL (2005)

64. M. Autischer, P. Beck, P. Kindl, M. Latocha, and S. Rollet, Calibration and background measurements with tissue equivalent proportional counter, Radiation Protection Dosimetry (2006), 1 of 4, doi:10.1093/rpd/ncl557.

65. S. Röttger, R. Böttger, F.D. Brooks, A. Buffler, J.-P. Meulders, R. Nolte, F.D. Smit, F. Wissmann, The PTB Neutron Reference Fields (PIAF) - Quasi-Monoenergetic Neutron Reference Fields in the Energy Range from Thermal to 200 MeV, Proceedings of the 4th international workshop on nuclear fission and fission-product spectroscopy, October 2009, Cadarache, France, AIP Conf. Proc. 1175, pp. 375-381, 2009

66. International Organization for Standardization, Guide to the Expression of Uncertainty in Measurement (GUM). ISO/IEC Guide 98 Part 3 (International Organization for Standardization, Geneva), 1995

67. M. Autischer, M. Latocha, P. Beck, Kaliebriermessungen mit dem TEPC, ARC Report, 2003

68. M. Autischer, Simulation von Kosmischer Strahlung und Vergleich mit experimentellen Ergebnissen, Dissertation at TU Graz, Austria, 2010

69. A. Mitaroff and M. Silari, The CERN-EU High-Energy Reference Field (CERF) Facility for Dosimetry at Commercial Flight Altitudes and in Space, Rad. Prot. Dosim., 102, No. 1., 7-22 (2002).

70. S. Rollet, M. Autischer, P. Beck, M. Latocha, Measurement and simulation of lineal energy distribution at the CERN high energy facility with a tissue equivalent proportional counter, Radiation Protection Dosimetry, Vol. 125, No 1-4, pp. 425-428, 2007

71. M. Latocha, M. Autischer, P. Bekc, J.F. Bottolier-Depois, S. Rollet and F. Trompier, The results of cosmic in-flight TEPC measurements during the CAATER flight campaign and comparison with simulations, Radiation Protection Dosimetry, Vol. 125, No. 1–4, pp. 412–415, 2007

72. P. Beck, M. Latocha, S. Rollet, G. Stehno, TEPC reference measurements at aircraft altitudes during a solar storm, Advances in Space Research, Vol. 36, No. 9, pp 1627–1633, 2005

73. DOSMAX project (Dosimetry of Air Crew Exposure during Solar Maximum) EC FP6 Euratom Programme, 2000-2004, Contract N° FIGM-CT-2000-00068

74. J.E Kyllönen, L. Lindborg and G. Samuelson, Cosmic radiation measurements on-board aircaft with the variance method, Radiation Protection Dosimetry, Vol. 93, No. 3, pp. 197–205 (2001)

75. Lillhök, J., Beck, P., Bottollier-Depois, J.F., Latocha, M., Lindborg, L., Roos, H., Roth, J., Schraube, H., Spurny, F., Stehno, G., Trompier, F., Wissmann, F.; A comparison of ambient dose equivalent meters and dose calculations at constant flight conditions, Radiation Measurements, Vol. 42, No 3, pp. 323–333, 2007

76. L. Lindborg, P. Beck, J. F. Bottolier-Depois, M. Latocha, J. Lillhök, S. Rollet, H. Roos, J. Roth, H. Schraube, F. Spurny, G. Stehno, F. Trompier, F. Wissmann, Determinations of H*(10) and its dose components onboard aircraft, Radiation Protection Dosimetry, Vol. 126, No 1-4, pp. 577-580, 2007

77. Lindborg, L., Bartlett, D., Beck, P., McAulay, I. R., Schnuer, K., Schraube, H. and Spurny, F. (eds), Cosmic radiation exposure of aircraft crew - Compilation of measured and calculated data. European Commission, Radiation Protection Issue No 140 (ISBN 92-894-8448-9), 2004.

78. Schrewe, U.J., ACREM Air Crew Radiation Exposure Monitoring Results from the in-flight measurement program of the PTB: Summary of the Radiation Monitoring Data. PTB Laboratorbericht PTB-6.31-99-1, Braunschweig, (1999)

79. P. Beck, P. Ambrosi, U. Schrewe, K. O'Brien, ACREM, Aircraft Radiation Exposure Monitoring, Final Report of EC contract F14P-CT960047, ARCS Report G-0008, 1999

80. M. Latocha, P. Beck, and S. Rollet, Cosmic Radiation Exposure at Aircraft Crew Workplaces. Proceedings of the Second European IRPA Congress on Radiation Protection, 15-19 May 2006 Paris, France, 15-5-0006. Accessible online at IAEA website: http://www.iaea.org/inis/collection/NCLCollectionStore/_Public/39/016/39016818.pdf

81. P. Beck, C. Dyer, N. Fuller, A. Hands, M. Latocha, S. Rollet, F. Spurný, Overview of on-board measurements during solar storm periods, Radiat. Prot. Dosim. Vol. 136, No. 4, pp. 297–303, 2009.

82. S. Agostinelli, et al., Geant4 – a simulation toolkit. Nuclear Instruments and Methods in Physics Research A, Vol 506, Issue 3, 2003, p. 250-303.

83. J. Allison et al. Geant4 developments and applications., IEEE TNS, Vol 53, Issue 1 part 2, 2006, p. 270-278.

84. L. Desorhger, Planetocosmics Software User Manual, 2005, http://cosray.unibe.ch/~laurent/planetocosmics/

85. Private communication with L. Desorhger, 2011

86. J. M. Picone A. E. Hedin, D. P. Drob, and A. C. Aikin, NRLMSISE-00 empirical model of the atmosphere: Statistical comparisons and scientific issues, J. Geophys. Res., 107, A12, 1468, doi:10.1029/2002JA009430, 2002.

87. Hedin A. E., Extension of the MSIS thermosphere model into the middle and lower atmosphere, J. Geophys. Res., 96, A2, p. 1159-1172, 1991.

88. Gleeson, L. J. and W. I. Axford, Solar Modulation of Galactic Cosmic Rays, Astrophys. J., 154, 1011, 1968.

89. Garcia-Munoz, M., G. M. Mason, and J.A. Simpson, The Annomalous 4He component in the Cosmic Ray Spectra of 50 MeV per Z nucleon during 1972-1974, Astrophys. J., 202, 265, 1975.

90. Usoskin et al., Heliospheric modulation of cosmic rays: Monthly reconstruction for 1951-2004, J. Geophys. Res., 110, A12108, 2005.

91. Dyer, C. S., et al. Calculations and observations of solar particle enhancements to the radiation environment at aircraft altitudes. Adv. Space Res. 32, 81–93 (2003).

92. Clucas, S. N., et al. The radiation in the atmosphere during major solar particle events. Adv. Space Res. 36, 1657–1664 (2005).

93. M. Pelliccioni, Overview of Fluence-to-Effective Dose and Fluence-to-Ambient Dose Equivalent Conversion Coefficients for High Energy Radiation Calculated Using FLUKA Code, Radiat. Prot. Dosim.88 (4)279-297 (2000).

94. P. Beck, M. Latocha, S. Rollet, SOLARDOS – Endbericht: Dosisabschätzung der Strahlenbelastung des fliegenden Personals verursacht durch Solar Events. AIT Report AIT-HNA-0008, ISSN 0253-527, 2009.

95. NASA, NASA Aircraft and operating problems, Vol.1 Proceedings of a conference held at Langley Research Center, Hampton, Virginia, 4-6 May 1971.

96. Fassò, A., Ferrari, A., Ranft, J., and Sala, P.R., FLUKA: a multi-particle transport code, CERN-2005-10 (2005), INFN/TC_05/11, SLAC-R-773.

97. Battistoni, G., et al., Proceedings of the Hadronic Shower Simulation Workshop 2006, Fermilab 6-8 September 2006, M. Albrow, R. Raja eds., AIP Conference Proceeding 896, 31-49, (2007).

98. Gaisser, T. K., et al., Primary Spectrum to 1 TeV and Beyond, Proceedings of the 27th International Cosmic Ray Conference (ICRC 2001), Hamburg, Germany, 643–646, 7–15 August 2001.

99. Battistoni, G., Ferrari, A. and Muraro, S., Primary Cosmic Rays Fluxes in FLUKA, INFN Report (DOSMAX Work Contract N. 451004269), (2004).

100. ICRU, 2010. Reference Data for the Validation of Doses from Cosmic-Radiation Exposure of Aircraft Crew. ICRU Report 84 (prepared jointly with ICRP). Journal of the ICRU 10 (2), 2010

101. Latocha, M., Beck, P., Rollet, S.; AVIDOS—a software package for European accredited aviation dosimetry, Radiation Protection Dosimetry, Vol. 136, No 4, pp. 286-290, 2009

102. Beck, P., et al., Measurements and simulations of the radiation exposure to aircraft crew workplaces due to cosmic radiation in the atmosphere, Radiat. Prot. Dosim. 126(1-4), 564-567 (2007)

103. Ferrari, A., Pelliccioni, M., and Rancati, T., Calculation of the radiation environment caused by galactic cosmic rays for determining aircrew exposure, Radiat. Prot. Dosim. 93(2), 101-114 (2001).

104. T. Sato, et. al, Fluence-to-dose conversion coefficients for neutrons and protons calculated using the PHITS code and ICRP/ICRU adult reference computational phantoms, Phys. Med. Biol. 54 (2009) 1997–2014, doi:10.1088/0031-9155/54/7/009.

105. G. Dietze, Implications of the new ICRP recommendations for aircrew dosimetry, Radiat. Prot. Dosim. 136(4), 240-243, 2009.

106. F. Clette, et al., Revisiting the Sunspot Number. A 400-Year Perspective on the Solar Cycle, Space Sci Rev, Vol. 186, Issue 1-4, pp. 35-103, 2014

107. T. Podladchikova, et al., Filter Technique for Improving Medium-Term Predictions of the Sunspot Number. Solar Physics, 2012, doi: 10.1007/s11207-011-9899-y

108. M. Latocha and P. Beck, Cosmic Radiation Assessment at ESA's Space Weather Portal with AVIDOS, Proceedings in TNS IEEE of RADECS 2016 conference, Bremen, Germany.

109. J.F. Bottollier-Depois, P. Beck, M. Latocha, V. Mares, D. Matthiä, W. Rühm, F. Wissmann (editors), EURADOS report, *Comparison of Codes Assessing Radiation Exposure of Aircraft Crew due to Galactic Cosmic Radiation*, Braunschweig, May 2012, ISBN 978-3-943701-02-9, also reprinted as EC Radiation Protection Nr 173, *Comparison of Codes Assessing Radiation Exposure of Aircraft Crew due to Galactic Cosmic Radiation,* ISBN 978-92-79-27036-9, Luxembourg: Publications Office of the European Union, 2012

110. Roesler, S., Journal of the ICRU, ICRU Report 84, reference data for the validation of doses from cosmi-radiation exposure of aircraft crew, Book review, doi:10.1093/rpd/ncr110, Radiat. Prot. Dosim., Published online on 11 May, 2011

111. H. Schuhmacher, and E. Fantuzzi, A co-ordinated network for radiation dosimetry (CONRAD): an overview. Radiat. Prot. Dosimetry vol. 131 (1) pp. 3–6, 2008

112. P. Beck, et al., Validation of modelling the radiation exposure due to solar particle events at aircraft altitudes. Radiat. Prot. Dosimetry vol. 131 (1), pp. 51–58, 2008

113. C. Plainaki et. al, Modeling of the GLE70 event, Proceedings of Solar Extreme Events 2007: Fundamental Science and Applied Aspects (Sept. 2007), Athens, Greece.

114. C. Plainaki et. al, Application of the NM-BANGLE model to GLE70, Proceedings of the 30th International Cosmic Ray Conference, 2007, Mexico

115. R. Bütikofer, E. O. Flückiger, L. Desorgher, and M. R. Moser: Analysis of the GLE on January 20, 2005: An update, Proc. 20th Europ. Cosmic Ray Symp., Lisbon, Portugal, 2006.

116. R. Bütikofer, E. O. Flückiger, Radiation doses along selected flight profiles during two extreme solar cosmic ray events; 2011, Astrophys. Space Sci. Trans., 7, 105–109, 2011

117. A. M. Shea, F. D. Smart, M. D. Wilson, and C. L. Gentile, Solar Cosmic Rays on 29 September 1989; An Analysis using the World-Wide Network of Cosmic Ray Stations. Proc. 22nd Intern. Cosmic Ray Conf., Dublin, Ireland, 11–23 August 1991, 3, 97–100, 1991.

118. J. L. Cramp et. al, The October 22, 1989, solar cosmic ray enhancement: An analysis of the anisotropy and spectral characteristics, Journal of Geophysical Research (1997) Vol. 102, No. A11.

119. R. Bütikofer, E. O. Flückiger, Y. Balabin, A. Belov: The reliability of GLE analysis based on neutron monitor data – a critical review; Presented at 33rd ICRC, Rio de Janeiro, 2-9 July 2013, and private communication 2016.

120. A. L. Mishev et. al Neutron monitor yield function: New improved computations, Journal of Geophysical Research (Space Physics), 118, 2783-2788, 2013

121. P. H. Stoker, Spectra of solar proton ground level events using neutron monitor and neutron moderated detector recordings, Proc. of ICRC 4,114S, 1985.

122. E. V. Vashenyuk, et. al, Some features of the sources of relativistic particles at the Sun in the solar cycles 21–23, Advances in Space Research 38 (2006) 411–417.

123. C. Plainaki et. al. Neutron monitor asymptotic directions of viewing during the event of 13 December 2006, Advances in Space Research 43 (2009) 518–522.

124. M. A. Shea and D. F. Smart, Possible evidence for a rigidity-dependent release of relativistic protons from the solar corona, Space Science Reviews, vol. 32, no. 1-2, 1982, p. 251-271.

125. D. J. Bombardieri et. al, Relativistic proton production during 2000 July 14 solar event: the case for multiple source mechanism, The Astrophysical Journal, 644:565–574, 2006

126. J. L. Lovell, M. L. Duldig, and J. E. Humble, An extended analysis of the September 1989 cosmic ray ground level enhancement Journal of Geophysical Research (Space Physics), 103, A10, 23733–23742, 1998.

127. E. Flückiger, M. Moser, B. Pirard, R. Bütikofer and L. Desorgher, A parameterized neutron monitor yield function for space weather applications, Proceedings of ICRC 2007, Mexico

128. M. Latocha, P. Beck, R. Bütikofer, and H. Thommesesn, AVIDOS 2.0 - Current developments for the assessment of radiation exposure at aircraft altitudes caused by solar cosmic radiation exposure, Oral presentation at 11th European Space Weather Week, Liege, Belgium, 2014

129. M. Latocha, Nowcast of Radiation Exposure at Aviation Altitudes with AVIDOS, Presentation during SEPRAD Workshop, http://www.seprad.eu, Seibersdorf, Sept. 2017, Book of Abstracts: ISBN 978-3-902780-09-6.

130. United Nations Scientific Committee on the Effects of Atomic Radiation, UNSCEAR 2008 Report to the General Assembly, with scientific annexes, Vol I: Sources, New York, 2010

131. ANEMOS, Real time GLE Alert System, A federated product from the Athens Neutron Monitor Station with ESA SSA Space Weather Portal, http://swe.ssa.esa.int/web/guest/anemos-federated

132. National Oceanic And Atmospheric Administration, Space Weather Prediction Center, Noaa Space Weather Scales, http://www.swpc.noaa.gov/noaa-scales-explanation

133. Austrian Government, Strahlenschutzverordnung fliegendes Personal FlP-StrSchV, Bundesgesetzblatt II, Nr. 235/2006.

134. ICAO, International Civil Aviation Organization https://www.icao.int/, Last accessed in September 2017.

135. Seibersdorf Laboratories, FDS-PV-0500 Erfassung der Strahlenbelastung in Flugzeugen (Revision 3, 2017)

136. European Commission, Council Directive 2013/59/EURATOM of 5 December 2013 laying down basic safety standards for the protection against the dangers arising from exposure to ionising radiation, and repealing Directives 89/618/Euratom, 90/641/Euratom, 96/29/Euratom, 97/43/Euratom and 2003/122/Euratom. OJ L 13, 17.1.2014, p. 1.

12. Appendix A – Microdosimetric distributions and their graphical representation

In this appendix, several technical aspects of microdosimetric distributions are presented.

12.1. Microdosimetric distributions

In microdosimetry, results are expressed as probability distributions of energy depositions in a volume that is crossed by a single ionizing particle.

The stochastic analog of the dosimetric quantity absorbed dose *D*

$$D = \frac{\mathrm{d}\bar{\varepsilon}}{\mathrm{d}m}$$

in a volume *V* surrounding the point where the absorbed dose is considered is the specific energy, *z*

$$z = \frac{\varepsilon}{\rho V} = \frac{\varepsilon}{m}$$

The specific energy, *z,* is a stochastic quantity. Its values occur randomly in the considered volume, however, the probability of any particular value of *z* is determined by its probability distribution function, *F(z)*. The value of *F(z)* is the probability, that specific energy is equal to or less than *z*. The derivative of *F(z)*:

$$f(z) = \frac{dF(z)}{dz}$$

is the probability density, *f(z)*. Probability, that specific energy produced by an event is in the range [*z, z+dz*] is then *f(z)dz*.

The expectation value of *f(z)* is the first moment of *f(z)*.It is called ***mean specific energy***, $\bar{z}$ and is non-stochastic quantity.

$$\bar{z} = \int_0^\infty z f(z) dz$$

The mean specific energy $\bar{z}$ in a site is equal to the absorbed dose *D* when the site is uniform and is exposed to a uniform radiation field. Otherwise, the mean specific

energy is equal to the average absorbed dose in the site: $\bar{z} = \bar{D}$. Under non-uniform conditions absorbed dose must be give as

$$D = \lim_{m \to 0} \bar{z}$$

Unlike to the lineal energy that by definition is produced by a single energy deposition event, the specific energy may be due to one or more energy deposition events. It is useful to consider situation when only one track overlaps some of the target volumes - one (and only one) event occurs. In this situation, the distribution function of the specific energy deposited in a single event, $F_1(z)$, is the probability that a specific energy less than or equal to z is deposited under condition that one (and only one) event occurred. The derivative of $F_1(z)$ is the probability density, $f_1(z)$:

$$f_1(z) = \frac{dF_1(z)}{dz}$$

and is called ***single-event frequency distribution of specific energy***. Probability that specific energy produced by single event is in the interval dz centered at z is then $f_1(z)dz$. The first moment of $f_1(z)$ is the expectation value of $f_1(z)$. It is denoted as $\bar{z}_F$, and called ***frequency-mean specific energy per event***:

$$\bar{z}_F = \frac{\int_0^\infty z f_1(z) dz}{\int_0^\infty f_1(z) dz}$$

The denominator in the above equation is a normalization factor. By convention $f_1(z)$ is normalized to one event and denominator is equal to unity.

It is also useful to consider dose distribution of z per energy deposition event. Let $D_1(z)$ be the fraction of absorbed dose, D, per event and delivered by energy deposition events having specific energy less or equal to z. Similarly to $f_1(z)$, one can define $d_1(z)$ as derivative of $D_1(z)$

$$d_1(z) = \frac{dD_1(z)}{dz}$$

It is the dose probability density called ***single-event dose distribution of specific energy***. Probability that a fraction of absorbed dose will be transferred to the targets with the specific energy in the range [z, $z+dz$] is then $d_1(z)dz$. First moment of $d_1(z)$ is

the expectation value of $d_1(z)$ called ***dose-mean specific energy per event*** and denoted as $\bar{z}_D$.

$$\bar{z}_D = \frac{\int_0^\infty z d_1(z) dz}{\int_0^\infty d_1(z) dz}$$

The denominator in the above equation is again normalization factor. Dose-mean specific energy is a non-stochastic quantity.

The relation between single-event frequency distribution of z, $f_1(z)$, and single-event dose distribution of z, $d_1(z)$ is:

$$d_1(z) = \frac{z}{\bar{z}_F} f_1(z)$$

The relation between frequency-mean specific energy per event, $\bar{z}_F$, and dose-mean specific energy per event, $\bar{z}_D$, is

$$\bar{z}_D = \frac{1}{\bar{z}_F} \int_0^\infty z^2 f_1(z) dz$$

Analogously to specific energy, similar quantities can be defined for lineal energy:

- $f(y)$ – frequency distribution of lineal energy,
- $\bar{y}_F$ - frequency-mean lineal energy,
- $d(y)$ – dose distribution of lineal energy,
- $\bar{y}_D$ - dose-mean lineal energy.

The relations between $f(y)$ and $d(y)$, and between $\bar{y}_F$ and $\bar{y}_D$ are analogous to relations for specific energy.

12.2. Graphical presentations of microdosimetric distributions

For better understanding of microdosimetric distributions, their graphical representations are very helpful. Microdosimetric distributions can be presented either

as a function of imparted energy, ε, or specific energy, *z*, or as a function of lineal energy, *y*. Microdosimetric distributions presented as a function of *z* or ε are rare. In experimental practice, microdosimetric distributions are typically presented as a function of lineal energy, *y*, especially when one is interested in radiation quality or radiations. This way of presentations is also recommended by ICRU [1].

In microdosimetry, it is very characteristic that lineal energy, *y*, spans over even several orders of magnitude, therefore a certain way of representation must be employed. A simple linear representation *f(y) vs. y* is very rarely used because in most cases it does not allow to appreciate all aspects of the distribution. Better representation would be a spectrum displayed on double logarithmic scale but it does not allow to directly estimating from the plot the fraction of events that have lineal energy values in a certain range of interest. The best representation is *yf(y) vs. log(y)*. The mathematical explanation for this way of presentation is based on a fact that:

$$\int_{y_1}^{y_2} f(y)\,dy = \int_{y_1}^{y_2} [yf(y)]\,d(\log y)$$

With this representation, the area enclosed between any two values of *y* is proportional to the number of events that have lineal energy in the delimited range of *y*.

The problem of graphical representation of microdosimetric distribution in practice calls for correct redistribution of events on a logarithmic scale of *y* and correct normalization. Redistribution of events can be achieved by a division of logarithmic scale into B increments per decade in such a way that the nth value of *y* is given by

$$y_n = y_0 10^{n/B}$$

where y_0 is the lowest considered value of *y*. The logarithmic increment of *y* is then given by

$$\Delta(\log y) = \frac{1}{B}$$

The number B of increments per decade should be large enough, that the difference between $d(\log y)$ and $\Delta(\log y)$ can be neglected. Usually B is set between 10 and 50.

Normalization uses the fact that the probability density, *f(y)*, is by definition normalized to one energy deposition event. This should stay unchanged regardless the type of the scale of *y*.

$$\int_0^\infty f(y)dy = 1$$

In order to correctly normalize a spectrum on a logarithmic scale one needs to apply mathematical relation between the linear, natural logarithmic and base-10 logarithmic differentials given by equation:

$$f(y)dy = yf(y)d(\ln y) = (\ln 10)yf(y)d(\log y)$$

Then, replace integration over $d(\log y)$ differentials with the sum of $\Delta(\log y)$, which is 1/B, as described above, therefore obtaining the correct normalization formula:

$$\int_0^\infty yf(y)d(\ln y) \approx \frac{\ln 10}{B}\sum_{i=0}^{\infty} y_i\, f(y_i) = 1$$

In a numerical normalization, the discussed problem is much simpler. One needs to apply *n*-th intervals of lineal energy y_n into normalized probability density and define $y_{i+1/2}$ as geometrical mean of $y_{i+1} - y_i$ interval, and similarly $y_{i-1/2}$ as geometrical mean of interval $y_i - y_{i-1}$ in order to obtain the formula:

$$\int_0^\infty f(y)d(y) \approx \sum_{i=0}^{\infty} f(y_i)\left(y_{i+1/2} - y_{i-1/2}\right) = \left(10^{B/2} - 10^{-B/2}\right)\sum_{i=0}^{\infty} y_i\, f(y_i) = 1$$

In the case of dose distribution, ***d(y)***, a characteristics providing qualitatively the same information as for frequency distribution, would be ***y²f(y) vs log(y)***. The normalization procedure of the dose distribution is the same as it is for frequency distribution. For the normalized dose distribution, the area between any two values of *y* gives the fraction of absorbed dose transferred to the matter in the selected range of *y*. This way of presentation of a microdosimetric spectrum is the standard one (Figure 88).

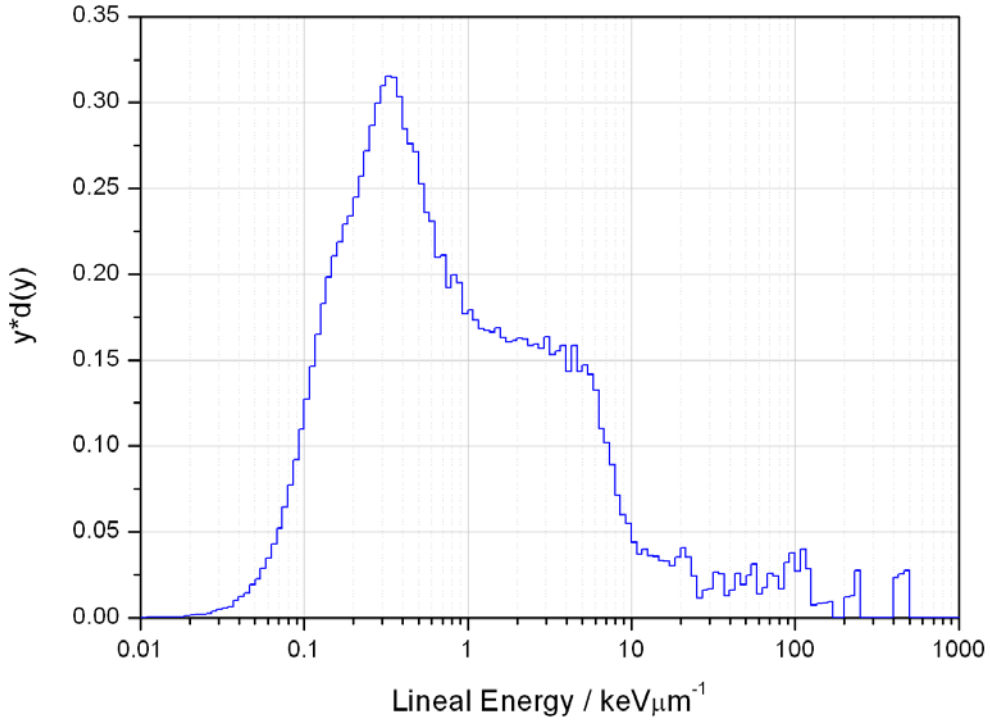

Figure 88 Normalized microdosimetric spectrum of cosmic radiation measured with TEPC over Rome at 9.8 km of altitude on 6th of May 2003.

13. Appendix B – AVIDOS 2.0 online

In this appendix, several technical aspects of AVIDOS 2.0 software are presented.

AVIDOS 2.0 can be accessed only after registration to the ESA SSA SWE portal.

Models described above in Chapters 6.1 and 6.3 were implemented by author in a computer program AVIDOS 2.0. Program AVIDOS 2.0 is provided to public as a web service of the Seibersdorf Laboratories federated with ESA's Space Situational Awareness Space Weather portal (SSA SWE). It serves as informational and educational online software for the assessment of cosmic radiation exposure at flight altitudes. It is freely accessible – only a free of charge registration at ESA SSA SWE portal is required. The user interface of AVIDOS 2.0 is designed in such a way, that it can be used by everyone, from a public person, through aircraft crew, up to experts and scientists.

13.1. Online access to AVIDOS 2.0

AVIDOS 2.0 is accessible only via ESA SSA SWE portal. ESA portal requires a user registration. Registration is free of charge and is open to everyone: public members and professionals. In order to access full AVIDOS 2.0 functionality one has to register as professional user (e.g. scientist). AVIDOS 2.0 distinguishes public users and professional users. Science mode is accessible only to professional users. In addition, one has to request access to "Service to Airlines NSO/air" in the Non Space System Operation section. The procedure of registration is described under the link: http://swe.ssa.esa.int/web/guest/request-for-registration (Figure 89). In case of problems user can get help from ESA's SSA Space Weather Coordination Centre helpdesk (SSCC, http://swe.ssa.esa.int/contact, helpdesk.swe@ssa.esa.int). If after registration access to "science mode" is denied, one shall ask SSCC helpdesk to change user profile from regular one into professional.

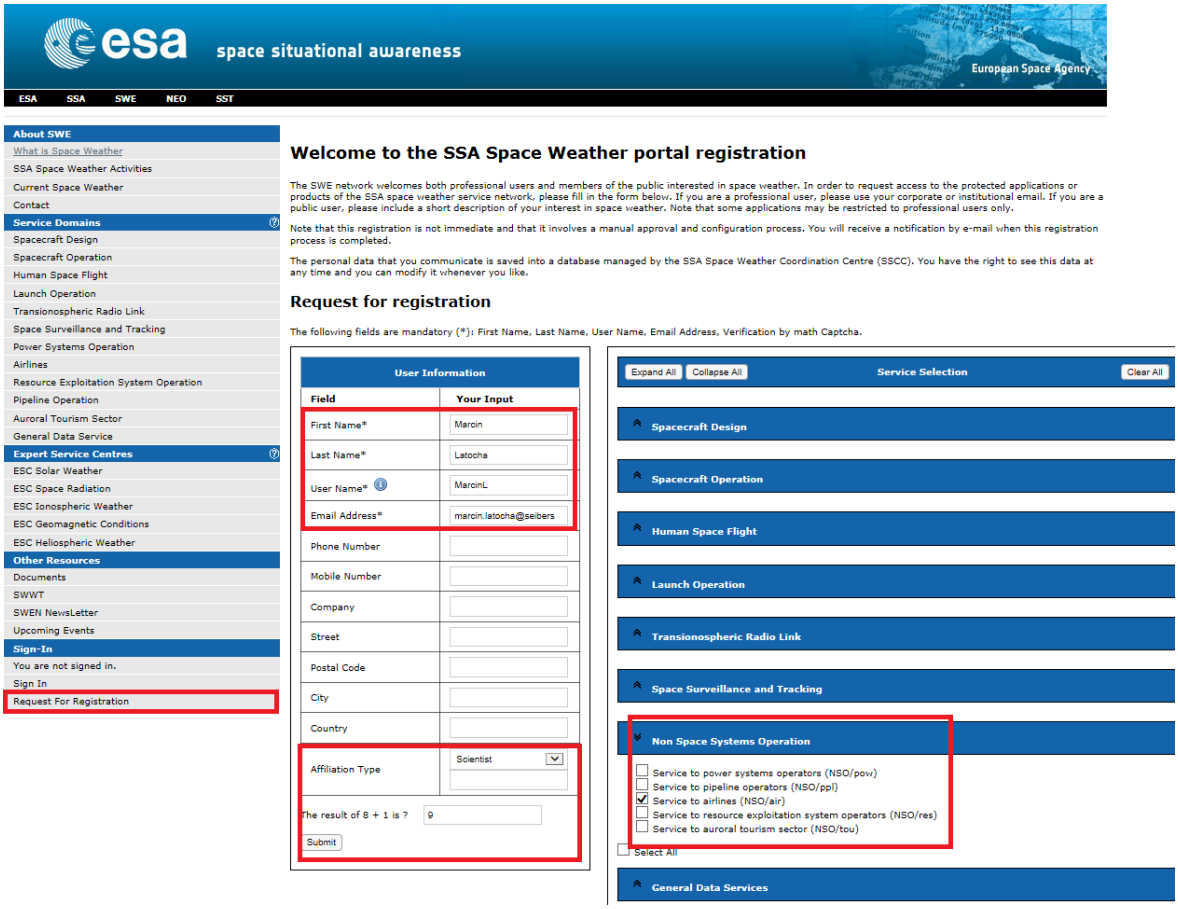

Figure 89 User registration on the ESA SSA SWE portal. Mandatory fields are marked with red boxes. (source http://swe.ssa.esa.int/web/guest/request-for-registration)

After registration, AVIDOS 2.0 can be accessed via Service Domain “Airlines” (Figure 90), or via Expert Service Center Space Radiation (Figure 91), or directly under the link: http://swe.ssa.esa.int/web/guest/avidos-federated

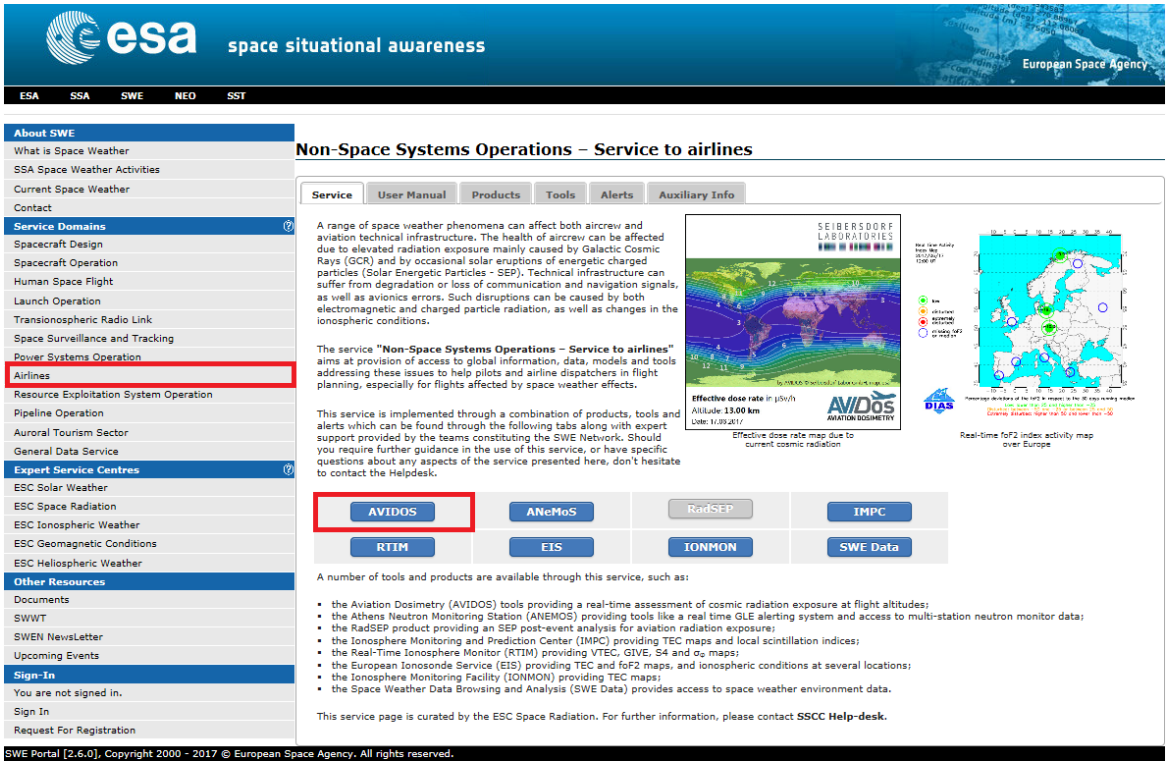

Figure 90 Accessing AVIDOS 2.0 via Service Domain “Airlines”. (From: http://swe.ssa.esa.int/nso_air)

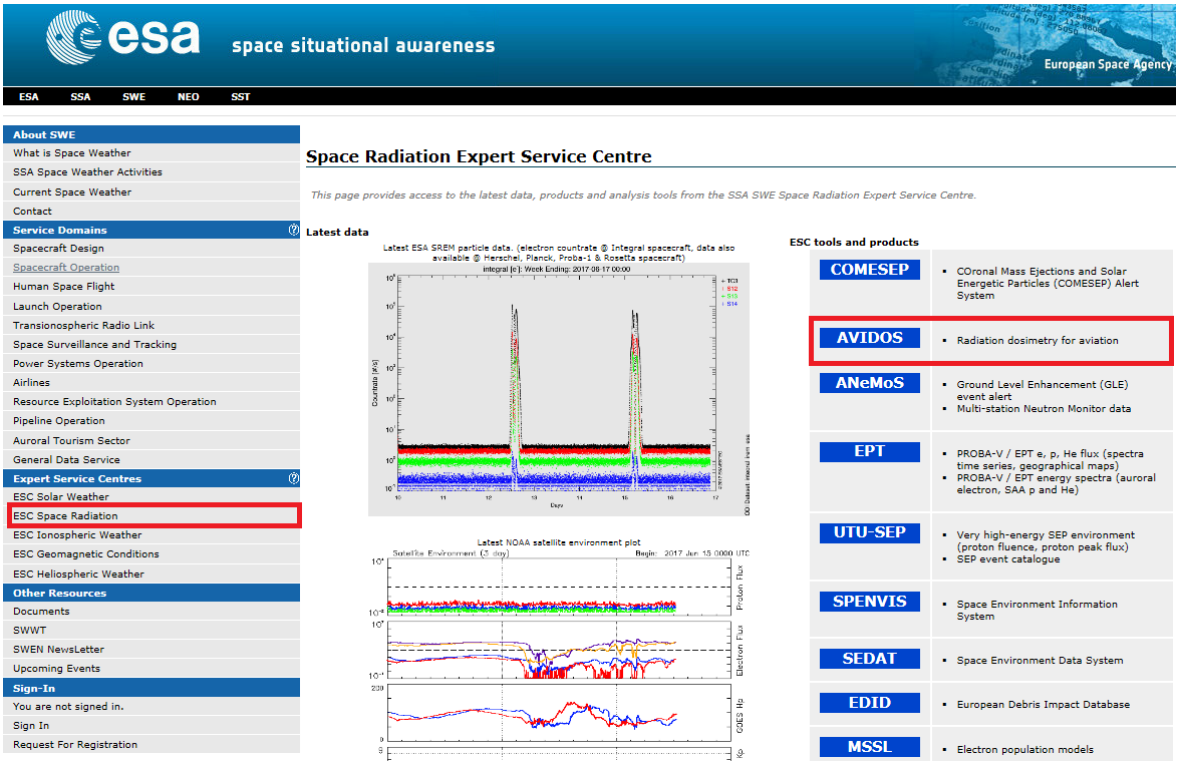

Figure 91 Accessing AVIDOS 2.0 via Space Radiation Expert Service Center (source : http://swe.ssa.esa.int/space-radiation)

13.2. Running AVIDOS 2.0 on a PC

First version of AVIDOS 2.0 has been available online in 2012 and its Graphical User Interface has been written in Java programming language using Java Plug-in technology. Therefore, to run AVIDOS 2.0, the user must have installed Java Runtime Environment (http://java.sun.com) with Java Plug-in on her/his PC. Nowadays, most web browsers do not support Java plug-in anymore (Figure 92), and user must use Internet Explorer web browser uder Windows operating system (up to Windows 7, Windows 10 is excluded). This is certain disadvantage for users, and author is currently taking best effort to change programming technology in order to overcome these restrictions. A new version of AVIDOS with new Graphical User Interface is expected with the end of 2017.

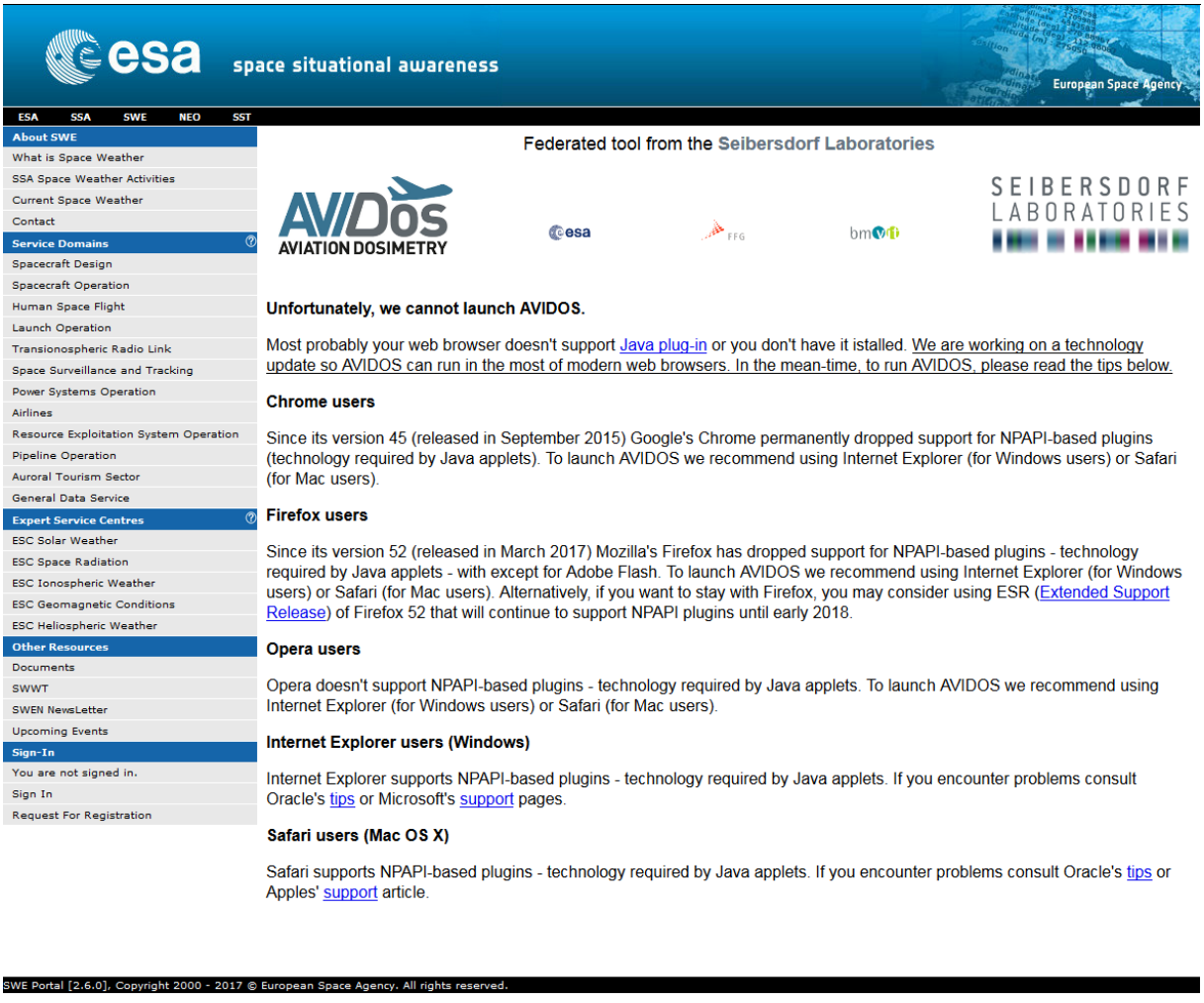

Figure 92 Technical tips to run AVIDOS 2.0 on a PC (Java Runtime Environment http://java.sun.com is necessary, Windows operating system and Internet Explorer web browser are recommended.)

13.3. AVIDOS 2.0 - user interface

When started, AVIDOS 2.0 displays its welcome screen (Figure 93). The welcome screen is divided in three parts. World map with current effective dose rates at FL350 (≈10.67 km) due to GCR is in the center, a set of control buttons and alert icon displaying current status of a GLE alert are on the right. GLE alert is reproduced after GLE alerting service available via ESA portal. The lower part of the welcome screen allows for accessing different user-modes.

Language of the user interface can be changed at any time. FAQ is structured in few chapters. It introduces the program, offers user manual, provides basic information on cosmic radiation and gives few references to scientific publications. Contact button displays contact details to the developers. Feedback questionnaire (displayed in a separate tab of the web browser) allows users to express their impressions and comments on the software. Disclaimer informs, that this version of AVIDOS cannot be used for radiation protection purposes (see Chapter 6.4). In acknowledgments author expresses recognition to external organizations for using their data/resources.

Figure 93 Welcome screen of AVIDOS 2.0 as appearing on the ESA Space Situational Awareness Space Weather portal (Source: http://swe.ssa.esa.int/web/guest/avidos-federated)

13.3.1. Public mode

The less complex is “public mode” (Figure 94). It is designed for a user that demands quick assessment of cosmic radiation exposure for a selected flight without considering all technicalities. To perform calculations in public mode, only the minimum set of information is required: date and time of the flight, departure, and destination. Other flight parameters are, for the sake of simplicity, fixed and hidden. Altitude is set constant at FL350 (≈10.67 km), flight route is always along Great Circle, and flight duration is calculated with specially developed algorithm. For this, a large set of real flights was analyzed. Flight duration is calculated based on the distance between departure and destination and selected cruising altitude.

Results of calculations are displayed in form of a table. The table shows the date and time of the flight, selected departure and destination, assessed effective dose, and information whether the flight occurred during a GLE event. For the flight selected in the output table, assessed effective dose is displayed graphically on the dial and on the “time-bar”. The maximum value on the dial corresponds to 2.4 mSv – a worldwide average of annual natural background radiation dose [130]. The “time-bar” shows amount of days that must be spent on the ground to obtain the same dose as during the selected flight.

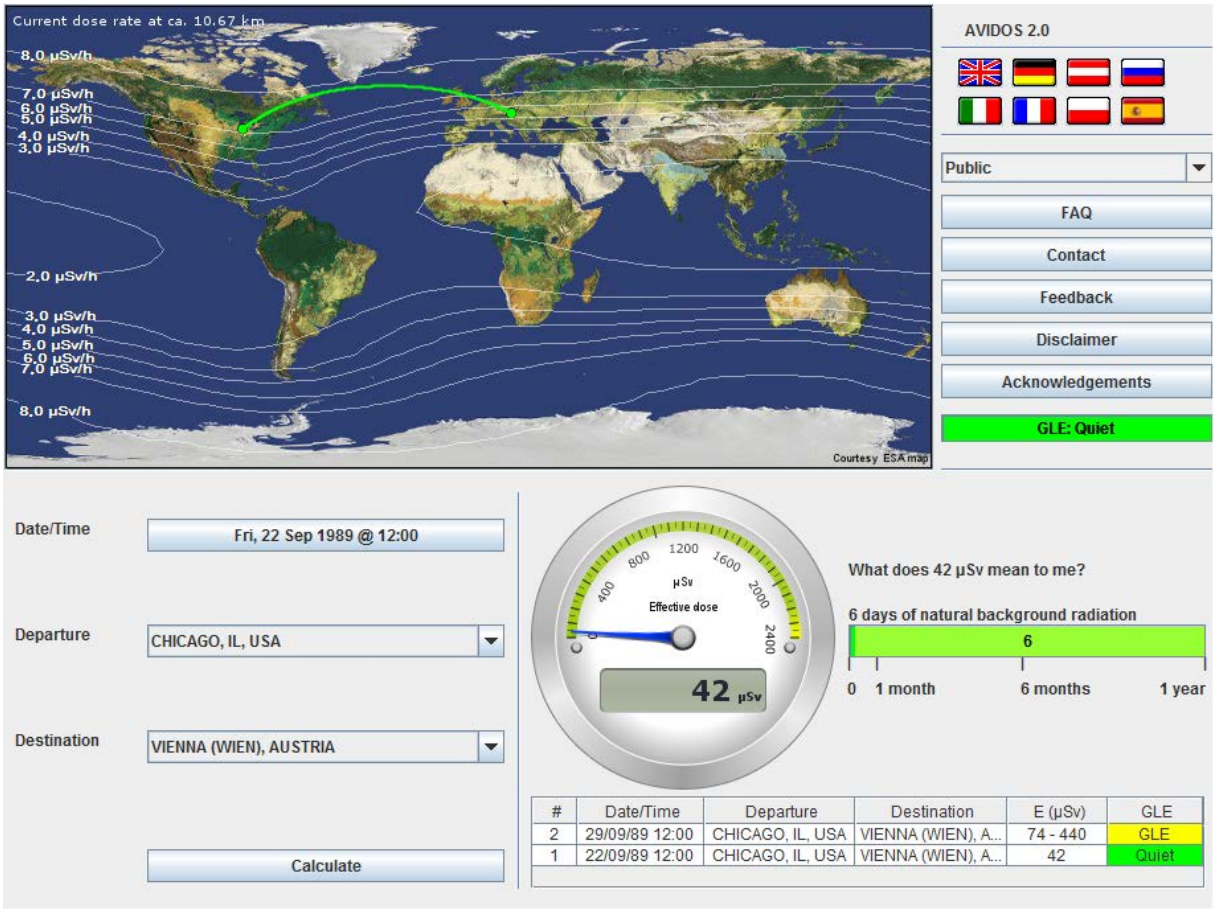

Figure 94 AVIDOS 2.0 online: public mode with examples of radiation exposure assessment for flight during GLE event (Flight#2, top in the table) and during normal solar conditions (Fligth#1, bottom in the table)

13.3.2. Aircrew mode

For those who are more enquiring and like to explore, AVIDOS 2.0 offers “aircrew mode”. In this mode user can easily appreciate influence of flight route, altitude, flight duration and even flight date on the assessed radiation exposure by having the possibility to change all those parameters. In this mode user can change date and time of the flight, departure, destination, cruising altitude, and flight duration. Figure 95 below presents effective dose assessment for two flights that differ only in cruising altitude. For Flight#1 (in the bottom of the table) performed on 16.06.2017 at 15:35 with cruising altitude at FL350 (≈10.67 km) and duration of 10 hours, effective dose is assessed to be 72 µSv. By changing the altitude to FL450 (≈13.75 km), the assessed effective dose rises to 112 µSv even though the flight was shorter: 8:15 hours. Similar analysis can be performed changing duration of the flight, or departure date setting in once in solar minimum (e.g. 1998) and once in solar maximum (e.g. 2002). Calculation results are displayed in the same way as in “public mode” but in “aircrew mode” user can download calculated flights for personal use. In addition, a total effective dose from all calculated flights is displayed.

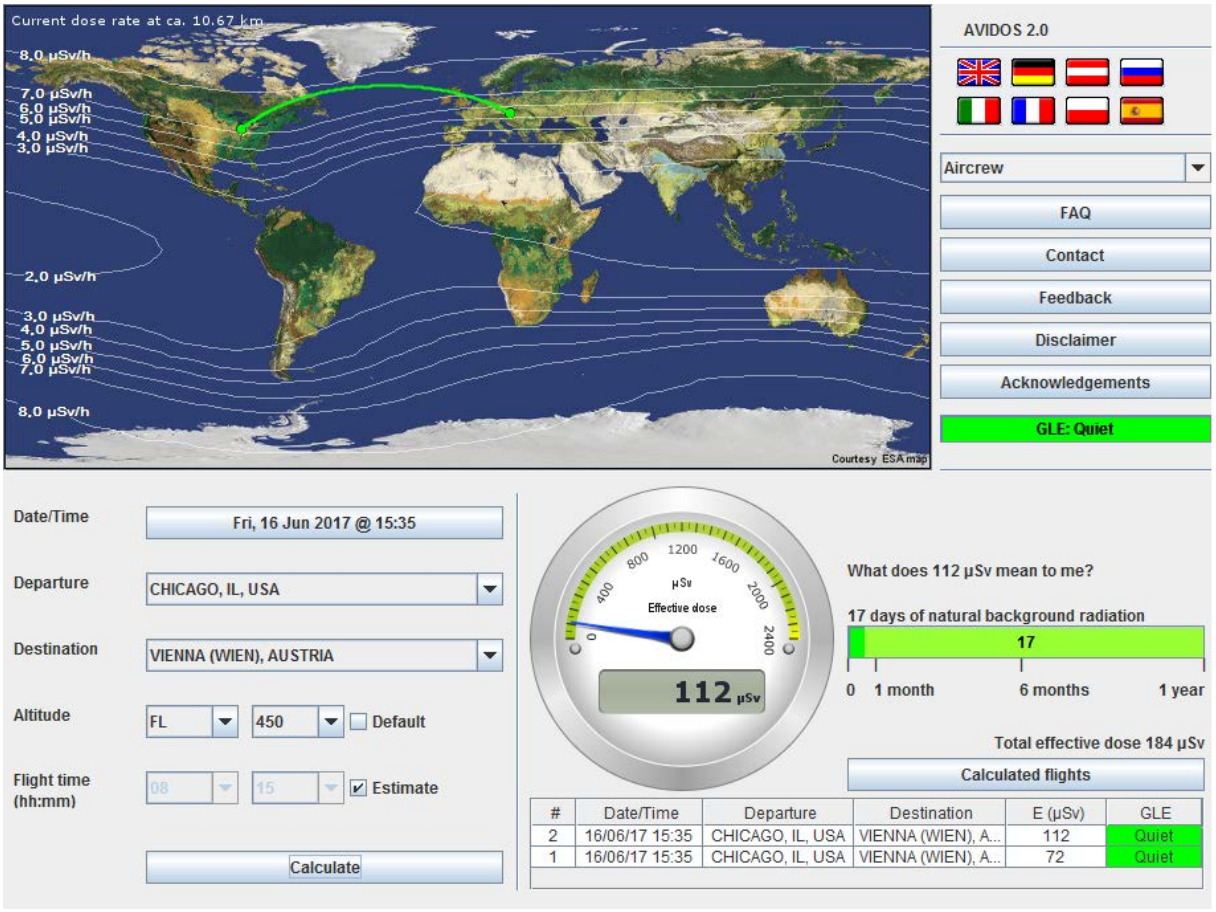

Figure 95 AVIDOS 2.0 online: aircrew mode with examples of radiation exposure assessment for flight at default FL350 (≈10.67 km) altitude and estimated 10 hours duration (Flight#1 bottom in the table), and flight at higher FL450 (≈13.75 km) altitude and estimated 8:15 hours duration (Flight#2 top in the table).

13.3.3. Waypoint mode

"Waypoint mode" (Figure 96) offers a maximum flexibility when entering flight data. This mode allows for dose assessment for a waypoint-by-waypoint designed flight that includes a complete set of parameters for each waypoint. Waypoints can be uploaded as batch file. Each waypoint has information on flight-id, waypoint-id, current altitude, date and time, and geographical position. The format of the input file is described in FAQ. An example of the input file can be obtained directly from the user interface; it can be modified and saved. User can load up to 10 different files at the same time. All files are analyzed and if error is encountered, an error-message is displayed. The error can be corrected from the user interface with "Edit" option. Calculations are performed only for files without errors. Results are presented in a similar manner as previously. In this mode user can obtain results not only in terms of effective dose, but also in terms of ambient dose equivalent – an option that can be useful when comparing calculated results with measurements on-board aircraft. User can download results for personal use.

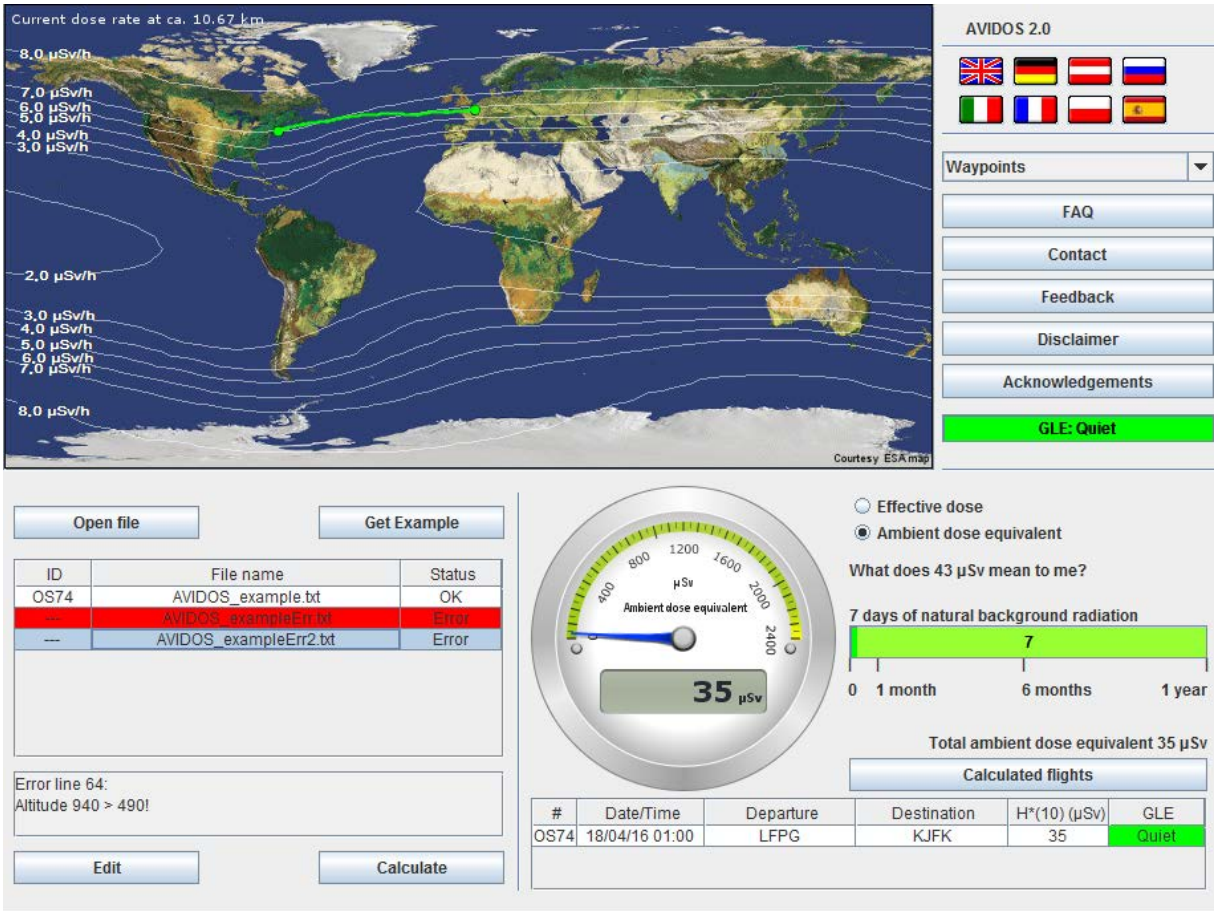

Figure 96 AVIDOS 2.0 online: waypoint mode with three input files: one correct, and 2 erroneous. Results are presented in terms of effective dose or ambient dose equivalent.

13.3.4. Science mode

"Science mode" is the most complex one. It allows for radiation dose assessment at flight altitudes during extraordinary solar conditions. In this mode, users can analyze dose dependency for different solar proton spectra or investigate different flight routes flown during the same extraordinary solar condition. Science mode offers several implemented solar proton spectra and a few representative flights. Currently, there are two GLE events implemented in AVIDOS 2.0: GLE42 from 29.09.1989 and GLE69 from 20.01.2005. It is planned to extend this set in future. For each GLE, AVIDOS offers its default-soft and default-hard spectrum calculated with algorithm described in 6.3.2 and at least one spectrum published in literature. AVIDOS 2.0 offers three representative flights: a northern Chicago-Beijing flight, a Sydney-Johannesburg flight on the southern hemisphere, and a San Francisco-Paris transatlantic flight. All parameters for the selected spectrum (dates, amplitude, and steepness) and of the selected flight (dates, altitude, and position) can be edited directly in the input tables. In this way, user can enter own spectrum or own flight. Results are calculated in terms of effective dose and ambient dose equivalent on the waypoint-by-waypoint basis separately for contribution due to GCR and due to solar event. This gives user a unique opportunity to analyze the temporal evolution of radiation exposure during the selected flight. As previously, results can be downloaded for personal use (Figure 97).

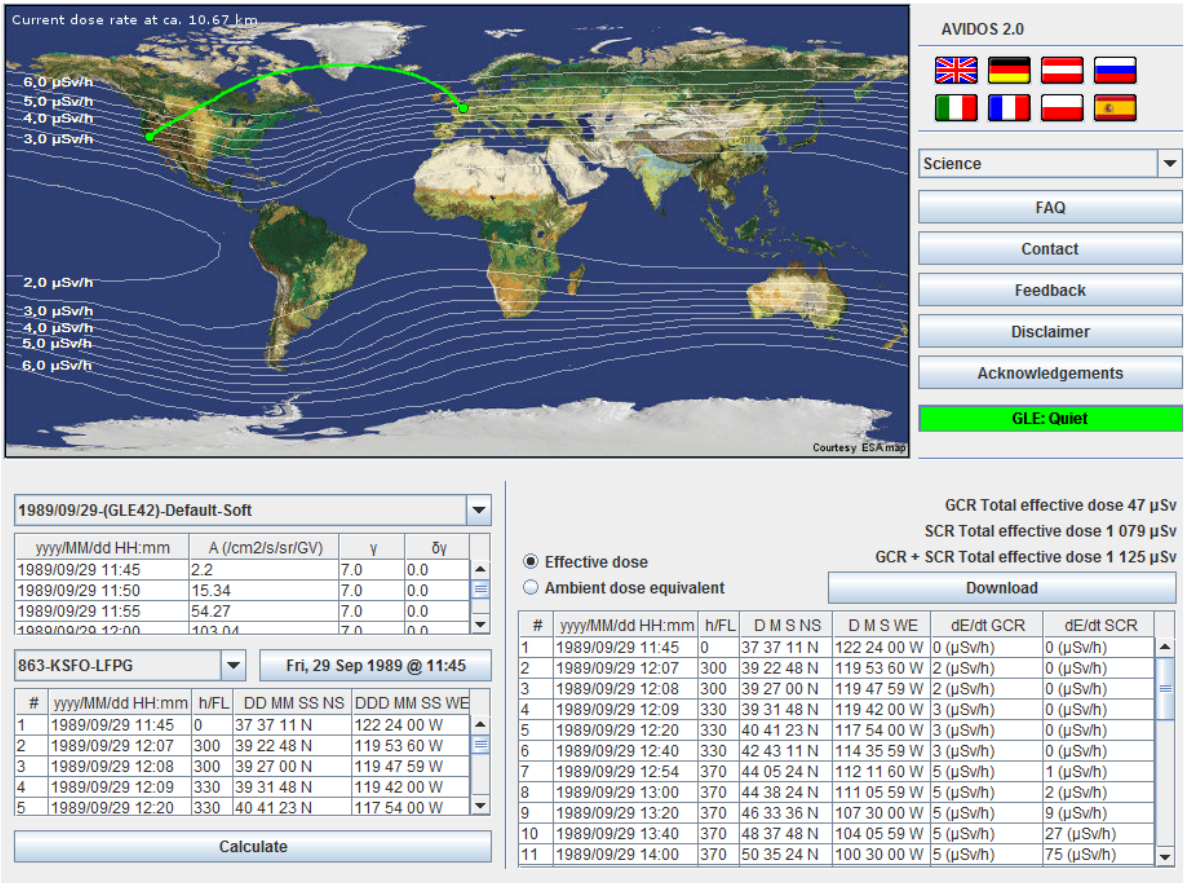

Figure 97 AVIDOS 2.0 online: science mode. All parameters of selected input spectrum and selected flights can be modified in the tables. Results (effective dose or ambient dose equivalent) are displayed on a waypoint-by-waypoint basis separately for contributions due to GCR and solar event.

13.4. AVIDOS' current cosmic radiation map

Algorithms developed for AVIDOS 2.0 were also used to build an automated procedure that creates daily an animated world map of current effective dose rate due to GCR at altitudes between 8 km and 15 km (Figure 98). The map is accessible via ESA's SSA SWE portal in the "Current Space Weather" section of the portal (http://swe.ssa.esa.int/swe). The map is free to use by everyone, e.g. it can be downloaded or linked to any web portal.

Figure 98 Animated map of current effective dose rate due to GCR at flight altitudes from 8 km – 15 km. (Source: http://swe.ssa.esa.int/swe).

13.4.1. Linking AVIDOS' current cosmic radiation map

The animated world map of current cosmic radiation exposure due to GCR (Figure 98) is free to use and can be linked into any internet web site. For example, author has linked the map on Seibersdorf Laboratories' web sites (Figure 99). The simplest HTML code to link the map is:

```
<img alt="© Seibersdorf Laboratories" title="AVIDOS Current cosmic radiation map"
  src=http://avidos.seibersdorf-laboratories.at/V2-0/CURRENT_AVIDOS.eu_c_SeibersdorfLaborGmbH.gif>
</img>
```

If clicking on the picture should open ESA portal in a new tab, the HTML code is:

```
<a
  href=http://swe.ssa.esa.int/web/guest/avidos-federated
  target="_blank">
  <img alt="© Seibersdorf Laboratories" title="AVIDOS Current cosmic radiation map"
    src=http://avidos.seibersdorf-laboratories.at/V2-0/CURRENT_AVIDOS.eu_c_SeibersdorfLaborGmbH.gif>
  </img>
</a>
```

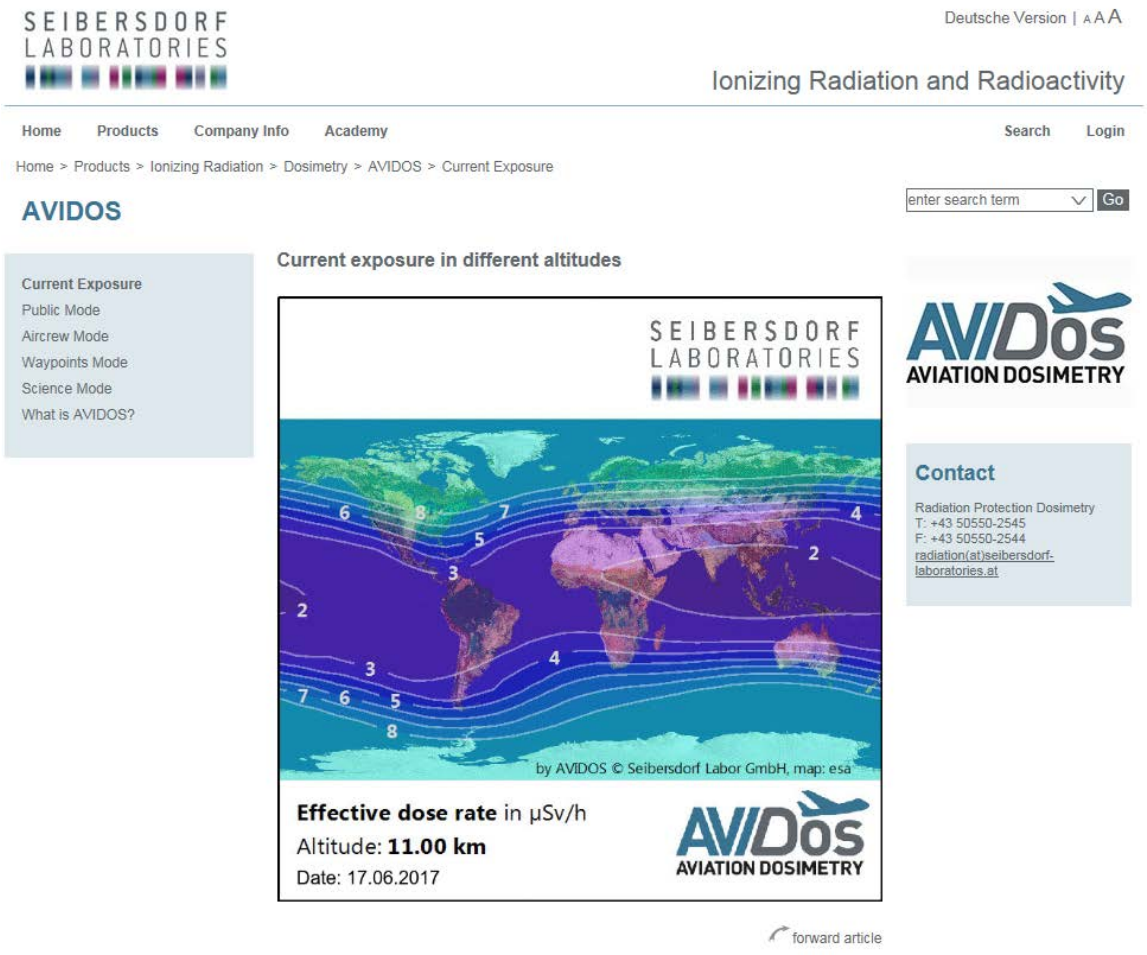

Figure 99 An Example of linking AVIDOS' current radiation exposure map on external web sites (source: https://www.seibersdorf-laboratories.at/en/products/ionizing-radiation/dosimetry/avidos/current-exposure)

14. Appendix C – Author's contributions to publications

14.1. List of scientific publications

1. **Latocha, M**., Beck, P., Rollet, S. *Cosmic radiation exposure at aircraft crew workplaces,* Proceedings of European IRPA congress on radiation protection - Radiation protection: from knowledge to action; Paris (France); 15-19 May 2006. Accessible online at IAEA website: http://www.iaea.org/inis/collection/NCLCollectionStore/_Public/39/016/39016818.pdf
2. **Latocha M**, Autischer M, Beck P, Bottolier-Depois JF, Rollet S, Trompier F., *The results of cosmic radiation in-flight TEPC measurements during the CAATER flight campaign and comparison with simulation,* Radiat Prot Dosimetry. 2007;125(1-4):412-5. Epub 2006 Oct 15.
3. **M. Latocha**, P. Beck, *Research on Radiation Effects in Aviation Altitudes During the Last Solar Cycle*, Proceedings of RADECS 2010, Tyrol, Austria, 2010
4. **Latocha M**, Beck P, Rollet S., *AVIDOS - a software package for European accredited aviation,* Radiat Prot Dosimetry. 2009 Oct;136(4):286-90. doi: 10.1093/rpd/ncp126. Epub 2009 Jul 15.
5. **M. Latocha**, P. Beck, *Cosmic Radiation Assessment at ESA's Space Weather Portal with AVIDOS*, Proceedings of RADECS 2016 conference, IEEE TNS in press, 2016

14.2. List of selected additional publications

1. Contribution to Chapter III Measured and calculated ambient dose equivalent rate data at aircraft altitudes (pp. 16 – 65) and Appendix A10 (pp 158 – 168) in: EC Radiation Protection 140, Cosmic Radiation Exposure of Aircraft Crew, Compilation of Measured and Calculated Data.

   also published as:
   Final Report of EURADOS WG5 edited by L. Lindborg, D. T. Bartlett, P. Beck, I. R. McAulay, K. Schnuer, H. Schraube and F. Spurný.
2. P. Beck, **M. Latocha**, S. Rollet, G. Stehno, TEPC reference measurements at aircraft altitudes during a solar storm, Advances in Space Research, Volume 36, Issue 9, 2005, Pages 1627–1633
3. M Autischer, P Beck, **M Latocha**, S Rollet, G Battistoni, J F Bottolier, F Trompier, A Ferrari, Simulation of TEPC response to cosmic radiation during dedicated flight campaign, The Monte Carlo Method: Versatility Unbounded In A Dynamic Computing World, Chattanooga, Tennessee, April 17–21, 2005, on CD-ROM, American Nuclear Society, LaGrange Park, IL (2005)
4. P. Beck, M. Wind, S. Rollet, **M. Latocha**, F. Bock, H. Böck, Y. Uchihori Microdosimetric GEANT4 and FLUKA Monte Carlo Simulations and Measurements of Heavy Ion Irradiation of Silicon and Tissue, IEEE Transactions on Nuclear Science (Volume: 53, Issue: 6, pp. 3701-3706, Dec. 2006)
5. Rollet, S., Beck, P., Bock, F., Ferrari, A., **Latocha, M.**, Uchihori, Y., Wind, M. Microdosimetric Monte-Carlo Simulations and Measurements of Heavy Ion Irradiation of a TEPC, 36th COSPAR Scientific Assembly. Held 16 - 23 July 2006, in Beijing, China. Meeting abstract from the CDROM, #2376
6. Autischer M, Beck P, Kindl P, **Latocha M**, Rollet S. Calibration and background measurements with a tissue equivalent proportional counter. Radiat Prot Dosimetry. 2007;125(1-4):429-32. Epub 2007 Feb 3.

7. Beck P, **Latocha M**, Dorman L, Pelliccioni M, Rollet S.Measurements and simulations of the radiation exposure to aircraft crew workplaces due to cosmic radiation in the atmosphere. Radiat Prot Dosimetry. 2007;126(1-4):564-7. Epub 2007 May 21.

8. Rollet S, Autischer M, Beck P, **Latocha M**. Measurement and simulation of lineal energy distribution at the CERN high energy facility with a tissue equivalent proportional counter. Radiat Prot Dosimetry. 2007;125(1-4):425-8. Epub 2007 Feb 3.

9. L. Lindborg, P. Beck, J. F. Bottolier-Depois, **M. Latocha**, J. Lillhök, S. Rollet, H. Roos, J. Roth, H. Schraube, F. Spurny, G. Stehno, F. Trompier, F. Wissmann Determinations of H*(10) and its dose components onboard aircraft, Radiat Prot Dosimetry (2007) 126 (1-4): 577-580

10. J. Lillhök, P. Beck, J.F. Bottollier-Depois, **M. Latocha**, L. Lindborg, H. Roos, J. Roth, H. Schraube, F. Spurny, G. Stehno, F. Trompier, F. Wissmann A comparison of ambient dose equivalent meters and dose calculations at constant flight conditions, Radiation Measurements, Volume 42, Issue 3, March 2007, Pages 323–333

11. Bottollier-Depois JF, Beck P, Bennett B, Bennett L, Bütikofer R, Clairand I, Desorgher L, Dyer C, Felsberger E, Flückiger E, Hands A, Kindl P, **Latocha M**, Lewis B, Leuthold G, Maczka T, Mares V, McCall MJ, O'Brien K, Rollet S, Rühm W, Wissmann F. Comparison of codes assessing galactic cosmic radiation exposure of aircraft crew. Radiat Prot Dosimetry. 2009 Oct;136(4):317-23. doi: 10.1093/rpd/ncp159. Epub 2009 Aug 23 also published in extended version as EURADOS Raport: EC Radiation Protection 173, https://ec.europa.eu/energy/sites/ener/files/documents/173.pdf

12. Beck P, Dyer C, Fuller N, Hands A, **Latocha M**, Rollet S, Spurný F. Overview of on-board measurements during solar storm periods. Radiat Prot Dosimetry. 2009 Oct;136(4):297-303. doi: 10.1093/rpd/ncp208.

13. S. Rollet, P. Beck, **M. Latocha**, M. Wind, G. C. Taylor, TEPC measurements and monte carlo calculations for evaluating ambient dose equivalent response in mixed radiation fields around the shielded area of a carbon ion accelerator. Nuclear technology 168(1):118-122, October 2009

14. P. Beck, Th. Berger, M. Hajek, **M. Latocha**, G. Reitz, S. Rollet, N. Vana, A. Zechner MATSIM: Development of a voxel model of the MATROSHKA astronaut dosimetric phantom exposed onboard ISS, Proceedings of Radiation and Its Effects on Components and Systems (RADECS), 2009 European Conference on Radiation and Its Effects on Components and Systems, DOI: 10.1109/RADECS.2009.5994675

15. P. Beck, **M. Latocha**, S. Rollet, SOLARDOS - Dosisabschätzung der Strahlenbelastung des fliegenden Personals verursacht durch Solar Events, Raport AIT AIT-HNA-0008, ISSN 0253-527, 2009

16. Beck, P., Rollet, S., Berger, Th., Bergmann, R., Hajek, M., **Latocha, M**., Vana, N., Zechner, Reitz, G. MATSIM -The Development and Validation of a Numerical Voxel Model based on the MATROSHKA Phantom, Proceedings of COSPAR 2010, Symposium F, session 24, paper number F24-0020-10 (Oral)

17. P. Beck, S. Rollet, M. Hajek, A. Zechner, **M. Latocha**, M. Wind, Th. Berger, G. Reitz, Ch. Hofstatter MATSIM: A voxel model for the astronaut dosimetric phantom MATROSHKA Proceedings of Radiation and Its Effects on Components and Systems (RADECS), 2011 12th European Conference on Radiation and Its Effects on Components and Systems, DOI: 10.1109/RADECS.2011.6131437 and IEEE Transactions on Nuclear Science 58(4):1921-6 August 2011 DOI: 10.1109/TNS.2011.2157704

18. Rollet S, Colautti P, Grosswendt B, Herault J, Wind M, Gargioni E, Beck P, **Latocha M**, Moro D. Microdosimetric assessment of the radiation quality of a therapeutic proton beam: comparison between numerical simulation and experimental measurements. Radiat Prot Dosimetry. 2011 Feb;143(2-4):445-9. doi: 10.1093/rpd/ncq483. Epub 2010 Dec 15.

14.3. Consultations to international organizations

1. Consultant to the Report Committee: ICRU REPORT 84, Reference Data for the Validation of Doses from Cosmic-Radiation Exposure of Aircraft Crew, Journal of the ICRU Volume 10 No 2 2010.
2. Regular participation in EURADOS (WG5 and WG11) since 2005.

14.4. Presentations and scientific posters on conferences and workshops

1. Presentation „The results of cosmic rays in in-flight measurements with TEPC during CAATER flight campaign and comparison with simulation." Workshop on individual monitoring of ionising radiation, IM2005, Vienna, Austria, 2005
2. Poster "Cosmic Radiation Exposure at Aicraft Crew Workplaces", IPRA 2006, Paris, France, 2006
3. Presentation „MATSIM - Numerical simulations of the radiation exposure of the MATROSHKA phantom" 13th Annual Workshop on Radiation Monitoring for the International Space Station, Kraków, Poland, 2008
4. Poster "Research on Radiation Effects in Aviation Altitudes During the Last Solar Cycle", RADECS 2010, Tyrol, Austria, 2010
5. Presentation "Overview on cosmic radiation at aircraft altitudes", European Space Weather Week, Brugge, Belgium, 2009
6. Poster „AVIDOS - a Tool at ESA's Space Weather Portal for the assessment of Space Radiation on-Board Aircraft", IEEE Nuclear and Space Radiation Effects Conference (NSREC), Paris, France, 2014
7. Presentation „AVIDOS 2.0 - Current developments for the assessment of radiation exposure at aircraft altitudes caused by solar cosmic radiation exposure", European Space Weather Week, Liege, Belgium, 2014
8. Presentation "Space Weather related activities at Seibersdorf Laboratories", Austrian Space Weather Workshop, Kanzelhöhe Observatory, 2015
9. Presentation „AVIDOS 2.0 - Current developments for the assessment of radiation exposure at aircraft altitudes caused by solar cosmic radiation exposure", Austrian Radiation Protection Association Conference, Baden, Austria, 2015
10. Presentation „AVIDOS 2.0 – a software tool for nowcasting radiation exposure at flight altitudes caused by cosmic radiation during solar storms", European Space Weather Week, Oostende, Belgium, 2015
11. Poster "Forecasting and Nowcasting of Radiation Exposure On-Board Aircraft with AVIDOS" on 13th European Space Weather Week, Oostende, Belgium 2016
12. Presentation „Monte Carlo modelling of the TEC-Laboratory" during inauguration of the TEC (Testing of Electronic Components) laboratory opening, Seibersdorf , Austria, 2016
13. Poster "Cosmic Radiation Assessment at ESA's Space Weather Portal with AVIDOS" on RADECS 2016, Bremen, Germany, 2016

This page is left blank

This page is left blank